CRANFIELD UNIVERSITY

DEFENCE COLLEGE OF MANAGEMENT AND TECHNOLOGY

DEPARTMENT OF APPLIED SCIENCE, SECURITY AND RESILIENCE

Ph.D. Thesis

Academic year 2007-2008

Scilla Roncallo

A study of electrostatically sprayed $CuInS_2$ and ZnS thin films

Supervisor: Dr J.D. Painter

May 2008

This thesis is submitted in partial fulfilment of the requirements for the degree of Doctor of Philosophy

ABSTRACT

The investigation of ternary compounds for the fabrication of thin film solar cells is well documented but the production of thin films by electrostatic spray deposition (ESD) is still limited. This thesis represents the first attempt to deposit photovoltaic thin films using this novel method.

The lack of information regarding the deposition of $CuInS_2$ by ESD required a statistical investigation of the effects of different deposition variables. To achieve this, a new image analysis method was developed to calculate the variation of the thickness of the as-deposited films using their optical density. The thickness variation across the sample was then used to define its uniformity.

Once the conditions for the best uniformity were defined, different needle and substrate materials were investigated to try and improve the performance of the ESD method for potential large scale production.

A formation of precipitates was observed during the preparation of the chloride precursor solutions (prepared from $CuCl_2$, $InCl_3$ and thiourea salts). A possible reaction mechanism was proposed and the chemical composition of precipitates analysed. An explanation of the absence of the precipitate during the preparation of a nitrate starting solution (from $Cu(NO_3)_2$, $In(NO_3)_3$ and thiourea salts) was reported.

The behaviour of the aerosol cone for the two different starting solutions (nitrate and chloride) was established using the laser-based particle image velocimetry (PIV) measurement technique. The properties of as-deposited films sprayed by the two precursor solutions were thoroughly investigated using a number of techniques including X-ray diffraction (XRD), Rutherford back-scattering (RBS), optoelectronic characterisation and miniSIMS.

The effect of different precursor molar ratios on the properties of as-deposited films was studied for both the nitrate and chloride based solutions using the above techniques.

ZnS films were also deposited using ESD for the first time. Using the information acquired during the deposition of the $CuInS_2$, a fully comprehensive analysis of the effect of different deposition conditions and starting solution properties was performed.

Finally, $CdS/CuInS_2$ and $ZnS/CuInS_2$ junctions were prepared and tested using EQE measurements in solution. Substrate and superstrate device configurations were used to prepare complete solar cells which were analysed using IV measurements.

Alla mia famiglia

ACKNOWLEGMENTS

THANKS TO…..

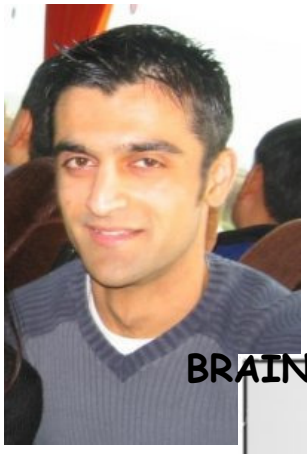

BRAINS

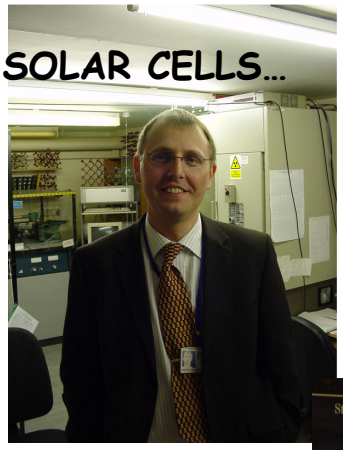

ENDARINO

Contents

List of figures

Chapter 1

Chapter 2

Chapter 3

Chapter 4

Chapter 5

Chapter 6

Chapter 7

Chapter 8

List of tables

Chapter 3

Chapter 4

Chapter 5

Chapter 6

Chapter 7

Chapter 8

Glossary

α = Absorption coefficient

α = Semi-angle of the Taylor's cone

ΔG^0_s = Free energy of solvatation

δ_u = Dimensionless parameter

ε = Liquid to vacuum permittivity ratio

ε_0 = Electrical permittivity of vacuum

ε_0 = Permittivity of free space

Φ = EQE

γ = Surface tension

η = Dynamic viscosity

η = Efficiency of the solar cell

λ = Mean free path

λ = Wavelength

μ = Viscosity

$\mu(t)$ = Variance of the thickness

μUT = Micro Uniformity Test

ν = Droplet velocity

ν = Frequency

π = Pi

θ = Angle

Θ = Photon flux

ρ = Density

σ = Surface tension

a = Acceleration

A = Amplitude

A = Area

A = Area of semiconductor

A = Path distance for the reflected rays

A = Peak area

A= Constant

AM =Air Mass

C = Correction coefficient

c = Speed of light

c,a = Lattice parameters

CBD = Chemical Bath Deposition

CCD = Charge Coupled Device

CIGS = Copper Indium Gallium Selenide

CIS = $CuInS_2$

CRM = Charge Residual Model

d = diameter of the droplets

d = Distance between electrodes

d = distance between two planes

D =1/W

DSC = Differential Scanning Calorimetry

D_v = Diffusion coefficient of the vapour solvent in air

E = electrostatic field

E = Ion energy

E_1 = Energy difference between the Fermi level and valance band for a p material

E_2 = Energy difference between the Fermi level and valance band for a n material

E_c = Conduction band

E_{cn} = Minimum energy of the conducting band for a n type material

E_{cp} = Minimum energy of the conducting band for a p type material

E_f = Fermi level

eff = efficiency

E_{fn} = Fermi level energy for n type material

E_{fp} = Fermi level energy for p type material

E_g = Band gap

Ei = Energy of incident ion

$E_{p = Energy\ of}$ photon

EQE = External Quantum Efficiency

ESAVD = Electrostatic assisted Vapour Deposition

ESD = Electrostatic Spray Deposition

E_{sp} = electrostatic field

E_{surf} = Electric field of the surface of the Taylor's cone

E_v = Valence band

E_{vn} = Maximum energy of the conducting band for a n type material

E_{vp} = Maximum energy of the conducting band for a p type material

f = Atomic wave factor

F = force

F = structure factor

f(ε) = Function of ε

FF= Fill factor

FTO = Fluorine-doped Tin Oxide

FWHM = Full-Width Half-Maximum

g = gravitational acceleration

grad(t) = Gradient of the thickness

h = Planck's constant

I = Intensity of transmit radiation

I = Output current

I= Spray current

I_0 = Diode saturation current

I_0 = Intensity of incident radiation

I_D = Diode current

IEM = Ion Evaporation Model

I_L = Light generator

I_M = Current at the maximum power point

I_{SC} = Short circuit current

ITO = Indium tin Oxide

I-V = Current-Voltage (curve)

k = Boltzmann's constant

k = Conductivity

K = Constant independent from the temperature

K = Liquid conductivity

k =Force constant

L = distance needle-substrate

L = Minority carrier diffusion

LDA = Laser Doppler Anemometry

LDA = Laser Doppler Anemometry

m = mass

M = Molecular mass of the solvent

MUT = Macro Uniformity Test

n = integer

N = Number of photon

N_p =Number of photon

P = power

P_∞ = Partial vapour pressure away from the droplets

P_d = Partial vapour pressure on the droplets surface

PIV = Particle Image Velocity

P_{MAX} = Maximum power

q = droplet charge

q = Electron charge

Q = Flow rate

qr = Rayleigh limit

R = Drop radius

r = Droplet diameter

R = Gas constant

r = ion radius

r = radius

R = Resistivity

R_{AC}, R_{BC} = Chemical bond (A-C, B-C) lengths

RBS = Rutherford Back Scattering

RMS = Root Mean Square

S = Conductance

s = Distance

SIMS = Secondary Ion Mass Spectroscopy

T = Absolute temperature

T = ambient temperature

t = Film thickness

t = Flight time

TCO = transparent conductive oxide

T_d = Droplet temperature

TGA = Thermogravimetric Analysis

V = Speed

V = Voltage

V_0 = Initial speed

V_M = Voltage at the maximum power point

V_{OC} = Open circuit

W = FWHM

W = Width of space-charge

$X_{A\infty}$ = Mole fraction of the species A far from the droplets

XRD = X-Ray Diffraction

Chapter 1

Introduction

In January 2007, the Intergovernmental Panel (a scientific intergovernmental body) published a scientific report about climate change with contributions from over 640 scientists in 40 countries (IPCC 2007). The message was clear: the climate is changing and immediate action is required.

The main reason for climate change (according to the IPCC) is an increase in the levels of greenhouse gases in the atmosphere. This phenomenon has been observed since the pre-industrial period and is inextricably linked to human activity; especially the burning of fossil fuels. Currently, 80% of the world's energy demand is met through the use of fossil fuels. This energy demand has been increasing steadily in the last few decades (IEA 2004) and by 2030, it is expected that demand will be 65% higher than today's levels. Thus, the

need for methods of producing energy which can reduce and even potentially stop the increment in greenhouse gases in the atmosphere are now a key requirement to combat global warming. This transfer from the use of fossil fuels to 'clean' renewable energy sources will only be possible when the renewable sources are able to compete economically with current sources.

Among the plethora of renewable energy technologies, solar has the most potential. The solar energy resource is by far the largest among renewable energy resources (Goldemberg 2000) and its conversion into electricity could play an important role in the supply of energy. The main barrier to widespread use of this environmentally-friendly form of energy over the last few decades has been the high unit energy cost for production of electricity by solar power (PV TRAC 2005). A reduction in turn-key photovoltaic system prices and further technological developments are necessary to allow the cell manufacturers to maintain and reinforce their position in the global market. Research and development will be the key to further success for photovoltaic applications (Working Group 3 2007).

Thin film-based technologies are potentially cheaper than silicon-based photovoltaic technologies since their production is not so heavily dependent on semiconducting materials, and thin films can be deposited onto low cost substrates at lower temperatures *etc* (Luque et al. 2002). They are also stable in outdoor conditions over a long period of time and have a small "energy pay back time" (= (energy input)/(annual energy saved) (Working Group 3 2007). Despite these highly desirable properties, thin film technology currently shares only a small part of the photovoltaic market (less than 10%) (PV TRAC 2005). Fundamental research is necessary to improve the market share. This can be achieved through for example research aimed at increasing device efficiency (by improving material quality), studying and controlling the optical and electrical properties of the as-deposited films and understanding the connection between the film deposition conditions and the properties of the complete devices.

This research contained within this thesis aims to addresses the key requirements outlined above. This research project represents the first attempt to deposit ZnS/$CuInS_2$ based solar

cells using electrostatic spray deposition (ESD) which may offer a suitable compromise between cell quality and cell price. $CuInS_2$ is one of most promising low-cost, non-toxic and potentially highly efficient materials for terrestrial photovoltaic applications. For economic reasons, ESD is an attractive cell construction method due to the large deposition areas attainable, the good uniformity of the as-deposited films and the relatively low cost of the setup. A water/alcohol precursor solution is atomised by an electrostatic field and is sprayed onto a heated substrate where the photo-active film is grown. A stable thin film with excellent adhesion on the substrate and a well controlled stoichiometry can be deposited in a single run and in an open atmosphere.

1.1. Introduction to solar cells

A solar (or photovoltaic) cell is a device that generates electricity when subjected to illumination. It is made from a semiconductor material and it is able to convert incident photons (quantum of energy) into direct current, a phenomenon called the photovoltaic effect. The principle of the photovoltaic effect can be better understood using the example of silicon. Silicon is an element from the 4th group of the periodic table. It crystallizes with a diamond structure where each atom has a tetrahedral coordinate.

The electrons of the crystal occupy defined bands: the valence and the conductive. The valence band (E_v) (Figure 1-1) is filled by the electrons responsible for the covalent bonds whilst the conduction band (E_c) is the first lowest empty band (for T=0K). The difference in energy between these two bands is called band gap (E_g) and is one of the most important parameters in the characterisation of a semiconductor material. The Fermi level (E_f) is located in the middle level between the conduction and valence bands. A pure semiconductor (also known as an intrinsic semiconductor) at a temperature, T, (different from the absolute zero) has a nearly filled valence band and a nearly empty conduction band. Carriers can be introduced in the intrinsic semiconductor through a process called doping. For example, let's suppose phosphorous impurities (an element of the 5th group of the period table) are introduced in to the silicon crystal. Four of the five phosphorous electrons are used to generate covalent bonds with the silicon atoms but the fifth electron of

each phosphorous is promoted to the conduction band. These electrons are mobile giving conduction properties to the solid. This class of semiconductors are called n-type semiconductors. When the semiconductor is doped with an element of the 3rd group of the periodic table (for example boron) an electron deficiency results. This is known as a p-type semiconductor and is capable of carrying current.

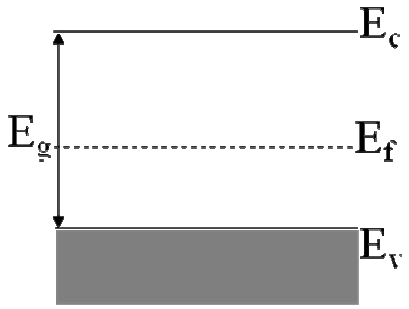

Figure 1-1: Band description for n-type and p-type materials

The heart of the solar cell device is the p-n junction which is formed when p-type and n-type materials are placed in contact with each other. Due to the charge concentration gradient, electrons move from the p-type to the n-type side of the junction and holes move in the opposite direction generating a depletion area close to the junction. The movement of electrons and holes leaves positive impurities in the n-type material and negative impurities in the p-type material. The total stationary charge is zero in the depletion area. The width of the depletion area depends on the concentration of the impurities. The flow of charge also generates an electric field as shown in Figure 1-2. The impurity atoms produce a potential barrier which prevents further diffusion of charge while the electric field drives holes and electrons in opposite directions. At this stage, equilibrium is reached and diffusion of charge across the junction ceases.

Due to the fact that the position of the Fermi level is fixed with respect to the energy band, an alignment of the Fermi level in the p-n junction can be obtained by a relative increase of the p-region energy (Figure 1-3).

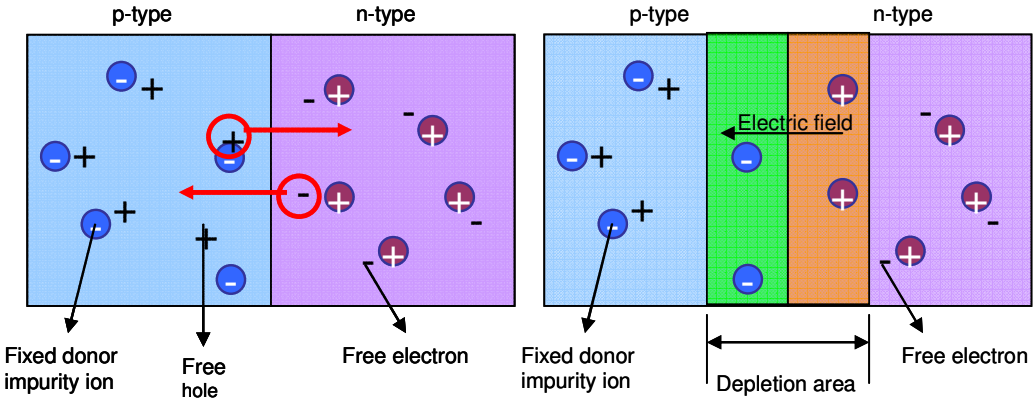

Figure 1-2: charge movement and depletion area formation.

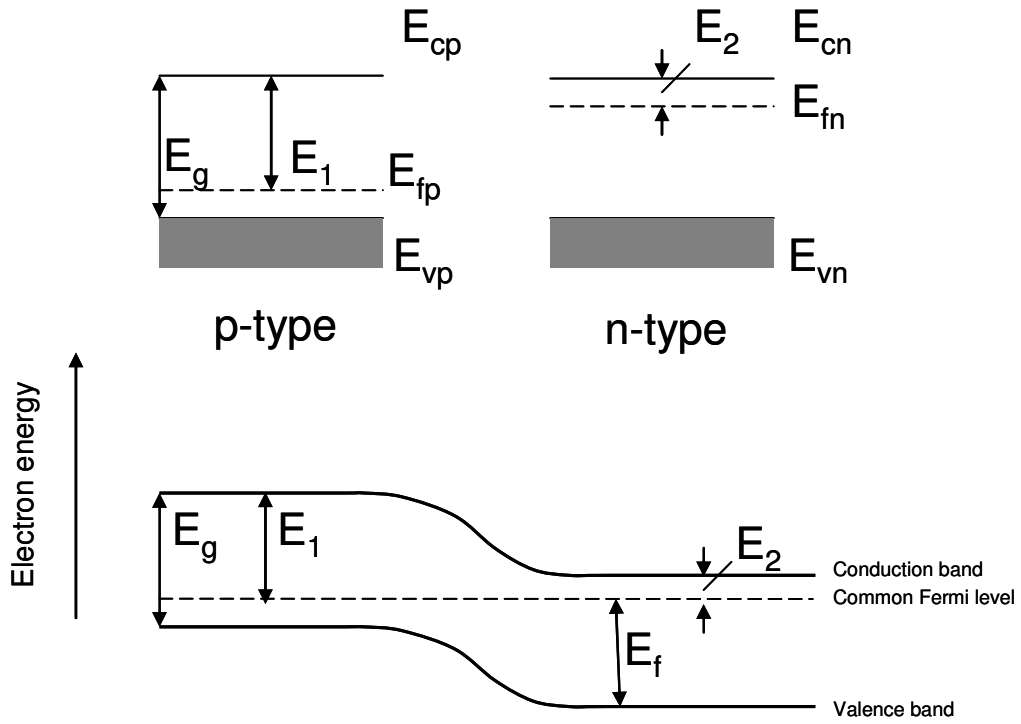

Figure 1-3: TOP: description of the band diagram for n and p materials. BOTTOM: diagram of the formation of a p-n junction. Ecp,Ecn = minimum energy of the conducting band for a p or n type material; Eg = band gap; Efp,n = Fermi level energy; Evp,Evn = maximum energy of the conducting band for a p or n type material; E_1 = Energy difference between the Fermi level and valence band for a p material; E_2 = Energy difference between the Fermi level and conduction band for an n-type material;

The current produced by the p-n junction is pulled out by the front and rear contacts which complete the cell. The performance of the cell can be measured using the I-V curve which is obtained when a cell is illuminated with constant light at constant temperature, varying the load resistance and measuring the current (Figure 1-4).

The I-V curve for a solar cell (Figure 1-4a) can be drawn using the so-called equivalent circuit (Figure 1-4b). The light generator (I_L) is represented by a current generator placed in parallel with a diode which simulates the p-n junction. The output from the circuit is given by the different between the I_L and I_D (the diode current)

$$I_D = I_0\left[\exp(qV/kT)-1\right] \tag{1.1}$$

and thus

$$I = I_L - I_0\left[\exp(qV/kT)-1\right] \tag{1.2}$$

where

I = output current

V = voltage

q = electron charge

T = absolute temperature

k = Boltzmann constant

I_0 = diode saturation current

The short circuit current (Isc) corresponds to the current produced when the solar cell terminals are short-circuited (in this condition V=0 and so R=0). Neglecting losses, each photon produces one electron and thus

$$I_L = NqA \tag{1.3}$$

Where N is the number of photons produced by the highlighted area

A = area of semiconductor

q = charge of the electron

The open circuit (Voc) corresponds to the voltage produced when the circuit is open (R=∞). Using the equation (1.2), V_{OC} can be written:

$$V_{OC} = \frac{kT}{q} \ln\left(\frac{I_L}{I_0} + 1\right) \tag{1.4}$$

I_{SC} has a small variation and thus the saturation current has the strong effect on V_{OC}. I_0 is proportional to recombination electron-hole and thus V_{OC} can be used to measure the recombination of the device. Under short or open circuit conditions, the device produces no output.

The maximum power from the cell can be calculated using equation (1.5), corresponding to the largest rectangular area under the I-V curve and is represented by "P_{MAX}" in the curve (Figure 1-4).

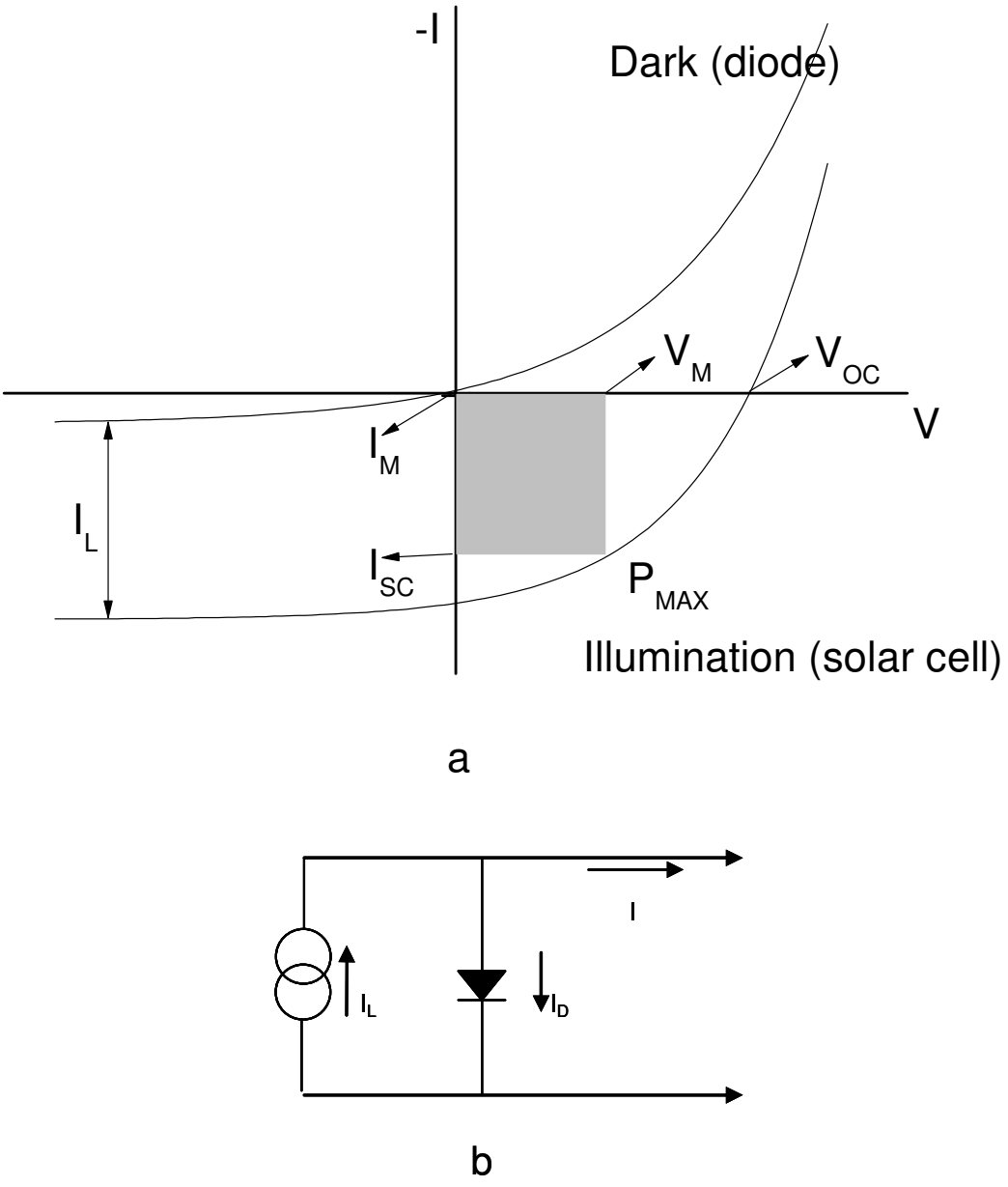

Figure 1-4: a) I-V solar cell compared with a diode; b) equivalent circuit. I_L = generation current; I_0 = saturation current; V_{OC} =open circuit voltage; I_{SC} = short circuit current; I_M = current at the maximum power point; V_M = voltage at the maximum power point; P_{MAX} = maximum power point

The fill factor (FF) is another parameter used with Voc and Isc to define the performance of the solar cell and it can be calculated from

$$P\max = V_M \cdot I_M = FF \cdot Voc \cdot Isc \tag{1.5}$$

$$\Rightarrow FF = \frac{V_M \cdot I_M}{Voc \cdot Isc} \tag{1.6}$$

where V_M and I_M are the voltage and current values at the maximum power point.

The efficiency of the solar cell (η) is the ratio of the maximum output power of the cell (obtained under standard conditions) to the power of the incident radiation (p).

$$\eta\% = \frac{P\max}{p} \cdot 100 = \frac{FF \cdot Voc \cdot Isc}{p} \cdot 100 \tag{1.7}$$

1.2. ABSORBER LAYER: $CuInS_2$

In this section, an introduction to the structure and chemical/physical properties of $CuInS_2$ will be made. (As a point of note, $CuInS_2$ and CIS will be used synonymously throughout the thesis.)

The optical and electrical properties offered by CIS have promoted a large number of fundamental studies [(Jaffe et al. 1983; Jaffe et al. 1983; Wei et al. 1999; Alonso et al. 2001)] and has resulted in considerable attention for possible applications in photovoltaic and optical devices.

1.2.1. Structural properties

The crystalline structure of $CuInS_2$ materials can be changed between two polymorph forms: sphalerite and chalcopyrite. The two structures differ in the order degree of the Cu and In and they can be identified by XRD analysis.

Chalcopyrite

The chalcopyrite cell structure can be seen in Figure 1-5 is the preferred order of $CuInS_2$ in thermal equilibrium up to 980°C (Hahn et al. 2001).

The chalcopyrite structure can be described by the I42d $\left(D_{2d}^{12}\right)$ space group and can be constructed coming from the cubic face centred structure. In fact, adding two lattice points along the diagonal line of the cube and shifting them by a/4, a/4, a/4, the diamond structure is obtained. The zincblende structure can be achieved by occupying the (001) planes in the diamond structure with two different kind of atoms. Finally, the chalcopyrite structure can be obtained by doubling the zincblende structure along the z-axis and following the rule that the anions remain on their sites while every second (001) plane is occupied by cation (Jaffe et al. 1983; Jaffe et al. 1983; Wei et al. 1999).

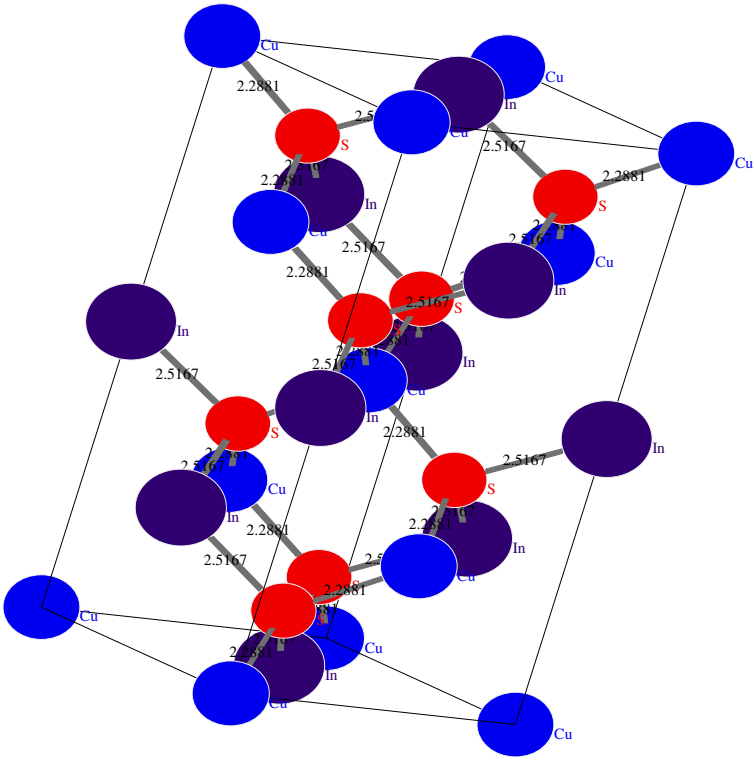

Figure 1-5: $CuInS_2$ cell

Due to the presence of two different types of cations in the unit cell, the volume of the chalcopyrite cell is four times bigger than zincblende. Moreover, in the cell, each anion, C, is tetra-coordinated by two A atoms and two B atoms, while each cation is coordinated by four C anions.

The properties of the chalcopyrite compounds are related to the zincblende structure via the facts that

- 2 different cations result in two different chemical bonds A-C and B-C with two different lengths ($R_{AC} \neq R_{BC}$)
- the tetragonal cell is distorted by the present of these cations. The tetragonal distortion (η) is given by

  $c/2a$

where *c* and *a* are the lattice parameters of the unit cell.

- The anion displacement in the chalcopyrite structure is defined as:

$$u = \frac{1}{4} + \frac{R_{AC}^2 - R_{BC}^2}{a^2}$$

In the ideal tetragonal cell u=1/4.

Using these two parameters, it is possible to define the bond lengths (Wei et al. 1999; Alonso et al. 2001):

$$R_{AC} = a \cdot \sqrt{u^2 \frac{1+\eta^2}{16}} \tag{1.8}$$

$$R_{BC} = a \cdot \sqrt{\left(u - \frac{1}{2}\right)^2 + \frac{1+\eta^2}{16}} \tag{1.9}$$

Sphalerite

The pseudo-binary diagram of $CuInS_2$ shows a solid phase transition at 980°C and 50.8 mole% In_2S_3 (Binsma et al. 1980). This transition corresponds to an order-disorder transformation from the chalcopyrite structure to the sphalerite structure. Sphalerite lattice is a cubic zincblende based unit cell and it can be described with a T_d^2 space group. The sphalerite structure is characterized by a disordering of the cation sublattice of the chalcopyrite structure. The tetragonal (chalcopyrite) - cubic (sphalerite) transition causes a statistical distribution of Cu and In on the cation sites.

1.2.2. Preparation technique

A variety of methods have been applied to the deposition of $CuInS_2$ thin films including, chemical bath deposition (CBD) (Garg et al. 1988; Sankapal et al. 2004), sputtering (Muller et al. 2004), electrodeposition (Yukawa et al. 1996) and spray pyrolysis (Tiwari et al. 1985; Marsillac et al. 2003; Peza-Tapia et al. 2005)

In this thesis, the use of electrostatic spray deposition to deposit $CuInS_2$ is investigated. ESD is a simple and very efficient deposition technique which can be used to spray CIS. Unfortunately, the application of this technique for photovoltaic devices is still limited. Although there is a paucity of literature on $CuInS_2$ by ESD, the technique shows a number of similarities with the spray pyrolysis deposition method. A review of this literature is described below.

Spray pyrolysis

Spray pyrolysis is an attractive technique as large-area films with good uniformity can be grown at low cost. Generally, the spray pyrolysis apparatus consists of a reaction chamber containing the atomizer, a heater with a temperature controller, a solution reservoir and a carrier gas (usually N_2) (Ortega-Lopez et al. 1998).

Several groups have deposited $CuInS_2$ by Spray pyrolysis including Zouaghi et al and Mere et al (Zouaghi et al. 2001; Mere et al. 2003; Oja et al. 2005). $CuCl_2$, Thiourea, $InCl_2$ and HCl (in different concentrations) are used in solution to deposit $CuInS_2$ thin films. Deionised water is used to prepare the acid-water solutions of the three chemicals.

The solution is fed through the nozzle by gravity where it is atomized and sprayed with the carrier gas onto the hot substrate.

The structure, composition and morphology of the as-sprayed films have been shown to depend on the growth temperature, pH, and the molar ratio of S/Cu and Cu/In of the solution.

The effect of a rise in the deposition temperature (between 260°C and 400°C) is an improvement in crystallinity and an increase of the preferred orientation along the 112 plane of the as-deposited films (Ortega-Lopez et al. 1996; Bouzouita et al. 1999). At high temperature (400°C) Bouzouita et al. (Bouzouita et al. 1999) observed the appearance of extra phases which have been attributed to indium oxide impurities.

An additional aspect must be taken into consideration: the connection between the substrate-temperature and solution composition. The temperature required for the growth of single phase $CuInS_2$ depends also on the Cu/In ratio of the starting solution (Tiwari et al. 1985; Krunks et al. 1999). For example, at 320ºC only copper-rich solutions can be used; if [Cu]/[In]=1 or [Cu]/[In]<1 multi-phase films are obtained.

The appearance of unidentifiable peaks in X-ray diffraction patterns depends also on the solution pH (Krunks et al. 1999). The use of a solution at pH=4 instead of a more acid solution (pH=3) decreases the height of these peaks.

Moreover, some as-deposited films from Cu-rich solutions show the presence of agglomerates (Krunks et al. 1999). The number and dimensions of these agglomerates increase with the copper concentration. The agglomerates are not surface defects but grow through the film. Moreover, a chemical etch of the film with KCN* shows different results for the agglomerates and for the film: whilst the composition of the film remains unchanged (and corresponding to $CuInS_2$), the chemical composition of the agglomerates corresponds to a ternary alloy deficient in sulphur ($CuInS_{2-x}$). An explanation may be the presence of a copper sulphide phase which may cover the agglomerates and fill the cavities. This phase is

* Binary Cu-S compounds (especially CuS) can segregate at the surface of the layer during the deposition process and/or at grain boundaries. The Cu-S phases behave like semimetallic p^+ semiconductors and thus must be removed through a chemical etching process. KCN is a selective etchant which reacts with Cu-S phases but not with $CuInS_2$. During the etch, the Cu_2S and CuS were dissolved and Cu cyanides and Cu cyanocuprates were formed.

soluble in KCN solution while the $CuInS_2$ is not. This assumption can't be confirmed because of the lack of information about the ternary diagram.

Impurities

Chlorine: the concentration of chlorine in the final sample depends on the growth temperature and the composition of the solution (Krunks et al. 2002). At a low temperature (260ºC-280ºC), the concentration of chlorine is found to be around 2-3%. Increasing the substrate temperature to over 400ºC decreases the chlorine concentration to below 0.5%.

Oxygen: The presence of oxygen can't be avoided because it is absorbed onto the surface of the film. More serious is the problem of the formation of oxygen-containing phases (such as In_2O_3) during the deposition process (Krunks et al. 2002) because they may change the properties of the samples.

Carbon and Nitrogen: The results proposed by Krunks (Krunks et al. 2002) show that the carbon concentration can be as high as 4-6 mass% while the nitrogen is lower (around 0.4 mass%). Both tend to decrease with increasing growth temperature.

Optical properties

The absorption coefficient and band-gap can be evaluated from optical transmission measurements (Tembhurkar et al. 1992). The absorption coefficient (α) can be written as:

$$\alpha t = ln\left(I_0 / I\right) \tag{1.10}$$

where: I_0=intensity of incident radiation

I= intensity of transmitted radiation

t= film thickness.

$CuInS_2$ has a high α in the visible region and near IR (Gurinovich et al. 1998; Moller et al. 1998). For a direct band gap material such as $CuInS_2$ (Gurinovich et al. 1998), the absorption coefficient can be correlated with the photon energy ($h\nu$) by the formula

$$\alpha h\nu = A(h\nu - Eg)^{1/2} \tag{1.11}$$

(where A is a constant, h is Planck's constant and ν is the frequency) and if plotted the intercept gives the band-gap (Eg).

A band gap of 1.45-1.46 eV are the reported values for spray deposited $CuInS_2$ (Krunks et al. 1999; Zouaghi et al. 2001; Marsillac et al. 2003).

Electrical properties

Resistivity shows different trends as a function of the deposition temperature, and the Cu/In molar ratio.

When the deposition temperature is increased, the resistivity decreases (Bouzouita et al. 1999). This phenomenon can be explained by an improvement in the film crystallinity and a reduction in the impurity concentration.

A study of resistivity of the as-deposited films as a function of Cu/In ratio of the starting solution at number a of different deposition temperatures but at constant S/Cu ratio has been proposed by Ortega-Lopez (Ortega-Lopez et al. 1998). Notably, the resistivity drops six orders of magnitude when the Cu/In ratio rises from 0.7 to 1.1. The increase in the amount of copper may cause the segregation of $Cu_{2-x}S$ (a highly conductive binary compound) on the grain boundaries. On the contrary an excessive raising of the sulphur in the initial solution results in an increase of the resistivity from 10 to 10^3 Ω cm (Bihri et al. 1999). This may be attributed to a substitution of Cu atoms with S which reduces the carrier density and increases the resistivity.

1.3. BUFFER LAYER: ZnS

CdS is widely used as a window and/or buffer layer in photovoltaic cells. High efficiency solar cells have been made using CdS/CIGS or CdS/CdTe junctions (Wu et al. 2001; Ramanathan et al. 2003). However, the environmental concerns regarding CdS waste have forced photovoltaic researchers to look for more environmentally friendly buffer layer materials. Amongst the candidates, ZnS appears to be the most promising due to the absence of toxic elements, a wide direct band gap of 3.65eV (Yamaga et al. 1990) (thus more energetic photons arrive at the junction) and a high level of transparency.

Several methods have already been successfully used to prepare ZnS films such as spray pyrolysis (Afifi et al. 1995; Lopez et al. 2005), chemical bath deposition (Gode et al. 2007) and sputtering (Blackmore et al. 1991). ZnS prepared by acid solution chemical bath deposition (Asenjo et al. 2008) produced $CuInS_2$-based devices with efficiencies of η=5.3%.

1.4. BACK CONTACTS: Molybdenum

Molybdenum is a transition metal (Group VIA) with an electronic configuration of [Kr] $4d^5$ $5s^1$ and a body centered cubic (bcc) structure (Greenwood et al. 1984). It is a hard metal with a high melting point and low volatility (Lee 1991). It is a relatively inert material and does not react with oxygen under standard conditions (i.e. room temperature and ambient pressure).

Mo has an application in photovoltaic device construction as a sputtered back contact material. It has been chosen for use in this study due to its low resistivity, stability at deposition temperature and good adhesion to soda-lime substrates (for the substrate configuration). It is essential that the back contact metal has a very low resistivity in order to minimise its contribution to the series resistance of the device. The resistivity of Mo is strongly dependent on the deposition parameters such as target power, substrate temperature and gas pressure. The films deposited at low pressure have low resistivity while the films deposited at high pressure have high resistivity (Scofield et al. 1995;

Assmann et al. 2005). This depends on mobility and carrier concentrations. A reduction in resistivity is also observed by increasing the target power due to an increase in the mobility of the carriers (Gordillo et al. 1998). The resistivity of the metals is also found to be dependent on the thickness of the deposited layer. In order to obtain a sheet resistance of less than 1Ω/sq (useful for solar cell applications), the thickness of the layer should be a minimum of 0.7µm (Guillen et al. 2003).

Mo layers show good adhesion to the glass substrate only when deposited at high pressure. Layers deposited at low pressure have been shown to peel off from the substrate (Scofield et al. 1995).

Another benefit to using Mo as a back contact material is its resistance to forming alloys with Cu and In even though some studies have shown evidence of a reaction between Mo and Se (Matson et al. 1984; Assmann et al. 2005).

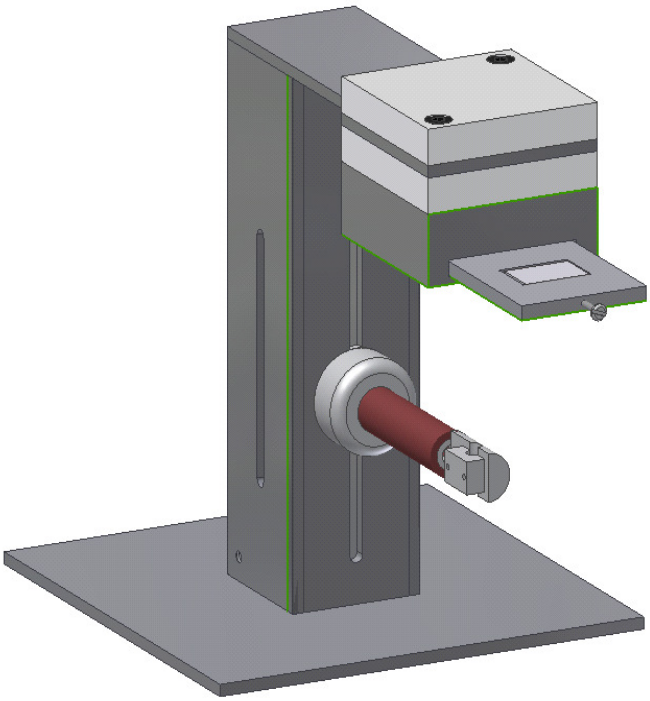

Chapter 2

Electrostatic Spray Deposition: Theoretical Aspects

Electrostatic spray deposition (ESD) is the technique used to deposit both the n-type and p-type materials utilised to make solar cells devices in this thesis. In this chapter, a theoretical introduction to the electrostatic spray deposition will be presented. The knowledge of the aerosol formation, gas transport and solvent evaporation is essential to attempt to optimise the deposition set-up and thus obtain high quality as-deposited films.

2.1. Emission of droplets

When a solution is forced to pass through a needle and an electric field is applied between the needle and a plate, the result is a jet formation. Atomisation takes place when the jet is broken into droplets. It happens when the Coulomb repulsion force exceeds the surface tension of the liquid. Under the right combination of solution properties, voltage, flow, temperature and system geometry, the drops may form a cone on the tip of the nozzle.

This phenomena was explained for the first time in 1917 by Zeleny (Zeleny 1917) whereas Taylor (Taylor 1964) gave a first explanation of the cone shape for a perfectly conducting liquid as a function of the surface tension and the electrical properties and he predicted that the semi-angle of the cone should be 49.3º. This cone is known as Taylor's cone and it is formed when the electrostatic force is equal to the surface tension of the solution. The following equation is used to calculate the electric field E_{surf} on the surface of the Taylor cone:

$$E_{surf} = 300\left(\frac{8\pi\gamma\cot\alpha}{r}\right)^{1/2} \qquad (2.1)$$

where

γ = the surface tension of the liquid,

α = semi-angle of the cone

r = the radius.

At the tip of the Taylor cone the electric field tends to infinity (because $r\rightarrow 0$) and the liquid surface becomes unstable and creates the aerosol.

The Rayleigh law (Rayleigh 1879) defines the limit after which the surface tension can not balance the electrical field and the drop will be ripped apart.

The Rayleigh limit states a drop of radius R and surface tension γ will be able to hold a maximum charge equal to:

$$q_R = 8\pi\sqrt{\varepsilon_0 \gamma R^3} \tag{2.2}$$

where q_R is the Rayleigh limit and ε_0 is the electrical permittivity of vacuum.

Assuming that the jet diameter is much smaller than the needle and in the high-conductivity regime, De la Mora (De La Mora 1992; De La Mora et al. 1994; Rosell-Llompart et al. 1994) proposed how the droplets size and spray current are related to the flow rate and liquid properties:

$$r = \left(\varepsilon\varepsilon_0 Q / K\right)^{\frac{1}{3}} \tag{2.3}$$

$$I = f(\varepsilon)(\gamma Q K / \varepsilon)^{\frac{1}{2}} \tag{2.4}$$

where

$r = droplet\ \ diameter$
$\varepsilon = liquid\ to\ vacuum\ permittivity\ ratio$
$Q = flow\ rate$
$K = liquid\ conductivity$
$I = spray\ current$
$f(\varepsilon) = function\ of\ \varepsilon$
$\gamma = surface\ tension$

In 1997 Ganan-Calvo et al. (Ganan-Calvo et al. 1997) presented a rather different dependence of the current versus flow rate in a liquid with low polarity.
They explained this different behaviour on the basis of the different viscosities and conductivities of liquids and introduced a dimensionless parameter (δ_u)

$$\delta_u = \rho Q_0 /(\mu d_0) = [\rho \varepsilon_0^2 \gamma^2 / K\mu^3]^{\frac{1}{3}} \qquad (2.5)$$

where: ρ = density

μ = viscosity

ε_0 = vacuum permittivity

γ = surface tension

K = conductivity

$I_0=(\varepsilon_0\gamma^2/\rho)^{1/2}$

$d_0=[(\gamma\varepsilon_0^2/(\rho K^2)]^{1/3}$

$Q_0=\gamma\varepsilon_0/\rho K$

Considering the first term of the equation, it can be explained in terms of velocities:

- Velocity of the liquid bulk Q_0 / d_0^2
- Velocity of propagation of a perturbation across the jet by diffusion $\mu / \rho d_0$

If the viscosity (μ) and conductivity (K) are large ($\delta_u << 1$) the spray current and the diameter of the droplets will be explained by the scaling law:

$$I \approx (QK\gamma)^{\frac{1}{2}} \qquad (2.6)$$

$$d \propto \left(\frac{\varepsilon_0 Q}{K}\right)^{1/3} \qquad (2.7)$$

In the opposite condition ($\delta_u >> 1$), for a liquid with a low conductivity and viscosity, the $Q^{1/4}$ law will be satisfied:

$$I \approx (\gamma^3 \varepsilon_0 K Q / \rho)^{1/4} \quad (2.8)$$

$$d \approx (\rho \varepsilon_0 Q^3 / \gamma K)^{1/6} \quad (2.9)$$

2.1.1. Emission mode

Clopeau et al (Cloupeau et al. 1989; Cloupeau et al. 1990; Cloupeau et al. 1994) described the different forms in which a liquid can be disintegrated in drops when it is subjected to a potential. For a given solution, these different behaviours are a function of the applied potential and flow rate (Jaworek et al. 1999).

- ***DRIPPING MODE***

In the absence of an electric field, the liquid will flow drop by drop from the tip of the needle (Berkland et al. 2004) (Figure 2-1). When a voltage is applied, a rise in emission frequency and a reduction in droplet size are observed (Cloupeau et al. 1990).

At low voltage, the drops have regular shapes. When the voltage is increased their dimensions decrease.

Raising the voltage to half of the Rayleigh limit $q_R/2$, the drop size distribution becomes irregular: drop number and sizes depend on properties of solution and flow rate.

- ***CONEJET MODE***

Increasing the voltage above half the Rayleigh limit, the Taylor cone appears at the tip of the needle from which a single jet is formed (Figure 2-1). The top of the jet tends to be unstable showing two possible behaviours called varicose and kink instabilities (Grace J. M. et al. 1994). In the first case, the axis of the jet is not deflected and the jet is disintegrated into equal droplets. In the second case the jet moves irregularly and it breaks into droplets of different dimensions (Chen et al. 2005).

- ***MULTIJETS MODE***

For higher voltages, the number of jets increases with each jet emitting simultaneously from the tip of the capillary. The meniscus becomes perfectly flat with only short cone at the emission point (Figure 2-2).

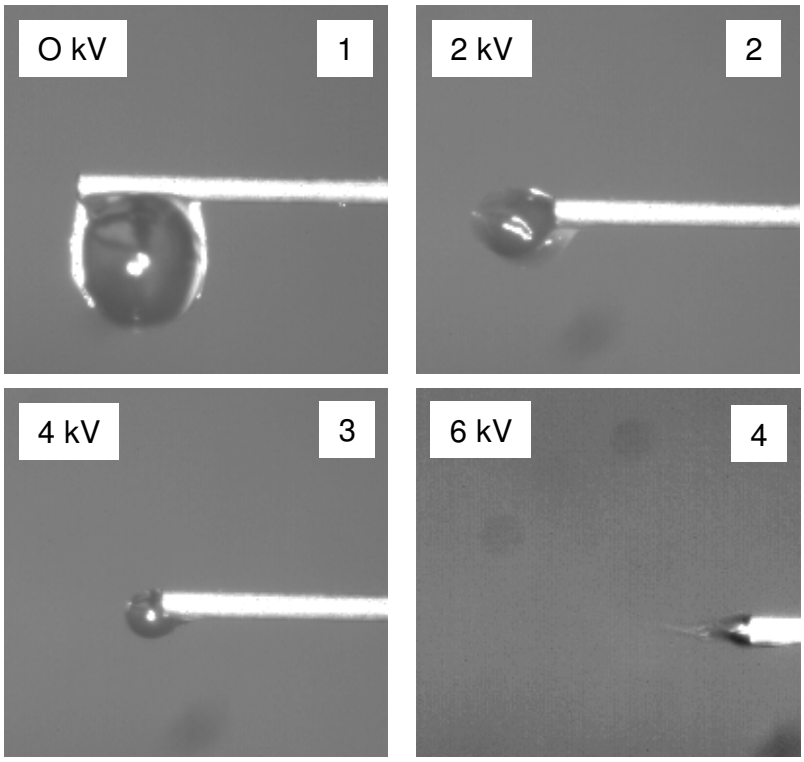

Figure 2-1: Jet formation using 1ml/h flow and increasing voltage: 1,2,3) dripping mode; 4) cone-jet mode;

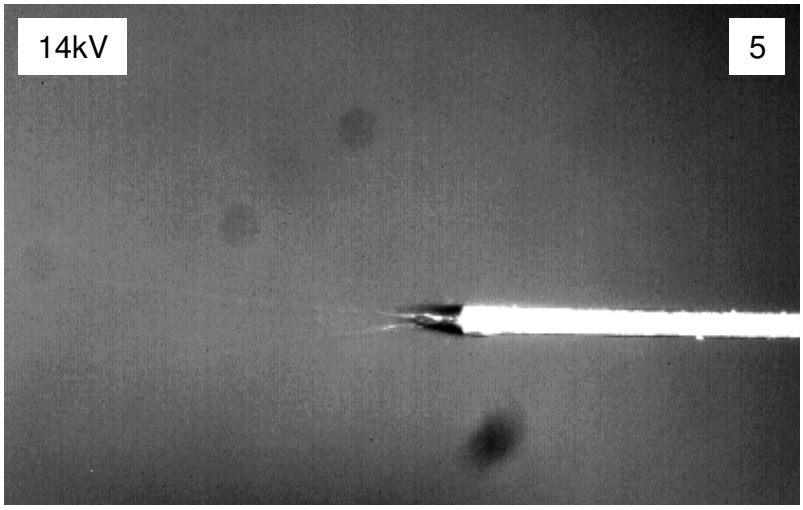

Figure 2-2: Jet formation using 1ml/h flow and 14 kV applied voltage: multi-jet mode

2.1.2. Aerosol transport

A charged droplet (with mass *m*) produced at the tip of the needle will be subjected to 3 different forces.

- Coulombic force (which pushes the drops from the needle toward the substrate), qE_{sp}, where q is droplet charge and E_{sp} is the electrostatic field
- gravitational force, mg (where g is the gravitational acceleration)
- viscous drag force $3\pi d\eta\upsilon C$ (where d is the diameter of the droplets, η is the dynamic viscosity of air, υ is the drop velocity and C is the correction coefficient).

The gravitational force can be neglected because the droplets have a very small mass.

Assuming

- a constant electric field in the travelling space,
- a short distance between the needle and the substrate (L)
- a constant temperature
- no drag force and solvent evaporation,

the flight time will be equal to

$$t = \left(\frac{2Lm}{qE_{sp}} \right) \tag{2.10}$$

2.1.3. Gas-phase ion generation

In spite of the considerable interest around the ESD technique, the process that generates the aerosol is not well understood.

Two mechanisms have been proposed to explain the formation of solute ions from the charged drops: the ion evaporation model (IEM) and the charge residual model (CRM) (Figure 2-3). Both theories may be applied for the Electrospray Ionization (a techniques used in mass spectrometry to produce ions) but they do not form a complete picture for the ESD technique because the gradient in temperature between the needle and substrate is not considered.

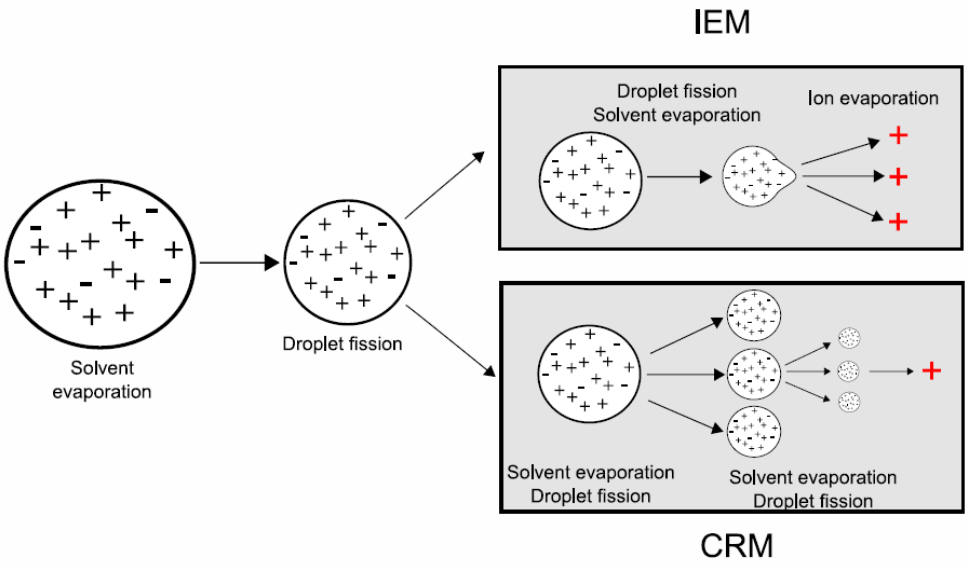

Figure 2-3: Two models for gas-phase ion generation: Ion Evaporation Model (IEM) and Charge Residue Model (CRM)

IEM

The Ion Evaporation Model (IEM) was proposed by Iribarne and Thomson (Iribarne et al. 1976; Thomson et al. 1979). They supposed that the solute ions were formed before the precursor reaction, when the field on the surface of the droplet was strong enough to overcome a solvation forces (Figure 2-3). The charge required for the evaporation is lower than required for Coulomb droplet fission. (Rayleigh limit (q_R), equation(2.2)).

They also predicted (Iribarne et al. 1976) the rate of ion evaporation from the droplets. If an ion of radius *r* is dissolved in a neutral drop of radius *R* (with $r<<R$), the free energy of solvation can be written as

$$\Delta G^{\circ}_{s} = -4\pi\sigma r^2 + \frac{e^2}{2r}\left(1-\frac{1}{\varepsilon}\right) \cong -4\pi\sigma r^2 + \frac{e^2}{2r} \tag{2.11}$$

where σ = surface tension

ε = dielectric constant of the liquid

If the drop is charged, the following equation has to be added to equation 2.11. This is due to the interaction between the drop and the ion.

$$\Delta G^{\circ}_{e} \cong \frac{Ne^2}{R} \tag{2.12}$$

Thus, the total free energy will be

$$\Delta G^{\circ} = \Delta G^{\circ}_{e} + \Delta G^{\circ}_{s} \tag{2.13}$$

For the evaporation of the ion from the drop to occur, it has to exceed an energy barrier (Figure 2-4).

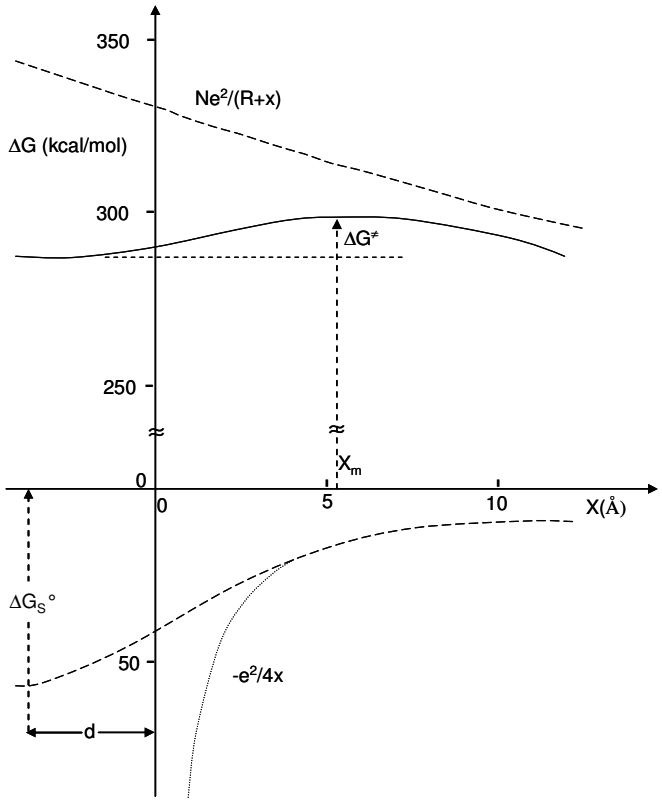

Figure 2-4: x=distance, d=equilibrium position of the ion inside the drop, lower dashed curve = solvation energy, upper dashed curve = electrostatic potential energy, full curve = resultant, dotted curve = electrostatic potential.

The lower dash curve of Figure 2-4 (Iribarne et al. 1976) shows the variation of the energy of the cluster from the equilibrium point (distance d beneath the surface of the drop) to a distance x from the surface of the drop.

The upper dash curve shows the trend of the electrostatic potential due to the repulsion of the charged drop.

The resultant curve (full line) shows a maximum where the height is equal to

(2.14)

$$\begin{aligned}\Delta G^{\ddagger} &\cong e^2\left(\frac{N}{R+x_m}-\frac{1}{4x_m}\right)-\left(\Delta G^{\circ}_{s}+\frac{Ne^2}{R-d}\right)\\ &=-\Delta G^{\circ}_{s}-e^2\left[\frac{N(x_m+d)}{(R-d)(R+x_m)}+\frac{1}{4x_m}\right]\end{aligned} \tag{2.15}$$

Suppose that the ion evaporation is a spontaneous process characterized by a rate constant *k (reaction rate)* and considering a first order kinetic reaction:

$$k=\frac{k_B T}{h}e^{-\Delta G^{\ddagger}/RT} \tag{2.16}$$

where

k_B = Boltzman's constant

h = Planck's constant

R= gas constant

T = temperature

The barrier of the process is due to:

- Strong attractive forces between ion and polarizable droplet (it decreases sharply with the distance)
- Long-distance repulsive Coulombic force between ion and charges on the droplet

It has been calculated that for small particles (radius < 10-20nm), k is $\geq 10^6$ s^{-1} and the charge necessary for the evaporation is lower than the charge required for the Coulomb fission.

CRM

The Charged Residue Model (CRM) has been proposed by Dole et al [(Dole et al. 1968)] and it was subsequently extended by Schmelzeisen-Redeker et al. (Schmelzeisen-Redeker

et al. 1989)]. It described the phenomena as a sequence of Rayleigh instabilities, solvent evaporation and Coulomb fission. The end of the process may result in droplets containing only one molecule of solute.

Figure 2-5 shows a schematic diagram proposed by both Choy and Hou (Choy et al. 2001; Hou et al. 2004) to explain the mechanism of the deposition of a charge droplet under the influence of temperature gradient.

After the aerosol formation, the charged drops are attracted to the hot substrate (earthed) by the electric field. During the journey, they undergo a sequence of chemical-physical processes which may be summarised as:

1) evaporations of the solvent
2) fission of the droplets
3) decomposition and chemical reaction of precursors
4) deposition of the thin film

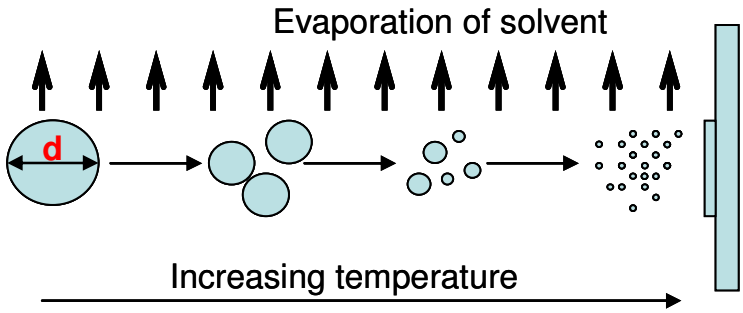

Figure 2-5: Deposition model of thin films from charge droplets

For the neutral droplet, the variation of diameter of droplet with the time is given by the equation:

$$\frac{dr}{dt} = -\frac{4D_v M}{R\rho r}\left[\frac{P_\infty}{T} - \frac{P_d}{T_d}\right]\left[\frac{2\lambda r}{r + 5.33\left(\lambda^2 / r\right) + 3.42\lambda}\right] \tag{2.17}$$

r = droplet diameter

D_v= diffusion coefficient of the vapour solvent in air

M = molecular mass of the solvent

R = gas constant

ρ = density

P_∞= partial vapour pressure away from the droplets

P_d = partial vapour pressure on the droplets surface

T = ambient T

T_d = droplet T which is < T because of evaporation process

λ = mean free path

$x_{A\infty}$ = mole fraction of species A far from the droplet

It has been taken into account that the temperature of the drops during solvent evaporation remains constant and so it will be lower than the ambient temperature.

The properties of the as-deposited films depend on voltage, substrate temperature, flow rate, distance substrate-needle and other experimental parameters but it is obvious that the temperature has a considerable effect. In fact, at low growth temperature the droplets will arrive on the substrate and a period of time will elapse before the solvent evaporates and the reaction takes place. The result will be an amorphous and porous film because the nucleation process will be dominant. At high temperatures the solvent will evaporate before reaching the substrate and additionally decompose. Hence, the sample will be rough and powdery (Choy et al. 2001) (Figure 2-6)

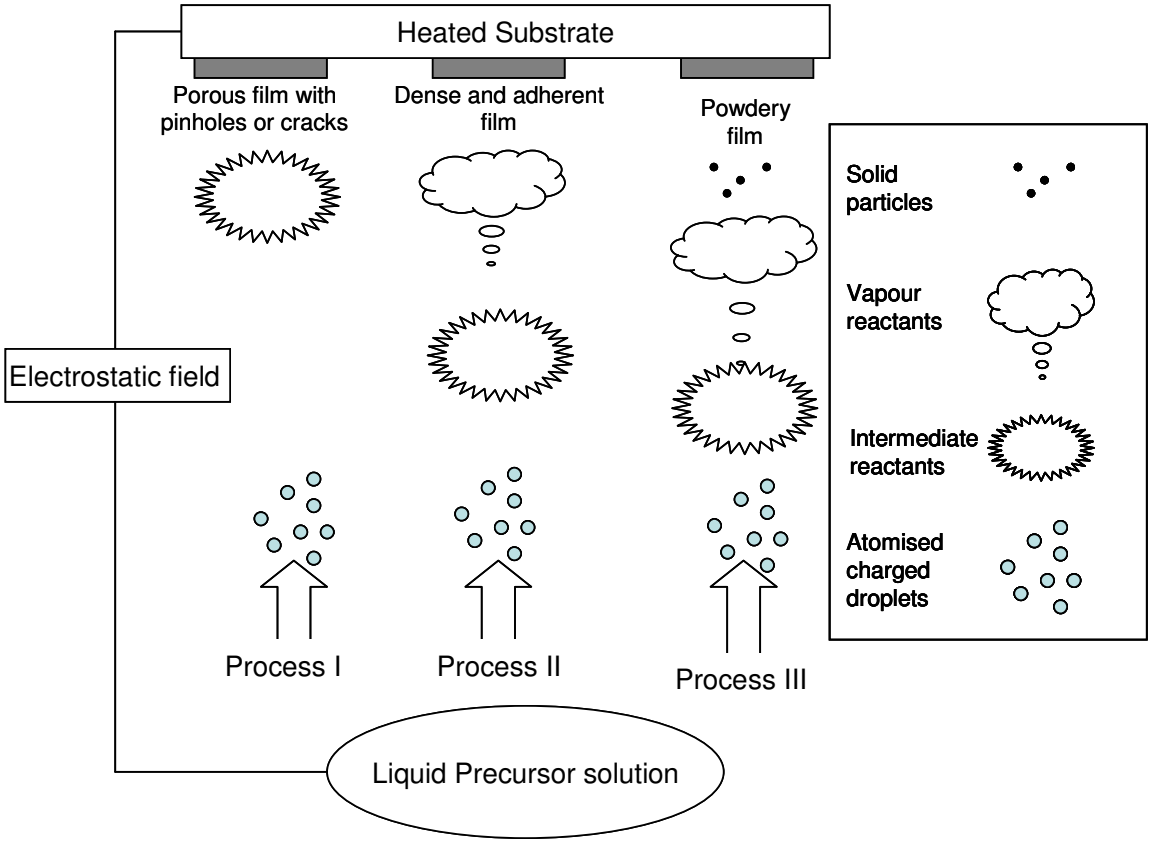

Figure 2-6: Schematic diagram of the electrospray deposition mechanism

If the temperature is correct, the precursors are decomposed near the substrate and absorbed on it. Only at this point the chemical formation reaction begins forming a dense film with a good adhesion on the substrate.

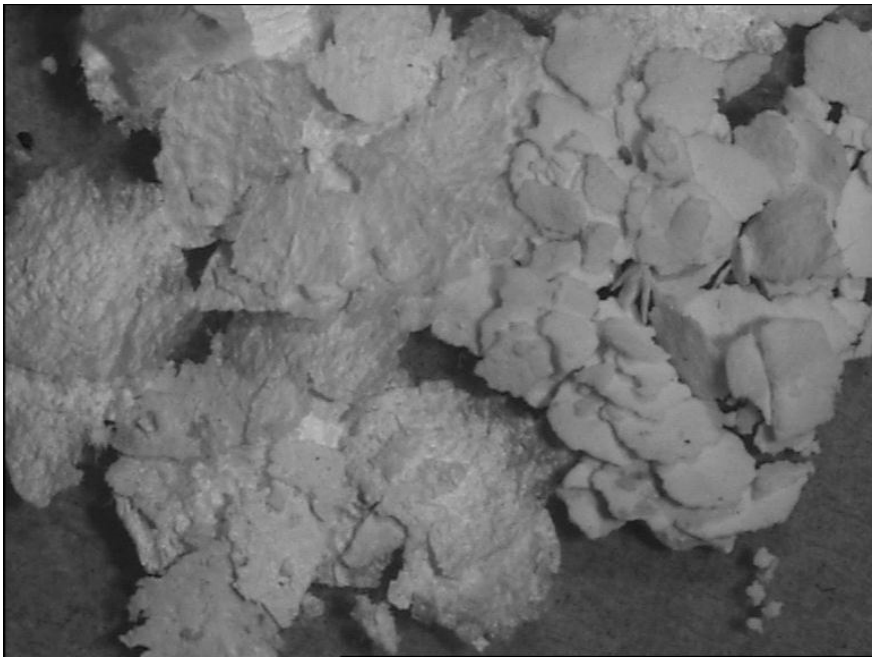

Chapter 3:

Analytical Techniques

In this chapter some of the methods used to characterize the samples prepared during this project will be briefly described. X-Ray diffraction (XRD) has been used for the structural characterization while particle image velocimetry (PIV) has been used for determination of the properties of the aerosol. Measurement of the surface roughness was accomplished by alpha-step techniques while the composition of the as-deposited films was analysed by Rutherford back-scattering (RBS) and Mini-SIMS measurements. The qualities of the solar cells were determined by optoelectronic measurements and by IV methods.

The main part of the chapter will be dedicated to the description of the self-developed uniformity test.

3.1. Uniformity Test

Thin film deposition by ESD is a complex process which needs to be fully understood in order to optimise the quality of the as-deposited films. The absence of previous applications of this technique for the deposition of $CuInS_2$ and ZnS thin films required that a statistical analysis of the effect each deposition variable had on the final properties of the films. As described in the next chapter, the number of samples necessary to fully investigate all possible variable combinations for this experiment was high and thus a self-designed method for determining the uniformity of as-deposited thin films was designed and is presented in this section[1]. The test is a simple and rapid method which quantifies the degree of uniformity using a simple image analysis process. Thin films were deposited by electrostatic spray deposition (ESD) from a water-alcohol based solution. Semitransparent chalcopyrite films produced in this way were illuminated by a light box and images subsequently captured by a digital camera were employed in this simple test to quantify the uniformity of the samples. A flow diagram of outlining the process in the uniformity test is given in Figure 3-1. In this study a film is described as uniform when the logarithm of the intensity of the image (and thus the thickness) is constant.

3.1.1. Test description

A light box (View box Quasar 3 electronic) was used to transmit light through the samples and a digital camera, with a macro lens attached, captured images which were stored on a desktop computer.

The colour images of the samples were converted to a two dimensional grey scale matrix. For each point of the matrix, the corresponding thickness was calculated using Lambert-Beer's law and assuming an absorption coefficient of 10^{-5} cm^{-1} (Pathan et al. 2004).
From this point, two different but complementary analyses were undertaken to examine the "macro" and "micro" uniformity of the samples. The first test gives information about the

[1] A journal paper entitled "A Method to Quantify the Degree of Uniformity of Thickness of Thin Films" which details the uniformity test has been accepted for publication in Thin Solid Films.

macro-uniformity of the films (selected area ≈ 30% of the total image dimension). From this a numerical threshold value (determined empirically) allowed grossly non-uniform samples to be discarded and the remaining samples to be further investigated.

The second test gives information about the degree of uniformity of the covering film by calculating the gradient of the thickness for each point of the matrix.

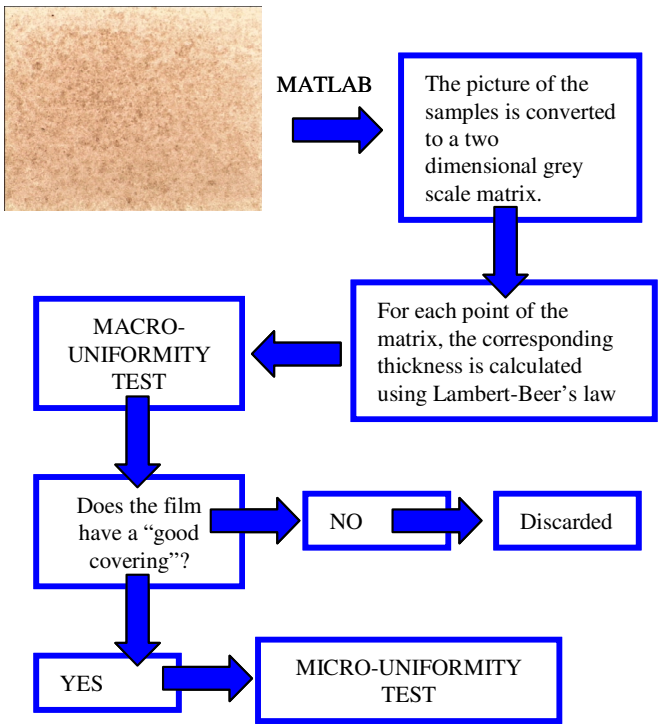

Figure 3-1: Flow diagram showing the sequence of steps followed in performing the uniformity test.

Macro-uniformity test (MUT)

The macro-uniformity test measures the variance of the film thickness $\mu(t)$.

The image-matrix is divided into blocks (see below) and the mean value of the thickness is evaluated for each block. The variance of the mean value of all the blocks is then calculated.

A program developed within Matlab ® can be summarized by the following

- During the first loop of the program, the block has a dimension equal to the maximum number in power of two which can be contained in the matrix thus the variance is zero because there is only one block.
- During each subsequent loop the block dimension is halved. The variance is then calculated between the blocks generated.
- The process repeats until the block size equals one pixel.

The MUT results are plotted in graphs in which the abscissa represents the block dimension while the ordinate is $\mu(t)$.

To validate the test, six artificial test images were produced with feature sizes varying in accordance with the Gaussian distributions (Figure 3-2).

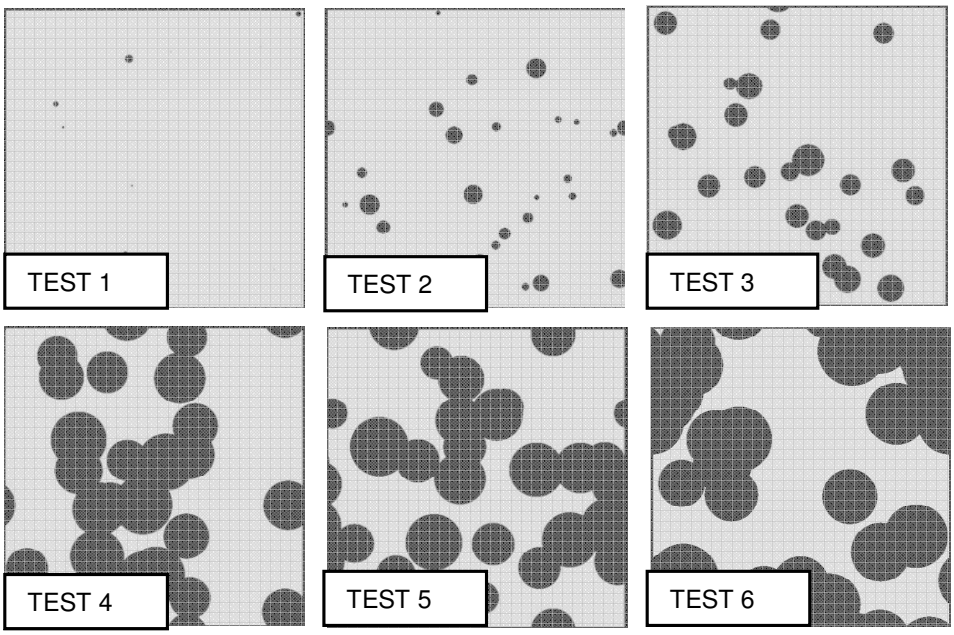

Figure 3-2: Synthetic images showing a Gaussian drops size distribution used to evaluate the test procedure

These were then analysed using the MUT (see Figure 3-3).

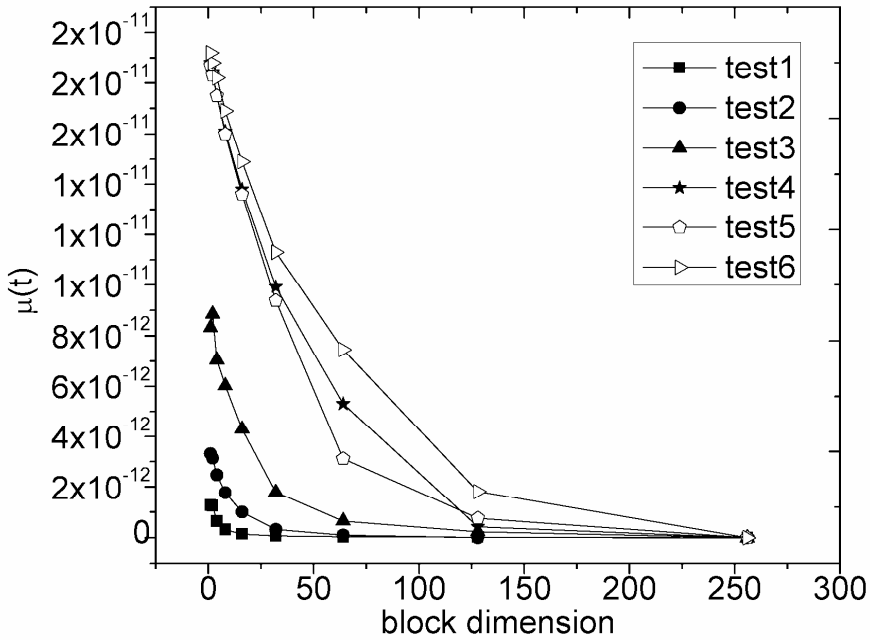

Figure 3-3: Results of the Macro-Uniformity- Test for the artificial images depicted in Figure 3-2. Graph shows the trend variance vs blocks dimension as described below.

The graph shows good agreement between the shape of the curves and the spot distributions. For a perfectly homogenous film, the variance would be zero because the difference in the mean values is zero (Test1). In contrast a non homogenous film produces a sharp increase in the standard deviation on reducing the block size (Test 6).

The analysis of real films produced the same trend. The images in Figure 3-4 are nine samples sprayed using different conditions (Table 3-1) and the corresponding MUT graphs are presented in Figure 3-5.

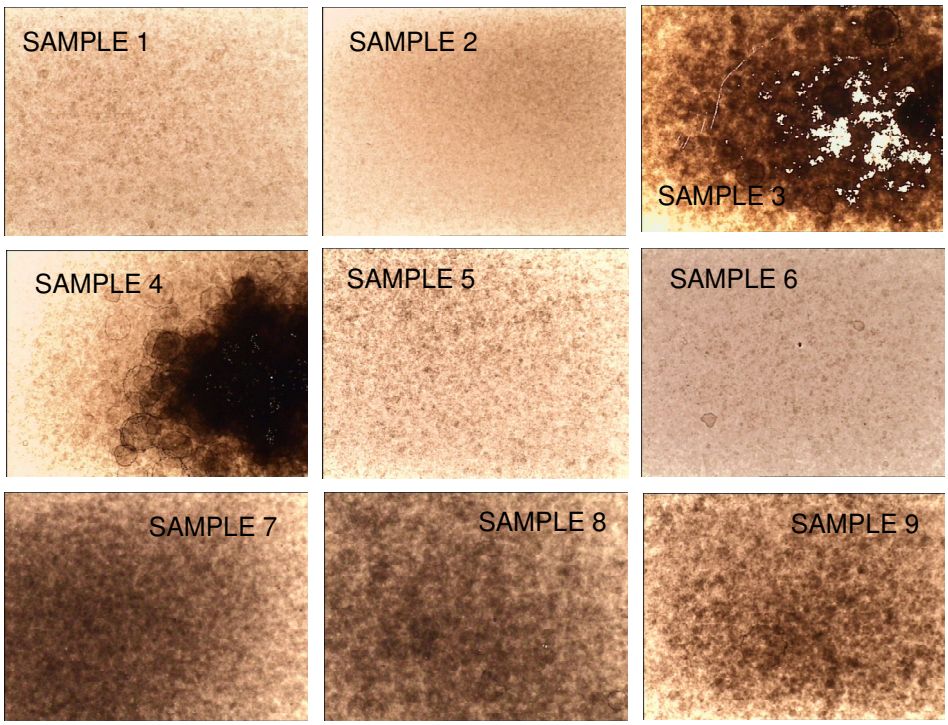

Figure 3-4: Digital images of samples sprayed following the test conditions summarised in Table 3-1.

Table 3-1: Film deposition conditions which correspond to the digital images in Figure 3-4. The nine samples were selected at random from the 400 samples sprayed during the preliminary investigation.

Sample Number	*Solution flow rate [μl/min]*	*Applied voltage [kV]*	*Distance needle-substrate [cm]*	*Deposition Temper. [°C]*	*Solution concentration [M]*	*Deposition Time [min]*
1	200	16	4	450	0.21	5
2	25	16	4	450	0.21	40
3	100	10	4	450	0.21	10
4	25	10	4	450	0.21	20
5	100	16	4	450	0.49	10
6	200	20	5	450	0.21	5
7	50	18	5	410	0.21	20
8	25	18	5	410	0.21	40
9	200	16	4	450	0.35 M	5

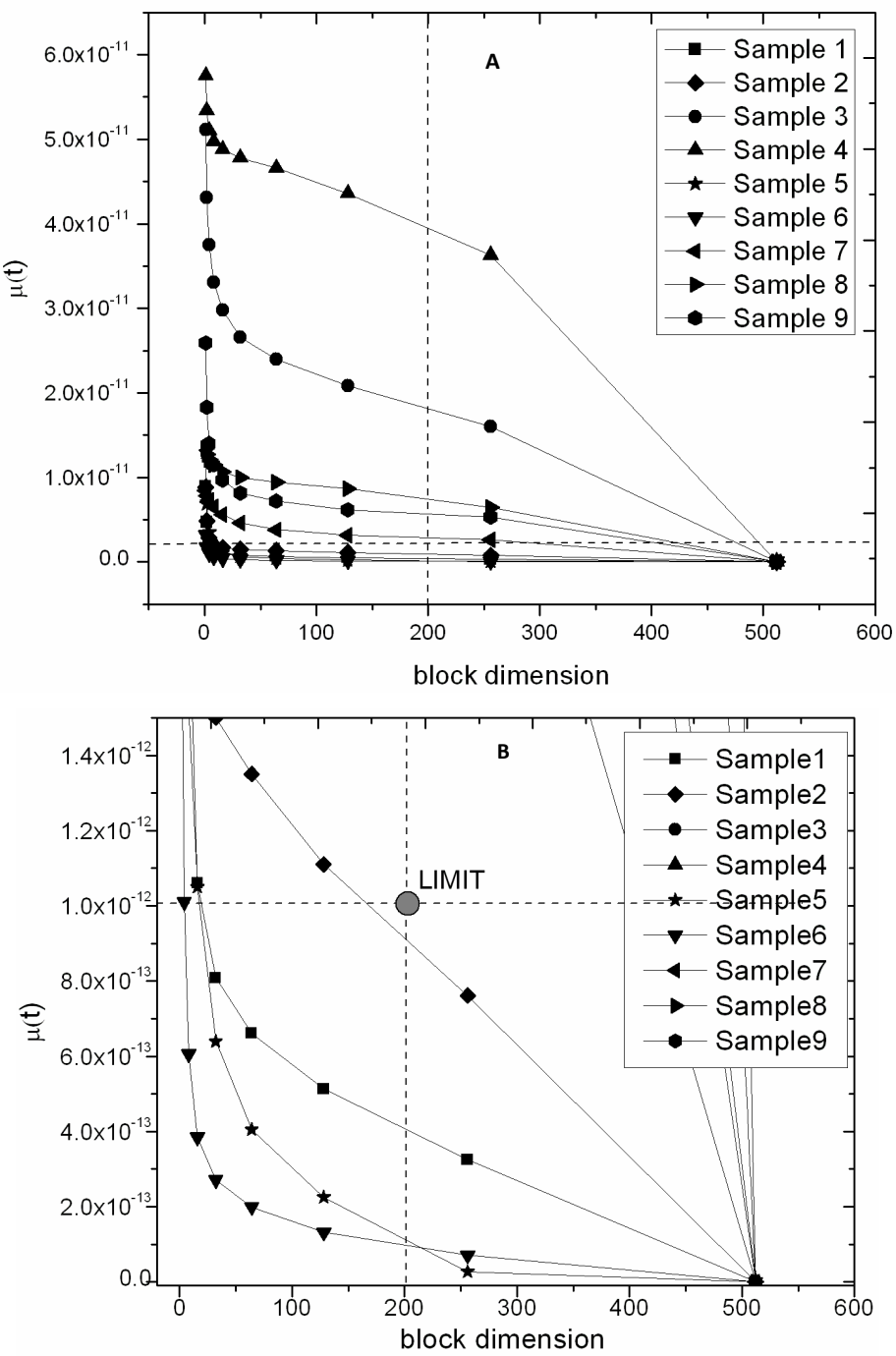

Figure 3-5: Macro-Uniformity-test results: (A) trend of variance as a function of blocks dimension for the nine samples in Figure 3-4 (B) close up of MUT variance graph showing the limit point for high quality films

Samples 3 and 4 show the highest range of variance. These trends reflect the visual non-uniformity of the samples. Conversely samples 1, 2, 5 and 6 produce a nearly flat $\mu(t)$ curve indicating that the variation in the optical intensity across the sample is small and thus the sample has acceptable uniformity. Samples 7, 8 and 9 are in intermediate positions. The deposited films have irregular spots and the thickness increased in some area of the samples.

By applying the MUT to more than 400 samples, the acceptability limit was defined to be $\mu(t) = 10^{-12}$ at 200 pixels (blocks dimension) (Figure 3-5B).

Micro-uniformity test

Samples which pass the MUT are re-analysed using the micro-uniformity test.

Again using the grey-scale image, gradients of the thickness along the column-direction and the row-direction of the matrix are calculated and a new matrix generated with these gradient values. A histogram is plotted, where the abscissa represents the gradient of the thickness (grad(t)) while the ordinate is the normalized frequency (υ/υ_0). The samples with a small Full-Width Half-Maximum (FWHM) are selected, ie are uniform.

Figure 3-6 shows the histograms of the micro-uniformity tests on samples which had initially passed the MUT. The results of the corresponding FWHM are summarised in Table 3-2. Sample number 2 has the smallest FWHM value because the difference of the thickness between each point of the image and its neighbour is minimal. On the other hand sample number 5 has the largest FWHM due to large variations in its thickness.

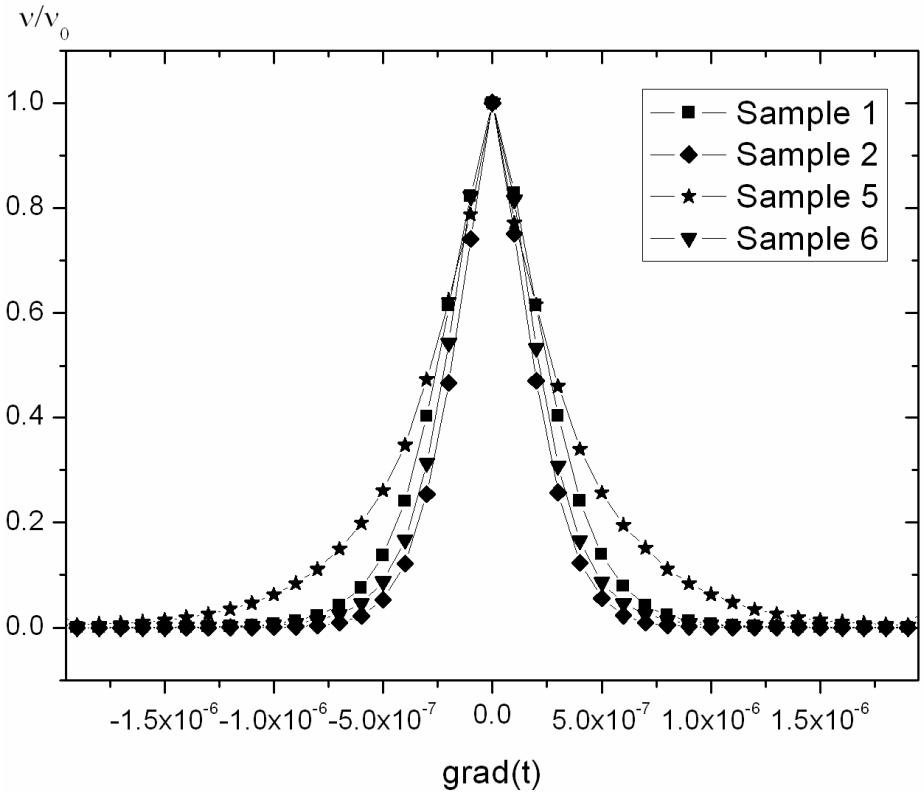

Figure 3-6: Results of the Micro-Uniformity-test (µUT) on four samples (number 1,2,5 and 6) which passed the MUT. The graph shows the distribution of gradient of the thickness against the normalized frequency.

Table 3-2: Summary table of FWHM

Sample	*FWHM [nm]*	*Error [nm]*
6	4.45	± 0.0350
2	3.95	± 0.0916
1	5.34	± 0.0899
5	5.89	± 0.1840

3.1.2. Roughness

In order to test the consistency of the method, the root mean square (RMS) roughness calculated for the thickness-matrix was compared with the RMS roughness measured with a mechanical surface-roughness analyser (Alpha-step 100). The technique works by recording the deflection of the reference needle about a starting zero position. As the needle is moved over the sample, any peaks and troughs are registered as positive and negative deflections of the needle. The roughness was measured across a distance of 2000 μm with a lateral resolution of 1 μm and a full scale deflection of 25000 Å. For each film, 3-4 measurements were taken in different areas of the sample then the mean value and standard deviation were calculated. The results are plotted together with the calculated roughness in Figure 3-7. The Alpha-step roughness depends on the position of the analysis because it investigates only a small area of the sample. This is evident for non-uniform samples (number 3 and 4) where the thickness changes considerably along the sample and the measurement gives three different results. On the other hand the calculated roughness gives an average value because it is estimated using all the points of the matrix.

Despite these differences, the graph shows that the results are comparable, thus validating the reliability of the test.

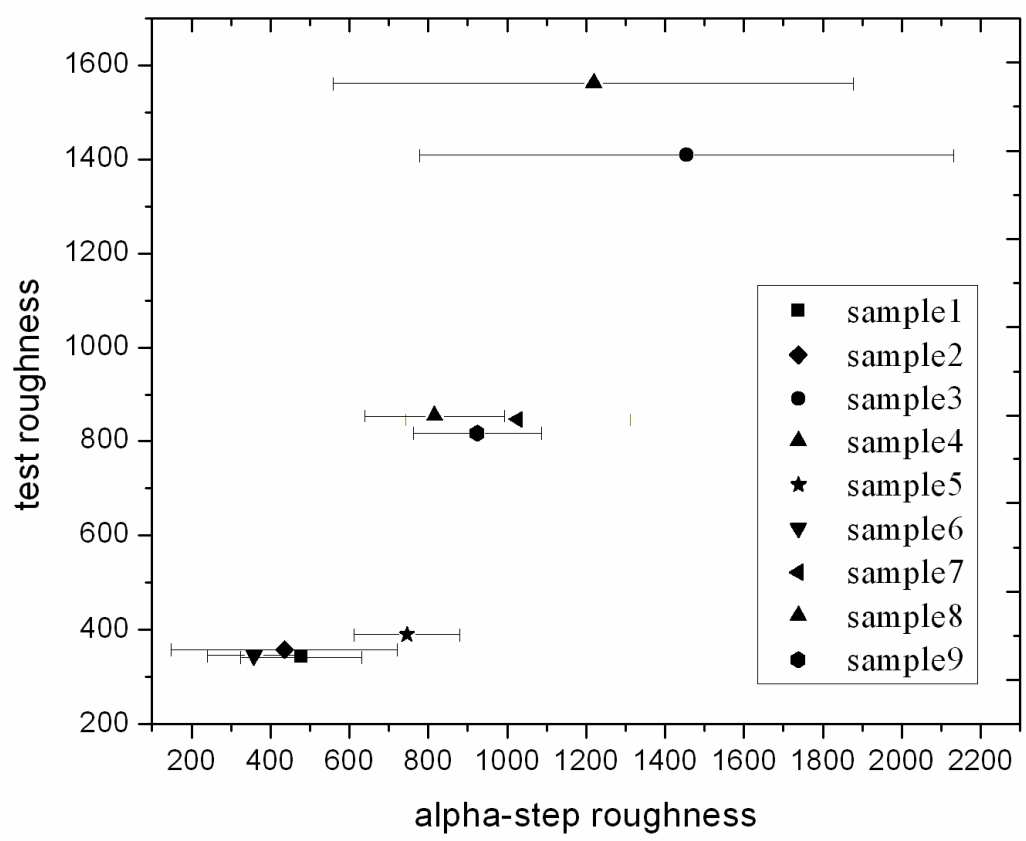

Figure 3-7: Comparison of the sample roughnesses. Experimental alpha-step roughnesses are compared with those obtained using the mathematical test.

3.2. Particle image velocimetry (PIV)

The particle image velocimetry (PIV) is a non-intrusive measurement technique for studying the velocity of particles in a flow. This technique was originally devised as a method for measuring fluid flow velocities by adding tracer particles to the flow but was found to be particularly suited to the measurement of the velocity of particles in an aerosol. The particles within the aerosol are illuminated periodically by a pulsed laser light source which has its incident beam focused into a planar light sheet (Figure 3-8 and Figure 3-9). The idea is to obtain successive digital images from a CCD camera which is oriented normal to the illuminated particles within the light sheet. These images can then be analysed by spatial correlation software, which determines the velocities of the particles by

tracking their movement between successive images. The main advantage of this technique is that it does not require the placement of any type of probe in the medium, which could affect the aerosol flow. This lack of interference is what gives PIV its non-intrusive characteristics. Also, where a probe can only measure the velocity at a single point, PIV is a global measurement technique which allows a full flow field to be analysed in a single measurement. The laser used during this experiment was a New Wave Gemini Nd:YAG pulsed laser (15Hz double pulse rate) and Kodak ES1.0 CCD camera (Figure 3-9). The energy of the light source was 120mJ per pulse at λ=532nm. Mean velocity distributions within the cone were calculated from the average of 700 pairs. Given a sample size of N=700, statistically the time-averaged results will have a 3.77% uncertainty (1/√N) (Coleman et al. 1999)

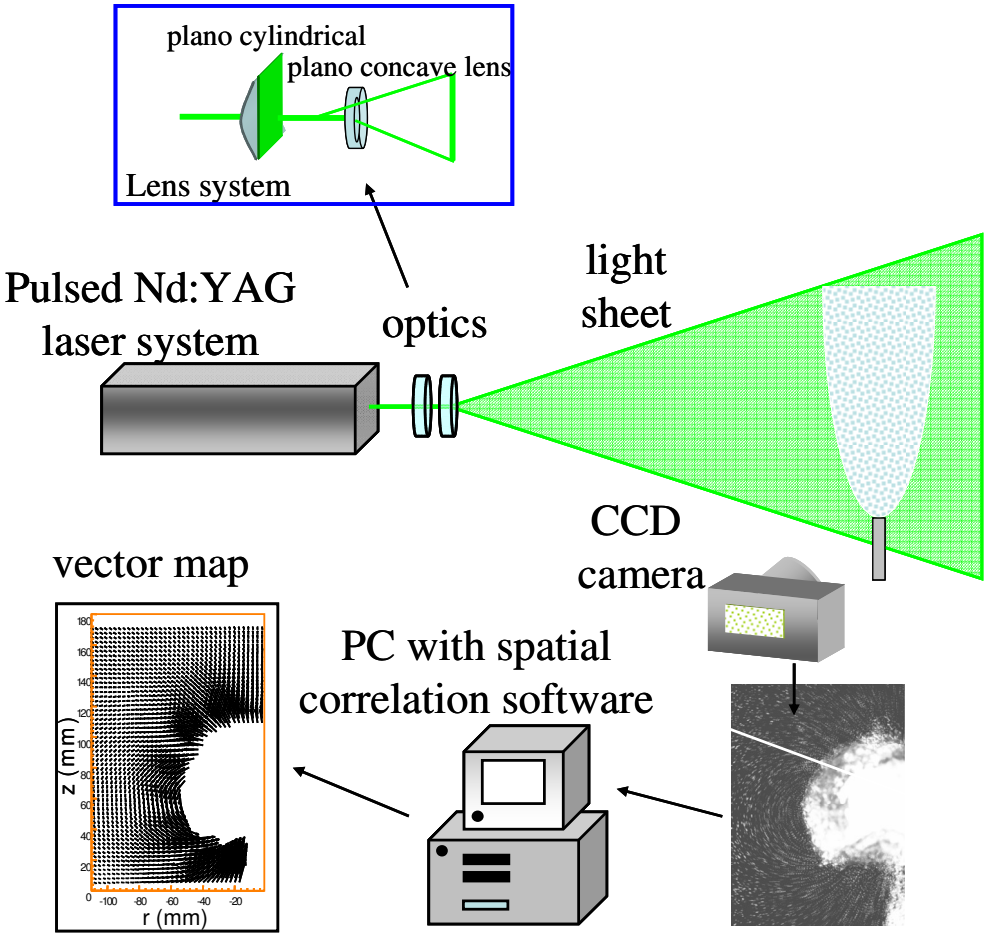

Figure 3-8: Schematic of PIV Set up for ESD

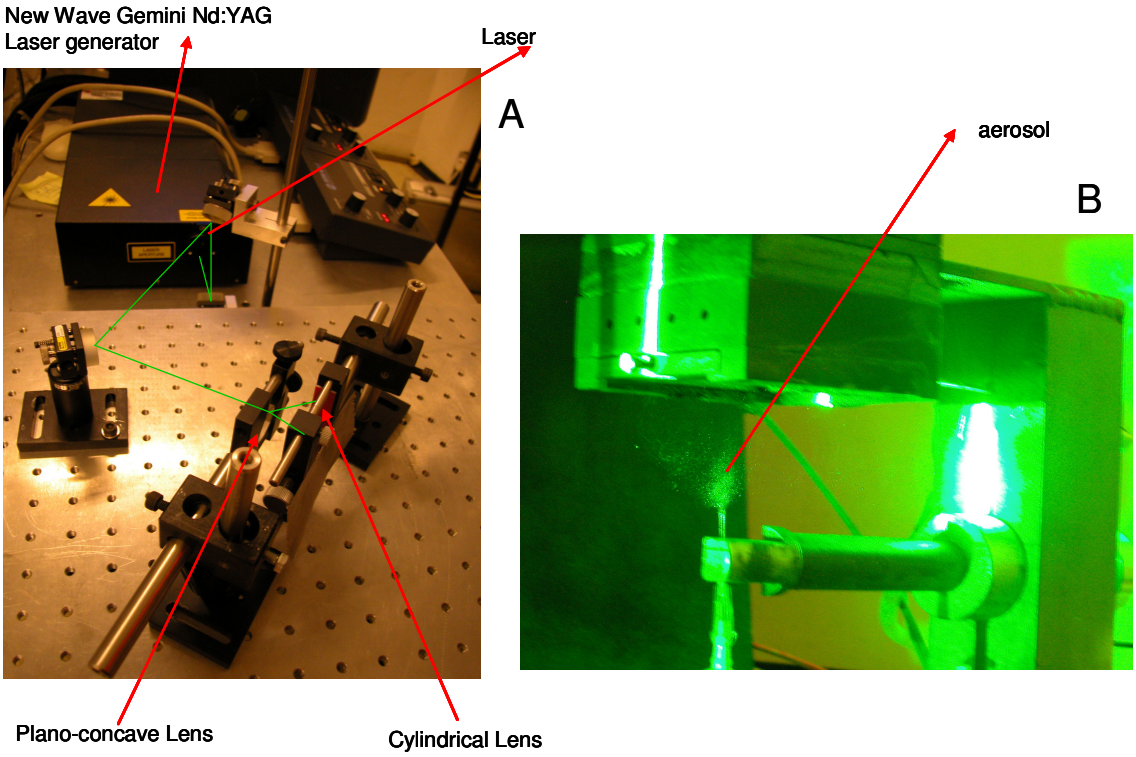

Figure 3-9: A) photographs of light sheet generated, optics and laser head; B) B) photograph of lightsheet projected into aerosl cone

3.3. IV curve, external quantum efficiency (EQE) and photo-voltammetry

3.3.1. IV curve

In order to determine the properties of a solar cell, a solar simulator (Sciencetech Inc.) was used with an air mass 1.5 filter and Xenon arc lamp. The current generated by the solar cell sample was measured using a Keithley 2400 source meter connected to a PC. The source meter was also used to bias the voltage. The equipment was calibrated using a GaAs

standard cell which was calibrated using an ESTM E892-87 standard for 100Wm^{-2} or AM1.5 solar flux at 25°C.

The sample holder used during the cell measurements can be seen in Figure 3-10. The current generated by the sample was measured at 8 different points of the cell.

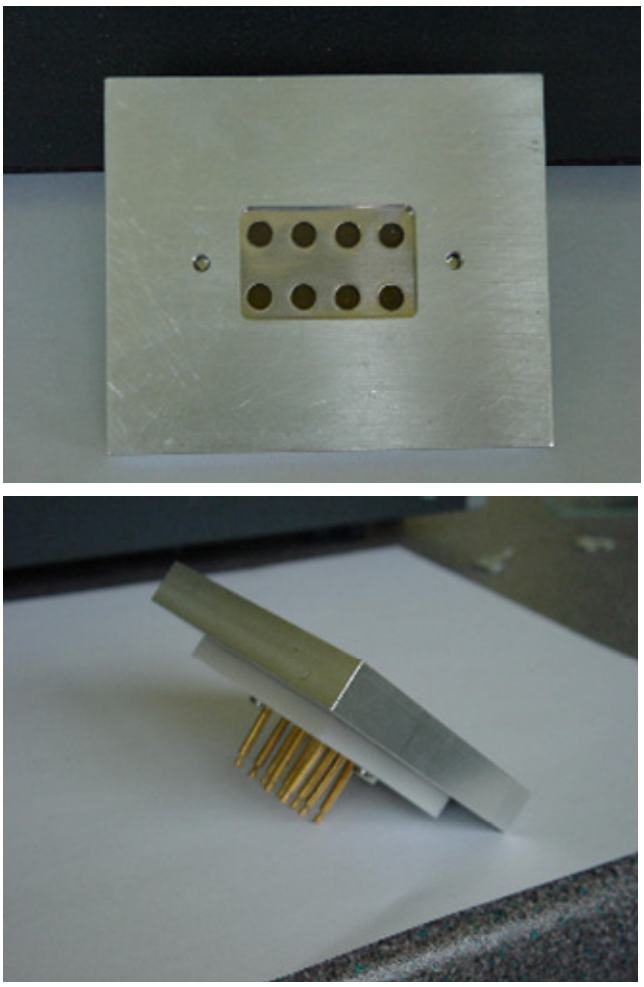

Figure 3-10: IV curve sample holder

3.3.2. EQE and photo-voltammetry[2]

External quantum efficiency (EQE) and photo-voltammetry were used to measure the photoelectrochemical properties of the as-deposited films. The photo-voltammetry was used to observe the response of the films and/or p-n junction to the light while the EQE was used to measure the conversion efficiency of the material (films and/or p-n junction).

The electrochemical cell was made of an electrolyte and three electrodes: a glass cell with an Ag | AgCl electrode was used as reference electrode, a platinum foil as counter electrode and the device as the working electrode. Two different electrolytes were used with the n or p materials. For the p-material ($CuInS_2$), Eu(III) nitrate was used. Eu(III) was reduced by collecting photogenerated electrons and it was supposed to be oxidised back to Eu(III) at the counter electrode. For the n-material (ZnS), Na_2S was used instead. In this case the S^{2-} is oxidised at the working electrode.

The samples were masked, thus only a small area ($A = 0.28cm^2$) was illuminated

EQE analysis measures the ratio of the electron flux to the incident photon flux. EQE measurements were carried out using a standard set-up which included a high pressure xenon lamp, monochromator and chopper, a potentiostat, a function generator and lock-in amplifier. Spectra were collected using chopped illumination with a 14Hz (or more) frequency and normalized against a calibrated silicon or germanium photodiode.

Photo-voltammetry was performed using an Autolab 20 potentiostat and an LED as a source of light. The potential was applied between the working electrode and the reference electrode while the current was measured between the working electrode and the counter electrode.

[2]The measurements were collected at the Chemistry Department of Bath University

3.4. X-ray diffraction

X-rays are electromagnetic waves with high frequency and short wavelength; a crystal may be studied using the diffraction of the X-ray beam from parallel planes of its lattice.

The first explanation of this phenomenon was proposed by Bragg. He supposed that to have a constructive interferences between incident and reflected beam, the incident and reflected angles should be equal ($\theta i = \theta r$).

Defining, d as the distance between two planes, the path difference for the reflected rays from two adjacent planes is:

$$2A = 2d\sin\theta \qquad (3.1)$$

Constructive interferences are possible only for path difference equal to an integer multiple of wavelengths λ

$$n\lambda = 2d\sin\theta \qquad (3.2)$$

Since $\sin\theta$ cannot exceed unity:

$$\frac{2d}{n\lambda} = \sin\theta < 1 \Rightarrow n\lambda < 2d \qquad (3.3)$$

Since the smallest value of n is 1

$$\lambda < 2d$$

An X-ray has a wavelength comparable with the typical lattice space.

In general any diffraction can be considered as first order in the d/n space and Bragg's law can be rewritten

$$\lambda = 2d\sin\theta \qquad (3.4)$$

In first approximation it is possible to consider the scattering of the incident beam as coherent (or elastic).

Any wave can be described as a product of amplitude A for its phase ϕ, in the case of elastic scattering the resulting wave can be written:

$$Ae^{i\varphi} = fe^{2\pi i(hu+kv+lw)} \qquad (3.5)$$

where f is the atomic wave factor and it describes the magnitude of the scattering for a single atom in a defined position, (h,k,l) are Miller indices and (u,v,w) are atom position indices.

The *structure factor F* is the resultant wave and it describes the contribution of all the atoms of the unit cell

$$F_{hkl} = \sum_{1}^{n} fe^{2\pi i(hu_n+kv_n+lw_n)} \qquad (3.6)$$

The intensity of the diffracted beam is proportional to $|F|^2$

All the diffraction measurements during this experiment were collected using the polycrystalline method. We consider a single plane (*hkl*); it may give diffraction when the diffraction angle complies with Bragg's law. In a polycrystalline material all planes (*hkl*) can be diffracted and the resultant will be a cone surface. One cone is formed for each distance of the same set of planes.

All the measurements were performed with a Philips PW1820 diffractometer using Cu-Kα radiation (λ = 1.5405Å).

3.5. Infrared spectroscopy

Spectroscopy is the study of the interaction between an electromagnetic wave and a sample. Mid-Infrared radiation (200-4000 cm^{-1}) is absorbed by molecules and transformed into molecular vibration.

The classical theory of vibration is based on the variation of the electric dipole of the molecule because of the interaction with the electrical component of the electromagnetic radiation

We can consider every molecule as an harmonic oscillator made up of two masses (atoms) linked by a spring and apply Hook's law.

$$F = -kx \tag{3.7}$$

The frequency of the vibration of the harmonic oscillator is given by the following formula in accordance with Hook's law

$$\nu = \frac{1}{2\pi}\sqrt{\frac{k}{m}} \tag{3.8}$$

where k = force constant

m = the mass

ν = is the frequency of the vibration

The energy is connected to the frequency by

$$E = \frac{1}{2}kx^2 = h\nu \tag{3.9}$$

with respect to the equilibrium position.

If this model was true, a molecule could absorb energy of any wavelength.

However, we know that the vibration energies are *quantized*: only some transitions are permitted:

$$E = \left(n + \frac{1}{2} \right) h\nu \qquad (3.10)$$

ν = the frequency of the vibration

n = is the integer number (0, 1, 2, 3, . . .)

The lowest energy level is $E_0 = 1/2\ h\nu$ and it corresponds to the equilibrium position, the first excited level is $E_1 = 3/2\ h\nu$.

There is a limit to a compression or expansion of the bond. The molecule has to be considered as an anharmonic oscillator.

The absorption frequencies are characteristic of each molecule so they are used to identify bonds of unknown compounds.

3.6. Thermal analysis

Thermal analysis is a generic term that groups together different techniques in which a physical property is measured as a function of temperature. During this experiment two kinds of techniques have been used: Heat-flux differential scanning calorimetric (DSC) and thermogravimetric analysis (TGA).

3.6.1. Heat-flux DSC

In general Differential Scanning Calorimetric measures the energy required to maintain the sample and the reference at the same temperature. The Heat-flux DSC is different from the DSC because the sample and the reference (an empty crucible) are inserted in the same reaction chamber and heated from the same furnace.

The peak area (*A)* in DSC will be proportional to

$$A = \pm \Delta H \, m \, K \qquad (3.11)$$

Where *K* is a constant independent of the temperature and it is determined during the calibration, *ΔH* is enthalpy and *m* is the mass.

The area of the peak is determined and it is possible to calculate the enthalpy of reaction.

3.6.2. Thermogravimetric analysis

Thermogravimetric analysis is a technique where the variation of the weight of a sample is measured as a function of temperature, during a controlled heating or cooling program.

The equipment which has been using for these experiments consists of a balance, a programmable heater and the reaction chamber.

3.7. Surface tension

Surface tension is a property connected to the liquid-air interface. A molecule inside the liquid is equally bonded with all the other surrounding molecules. On the other hand, a molecule on the surface of the liquid is bonded only with the molecules below and thus is subjected to a force directed to the centre which is balanced by the resistance of the liquid to be compressed. This is an easy explanation for the spherical shape of drops of water. Moreover the distance between molecules on the surface is larger so the attractive force exceeds the repulsive force.

The Du Nouy ring method is used to measure the surface tension of samples. A platinum ring is immersed into the solution, and the instrument measures the force necessary to pull out the ring through the liquid surface.

3.8. Solution conductivity

Conductance measurements are performed using a conductivity cell which consists of two platinum electrodes and a conductivity bridge (Wheatstone bridge) .

When the cell is immersed in a solution and a voltage is applied between two electrodes a current may flow through the circuit. This phenomenon is due to the movement of ions in the solution. If any kind of reaction occurs, the observed current follows Ohm's Law:

$$V = IR \qquad (3.12)$$

where V = potential
I = current
R = resistance of the solution.

The conductivity bridge is used to measure the resistance of the solution. A Wheatstone bridge consists of four resistances (R1, R2, R3, R4). The values of R1 and R4 are known while R2 is a variable resistance which can be obtained during the calibration. When the bridge is balanced (R1/R4=R2/R3) no current can flow through the circuit. When the bridge is immersed in the solution, the resistance of the solution causes an imbalance in the bridge. The amount by which R3 must be increased in order to restore the balance is equal to the resistance of the solution (R2).

Conductance *(S)* is expressed in Siemens (*S*) and can be calculated by

$$S = \frac{1}{R} = k\frac{A}{d} \qquad (3.13)$$

d = distance between the electrodes (cm)
A = area (cm^2)
κ = conductivity [S/cm]

3.9. MiniSIMS (secondary ion mass spectroscopy)[3]

During MiniSIMS analysis, the sample is bombarded with an ion beam accelerated by a potential difference of 1-25keV. The impinging ion collides with the surface of the sample and results in the emission of material which is usually electrically neutral but a small percentage is emitted as charged particles (secondary ions). These ions are filtered (in this case using a quadrupole) and collected during the MiniSIMS analysis.

Depth profiling and investigations of lateral uniformity of the layers were investigated in detail using a bench-top Millbrook MiniSIMS system with a Ga^+ primary ion energy of 6 keV and a crater area of 100 x 100 µm. The measurement yields a qualitative analysis and is not calibrated to give absolute concentrations.

3.10. Ion Beam Analysis

The interaction between an ion beam and a target can generate atomic and/or nuclear processes which can terminate with the emission of products. These products contain information about the composition of the sample and its properties.

Ion beam analysis is a broad family of methods and includes the Rutherford back scattering (RBS) technique which has been used during this project. RBS uses high energy hydrogen or helium ions as the probe. The high energy ions penetrate the sample, collide with the nuclei of the atoms of the sample and may be elastically scattered. The energy of the backscattered ions depends on the mass of the ions and on the depth at which the scattering happened.

The ratio between the energy of the ion beam after a collision and before the collision is called the kinematic factor and depends on the masses of the beam ions and of the sample atoms.

[3] Results were collected at Northumbria Photovoltaics Applications Centre (Northumbria University)

$$k = \frac{E_{scattered}}{E_{incident}} = \left\{ \frac{\sqrt{m_2^2 + m_1^2 \sin^2 \theta} + m_1 \cos \theta}{m_1 + m_2} \right\}^2 \qquad (3.14)$$

Where E = ion energy

m_1 = mass of incident ion

m_2 = mass of target atom

θ = scattering angle

The mass of the nuclei of the sample can be determined using the previous equation if the mass and energy of the incident ion beam and scattering angle are known.

The differential scattering cross section ($d\sigma/d\Omega$) can be correlated with the number of backscattered particles onto a solid angle for a given number of incident ions as follows

$$\frac{d\sigma}{d\Omega} = \left(\frac{z_1 z_2 e^2}{4\pi\varepsilon_0 Ei} \right)^2 \frac{1}{sin^4(\theta/2)} \qquad (3.15)$$

where z = atomic number of incident (1) and target (2)

Ei = energy of the incident ion

ε_0 = permittivity of free space

θ = scattering angle

The compositional depth profile of a sample can also be determined by RBS analysis. This can be achieved from the position of the peaks of the RBS spectra. The thickness can be determined by the width of the peaks while the relative concentration can be calculated by the peak heights.

Chapter 4:
Experimental Programme

A description of the experimental method used during this project has been presented in this chapter. The description of the rig and devices used during the experiment has been followed by an explanation of the method used to reduce the number of variables and the organisation of the project.

4.1. Electrostatic Spray Deposition (ESD) Rig

As described previously in chapter 2, ESD uses an electrostatic field to atomise a liquid precursor solution in order to form an aerosol (Schoonman et al. 1997; Leeuwenburgh et al. 2003; Leeuwenburgh et al. 2004; Leeuwenburgh et al. 2005; Yu et al. 2005; Zhang et al. 2005; Leeuwenburgh et al. 2006; Leeuwenburgh et al. 2006; Yu et al. 2006). This aerosol is then directed towards a heated substrate where it forms the desired thin film (Choy et al. 1998; Choy 2001; Choy et al. 2001; Choy 2003).

4.1.1. Cranfield ESD Rig

In the device design for this project, the potential required to atomise the precursor solution is applied between a stainless steel or glass spray needle and a heated substrate holder. A schematic diagram of the experimental set-up can be seen below in Figure 4-1.

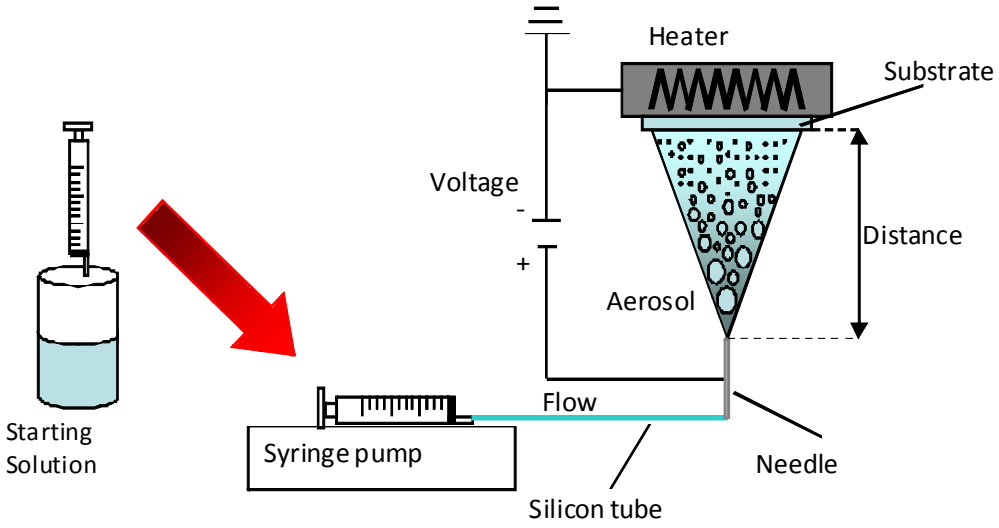

Figure 4-1: schematic of the ESD rig

Photographs of the ESD rig can be seen in Figure 4-2 which shows the layout of the rig and the arrangement of the substrate holder within the heated holder block.

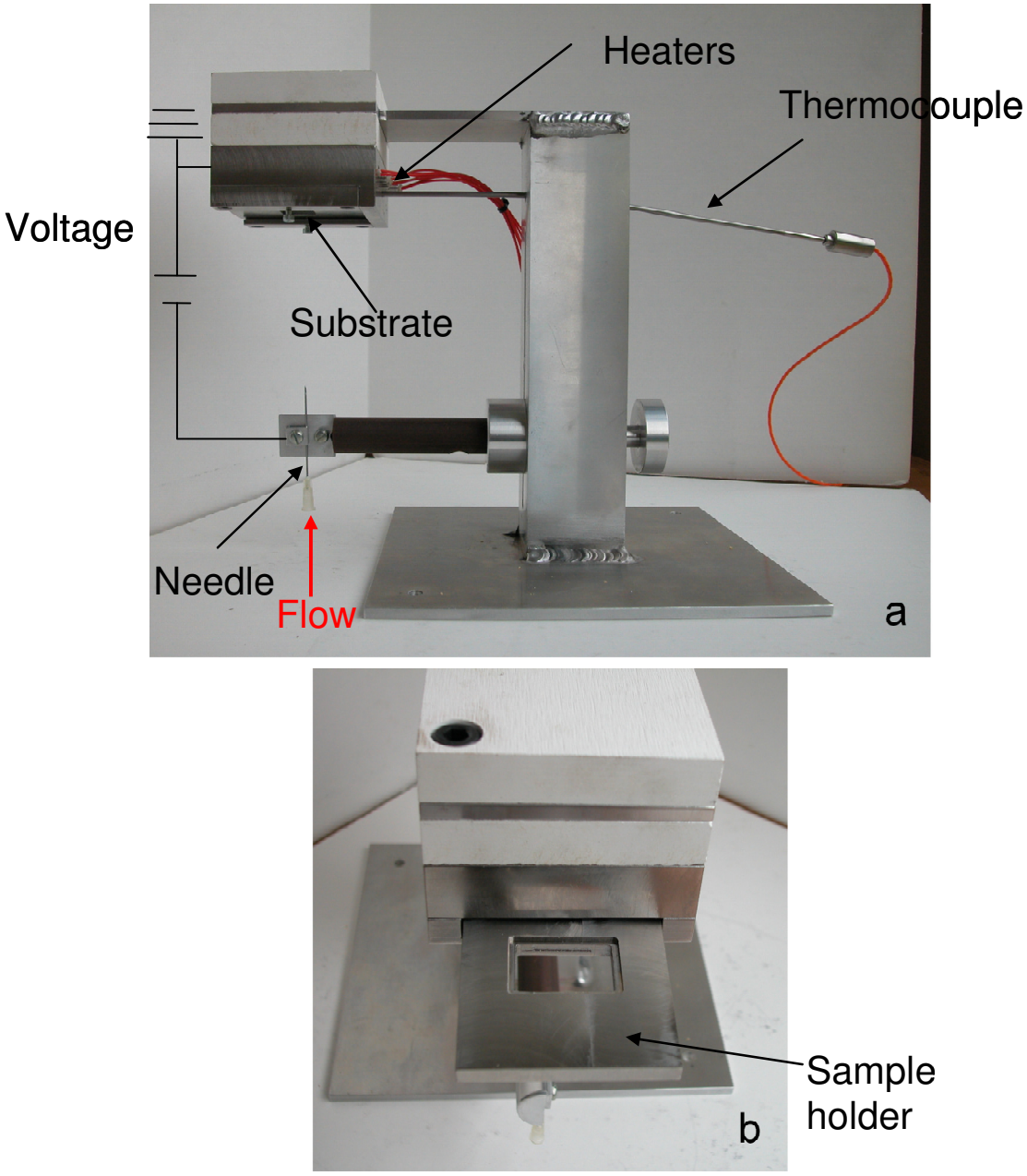

Figure 4-2: Photographs of the Cranfield ESD rig showing details of (a) the layout and (b) the sample holder arrangement

The potential was supplied using a Glassman EL40P1 stabilised DC supply. The DC supply could be varied in the range 0-40kV with a quoted accuracy of 2% full scale. A positive potential (Chen et al. 1996; Chen et al. 1996; Chen et al. 1999; Taniguchi et al. 2003; Huang et al. 2004) was applied to the needle via an aluminium needle holder block. The substrate holder was connected to earth.

Two types of needle were used: stainless steel and glass. The stainless steel needles used were Terumo hypodermic syringe needles with a length of 25mm and an external diameter of 0.5 mm and a 25 gauge wall thickness. In order to prevent arcing between the tip of the needle and the substrate, the sharp tip was ground off to leave a flat tip. The glass needle had a platinum wire embedded through the wall and into the needle internal channel in order to make an electric contact with the high voltage source and atomise the solution as it passed over the wire.

The distance between the tip of the needle and the substrate could be varied by raising or lowering the arm which held the needle.

The precursor solution was fed to the needle through a silicone, acid-resistant tube connected to a polypropylene syringe (Volume = 30ml). The solution flow rate from the syringe to the needle was controlled using a KDS270 syringe pump (Taniguchi et al. 2003; Taniguchi et al. 2003; Neagu et al. 2006; Neagu et al. 2006). The flow rate could be varied between a minimum of 0.001μl/h and a maximum of 86 ml/min with a quoted accuracy of ±1% full scale and repeatability of ±0.1% full scale.

The substrate, and thus deposition, temperature was controlled by 4 heating elements connected to a temperature controller. The temperature could be controlled between 25°C and 600°C with a quoted accuracy of ±1°C. The location of the heating elements in the ESD rig can be seen in Figure 4-3.

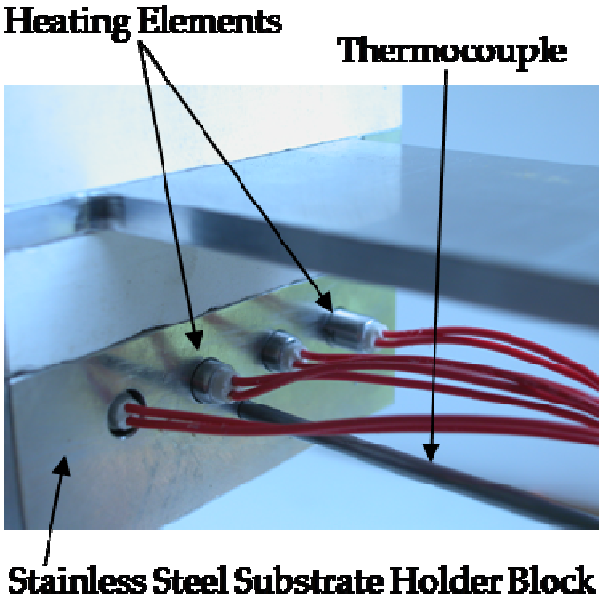

Figure 4-3: heating system of the ESD rig

The heating elements were inserted into the stainless steel block which was used to keep the substrate temperature stable during the deposition process. A K-type thermocouple was inserted into the stainless steel block near the heater elements and connected to the temperature controller in order to provide an accurate feedback reading for the controller.

The substrate dimensions were fixed at 20mm x 30mm x 5mm. The size was determined for the suitability for the characterization tests to follow.

The rig was fixed to a Bakelite insulated tray base in order to ensure that the rig remained isolated from the surroundings. The depositions were performed inside an interlocked fume cupboard in order to prevent any risk of inhalation of the atomised solution and also to prevent the DC supply from being activated accidentally whilst adjustments were being made on the rig.

4.2. Reduction of the Experimental Variables

During the initial set-up and calibration of the ESD process, a study was performed in order to assess and quantify the effects of numerous variables so that the best combination could be identified to optimise the quality of the as- deposited films. The variables identified for study in the initial stage are summarised in Table 4-1 below.

Table 4-1: Experimental Variables and Associated Units

Variable Name	*Units*
Potential between needle and substrate	Kilovolts (kV)
Precursor solution flow rate	Microlitres per minute (µl/min)
Deposition temperature	Degrees Celsius (°C)
Distance between needle tip and substrate	Centimetres (cm)
Precursor Solution Concentration	Mol (M)
Spray Needle Material	-
Precursor Solution Type (chloride and nitrate)	-
Precursor Solution Molar Ratios	-
Substrate Material	-

A full statistical analysis of the interaction between each of the variables would require each variable to be changed while the others are maintained constant in order to evaluate the effect of each individual variable on the final sample. However, if each of the 9 variables had, for example, 4 values, the number of samples required for a full analysis would be 4^9 (=262 144) samples. Clearly, an analysis of the variable interaction this in-depth is neither sensible nor possible during a PhD research programme.

Therefore as first step to reduce the number of samples, the variables were divided into two independent groups as summarised in Table 4-2. Group 1 variables determine the physics

of the experiment (i.e. jet and Taylor's cone dimensions), whilst the Group 2 variables determine the properties of the as-deposited films.

Table 4-2 : Summary of Group 1 and Group 2 Variables

Group 1 Variables	*Group 2 Variables*
Precursor solution flow rate	Precursor Solution Type
Potential between needle and substrate	Precursor Solution Molar Ratios
Precursor Solution Concentration	Spray Needle Material
Distance between needle tip and substrate	Substrate Material
Deposition temperature	

This division of the variables is based on the assumption that the characteristics of the aerosol are independent of the solution type and its molar ratios, but, dependent on its conductivity and the surface tension. Further, it is thought that different precursor solutions will likely exhibit the same behaviour at different experimental conditions. For example, the aerosol cones for ethanol and water will exhibit the same trend when the voltage is changed, but the actual voltage at which the aerosol will form will be different for the two solutions due to the difference in their conductivity and surface tension.

The second step considered the effect that each Group 1 variable had on the other Group 1 variable using a multi-dimensional regression analysis. In this analysis, all Group 2 variables were held constant. The conditions for the regression analysis are summarised in Table 4-3 below.

Table 4-3: Group 1 and Group 2 Variables and Values for Regression Analysis

Group 1 Variables and Values	*Group 2 Variables and Values*
Flow rate: 25, 50, 100, 250µl/min	Solution Type: Chlorine
Applied voltage : 14, 16, 18, 19, 20, 21, 22, 23, 24, 26 kV	Molar ratios : Cu/In=1 and S/Cu=5
Solution concentration: 0.21, 0.35, 0.49M	Needle type : Stainless steel
Needle substrate distance: 4, 5, 6, 7cm	Substrate type: SnO_2:F (FTO) coated glass
Deposition temperature: 380, 410, 450ºC	

Although the number of the samples was drastically reduced to 256 using this procedure, it was still too high to deposit thin films and fully analyse them using the standard characterisation methods described in chapter 3.

Thus, the uniformity test for semi–transparent films, as described in detail in chapter 3, was developed. This test allowed a reduced deposition time per sample which was, however, still sufficient for the statistical analysis of each of the combinations of variables. As described, the test calculates the uniformity grade of thin films deposited on SnO_2:F (FTO) coated glass using a Matlab algorithm. This powerful test allowed samples (and thus the deposition conditions) to be discarded from further investigation when the films were non-uniform.

Once the valid experimental conditions were established by the results of the uniformity test, the Group 2 variables were investigated by holding a constant set of Group 1 variables and spraying thick films for each of the combinations of Group 2 variables. A summary of Group 2 variables and their different values is given below in Table 4-4.

Table 4-4: Group 2 variables

Group 2 Variable	*Variable Values*
Needle Type	Stainless Steel and Glass
Substrate Type	Aluminium, FTO Coated glass
Precursor Solution Type	Chloride and Nitrate
Molar Ratios	Cu/In = 0.6, 0.75, 1., 1.5, 3 S/Cu =5, 5.3, 5.5

Each of the samples sprayed during the second step were fully characterised using a number of different analysis techniques such as X-ray, SEM, RBS, mini-SIMS, etch. Each of the techniques used allowed a different property of the as-deposited film to be investigated. The combination of techniques allowed the atomisation process, film morphology, composition, thickness, photo-response and electrical properties to be analysed fully and the most suitable candidate spray conditions to be taken forward to the fabrication stage for a full cell device.

4.3. Window Layer Deposition

Using the information and experience gained in the deposition of the absorber layer ($CuInS_2$), the window layer (ZnS) was deposited using the ESD. All the precursor solutions were prepared using a molar concentration of 0.21M as this was identified as the most suitable value from the absorber layer uniformity test. Due to the difference in surface tensions between $CuInS_2$ and ZnS solutions, the window layer films were grown at a series of different temperatures, voltages, flow rates and molar ratios in order to confirm that the results from the $CuInS_2$ study were valid for ZnS films. The deposition conditions considered for the ZnS stage are summarised in Table 4-5 below.

Table 4-5: Deposition conditions used for ZnS layer

Variable	*Values*
Deposition Temperature	380, 450, 500°C
Applied Voltage	16, 18, 22kV
Solution Flow Rate	50, 100, 200 µl/min
Solution Molar Ratios	S/Zn = 0.5, 1,2 ,3

The best quality samples (i.e. highest photocurrent response) were taken forward to the device fabrication stage of the project.

4.4. Super/Substrate Solar Cell Configurations

The most effective absorber and window layers from the previous two studies were used to create two different configurations of solar cell device; superstrate and substrate. The details of the two different configurations can be seen in Figure 4-4. In the superstrate configuration, FTO glass was used as a substrate onto which ZnS and $CuInS_2$ were sprayed as consecutive layers. The circuit was completed with a sputtered molybdenum back contact applied on top of the $CuInS_2$ layer. Alternatively, in the substrate configuration, a molybdenum layer is sputtered onto glass slide onto which $CuInS_2$ and ZnS were sprayed consecutively. A ZnO back contact was sputtered on top of the ZnS layer to complete the cell.

The completed cell configurations were characterised for photocurrent response using an IV curve method.

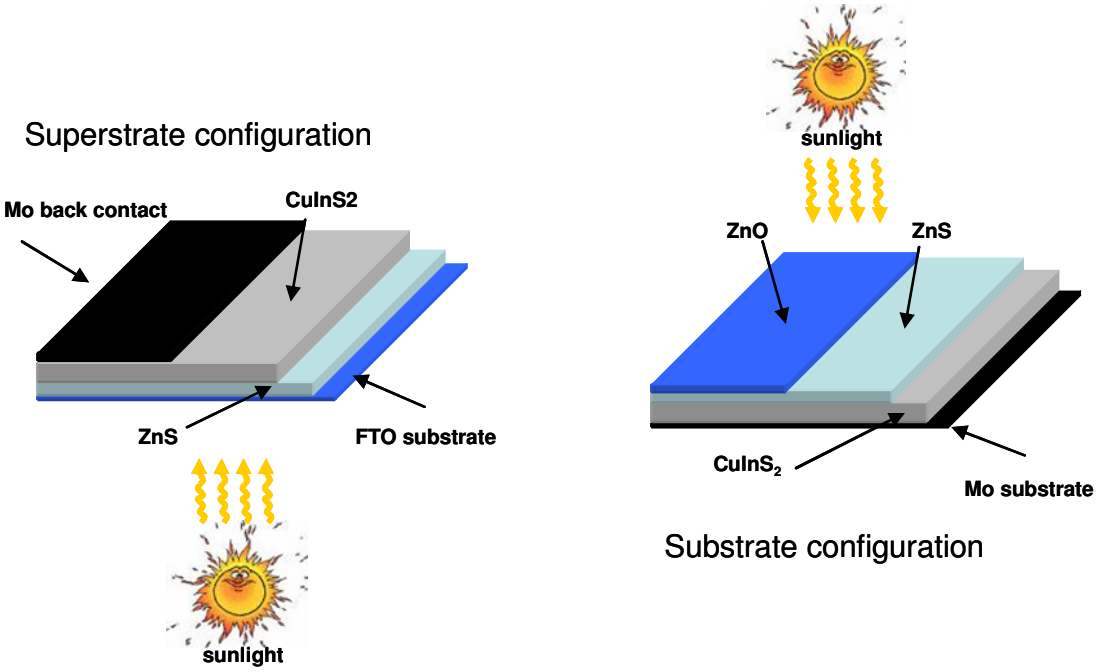

Figure 4-4: superstrate and substrate configurations

Chapter 5

Establishing ESD as a Deposition Technique

As previously mentioned, the ESD rig and procedure had to be established at Cranfield for the first time. Starting with CIS films this section describes the investigation into the spray parameters which can be used to produce uniform thin films.

As described in the following section, numerous films were sprayed under different conditions. For a functional device, the deposited films have to be continuous, otherwise shorting may occur as additional layers are deposited. To this end, the uniformity test (described in section 3.1) was developed and applied to the as-deposited film (produced using stainless steel needle). This enabled spray conditions which produce non-continuous films to be discarded and allowed the selection of those conditions which produced the most uniform films (Section 5.1).

In addition, during this initial experiment using a stainless steel needle, an interruption of the spray was observed which prompted an investigation into the material from which the needle was made. Glass needles produced in-house were used instead of stainless steel and the properties of the films compared. The results of this investigation will be described in section 5.2. Finally, ESD should have the ability to deposit these films onto different types of substrate. This could be of major interest for the commercialisation of the sprayed solar cells, e.g. in architectural panels. The overview of this experiment is given in section 5.3

5.1. Uniformity test: Effect of depositions conditions

To estimate the effect of deposition conditions on the uniformity of $CuInS_2$ thin films, the uniformity test presented in chapter 3 was used in combination with particle image velocimetry (PIV) measurements (chapter 3).

5.1.1. Analysis of data / presentation of results

The effects of five variables (deposition temperature, applied voltage, flow rate, precursor solution concentration and distance) on the uniformity and velocity distribution have been investigated. The results of the uniformity test will be expressed by using:

- The number of samples which pass the MUT
- Micro uniformity where *W* is the full width half maximum (FWHM) of the μUT graphs (section 3.1). This will be expressed as U (=1/*W*) in order that a highly uniform film is denoted by a high value of U.

The PIV data was analysed and transformed into two-dimensional velocity vector maps from which velocity profiles from the tip of the needle to the substrate were extracted and could be compared for the different experimental conditions. The contour map with vector shows the velocity field and flow structure in the aerosol cone being emitted from the tip of the flow needle. The centre line needle tip (5 mm below the visible axis) is located at 0 mm vertical position and 0 mm horizontal position (i.e. the centre of the abscissa). The contours show the velocity magnitude of the cone whilst the vectors show the flow directions at a number of points.

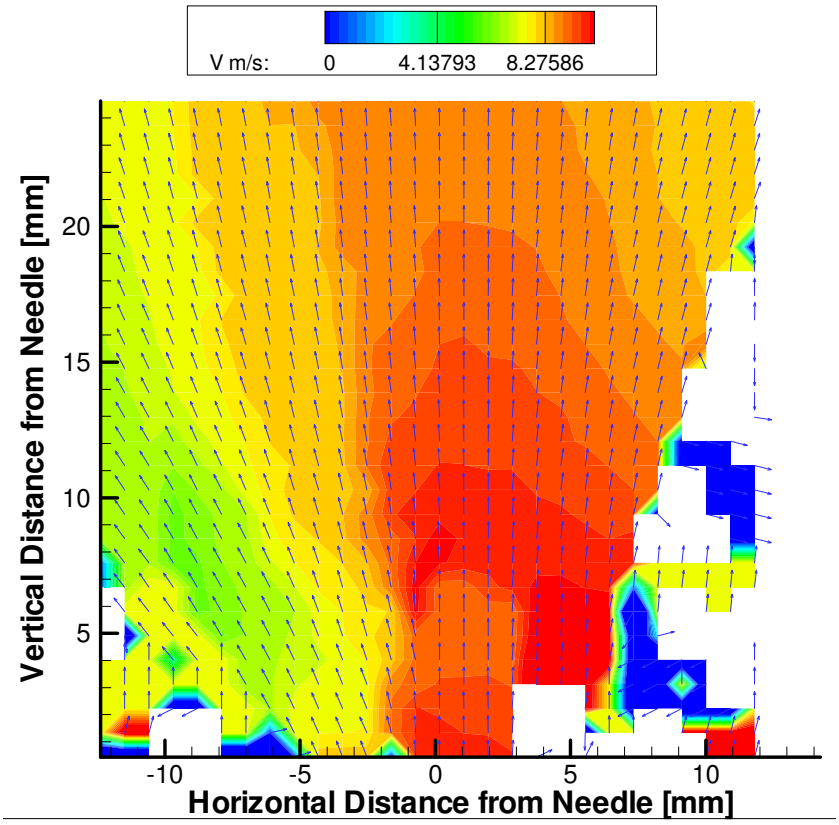

Figure 5-1: velocity contour map of velocity magnitude in aerosol cone. Overland with velocity magnitude vectors to show the structure of cone.

Due to the complexity of the analysis (more than 400 samples were sprayed), the results have been split into two groups. The first one (which includes the PIV) called "isolated variable analysis" shows the effects of the variation of one variable when all others were held constant. The uniformity test results were validated against the PIV data (which contain information about the homogeneity of the aerosol cone) in order to definitively state the effect of different conditions.

The second group (called" parametrical analysis") identified the most uniform sample from all samples sprayed in specific conditions. For example, when analysing the effects of temperature, the best uniformity test values obtained at 380°C, 410°C and 450°C were chosen from all the samples sprayed in these conditions. This allowed the effect that all the

possible combinations of the five variables have on the as-deposited films to be estimated (and the link between them) and provide a better understanding of the ESD technique.

5.1.2. Deposition conditions

As described in the chapter 2, ESD is a complex phenomenon based on a sequence of processes such as breakdown of charged droplets, evaporation of a solvent, decomposition of chemical precursors, formation of ternary compounds and deposition of the film. Each process is affected by the deposition temperature which controls the final dimension of the droplets impinging on the substrate and the nucleation/growth of the as-deposited films.

The effect of temperature

Isolated variable analysis

During this experiment the deposition temperature was varied between 380°C and 450°C while the other variables are maintained constant as shown in Table 5-1.

The velocity of the droplets is connected with their dimension and depends on the temperature gradient between the substrate and needle. An increase in temperature increases the evaporation rate (if the other variables are maintained constant) thereby reducing the droplets dimensions (William 1982). A decrease in the droplets diameter increases the charge density on the surface of the droplets which will increase the possibility of the Rayleigh limit being reached and hence droplets being ripped apart.

The PIV graphs of the aerosol cone of the samples deposited at different temperatures are shown in Figure 5-2 a, b and c. At low temperature (380°C), the PIV vector map shows a "jet" on the right side of the cone area. The dimension of jet is reduced when the temperature is increased to 410°C and a homogenous aerosol is formed at 450°C. The jet is constituted by faster particles (which have an average velocity of 9.9 m/s). This result was unexpected because of the correlation between the gradient in temperature and droplets dimension (as described below).

Table 5-1: Deposition conditions used during the "the effect of temperature: isolated variable analysis" experiment

Variable	*Value*
Voltage	18 kV
Flow rate	100 µl/min
Distance	6cm
Concentration	0.21M

As described by Miao et al (Miao et al. 2001) larger droplets move closer to the centre of the cone while smaller droplets move to the outer edge. Grigoriev et al (Grigoriev et al. 2004) showed that at 447°C the solvent evaporates half way between the needle and substrate then the precursor reaction occurs. Droplets formed by the solvent (which have the lower surface tension and thus smaller dimension) are distributed at the edge of the cone. At low temperature (380°C and 410°C) the solvent doesn't have time to evaporate before the droplets arrive on to the substrate because of the small evaporation rate. The resulting as-deposited films are porous which give a low value in the uniformity test as shown in Figure 5-3 where the uniformity tests results are presented. Increasing the deposition temperature results in a more uniform droplet size distribution and hence a more uniform velocity field. At 450°C a homogeneous size aerosol is formed showing uniform particle size and velocity (Figure 5-2). This reduces the number of defects on the final films because the precursors are decomposed near the substrate and then absorbed on to it. At this point the chemical formation reaction begins forming a dense film with good adhesion to the substrate increasing the uniformity test value (*U*).

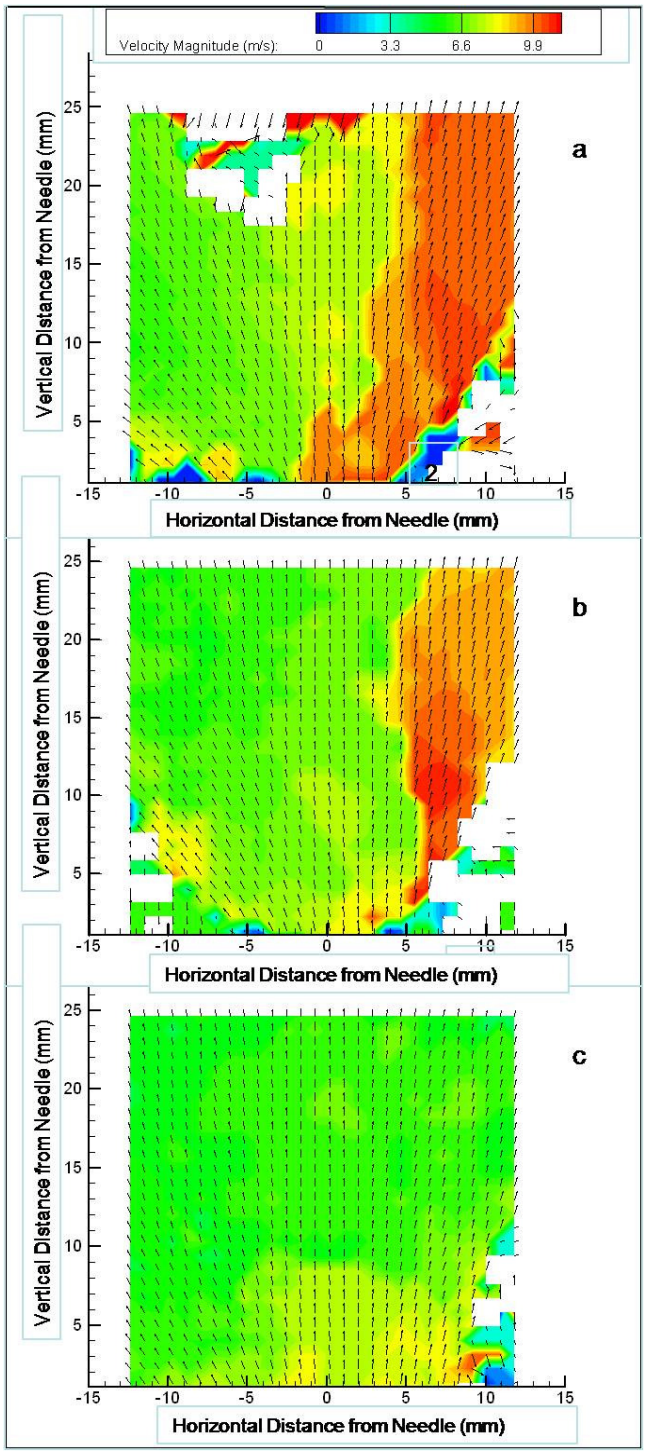

Figure 5-2: Velocity vector map coloured by velocity magnitude for temperatures: (a) 380°C (b) 410°C (c) 450°C.

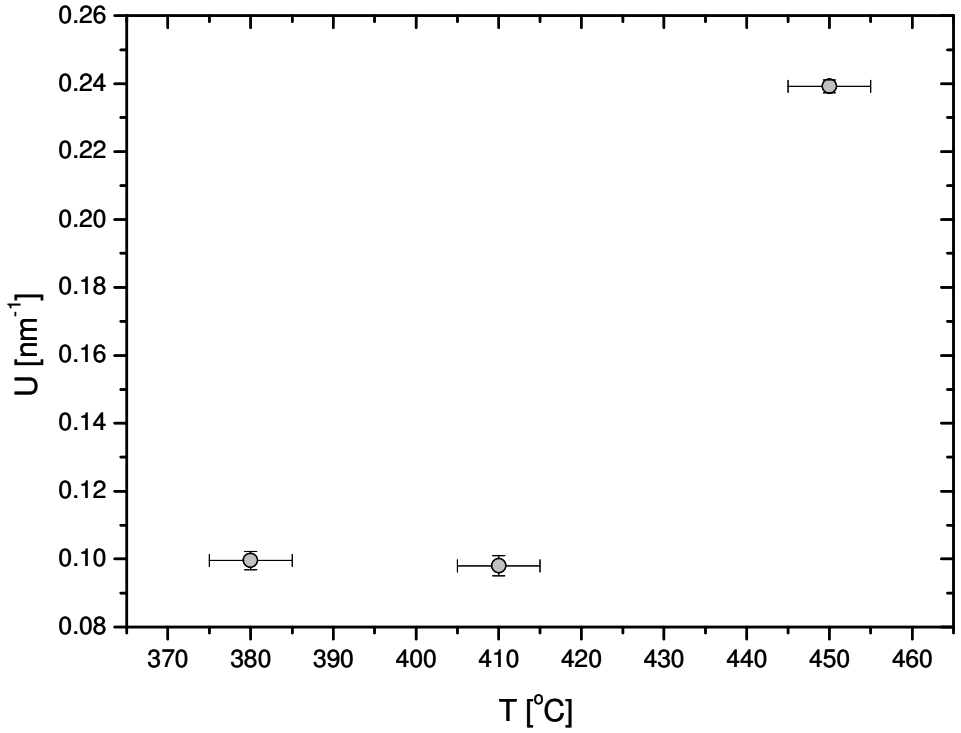

Figure 5-3: Variation of the micro-uniformity at different temperatures when applied voltage, solution flow rate, needle-substrate distance and solution concentration are maintained constant (see table 5-1)

Parametrical analysis

The parametrical analysis of the effects of the temperature shows similar results. The number of samples which passed the test increases with the temperature (Figure 5-4b) demonstrating that more samples reached a minimum uniformity at higher temperature (450°C). The uniformity value (*U*) also increased with the temperature (Figure 5-4a) suggesting that this is the dominant variable since a higher temperature produces more uniform samples even when the other variables are not optimised. This behaviour is not seen for any of the other variables as described in the following sections.

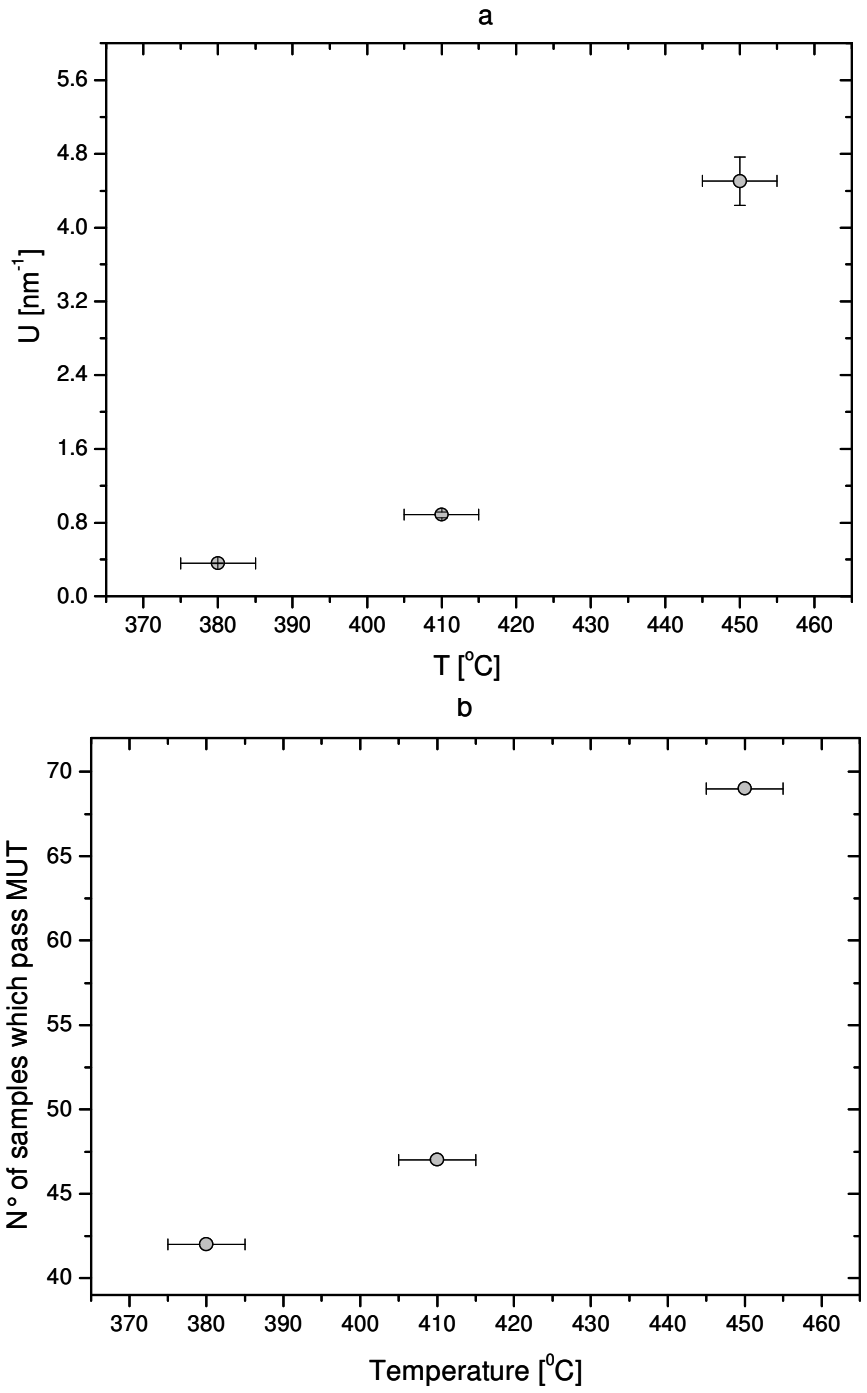

Figure 5-4: Variation of the uniformity (a) and "number of samples which passed the uniformity test" (b) with the temperature during the parametrical analysis. The uniformity value and the number which pass the uniformity test increase when the T is raised as observed during the isolate variable analysis.

The effect of the applied voltage

Isolated variable analysis

To assess the influence of variation in voltage a precursor solution with a concentration of 0.21M was sprayed onto FTO coated glass substrates from a distance of 50 mm, at a flow rate of 100 µl/h and with the substrate temperature at 450°C. The applied voltage was changed between 12 kV and 18kV. Increasing the voltage increases the charge density on the droplets surface, the Rayleigh limit is reached and a fine aerosol is formed. The velocity of the particles is also increased because it is dependant on the force associated with the electrostatic field generated by the applied voltage. This is confirmed by the PIV measurements which show an increase in the velocity within the cone as the potential increases between 12 and 18 kV. Figure 5-5 shows the velocity profiles measured vertically from the tip of the needle and reveals the magnitude of the velocity changes with the voltage. The PIV analysis doesn't show any inhomogeneity of the aerosol cone when the voltage is changed as seen for the temperature (Figure 5-2).

The uniformity test results are shown in Figure 5-6. The increase in the particle velocity in the aerosol results in 'pin-holed' films with low uniformity while the samples sprayed at 12 kV have fewer defects because the solvent in the droplets evaporates completely before arriving on the substrate, giving a more uniform covering.

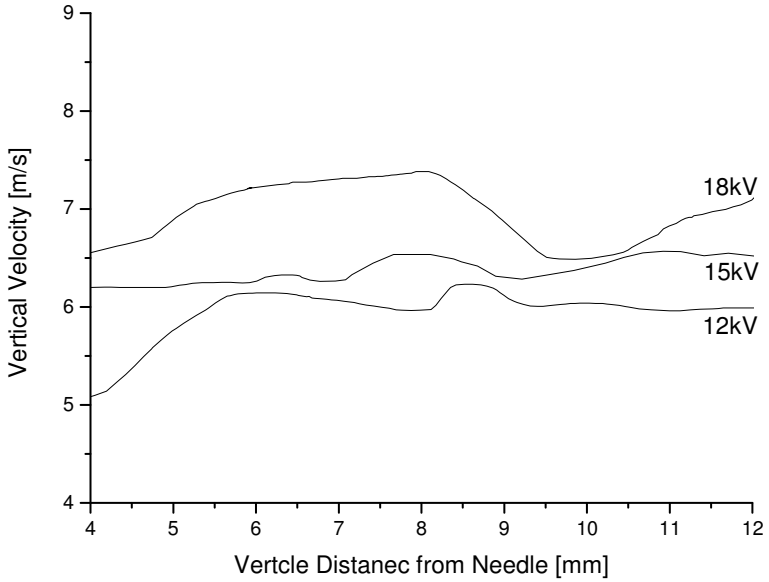

Figure 5-5: Vertical velocity profile from needle towards substrate for different voltages

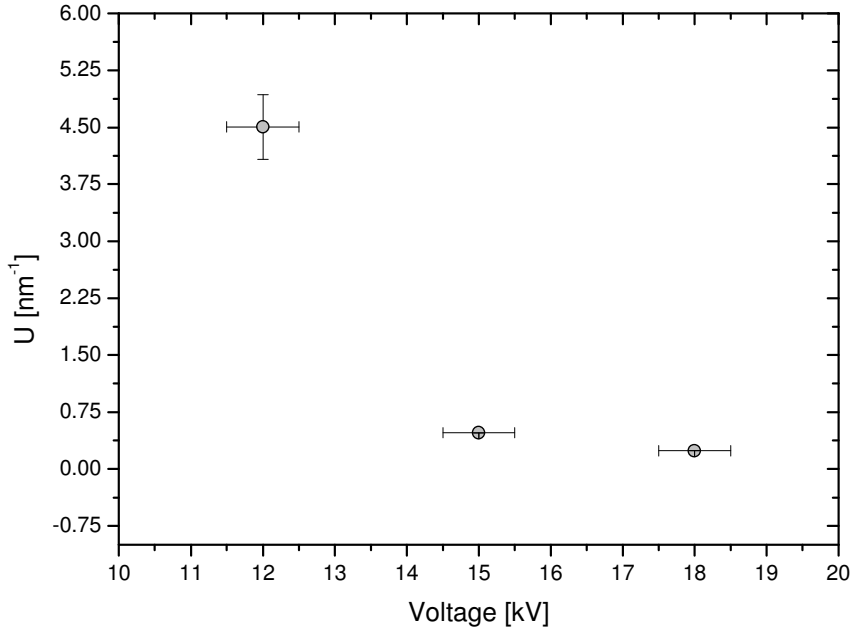

Figure 5-6: Variation of uniformity values with the applied voltage when the other variables are kept constant (deposition temperature = 450°C, solution flow rate = 100µl/min, needle-substrate distance = 5cm, solution concentration = 0,21M)

Parametrical analysis

The statistical analysis of the effects of the voltage have been analysed at different temperatures showing different trends. At higher temperature (450°C, Figure 5-7) it is the same obtained in the "isolated variable analysis". At lower temperatures (between 380 and 410°C), the trend of the uniformity graph is completely different as shown in Figure 5-8. At lower voltages, the droplet charge density is too low to generate a fine aerosol. The as-deposited films produced in this condition are non uniform due to the impingement of 'large' droplets onto the substrate. When the voltage is increased the coating defects decrease because the dimension of the droplets approaches their optimum size for uniform films.

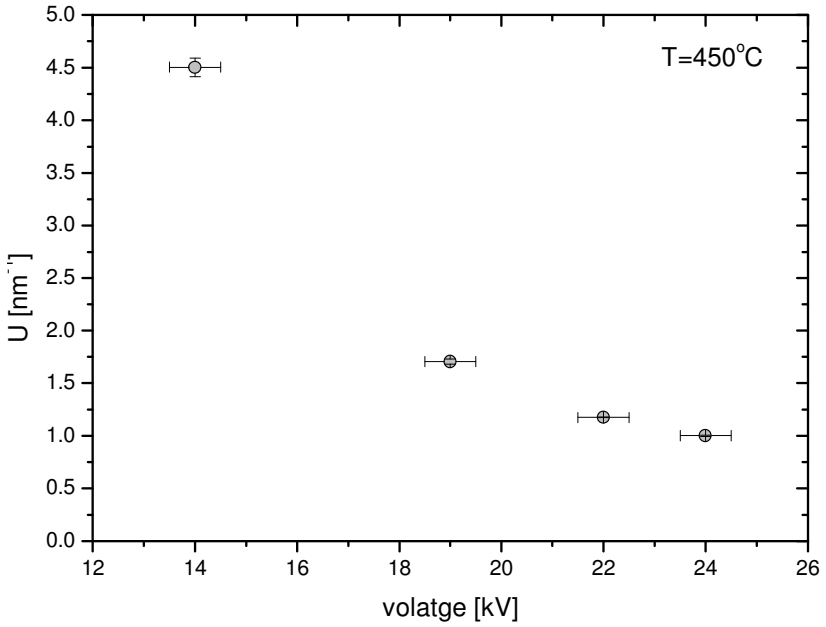

Figure 5-7: Variation of the uniformity values with voltage at 450°C during the parametrical analysis. The trend is the same obtained during the isolated variable analysis (Figure 5-6).

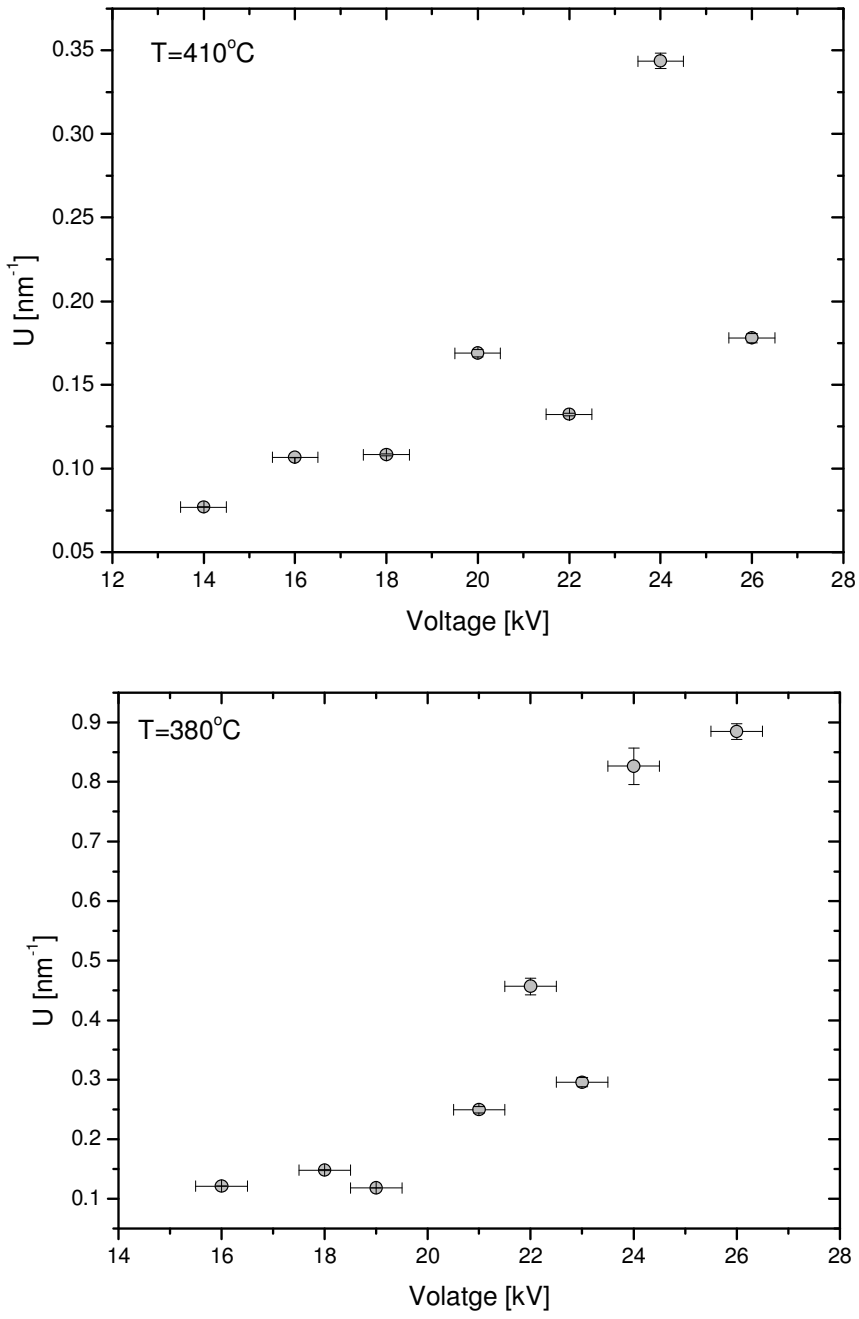

Figure 5-8: Variation of the uniformity values with voltage at lower temperatures (T=410°C and 380°C) during the parametrical analysis.

Effect of the flow rate

Flow rate affects the dimension of the droplets but also the growth rate of the films. When droplets arrive near the substrate, the solvent evaporates and drops are adsorbed onto it. The adsorbed molecules do not remain in their original positions, but may be re-evaporated or migrate to more stable sites. At the same time, other processes can occur due to collisions and combinations of adsorbed molecules. Depending on the deposition rate, some molecules can bond with others and form the first aggregate (usually the most stable of the single particles). These "islands" of molecules can grow or decay. If they become stable, they will grow until they may touch a neighbouring aggregate. The process continues till the film is formed. To evaluate the effect of the flow rate, PIV particles images of the spray cone at 200, 100, 50 and 25 μl/min respectively were captured (Figure 5-9). The images were analysed using imageJ (Rasband 2007) in order to calculate the number of droplets within each image or different flow rates. Figure 5-10 shows clearly a linear reduction of number of particles as the flow rate is reduced which results in less material arriving on the substrate.

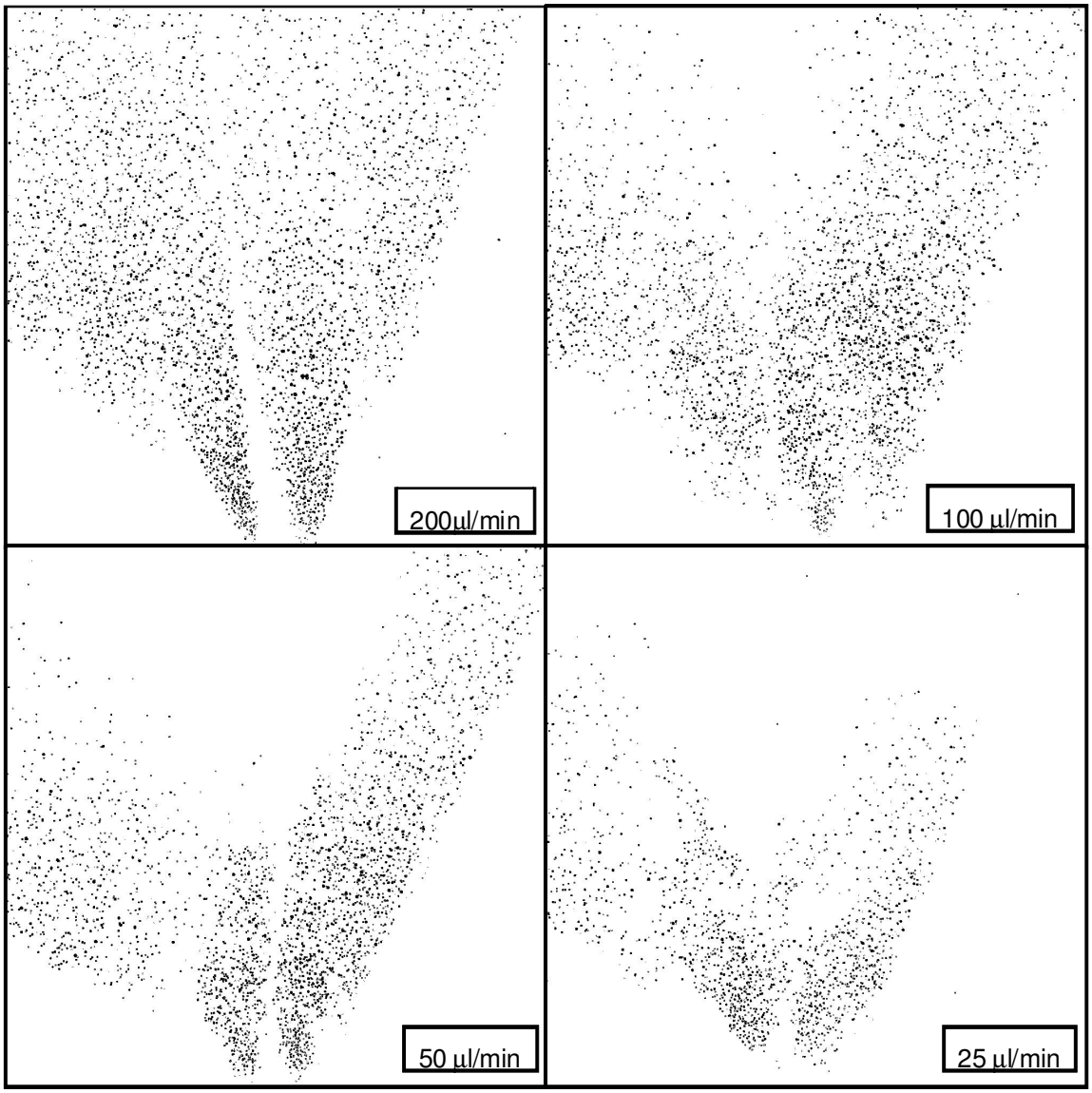

Figure 5-9: Cone jet shapes at different flow rates (200µl/min, 100 µl/min , 50 µl/min and 25 µl/min) when deposition temperature = 450°C, applied voltage = 18kV, needle-substrate distance = 6cm and solution concentration = 0.21M.

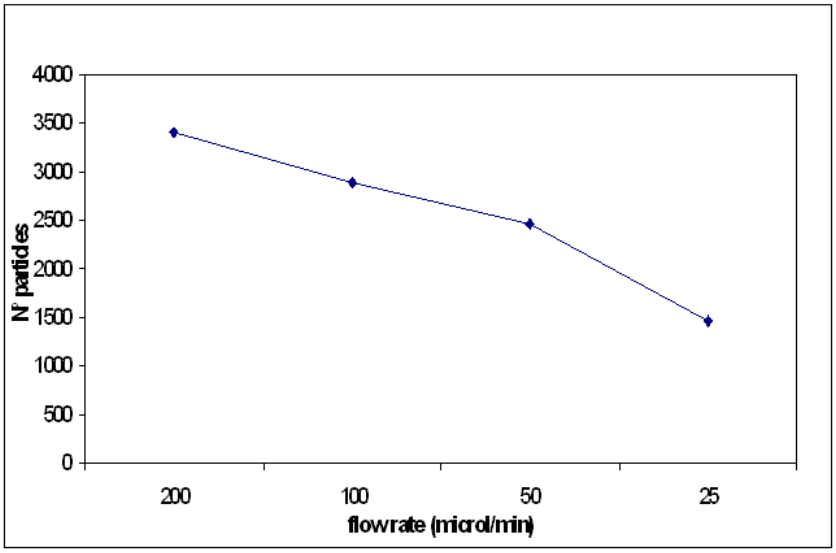

Figure 5-10: The number of droplets within each image (Figure 5-9) for different flow rates

Isolated variable analysis

The deposition conditions used in this study are shown in Table 5-2.

Table 5-2: Deposition conditions use to evaluate the variation of the flow rate on the uniformity of the as-deposited films

Variable	*Value*
Voltage	18 kV
Temperature	450°C
Distance	6cm
Solution Concentration	0.21M

A variation in flow rate has an effect on droplet size as predicted by Guanan-Calvo (chapter 2): as the flow rate is increased the droplet size increases. Figure 5-11 shows the variation in droplets velocity; the increase in velocity is correlated with a decrease in droplets size. For a given applied voltage, the force on the particles will be the same. Therefore a reduction in the mass of the droplets (caused by reduction of the droplets size with the drop of the flow rate) results in an increase in the droplets acceleration (Newton's 2nd law). Applying

$$V^2 = V_0^2 + 2as \tag{5.1}$$

Where V = speed [m/s]

V_0 = initial speed m/s] (is equal zero)

a = acceleration [m/s^2]

s = distance [m] (constant)

it can be seen that an increase in "*a*" for a constant distance (*s*) results in an increase in the final velocity.

The uniformity graph shows only a small variation of *U* suggesting less effect of the flow rate on the final films (Figure 5-12). The samples deposited at a high flow rate (200µl/min) produces a less homogeneous film while the samples deposited a low flow rate (25µl/min) have a more uniform covering. This can be explained by a variation in the droplet dimension and also by the different growth rate as discussed above. As the temperature and the charge density are constant (William 1982), the evaporation rate doesn't change during this experiment. The dimension of the droplets can be calculated using the following equation (equation 2.7, page 22):

$$d \propto \left(\varepsilon_0 \frac{Q}{k} \right)^{1/3}$$

When the flow rate is high, droplets arrive on the substrate and then evaporate. In this condition, a non-homogenous covering layer is deposited because the mechanical stress due to the shrinkage of the liquid observed during evaporation. This phenomenon is attenuated by a reduction of the flow rate and the most uniform films are deposited at 25µl/min. A low flow rate corresponds to a low growth rate which reduces the number of defects in the final films.

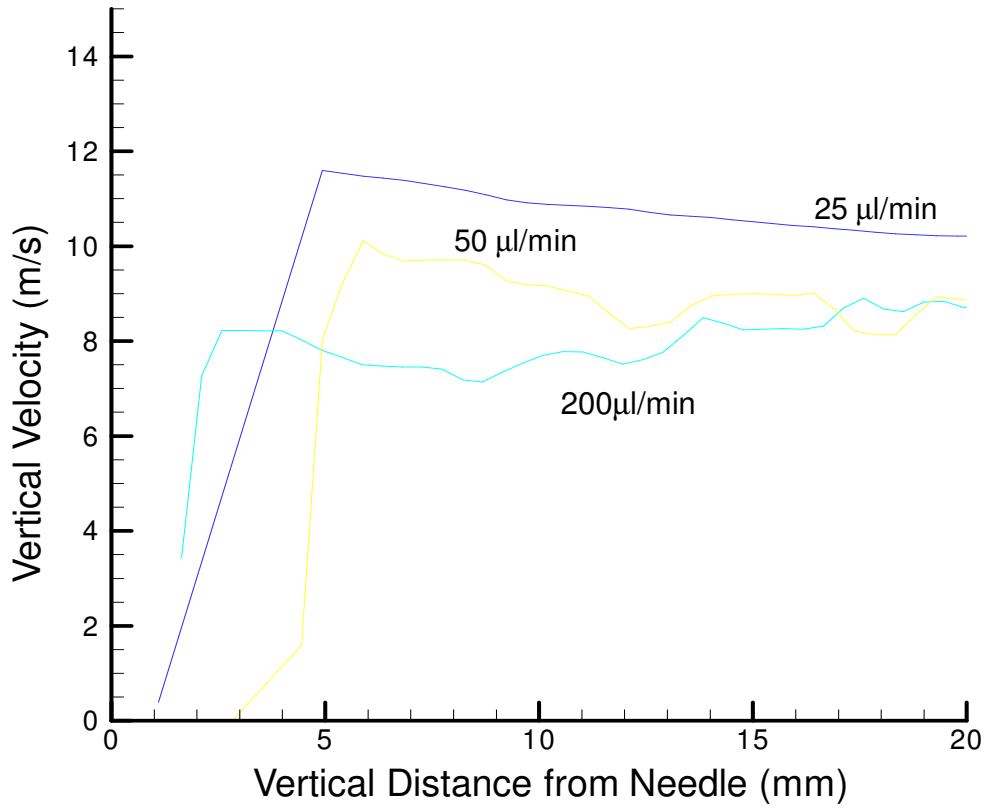

Figure 5-11: Vertical velocity profile from needle towards substrate for different flow rates

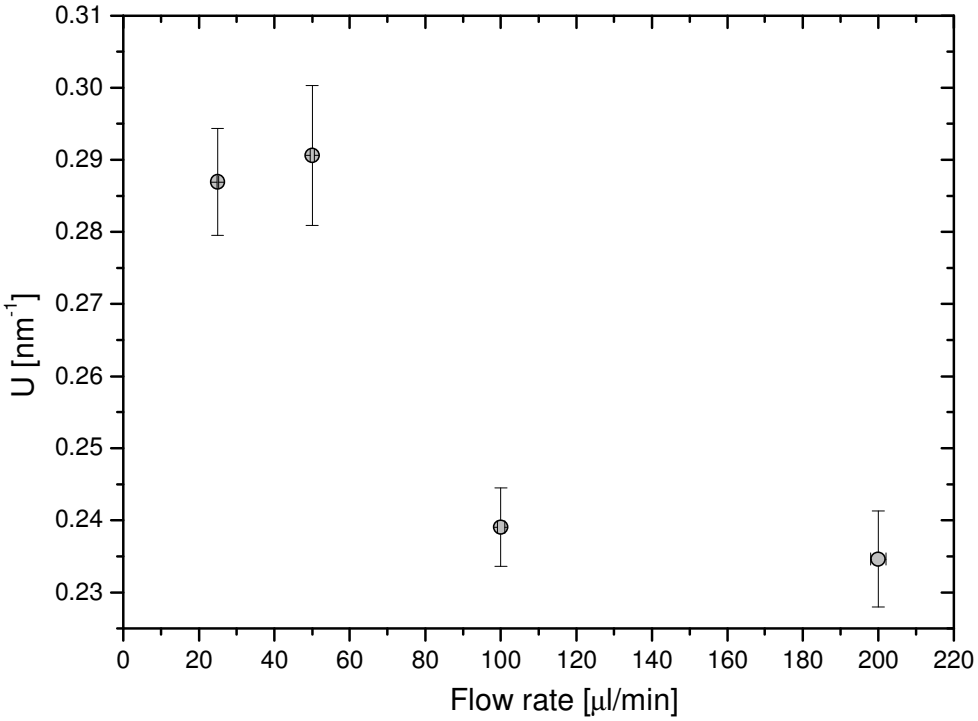

Figure 5-12: Variation in uniformity of the as-deposited films with flow rate

Parametrical analysis

The results of the statistical analysis are presented in Figure 5-13. The trend indicates a degradation of the film uniformity in samples deposited at low flow rates (25µl/min). In this case it is though that smaller droplets arrive at the substrates, the evaporation rate is high and dry particles strike the substrate generating 'pin-holed' films. At the highest flow rate (200µl/min), wet particles impinge onto the substrate generating 'spotted' samples. The most uniform sample is prepared from a flow rate of 100µl/min where the required droplets average size is reached. In this condition the films also grow in "equilibrium" reducing the amount of defects in the as-deposited samples.

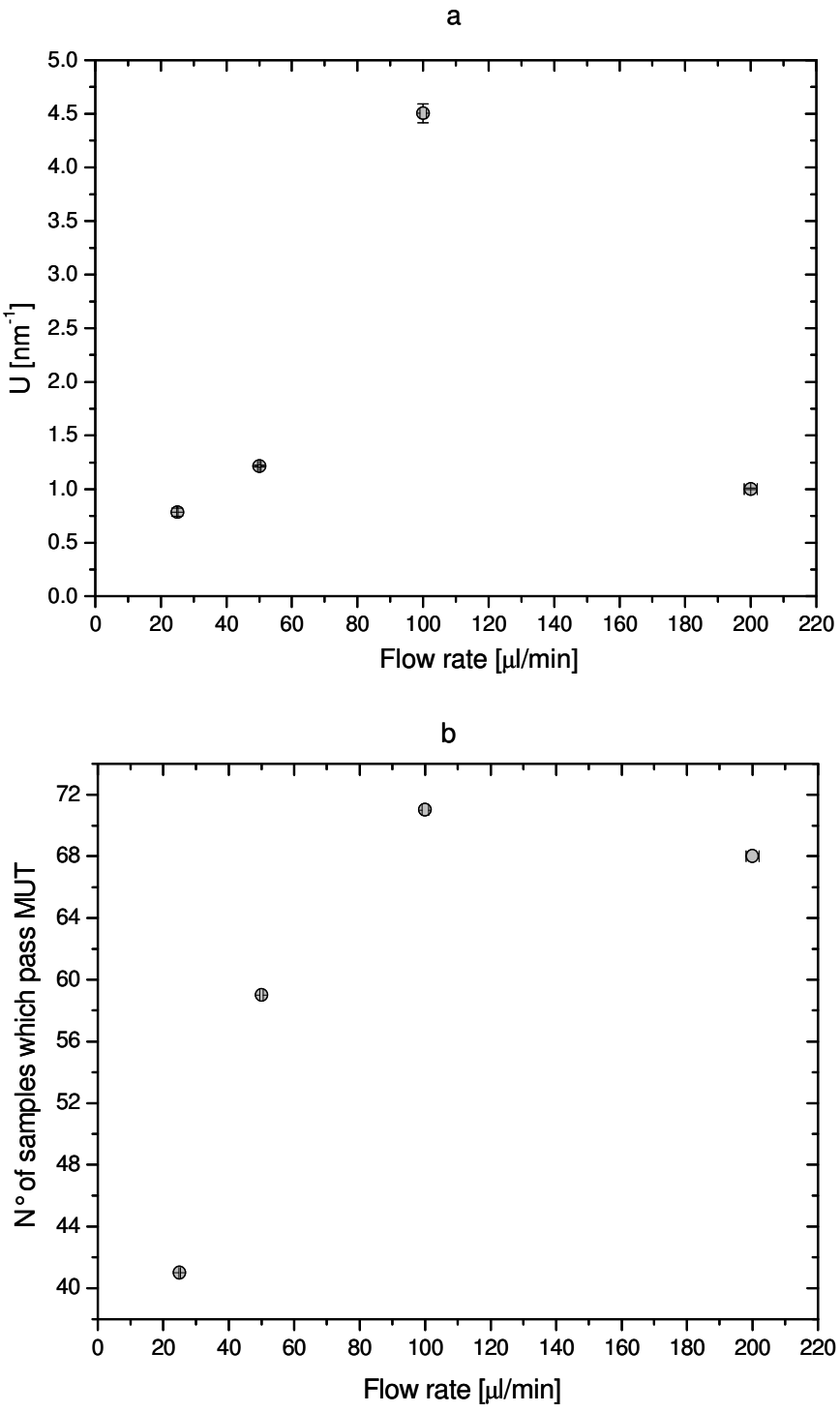

Figure 5-13: Variation in uniformity value (a) and of "number of samples which pass the MUT" (b) with flow rate.

Effect of distance

The needle-substrate distance controls the size of the droplets impinging on the substrate (as previously stated) but also affects the coverage area during the deposition process.
Assuming a constant evaporation rate and a homogenous electrostatic field between the needle and the substrate, the flight time (t) of the droplets can be calculated as follows:

$$t \approx \left(\frac{Lm}{qE} \right)^{1/2} \tag{5.1}$$

where L = needle-substrate distance
m = mass of the droplets
E = electrostatic field
q = charge

At large distances, the flight time increases and thus the dimension of the droplets are reduced. Vice-versa at short distances, the flight time is reduced and the evaporation time drops and thus the dimension of the droplets impinging onto the substrate is increased.
The flow rate also controls the area of materials deposited on the substrate. Assuming the formation of a cone at the top of the needle, at short distance the cone will not achieve a complete coverage of the substrate (Figure 5-14).

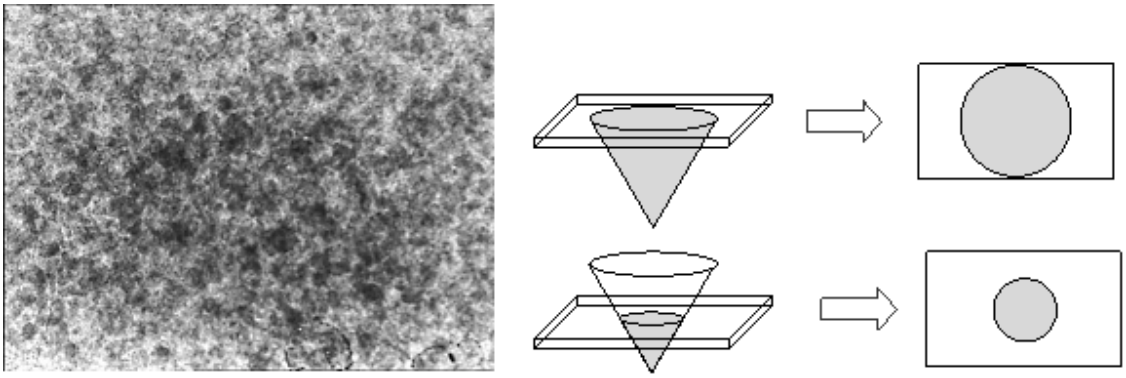

Figure 5-14: left) picture of a samples sprayed at 4 cm; right) representation of the change in cone deposition area with the distance

Isolated variable analysis

During this experiment the needle-substrate distance was varied between 4 and 6 cm while the other variables were maintained constant.

Table 5-3: Summary of deposition conditions used in distance variation analysis.

Variable	*Value*
Voltage	18 kV
Flow rate	100 µl/min
Temperature	450°C
Concentration	0.21 M

The uniformity test results for the variation in needle-substrate distance are presented in the following graph (Figure 5-15) which shows a maximum of the uniformity at 5 cm

At short distance (4 cm), the deposited area (cone deposition area of Figure 5-14) is reduced. This raises the thickness of the layer in some zones of the samples reducing the uniformity of the as-deposited films. The uniformity is also reduced by the large droplets impinging onto the substrate caused by the short flight time.

When the needle-substrate distance is at 5 cm, the droplets impinging on the substrate have similar dimensions. This produces an as-deposited film with fewer defects. Increasing the distance to over 5cm causes the dimension of the droplets inside the cone to become more varied; producing a non homogeneous film.

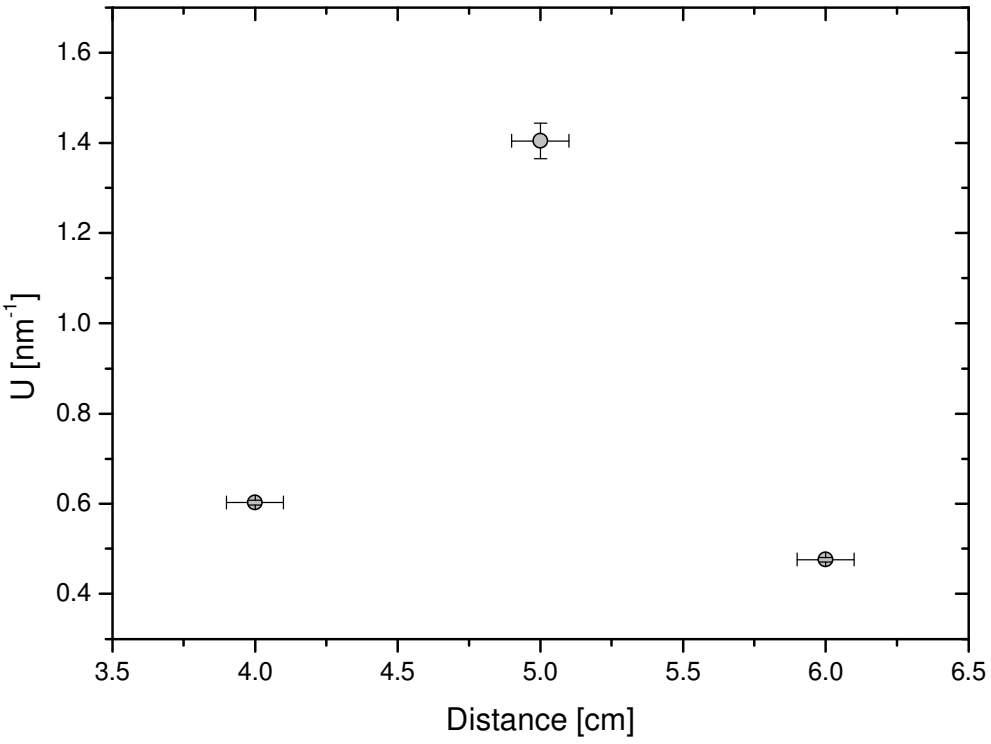

Figure 5-15: Variation in uniformity value with spray distance (from needle to substrate)

Parametrical analysis

Number of samples which passed the MUT During this experiment the maximum and minimum needle-substrate distance was influenced by the temperature. The minimum distance was determined by the electrical breakdown point (which is influenced by the temperature of the medium) while the maximum distance was controlled by the evaporation rate.

Figure 5-16 shows the numbers of samples which pass the macro-uniformity test (MUT). This number increases with needle-substrate distance but the slope of the curve depends on the temperature. As seen in "the effect of temperature" subsection of 5.1.2, the samples deposited at higher temperatures result in more uniform films. This demonstrates the importance of this variable during the ESD deposition process.

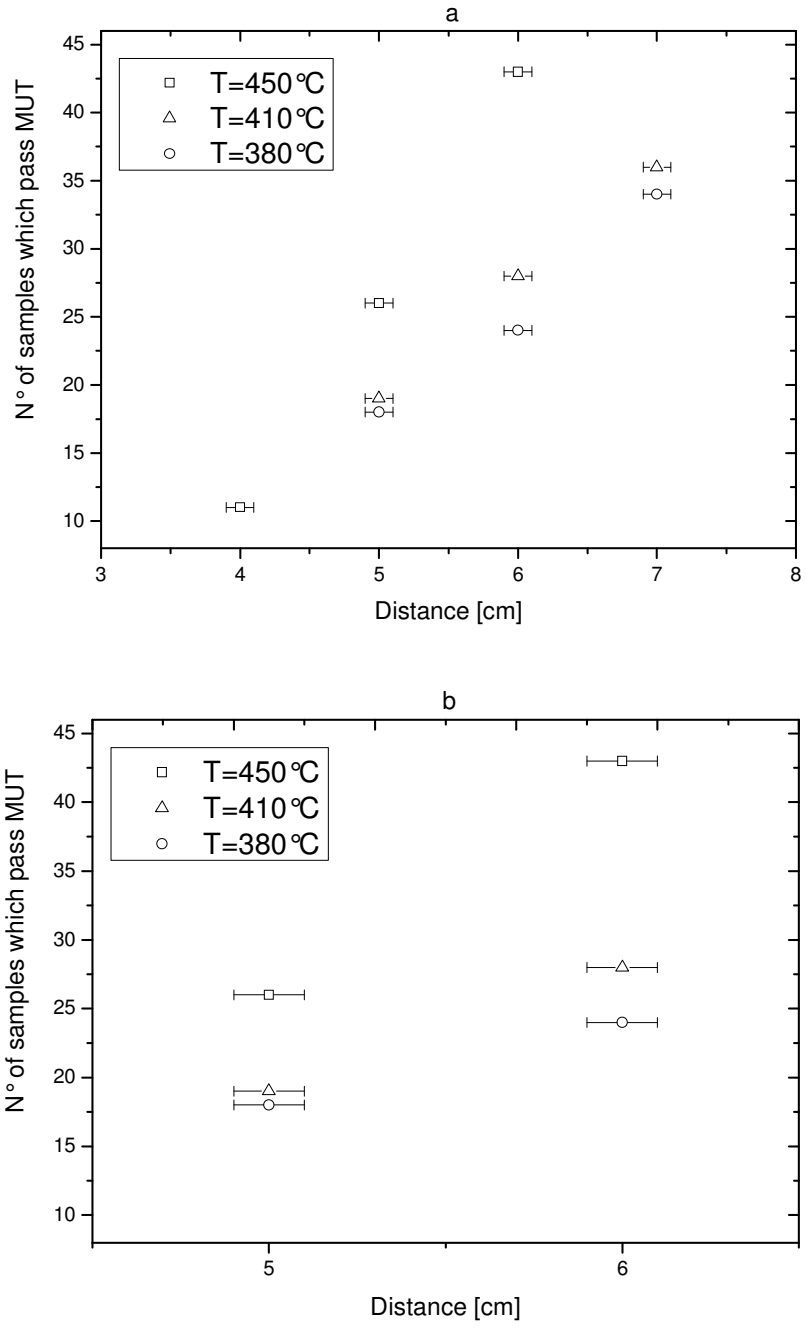

Figure 5-16: (a) Number of samples which pass the MUT vs the distance. (b) Close up of the graph between 4.75 and 6.25 cm

Uniformity test A reduction in needle-substrate distance also reduces the flight time (equation 2.10) or the quantity of solvent which evaporates. Consequently, wet droplets arrive on the substrate (the solvent doesn't have time to evaporate), increasing the probability for cracks to appear and producing pinhole as-deposited films. This affects the uniformity of the samples as shown in the μ-UT graphs (Figure 5-17). Increasing the distance (to over 6 cm) causes dry particles to strike the substrate, generating pinholes in the films. At 5 cm, the semi-dry droplets arrive at the hot plate and spray on it making a smooth film. This is confirmed by the uniformity test which gives the highest value for this distance (Figure 5-17).

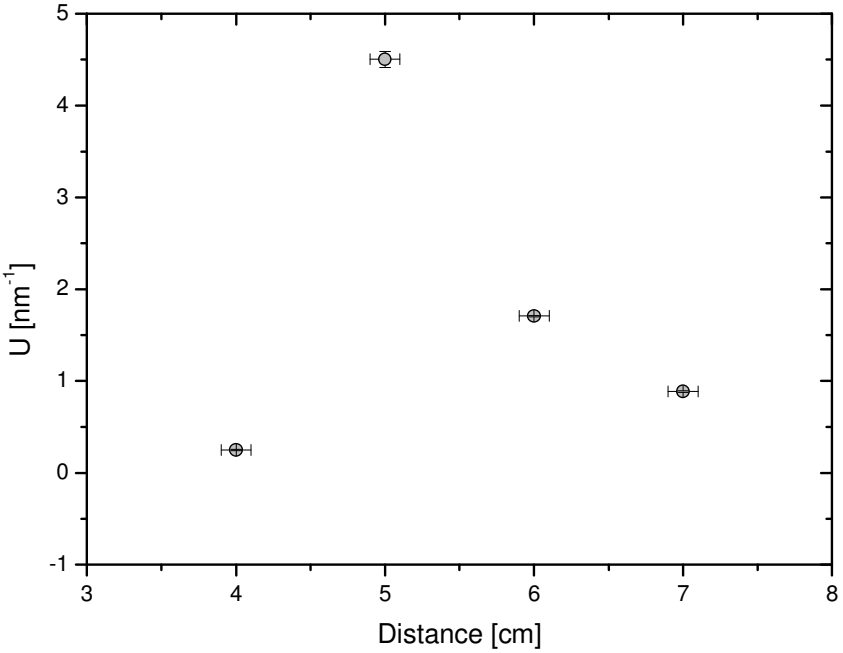

Figure 5-17: The Statistical results of uniformity value variation with needle-substrate distance

Effect of solution concentration

Isolated variable analysis

During this experiment the solution concentration was varied between 0.21M and 0.49M while the other variables were unchanged as shown in Table3

Table 5-4: Summary of deposition conditions used in solution concentration variation analysis

Variable	*Value*
Voltage	18 kV
Flow rate	100 µl/min
Distance	6 cm
Temperature	450°C

The PIV results for this study are present in Figure 5-18. The PIV analysis shows an inhomogeneity of the aerosol cone for the samples deposited at higher concentration (Figure 5-18C). The cone has a thick jet on the right side of the graph which corresponds to a flux of particles at higher speed (above 9.9m/s). As seen during voltage and temperature analysis, high velocity corresponds to small particles.

Concentration controls the conductivity of the starting solution as shown in Figure 5-19 where the conductivity increases proportionally with the concentration. In accordance with equation (2.7), a rise in the conductivity produces smaller droplets. These results are in agreement with the uniformity test which shows a minimum of the uniformity at high concentration (Figure 5-20).

The velocity of the droplets inside the aerosol cone is reduced (between 6.6m/s and 9.9m/s) when the concentration of the starting solution is dropped to 0.35M. The area of the inhomogeneity is dramatically cut down and is concentrated near the right side of the cone. This corresponds to a small increment of the uniformity of the as-deposited film due to a more smooth size distribution of the impinging droplets. At lower concentration (0.21M), the velocity distribution is more uniform across the cone which allows uniform samples to grow as shown by the uniformity test results.

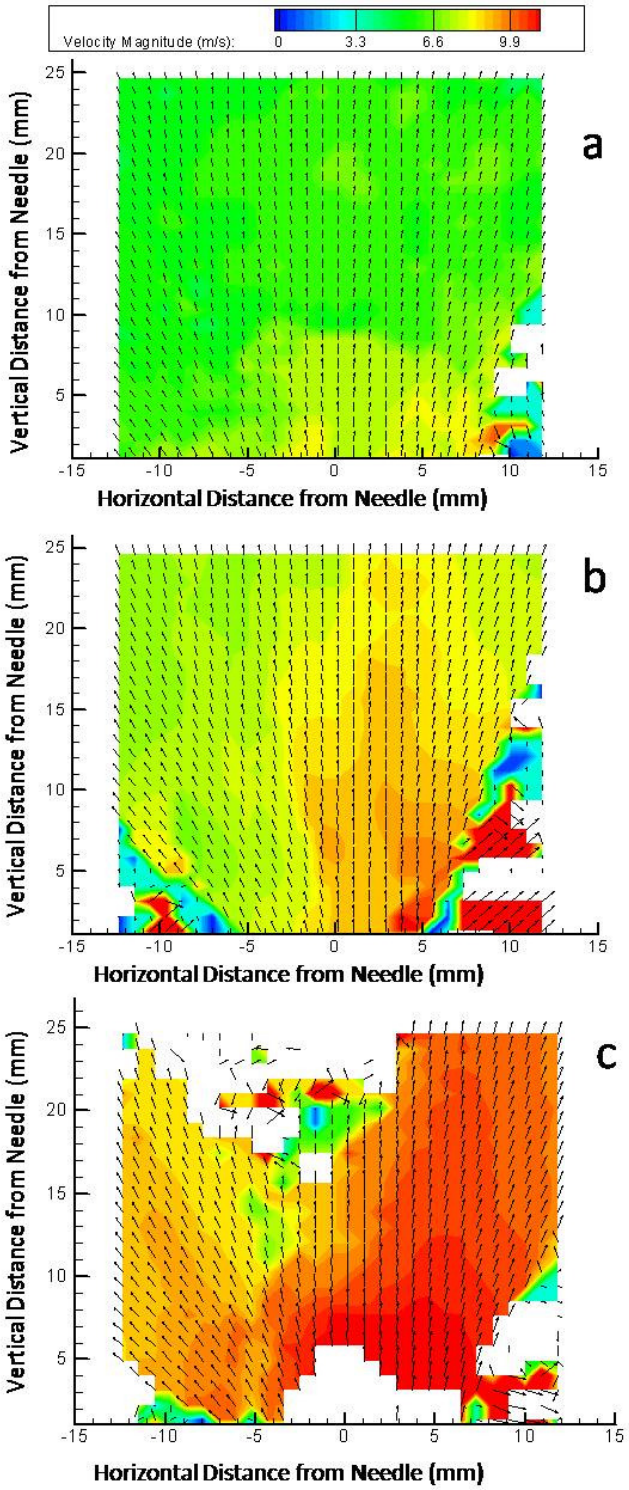

Figure 5-18: velocity vector map coloured by velocity magnitude for starting solutions concentrations: (a) 0,21M (b) 0,35M (c) 0,49M

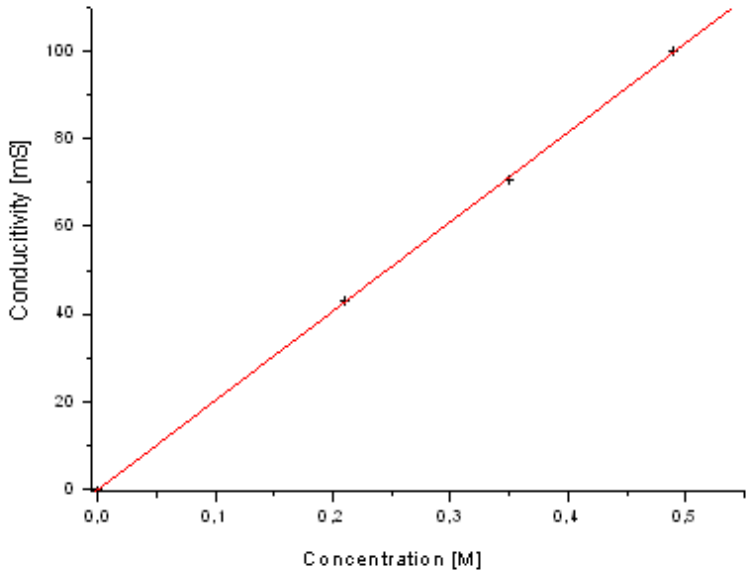

Figure 5-19: Variation in conductivity with concentration of the starting solution

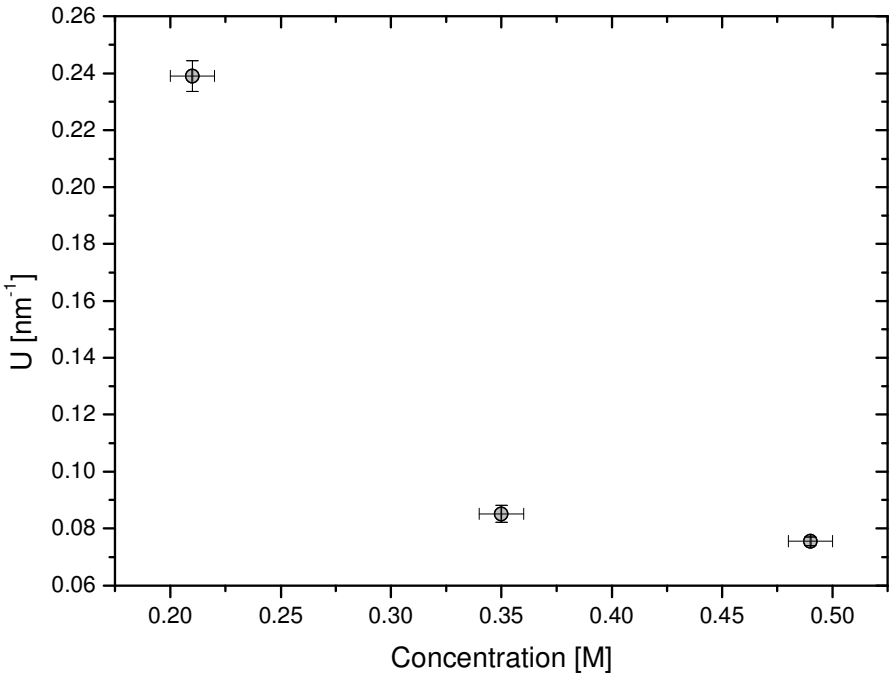

Figure 5-20: Variation in micro-uniformity values with solution concentration

Statistical analysis

The uniformity test (Figure 5-21) and "Number of samples which passed the MUT" graphs (Figure 5-22) have the same trends showing a maximum at 0.21M (the lowest concentration) and a sharp decrease with the concentration.

At low concentration, the films grow slowly and the molecules have time to occupy the lower energy positions. The result is good quality, uniform as-deposited samples. This is the reason of the high uniformity of the films. Increasing the concentration of the solution, decrease the droplets size. This in turn increases the velocity of the droplets which affects the growth rate. The results are rough and porous samples with a low uniformity as shown in the Figure 5-22.

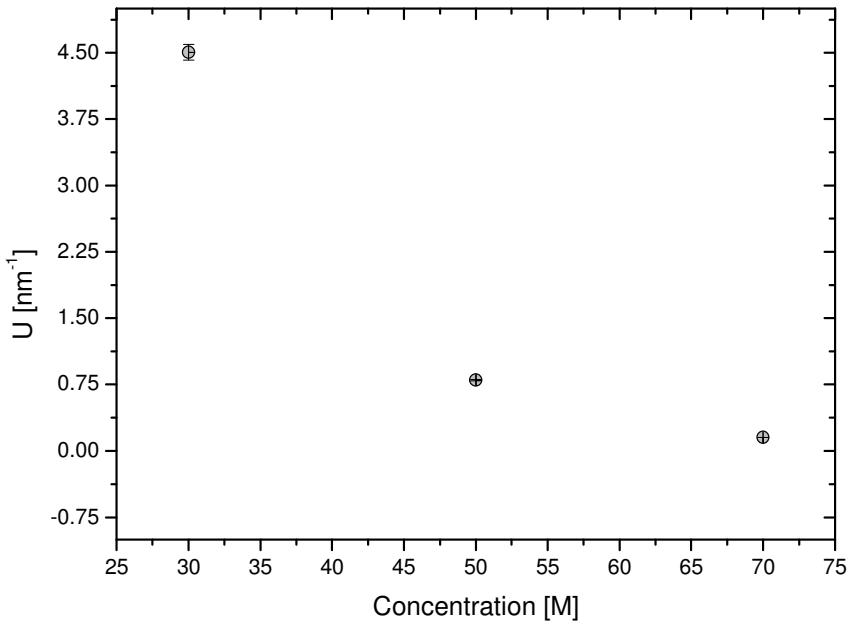

Figure 5-21: Variation of the statistical uniformity with the solutions concentration

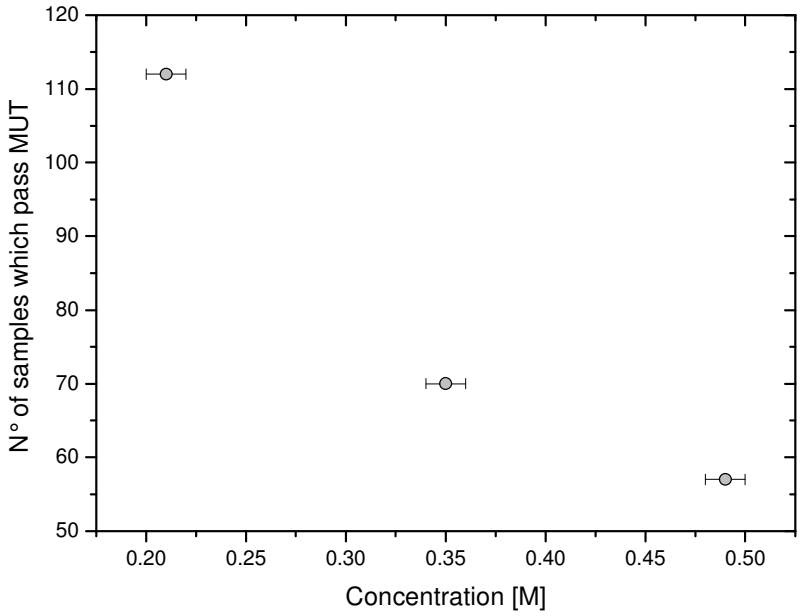

Figure 5-22: Variation of "number of samples which pass the MUT" with the solutions concentration

5.2. Effect of needle type: problems with stainless steel needle

This experiment was carried out during the study in order to analyse the effect that different needles have on as-deposited films. During this experiment, CIS films were deposited using two different needles: stainless steel and glass. The stainless steel hypodermic needle had a external diameter of 0.5 mm and a 0.1mm wall thickness. The tip of the needle was flattened prior to use to remove the sharp tip and avoid sparking between the needle and substrate. The glass needle (produced in house) had a platinum wire embedded through the wall of the needle in order to make an electric contact with the high voltage source and atomise the solution as it passed over the wire. The external diameter of the needle at the tip is 0.6 mm with a wall thickness of approximately 0.1mm.

$CuCl_2 \cdot 2H_2O$ (99.99%, Sigma Aldrich), $InCl_3$ (99,99%, Alfa Aesar) and thiourea (99%, Alfa Aesar) were dissolved in deionised water (18 $M\Omega cm^{-1}$ at 25°C) and ethanol (99.99%,

Fisher Scientific). The starting solution concentration, and the [S]/[Cu] and [Cu]/[In] molar ratios were fixed at 0.21M, 5 and 1 respectively . The solution had a low pH (=2.2) because HCl was added to facilitate the dissolution of the three chemicals.
All the samples were deposited on SnO_2:F coated glass (FTO) substrates.

5.2.1. Glass and steel needles

To study the effect of needle type on the film properties, the spray conditions were fixed (distance substrate-needle= 5 cm, applied voltage=18kV (section 5.3.2), solution concentration =0.21M, flow rate=100µl/min). Deposition temperature and time were varied as summarized in Table 5-5.

Table 5-5: Deposition conditions of $CuInS_2$ films on SnO_2:F coated glass using steel and glass needles

Sample Name	*Needle*	*T [°C]*	*Time [h]*
S1	STEEL	450	2h
S2	STEEL	450	3h
S3	STEEL	500	2h
S4	GLASS	450	2h
S5	GLASS	450	3h
S6	GLASS	500	2h

The X-ray diffraction analysis conducted on the films deposited using the two different needles (stainless steel and glass) can be seen in Figure 5-23 and Figure 5-24. The diffractograms are very similar suggesting that the type of needle used has no effect on the phase formation of the as-deposited films. It can clearly be observed that the samples show a sharp peak at $2\theta = 27.9°$ which represents the most intense peak and two further peaks at $2\theta = 46.4°$ and $2\theta = 55.1°$. These peaks were attributed to the $CuInS_2$ sphalerite structure when compared with the theoretical XRD data for sphalerite. The most intense peak is due to the (111) plane and the two lower intensity peaks are due to the(220) and (311) planes

respectively. No extra peaks are detected by XRD suggesting an absence of other phases. Impurties are observed in samples deposited with other methods such as electrochemical (Asenjo et al. 2006) and Spray ion layer gas reaction (Camus et al.).

The XRD of the samples deposited at 500°C for two hours show the largest (111) peak area and the smallest FWHM value as shown in Table 5-6. The two samples deposited at 450°C for two and three hours have smaller peak areas and larger FWHM. The results for these samples are similar to each other.

Similar behaviour can be observed for the samples deposited with the glass needle. The high value of the area and smaller value for the FWHM could suggest a high crystallization of the sample which could be caused by the higher deposition temperature which could favour the film growth process. The similar properties of the samples deposited at 450°C for two and three hours could suggest that an increase of the thickness of CIS (which has higher resistivity than FTO) could affect the deposition process.

Table 5-6: Summary of XRD Results for Glass and Steel Needle Deposited Samples

SAMPLE	*Needle*	*T [°C]*	*Time [h]*	*AREA*	*Error(AREA)*	*FWHM*	*Error(FWHM)*
S3	STEEL	450	2h	2374.61	213.45	0.42	0.14
S1	STEEL	450	3h	1953.82	270.44	0.73	0.05
S2	STEEL	500	2h	1463.94	45.42	0.90	0.01
S6	GLASS	450	2h	3241.13	39.85	0.31	0.01
S5	GLASS	450	3h	1607.77	134.07	0.56	0.02
S4	GLASS	500	2h	1882.28	125.66	0.56	0.02

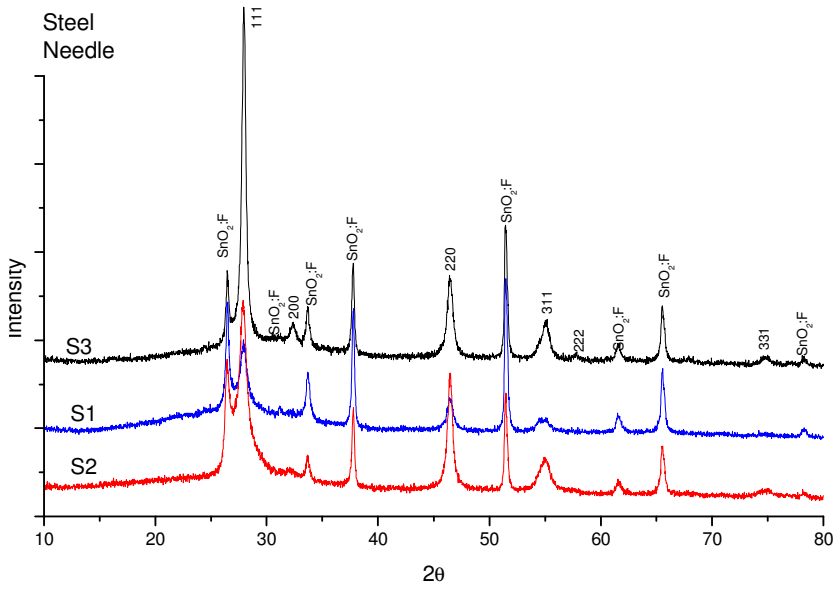

Figure 5-23: Diffractogram of the $CuInS_2$ as-deposited films sprayed using steel needle (summary of the deposition conditions can be seen in Table 5-6)

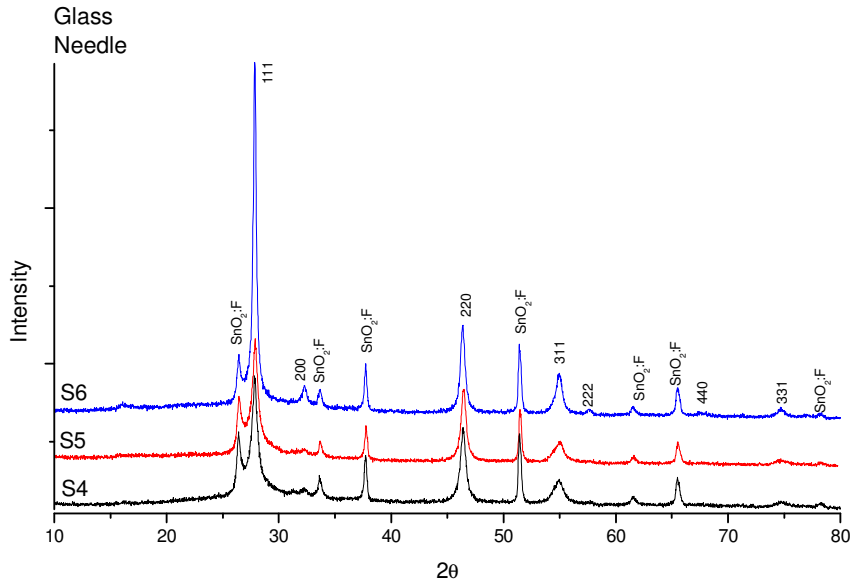

Figure 5-24: Diffractogram of the $CuInS_2$ as-deposited films sprayed using glass needle (summary of the deposition conditions can be seen in Table 5-6)

The SEM pictures of the morphology of two samples (S1 and S4) deposited with two different needles are shown below (Figure 5-25). On the left side, the steel needle film (S1) produces a rougher coating layer compared with the smooth and continuous film obtained with glass needle. This suggests a different particle size distribution inside the two aerosol cones or a different atomisation process of the precursor solution. The electric field profile is dependant on many factors, one of the most important being the shape of the conductive parts of the needle. For the steel needle this includes both the needle and the electrically conducting precursor solution, whereas for the glass needle only the precursor solution conducts. The high electrical conductivity of the steel needle may dominate the electric field profile and effectively fix the geometry of the spray, making it less sensitive to changes in the shape of the precursor meniscus. Whereas for the glass needle only the precursor solutions conducts and the electric field in the vicinity of the tip is solely defined by the shape of the meniscus. As the high electric field will distort the meniscus during deposition the spray from the glass needle is expected to be more diffuse due to rapid changes in meniscus shape

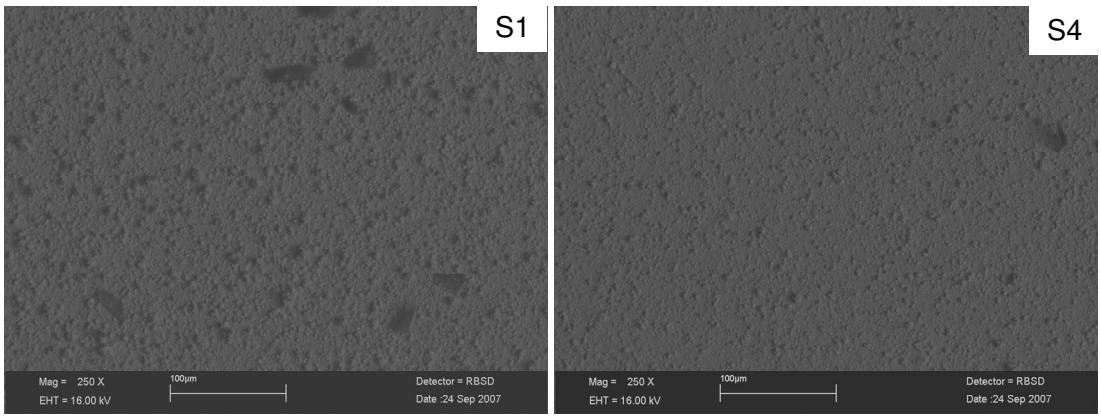

Figure 5-25: SEM pictures of the $CuInS_2$ films deposited using steel needle (left hand side) and glass needle (right hand side)

Figure 5-26 shows the Mini-SIMS depth profiles of 2 films sprayed using a steel and glass needle. The Figure 5-26 shows the profiles of the film constituents (Cu, In and S) and the main contaminants (Cr and Fe). For both films the level of the three absorber layer

constituents are uniform and of identical concentration (indicated by the same level of intensity in the same matrix system).

A difference is seen in the impurity concentration in the CIS films. Cr and Fe, at the background level for the glass needle, are present in films sprayed using steel needle. It also seems that the contamination increases with time of deposition as both traces increase towards the surface of the film possibly due to a prolonged corrosion process of the needle.

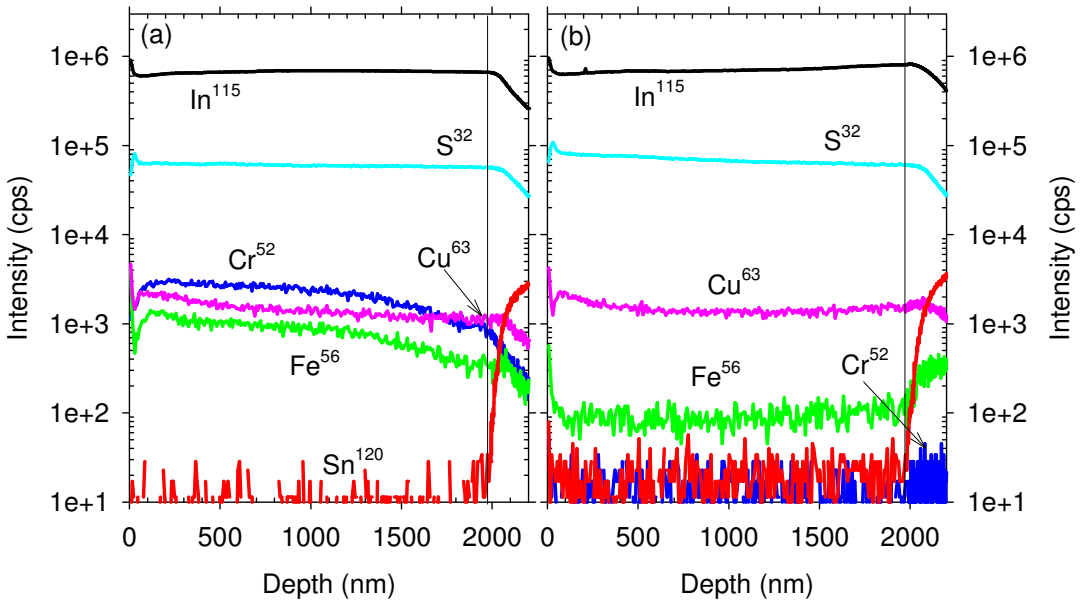

Figure 5-26: Depth profiles of 2 films sprayed using a stainless needle (left hand side) and glass needle (right hand side)

To explain, the acidity of the starting solution results in degradation of the integrity of the internal walls of the steel needle as shown by microscopy images of the cross section of the needle in Figure 5-27. The solution must result in de-passivation of the inside of the stainless steel needle. This could occur when the protective chromium oxide layer has been attacked by the solution, to then give subsurface corrosion.

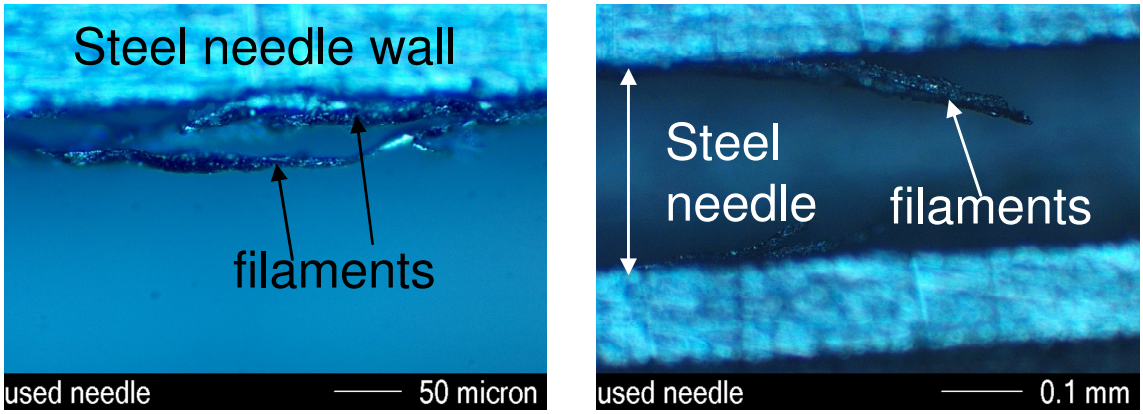

Figure 5-27: Cross section images of the steel needle after 3 h deposition

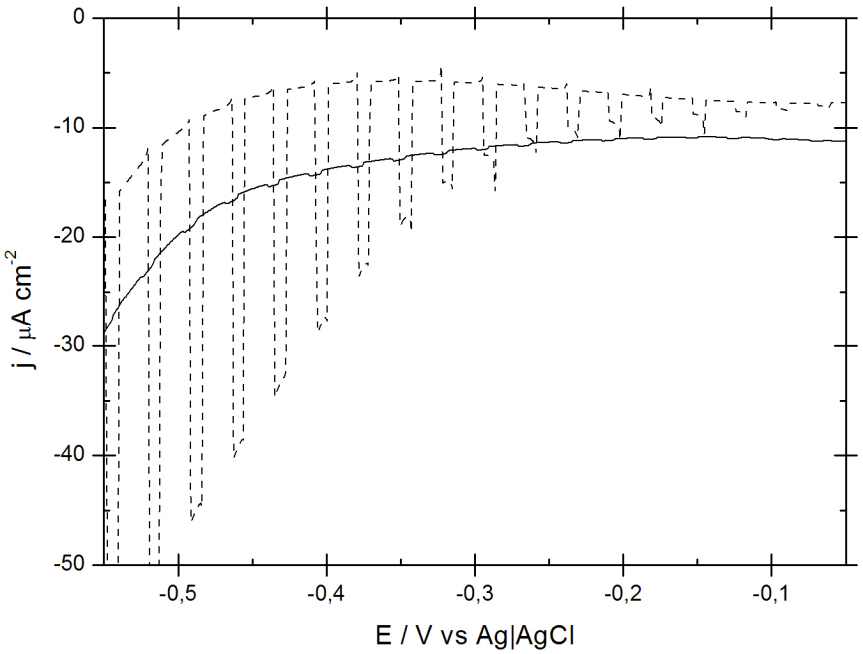

Figure 5-28: photo-voltammograms of CIS deposited by glass needle (----) and steel needle (__)

Figure 5-28 shows two typical photo-voltammogram responses for thin films under pulsed white light illumination where the light is on for a shorter period than it is off. The thin film deposited with the glass needle shows a negative photocurrent increasing with applied negative voltage. At greater negative potentials the Fermi level in the film is higher filling

trap states and increasing the band bending at the film electrolyte interface thus giving an increased photocurrent. Also, the photocurrent rise time is fast, and indicates good quality material. The dark current is small except at negative voltages above -0.5 V where the dark current increases. This is attributed to different causes such as oxidation of the material (example $Cu^{+} \rightarrow Cu^{2+} + 1e^{-}$) which dissolves into the electrolyte, pinholes or cracks going through to the substrate so the redox couple reacts directly with the substrate and finally that the material is highly doped thus the electron can tunnel through the barrier. This list is not exhaustive but gives an overview of the phenomena. The thin film deposited with the steel needle has a larger dark current and has only a small photo-response, indicating that the material is of poor quality.

5.2.2. Uniformity and PIV of glass needle

In order to investigate the differences between samples sprayed with a glass and stainless steel needle, the uniformity and PIV tests were used.

The tests were performed on a limited number of variables since the trends were expected to be the same between the two needles. The variables investigated were deposition temperature, applied voltage and flow rate.

Effect of deposition temperature

The deposition temperature was varied between 380°C and 450°C while the other variables were held constant (as in section 5.1.2).

The change in the aerosol cone structure within the increasing temperature is the same as seen for the stainless steel needle. The cone appears most homogenous at the highest temperature (450°C) (Figure 5-29(A)) but begins to break down as temperature reduces due to a variation in particle size across the cone (Figure 5-29(B,C)). Thus the conclusions drawn for the stainless steel needle are also valid for the glass needle.

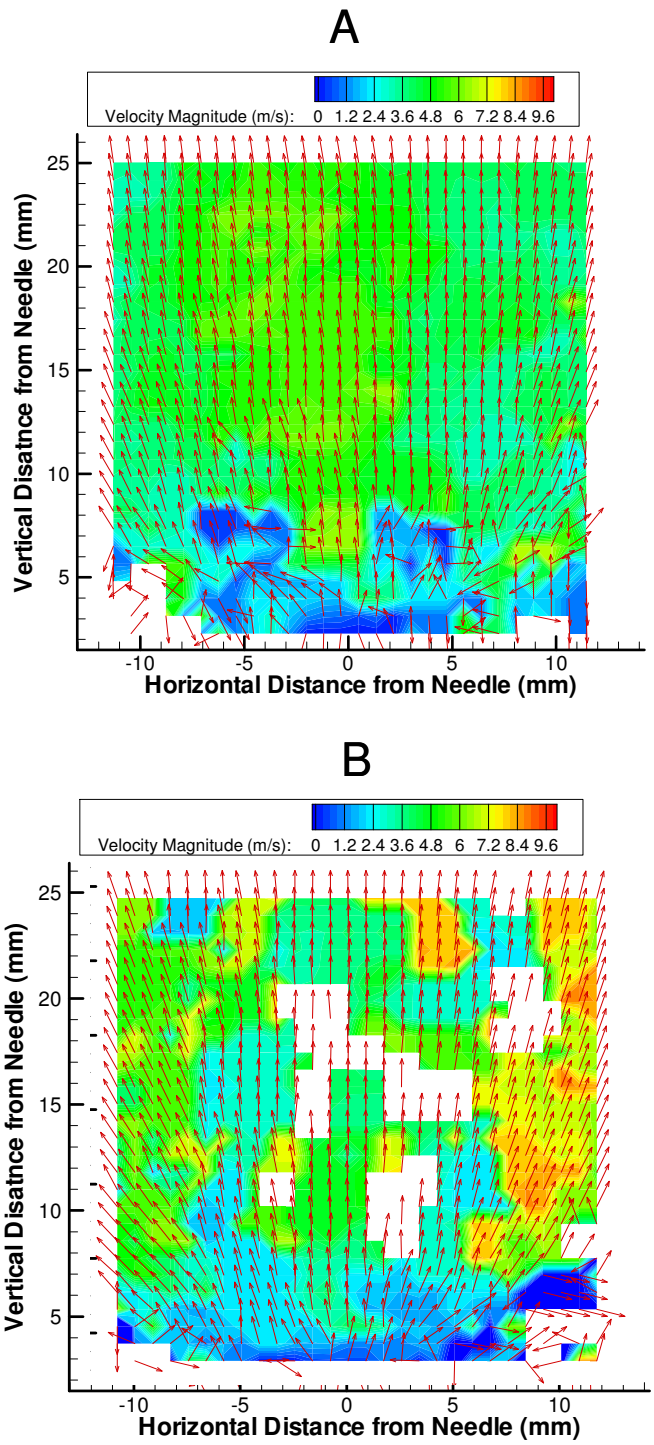

Figure 5-29: continued

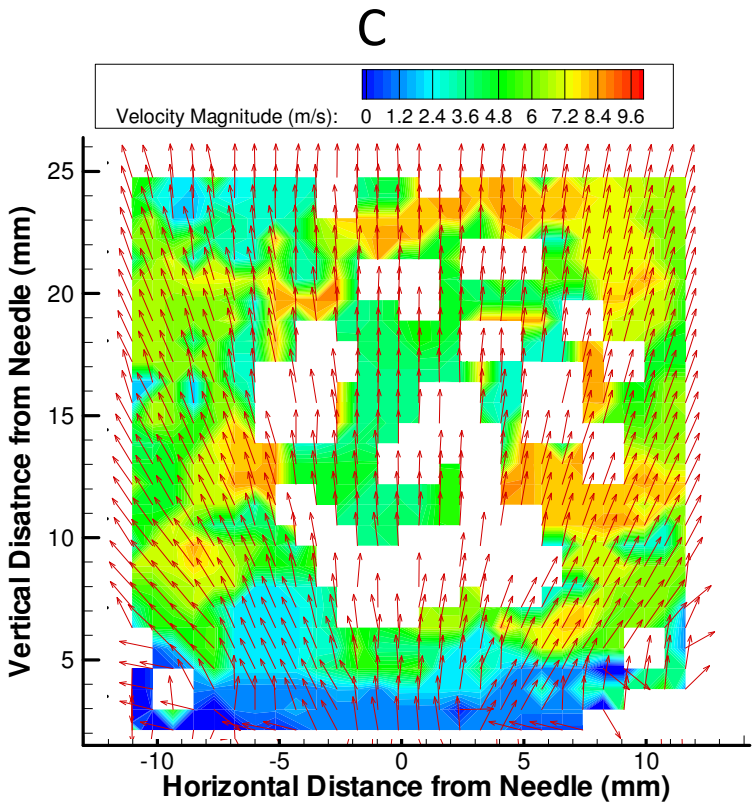

Figure 5-29: velocity vector map coloured by velocity magnitude for deposition temperatures: (a) 450°C, (B) 410°C, (C) 380°C

PIV results are in agreement with the uniformity test results shown in Figure 5-30.

The uniformity test results show the same trend as seen for the stainless steel needle but the magnitude is lower which indicates samples with lower uniformity.

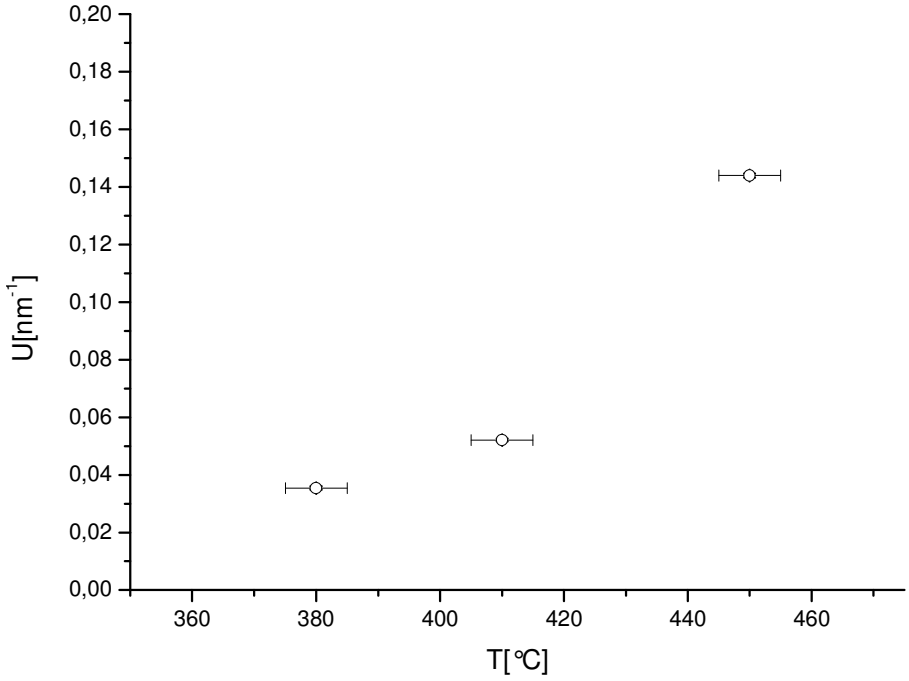

Figure 5-30: Variation in micro-uniformity value with the deposition temperature (glass needle)

Effect of flow rate

Similar to the results of the steel needle at the lowest flow rate the droplets within the aerosol have the highest velocity for the flow rates investigated (Figure 5-31). The combination of high velocity and small droplets size results in the most uniform samples being deposited at the lowest flow rate (Figure 5-32); as was the case for the steel needle.

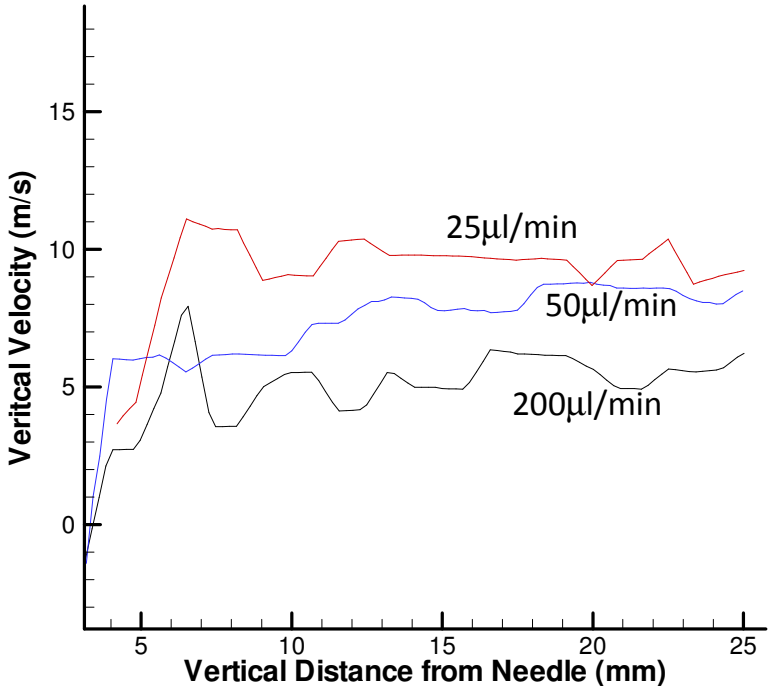

Figure 5-31: vertical velocity profile from the glass needle to the substrate for different flow rates

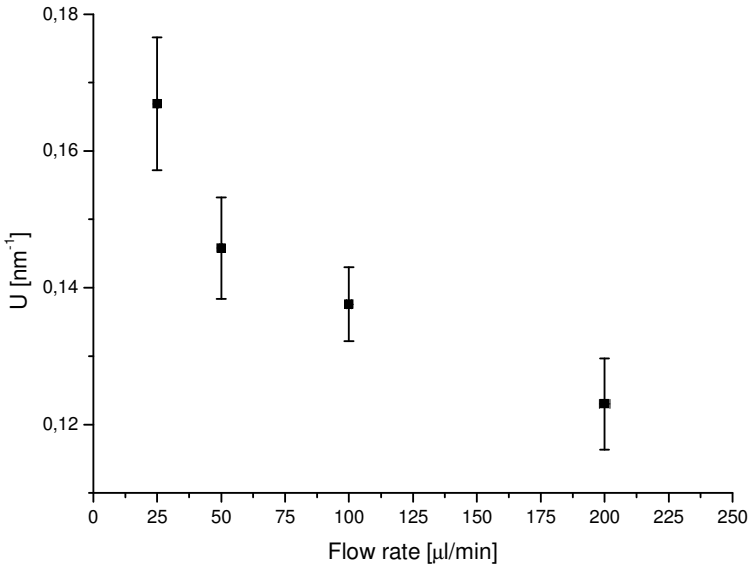

Figure 5-32: variation in uniformity value with flow rate for samples deposited using glass needle.

5.3. Effect of different substrates

The chemicals used to prepare the starting solutions are summarized in the Table 5-7 below. The solution concentration was maintained at 0.21M while the [S]/[Cu] and [Cu]/[In] molar ratios were fixed at 5 and 1 respectively (Roncallo et al. 2007). The solution has a low pH (=2.2) because HCl has to be added to facilitate the dissolution of the three chemicals.

Table 5-7: Chemicals used during this experimental work

Chemical	*Chemical formula*	
Copper chloride	$CuCl_2$	99.99%, Sigma Aldrich
Indium chloride	$InCl_3$	99,99%, Alfa Aesar
Thiourea	$SC(NH_2)_2$	99%, Alfa Aesar
Deionized water	H_2O deionized	18 $M\Omega cm^{-1}$ at 25°C
Ethanol	CH_3CH_2OH	99.99%, Fisher Scientific

During this experiment, the starting solutions were sprayed on two different substrates: aluminium (Al) and SnO_2:F coated glass (FTO) using the in-house glass needle. The substrates had a dimension of 1.8mm x 30mm x 10mm in thickness, length and depth respectively. Deposition temperature and needle-substrate distance were fixed at 450°C and 5cm respectively. The positive voltage applied between the needle and substrate was varied between14kV and 18kV. The starting solutions were sprayed using the same volume. The flow rate was changed between 25µl/min and 100µl/min and the deposition time was set to spray 18ml in total. This resulted in spray times between 3 and 12 hours. The effects of these deposition variables on the properties of the thin films have been examined.

5.3.1. Sample preparation

Aluminium

All the aluminium samples were polished using sandpaper (up to 2500 grit) and a 6 micron diamond suspension reducing to 1 micron for final polishing.

Glass/SnO_2

The glass substrate used for deposition was commercially available Nippon SnO_2:F transparent coated glass (FTO).

The surface roughness of the substrates was measured using the surface profile based on the interferometer technique. The surface roughnesses of the substrates are reported in Table 5-8.

Table 5-8: Summary of the roughness values for the two substrates used during the deposition

Test Point	*FTO [nm]*	*Al [nm]*
1	52.87	313.92
2	85.60	352.43
3	27.48	251.75

The roughness of the substrate can have a direct effect (positive or negative) on the growth of the films because it could interfere which the migration of molecules on the surface during the deposition process or improve the adhesion of the film on the substrate.

5.3.2. Glass substrate

The SnO_2:F transparent coated glass (FTO- Nippon Sheet Glass Co. Ltd)) were subjected to a cleaning process using acetone, Decon90 and deionised water in three consecutive ultrasonic baths.

The FTO substrate was chosen because it is more stable and hence has a higher resistance to oxidation than the ITO (Annica Andersson 1998). The deposition conditions of $CuInS_2$ films on FTO glass are summarized in Table 5-9. The deposition conditions were chosen to deposit films of the same thickness.

Table 5-9: Deposition conditions used to spray CIS on FTO

Sample	*V [kV]*	*F[µl/min]*	*Time [h]*
G1	18	100	3
G2	18	50	6
G3	18	25	12
G4	16	100	3
G5	16	50	6
G6	16	25	12
G7	14	100	3
G8	14	50	6
G9	14	25	12

The X-ray diffraction of the samples deposited on FTO at different voltages and flow rates are typical of CIS without co-deposition of other phases such as Cu_xS or In_xS_y. The diffraction peaks at 27.9°, 32.4°, 46.3°, 55.1°, 57.5°, and 47.6° could be assigned to $CuInS_2$ chalcopyrite (112), (004/020), (024/220), (116/132), (224) and (332/136) planes respectively. The XRD diffractograms of the samples deposited at 18kV and different flow rates are shown in Figure 5-33

The absence of the diffraction peak (103) at $2\theta = 28.99°$ (which is characteristic of chalcopyrite structure), together with the absence of the splitting of (024) and (220) peaks indicate that the structure may be sphalerite. In order to investigate this further, the Crystallographica© software package was used to simulate the XRD results for both

sphalerite and chalcopyrite structures. The chalcopyrite structure were generated using crystal symmetry corresponding to the space group I42m and the lattice parameters equal to a=b=5.52Å and c=11.12Å. The sphalerite was generated using F43m space group and a=b=c= 5.53Å lattice parameters.

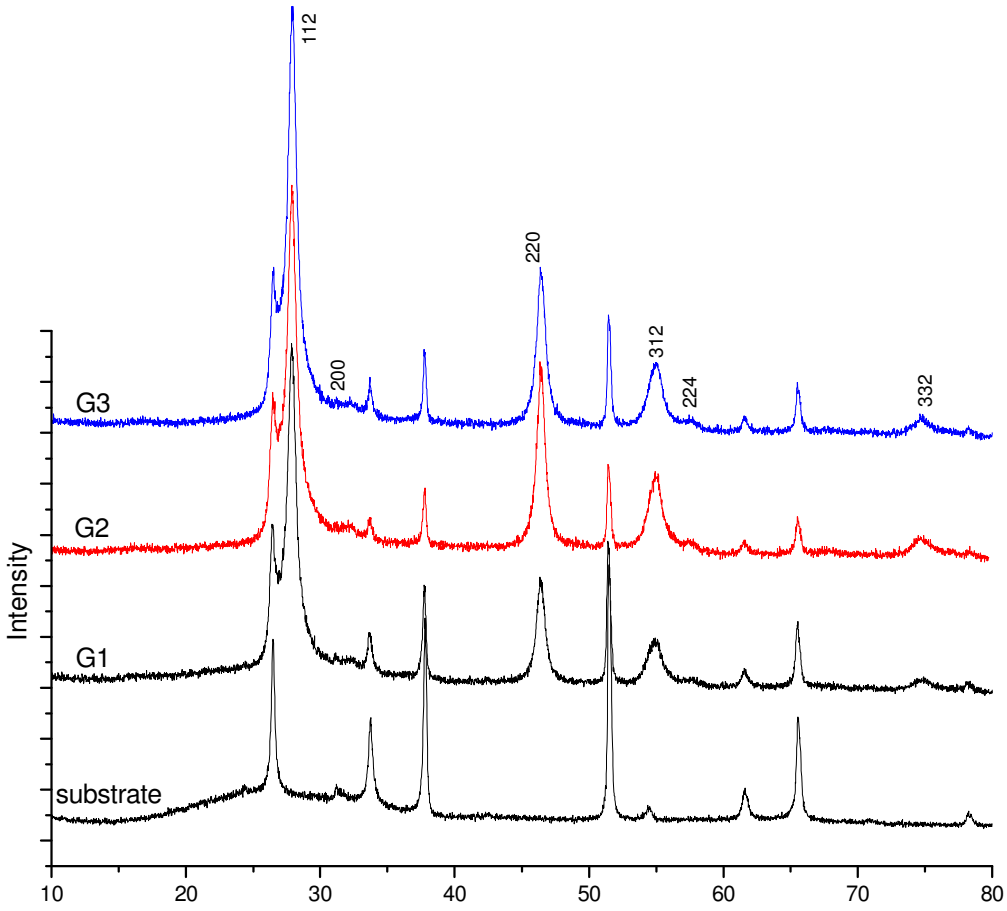

Figure 5-33: XRD samples deposited on glass at 18kV and different flow rates. The planes have been assigned using the sphalerite structure

The sphalerite structure fits better the XRD results as shown in Figure 5-34. Point A in Figure 5-34 shows the theoretical peak for chalcopyrite at 2θ=44.0 which is not seen in the experimental sample (G1). However, a similar intensity peak (point B) in the sphalerite simulation at 2θ=57.6 is seen in the experimental data. As described above, the absence of the splitting peaks is matched more closely with the sphalerite simulation.

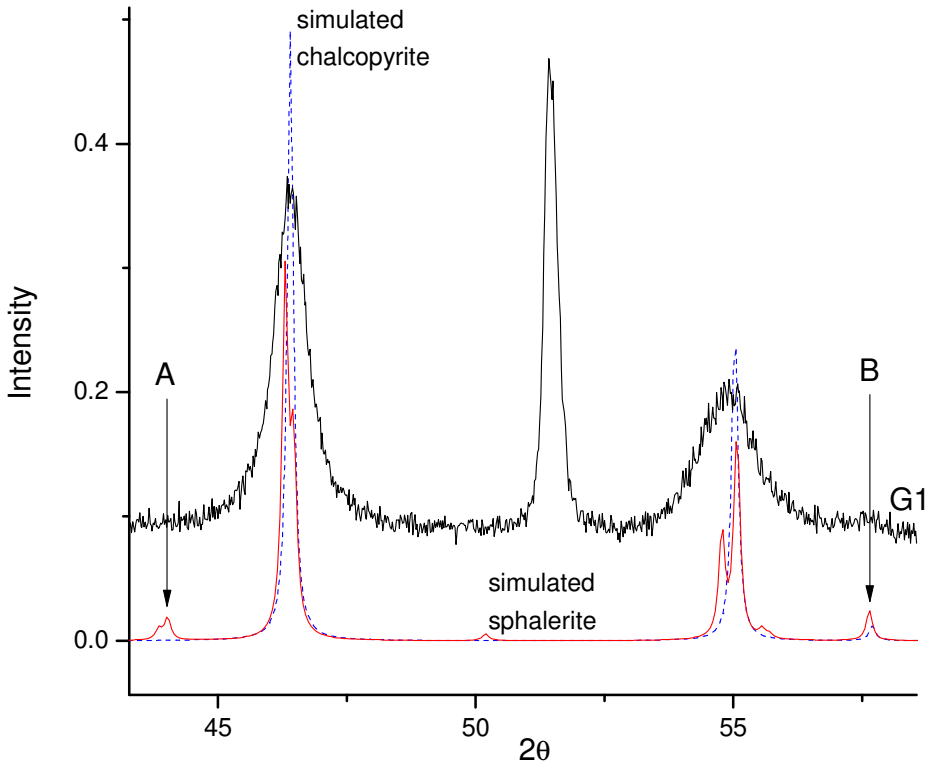

Figure 5-34: Comparison of the experimental XRD (sample G1) with the theoretical sphalerite and chalcopyrite diffractograms

Previous studies (Leicht et al. 1999; Olekseyuk et al. 2000; Hahn et al. 2001) show that the sphalerite is a more common at high temperature growth conditions (above 980°C). The sphalerite XRD peaks are a subset of the chalcopyrite but the structure has a disorder on the cation sublattice. It is thought that a sphalerite structure is obtained due to the fact the deposition method prevents the migration of the atoms and so prevents the films being deposited in the more ordered chalcopyrite structure. This property seems to be intrinsic of the deposition method and independent of the depositions conditions.

The as-deposited films do not show a preferred orientation because the intensity of the peaks match the corresponding theoretical intensity ratios as shown in Table 5-10 where I2/I1 and I3/I1 are the intensity ratios of the peaks 2θ = 46.8° and 2θ = 27.9°, 2θ = 55.1°and 2θ = 27.9° respectively

Table 5-10: The table summarizes the results of the XRD analysis. The intensity ratios of the these peaks are shown in the second and third column while area and FWHM of the first peaks (112) are given in last 4 columns.

	intensity		*112 Area*		*112 FWHM*	
samples	I2/I1	I3/I1	A1	Error A	W1	Error W
G1	0.40	0.20	4736.48	160.65	0.83	0.02
G2	0.55	0.28	5510.34	227.49	0.87	0.03
G3	0.44	0.22	5750.52	209.40	0.82	0.02
G4	0.45	0.23	6645.42	193.75	0.71	0.02
G5	0.53	0.23	5718.77	197.63	0.73	0.02
G6	0.42	0.22	7689.83	383.97	0.95	0.03
G7	0.43	0.24	4256.49	136.98	0.72	0.02
G8	0.35	0.18	5039.65	143.09	0.61	0.02
G9	0.48	0.28	5078.09	187.64	0.83	0.02

Sphalerite	*intensity*	
theoretical	I2/I1	I3/I1
	0.49	0.24

The area and the FWHM of the first CIS peak are summarised in Table 5-10. The two values are similar for all the samples deposited on glass suggesting a independency of grain size from the deposition condition.

Figure 5-35 shows an SEM image of the cross-section of the $CuInS_2$ film on FTO glass (sample G3). The $CuInS_2$ absorber layer in this sample has a thickness of approximately 1.8µm. The picture shows the good adhesion of the film on the substrate and also the good density and columnar shape of the layer.

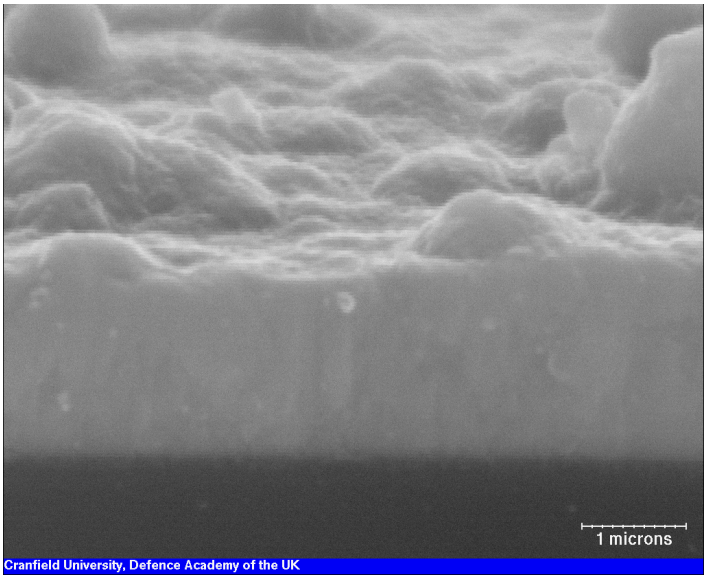

Figure 5-35: Cross section of the sample G3

The SEM pictures of the samples deposited at low voltage show cracks and defects. The sample G7 (14kV) is shown in Figure 5-36 as an example. As seen in section 5.1, the applied voltage and flow rate controls the size of the incoming droplets against the substrate (Choy et al. 1998; Roncallo et al. 2006) . At low voltage and high flow rate, "big droplets" arrive on the hot substrate but the solvent doesn't evaporate immediately, leaving a thin liquid layer on the substrate. This phenomenon produces a mechanical stress on the film when the evaporation process is terminated. This is confirmed by the pictures in Figure 5-36 which show the deterioration of the coating layer during the drying process. When the solvent evaporates, a change in volume is expected. Since the layer is not able to shrink freely due to the adhesion on the substrates, cracks appear on the films. Figure 5-36 (right) shows the details of the cracks in the film and the regions where poor adhesion of the film has resulted in the film breaking away from the layers beneath. Figure 5-36 (left) shows details of the microscopic defects present in the uniform as deposited film. The indented regions on the surface of the film are thought to be caused by large droplets reaching the substrate. The evaporation of the solvent in the droplets leaves the resulting 'pin-holed' film structure.

Figure 5-36: SEM pictures of the sample G9.

The photocurrent conversion efficiency has been measured with the standard photochemical set up discussed in section 3.3.2 using three-electrode configuration with europium nitrate solution (0.2M) saturated in potassium perchlorate. The pH was adjusted to 2 by adding HNO_3.

The maximum EQE values for the samples deposited at different flow rates and applied voltages are summarized in Table 5-11.

At high voltage, the best sample is obtained at 25 µl/min probably because the film growth is slower thereby reducing the number of defects. At lower voltages (16 and 14 kV), the quantum efficiency decreases with the flow rate in spite of the fact the samples deposited at low voltage and high flow rate show a non-uniform covering.

The photocurrent response of the non-uniform samples is a direct result of in-solution method used for the analysis. This technique uses a Eu3+/2+ solution to capture the electrons produced by CIS during the illumination. The use of a solution bath means that no recombination electron-hole can affect the efficiency as the solution can fill the surface defects and the electrolyte can react with the electrons to generate a current response. In a p-n junction, the non-uniformity of the samples would yield an inefficient cell even though the same degree of non-uniformity gives good conversion in solution. An example of an EQE curve is shown in Figure 5-37 (for example G3). The EQE curve drops off rapidly

with increasing the wavelength. This behaviour is thought to be due to the high doping level from Chlorine or small grain size.

Table 5-11: Resume of the EQE values of the samples deposited on FTO

	Maximum photo-current conversion efficiency %		
Voltage [V]	Flow rate 100µl/min	Flow rate 50µl/min	Flow rate 25µl/min
18	28	23	35
16	25	23	18
14	26	23	16

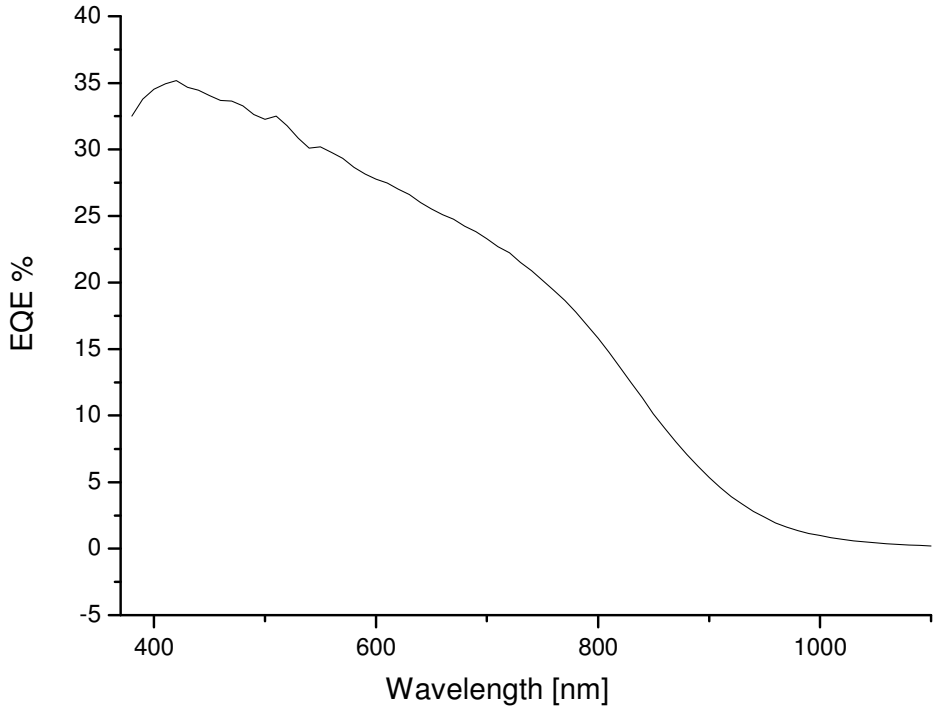

Figure 5-37: EQE curve of the sample G3

The samples were etched in 5wt% KCN. This solution is usually used to remove a Cu_xS segregated phase from the as-deposited films (Camus et al.; Krunks et al. 2005; Wilhelm et al. 2006).

The maximum value of EQE remained unchanged after etching with KCN. This indicates that the samples do not contain an excess of Cu in the form of sulphidic phases on the surface or at the grain boundaries. According to the Gibbs diagram, CuS exists only in the Cu-rich region (Dzionk et al. 1992; Muller et al. 2004). It is well known that an excess of Cu accelerates the growth process of the grains (Krunks et al. 1999). The absence of excess would suggest that grain size remains small and thus results in the trend seen in the EQE curve (Figure 5-37).

5.3.3. Aluminium substrate

The deposition conditions considered for film spraying onto aluminium substrates are summarised in Table 5-12 below.

Table 5-12: Table of the deposition conditions for the samples sprayed on Al substrate

Sample	*V [kV]*	*F[µl/min]*	*Time [h]*
A1	18	100	3
A2	18	50	6
A3	18	25	12
A4	16	100	3
A5	16	50	6
A6	16	25	12
A7	14	100	3
A8	14	50	6
A9	14	25	12

The X-ray diffractions patterns for the 9 samples sprayed onto an aluminium substrate display the three main $CuInS_2$ peaks (2θ=27.9°, 2θ=46.4° and 2θ=55.0°) although the intensity is weak. The small intensity of the peaks doesn't allow the identification of the structure. In this case the chalcopyrite structure has been used.

The preferred orientation can be calculated from the intensity values displayed in Table 5-13. The intensity ratios of the peaks 2θ = 46.8° and 2θ = 27.9° (called I2/I1), 2θ = 55.1°and 2θ = 27.9° (called I3/I1), 2θ = 55.1° and 2θ = 46.8° (called I3/I2) were calculated for the samples and compared with the theoretical values. It is observed that the ratios I2/I1 and I3/I1 have values lower than theory suggests while the ratios I3/I2 are similar for all the samples. The higher intensity of the I1 peaks suggests a preferred orientation along the 112 plane.

Table 5-13: The intensity ratios of the peaks 2θ = 46.8° and 2θ = 27.9° (called I2/I1), 2θ = 55.1°and 2θ = 27.9° (called I3/I1), 2θ = 55.1° and 2θ = 46.8° (called I3/I2) calculated for the samples and for the theoretical value

		Intensity	
Sample	*I2/I1*	*I3/I1*	*I3/I2*
A1	0.26	0.14	0.54
A2	0.36	0.19	0.53
A3	0.24	0.13	0.54
A4	0.25	0.14	0.56
A5	0.11	0.06	0.55
A6	0.27	0.15	0.55
A7	0.14	0.08	0.57
A8	0.17	0.10	0.58
A9	0.26	0.14	0.52
Theoretical		*Intensity*	
	I2/I1	I3/I1	I3/I2
	0.40	0.21	0.53

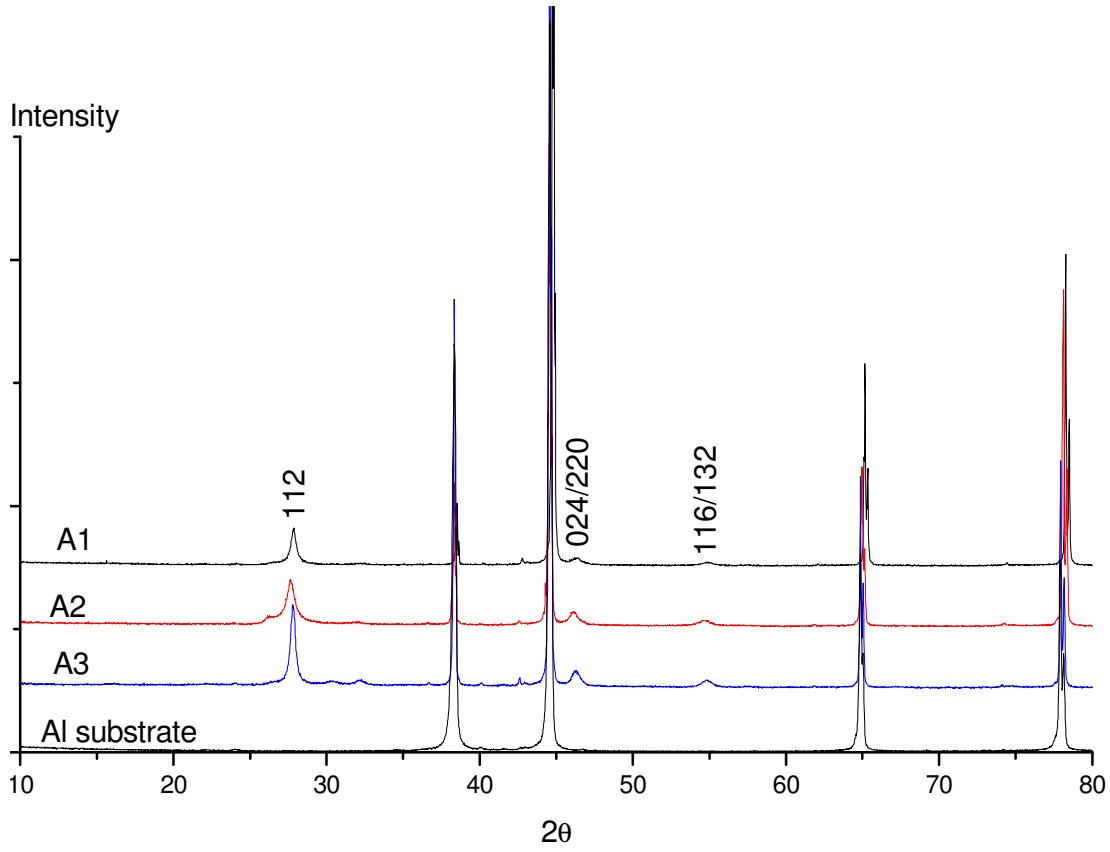

Figure 5-38: Diffractogram of the CuInS2 deposited at18kV on aluminium

The thickness of the samples has been determined by RBS analysis. The RBS measurements have been performed using a 2.2MeV helium-3 (3He) beam with a detector solid angle of 5msr and 170° back scattering angle. RBS spectra of the sample Al3 and a theoretical CIS layer grown on aluminium are shown in Figure 5-38 and Figure 5-39. The theoretical curve shows the three peaks of the CIS layer (Cu, In and S) and one peak from the aluminium. The contribution of the four peaks is calculated by the SIMRA software to generate the simulated curve. The difference between this spectrum and the experimental spectra is due to the large roughness of the CIS layer which is characteristic of the deposition method

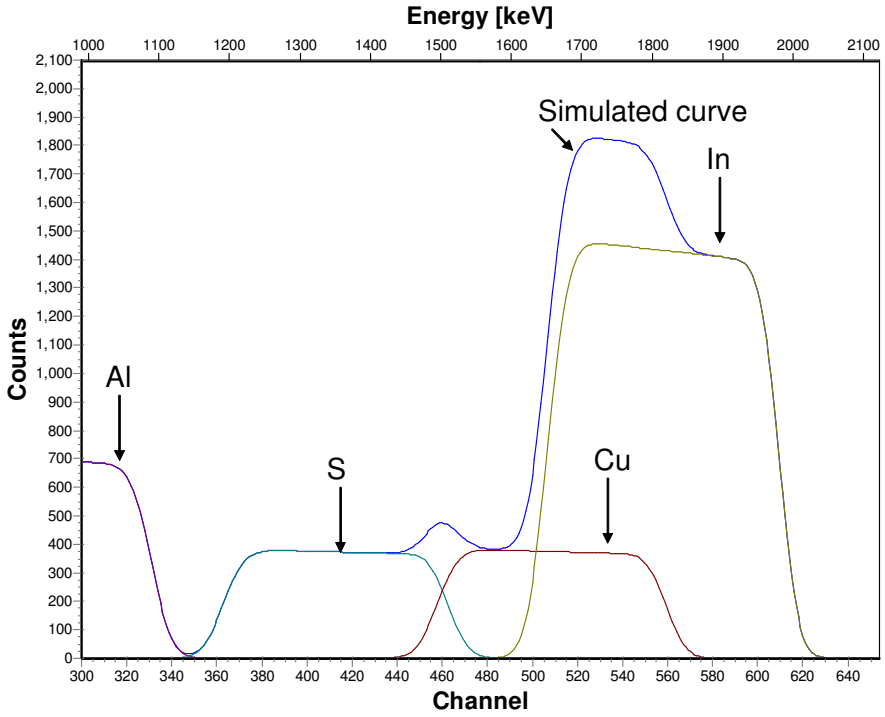

Figure 5-39: Theoretical RBS spectra of CIS layer growth on Al substrate

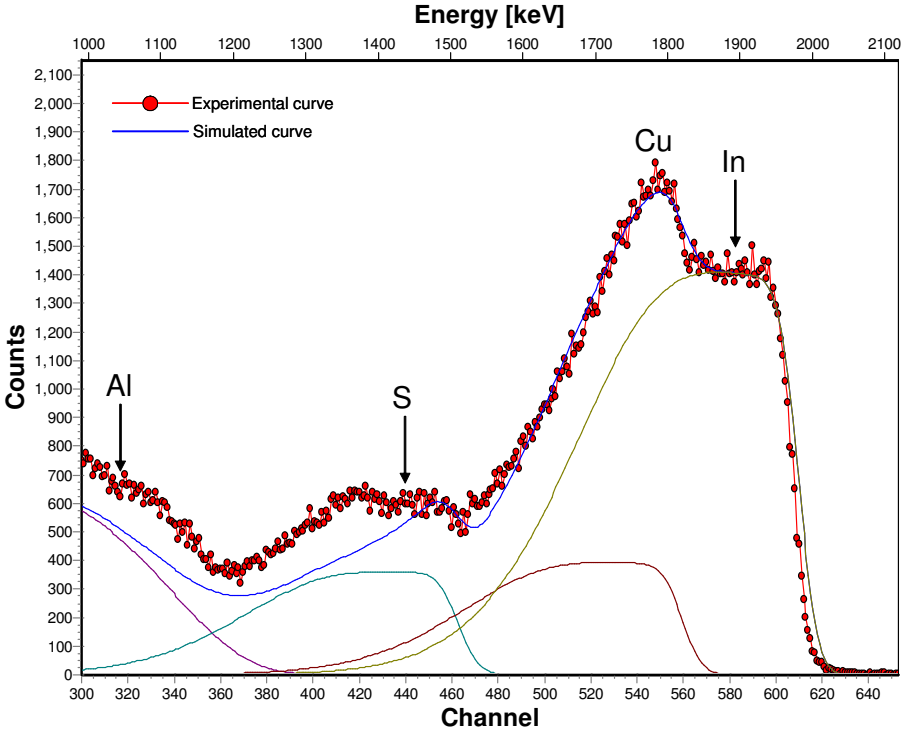

Figure 5-40: RBS spectra of the sample Al3

The RBS spectra have been fitted assuming the presence of a single homogeneous layer of CIS on the aluminium substrate. The stoichiometry of the samples deposited on aluminium appears to be constant for all the as-deposited films (Table 5-14) suggesting that the voltage and flow rate don't effect the composition of the sprayed layer.

The thickness of the as-deposited films has a similar value for the all the deposition conditions considered and is 500nm (based on the density of $CuInS_2$ = 4,748 /cm^3). A maximum value (around 890nm) is reached for the samples deposited at low voltage (sample Al7 and Al8). This could be due to a reduction of the diameter of the spray cone resulting in a higher solution volume per unit area incident on the substrate.

Table 5-14: Resume table of the composition analysis of the samples sprayed on Al (from RBS)

	Cu%	*error*	*In%*	*error*	*S%*	*error*	*Thickness [µm]*	*Error [µm]*
Al1	0.24	0.01	0.16	0.01	0.60	0.03	0.48	0.02
Al2	0.22	0.01	0.25	0.01	0.49	0.02	0.53	0.02
Al3	0.19	0.01	0.23	0.01	0.58	0.03	0.50	0.02
Al4	0.26	0.01	0.25	0.01	0.49	0.02	0.53	0.02
Al5	0.24	0.01	0.16	0.01	0.60	0.03	0.41	0.02
Al6	0.28	0.01	0.22	0.01	0.50	0.03	0.62	0.03
Al7	0.28	0.01	0.22	0.01	0.50	0.03	0.89	0.04
Al8	0.22	0.01	0.25	0.01	0.53	0.03	0.89	0.04
Al9	0.28	0.01	0.22	0.01	0.50	0.03	0.57	0.03

Some additional peaks also begin to appear in the diffractograms of the samples sprayed using different voltages for all the aluminium substrate samples. The number of these peaks is inversely proportional to the applied voltage but appears to be independent of solution flow rate as shown in Figure 5-41. The intensity of the peaks is small and thus they are difficult to positively identify. They could be due to an aluminium oxide layer formed during the deposition process. The HCl acid present in the starting solution couldn't evaporate completely before arriving on the substrate when a low voltage is applied. The HCl can corrode the substrate and produce an aluminium oxide layer between the substrate and CIS film. The high deposition temperature may facilitate this process. This explains the presence of the extra phases visible in the X-ray diffractograms

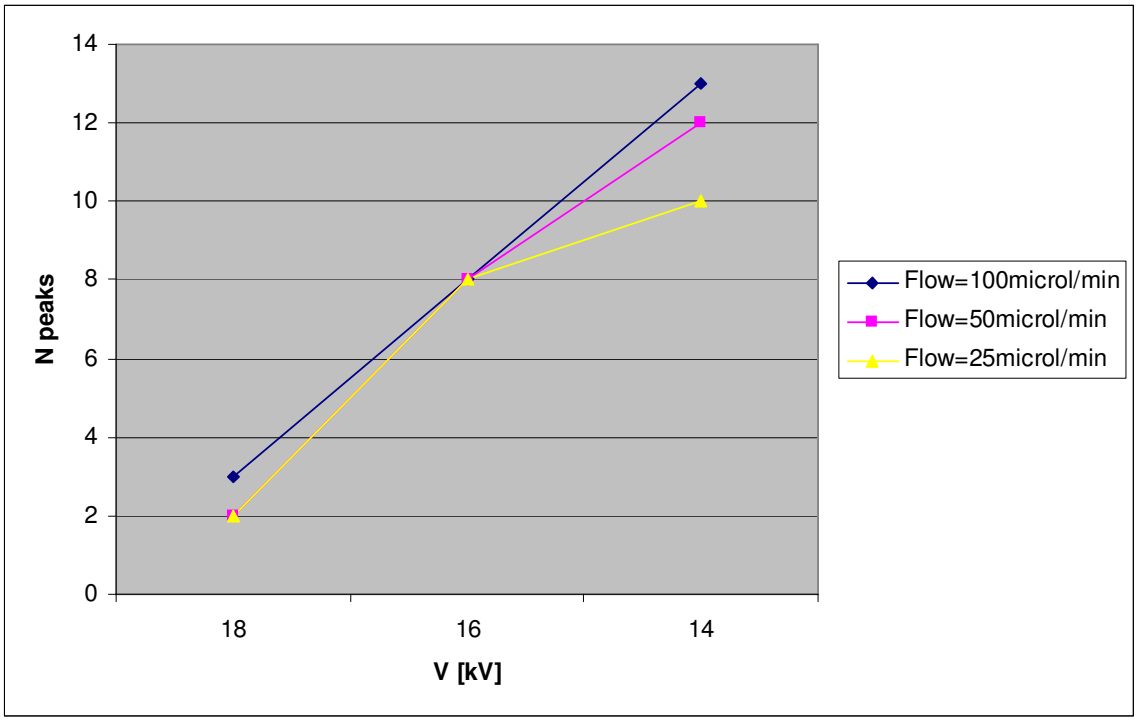

Figure 5-41: Increasing of the external peak number with the applied voltage and flow rate

To try to demonstrate the previous hypothesis, an aluminium substrate was subjected to a heat treatment at 450°C for 30 min and an XRD analysis was performed on it. The analysis (Figure 5-42) shows the presence of external peaks which correspond to different Al_2O_3 polymorph forms. Aluminium oxide is an excellent thermal and electrical insulator. Metallic aluminium is very reactive with atmospheric oxygen and a thin passivation layer of alumina quickly forms on any exposed surface. This layer protects the metal from further oxidation.

The issue of aluminium oxide being formed when the Al substrate is heated to 450°C is compounded by corrosion of the substrate due to the high acidity of the sprayed solution.

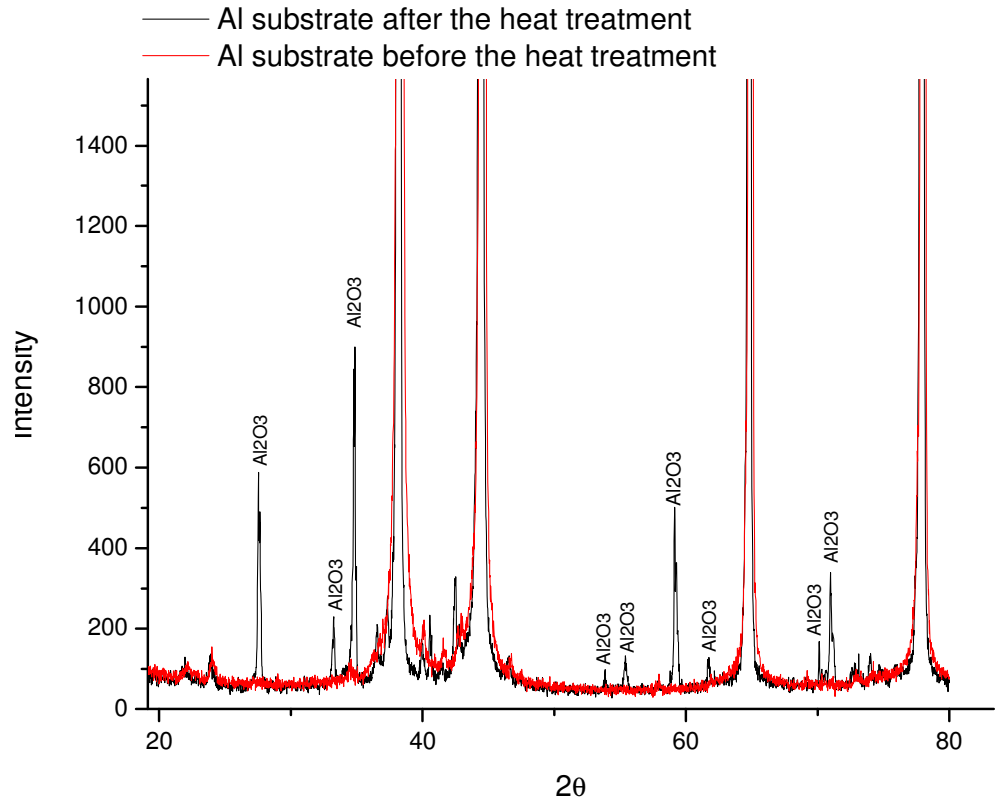

Figure 5-42: XRD of the aluminium substrate before and after the heat treatment

The photo-response of the samples have been studied using three probe configuration photo-voltammetry (as described in section 3.3.2.), europium nitrate solution and a white

LED as the light source . None of these samples deposited on aluminium showed any photocurrent response, probably because the thin aluminium oxide layer is formed between the substrate and CIS and acts as an insulator layer.

5.3.4. Discussion of the differences between films deposited on aluminium and glass substrates

The difference in thickness of the films deposited on the aluminium and FTO substrates can be explained by the difference in conductivity of the two materials. The Al has higher conductivity than the FTO which could result in different electrostatic fields. This in turn could affect the spray cone. The Al could have a larger cone angle as the columbic repulsion between the droplets is stronger and results in a longer cascade of particle splitting than seen in the lower intensity TCO case where the final particle size is larger.
This has been confirmed by analysis of the images seen in Figure 5-43 which are from the laser particle visualisation study.

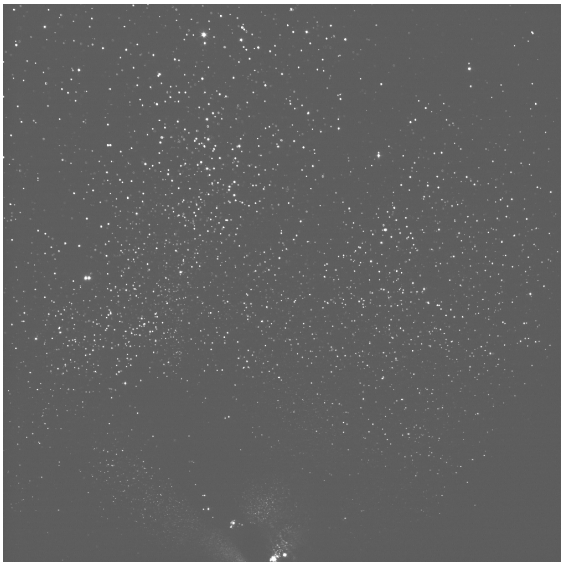

A

B

Figure 5-43: PIV images of the aerosol cone generate by the FTO (A) and aluminium (B) substrates

The pictures show the difference in cone shape between the two substrates. Figure 5-43A shows a larger cone area while the Figure 5-43B shows a more compact aerosol cone. This is consistent with the film thickness results obtained using XRD, SEM and RBS which

show the aluminium substrate to have a thinner CIS layer than that seen on the FTO substrate. The more dispersed cone area results in the solution being deposited over a larger area but with lower thickness than the more compact cone which concentrates the deposition in a smaller area but with a greater thickness.

5.3.5. Summary

Based on the results from the study performed during the assessment of the ESD technique as a candidate for use in PV applications, the following statements can be made.

The in-house developed uniformity test is a powerful and simple method for the assessment of as-deposited film uniformity. The test allows the effects of a number of different deposition variables to be assessed and a set of recommendations to be made as to the best combination of conditions whilst striving towards optimum uniformity. The technique is designed for use on semi-transparent films and as such cannot be extended to thick films. Should a thin film show good uniformity for a given condition, this is no guarantee that a thick film sprayed under the same conditions will result in good uniformity. However, it can be said that a non-uniform thin film will result in a non-uniform thick film under the same conditions.

For compositionally uniform films the results achieved show that the uniformity test enables the determination of the thickness uniformity through the variation of the brightness of the images of the sample. Alternatively, the test could be applied to monitor variations in film composition which produce localised optical density differences and hence affect the brightness of the sample image. Although this method was used on electrostatic spray deposited films, it is equally applicable to any semi-transparent film prepared by other deposition techniques.

The uniformity test results allow samples deposited at high starting solution concentrations and low deposition temperatures to be discarded from further analysis. The most suitable distance to spray a uniform film has been found to be 5cm.

The effect of flow rate and applied voltage is inconclusive and would need to be carried out on thick film samples in order to give a definitive answer on the best conditions.

Variation of the applied voltage causes changes in droplet dimensions but does not produce inhomogeneity inside the cone which was observed at low temperatures during the temperature variation tests. The uniformity test provides evidence that more uniform samples are deposited at low voltage but further studies on thick films are necessary.

The results of the study on the needle and substrate material are definitive. All the samples deposited with a steel needle show no photoactivity as do the samples sprayed on metal substrates. This behavior is attributed to two different causes: the steel needle contaminating the solution and thus the as-deposited films; the metal substrate is corroded by the acid solution resulting in impurity phases in the film.

Chapter 6:

$CuInS_2$ - Absorber Layer

In the previous chapter, the feasibility of ESD deposition as a method to grow $CuInS_2$ films was proven. In this chapter the properties of $CuInS_2$ spray solution and as-deposited films are further investigated. The solutions were prepared using either chloride or nitrate salts. These salts were selected because previous spray pyrolysis and electrostatic assisted vapour deposition (ESAVD) studies have shown good results (Bouzouita et al. 1999; Krunks et al. 2002; Hou et al. 2005; Oja et al. 2005; Krunks et al. 2006). Precursor solution parameters were also expected to have a strong impact on the property of the as-deposited films. One of the most important parameters in $CuInS_2$ thin films is the stoichiometric ratio of Cu/In (Tembhurkar et al. 1992; Ortega-Lopez et al. 1996; Ortega-Lopez et al. 1998; Bihri et al. 1999; Bouzouita et al. 1999; Krunks et al. 1999; Krunks et al. 2006). Close control of the ratio of the two elements allows n-type or p-type $CuInS_2$ films to be deposited (Tiwari et al.

1985). Indium-rich precursor solutions result in the formation of n-type films, while copper-rich solutions result in p-type films. The close control of the stoichiometric ratio between copper and indium should be achievable using the ESD technique due to the fact that it is possible to create a precursor solution in the desired ratios prior to film deposition.

The main purpose of this work is to show how different salts used to prepare starting solutions (chloride and nitrate) can affect the properties of as-deposited films prepared by electrostatic spray deposition (ESD). Further to this, an analysis of the precipitates (which were obtained during the preparation of chloride starting solution when the [S]/[Cu],5) through which were formed was conducted to better understand the formation mechanism of CIS. Krunks et al (Krunks et al. 1997), showed that the CIS formation reaction involves the formation of an Cu-thiourea intermediate complex in the starting solution which decomposes at high temperature.

6.1. Precipitate

When $CuCl_2$ and thiourea solutions are combined ([S]/[Cu]<5), a precipitate is formed which settles to the bottom of the volumetric flask. However, there is no evidence of a precipitate when $Cu(NO_3)_2$ and thiourea solutions are combined in the same ratios.

To investigate the precipitate reaction and explain the difference between the nitrate and chloride solutions ($CuCl_2$ and $Cu(NO_3)_2$) in combination with thiourea, solutions were prepared and mixed in different proportions.

$CuCl_2$ (1M) and thiourea (0.5M) solutions were separately heated to 70ºC in the water bath. 3 ml of $CuCl_2$ solution were transferred to a flask and different amounts of thiourea were added in the molar ratios shown in Table 6-1. The blue colour of the $CuCl_2$ solution disappeared (it becomes transparent) and a precipitate formed when [S]/[Cu]≤5. The precipitates and/or solutions were allowed to cool naturally to room temperature and the precipitates filtered using a paper filter then rinsed with deionised water and dried in an oven at 80°C for four hours. Depending on the [S]/[Cu] molar ratio value of the starting solution, a white or a yellow precipitate was obtained. The colour of the precipitate as a function of molar ratio can be seen in Table 6-1.

Table 6-1: Type of precipitate obtained using different S/Cu molar ratios

Sample	*[S]/[Cu]*	*Result*
S1	1	White precipitate
S2	2	White precipitate
S3	3	White precipitate
S4	4	Yellow precipitate
S5	5	Solution

As described above, copper chloride and thiourea were blended in different proportions. When [S]/[Cu] was less than 3, an instantaneous reaction took place and a white precipitate was obtained. When the molar ratio was between 3 and 4, a small amount of yellow precipitate (S4) was the result of a slow reaction. When [S]/[Cu]≥5 a clear solution (S5) was obtained. The solution was stable for approximately twenty four hours after then a yellow precipitate is formed.

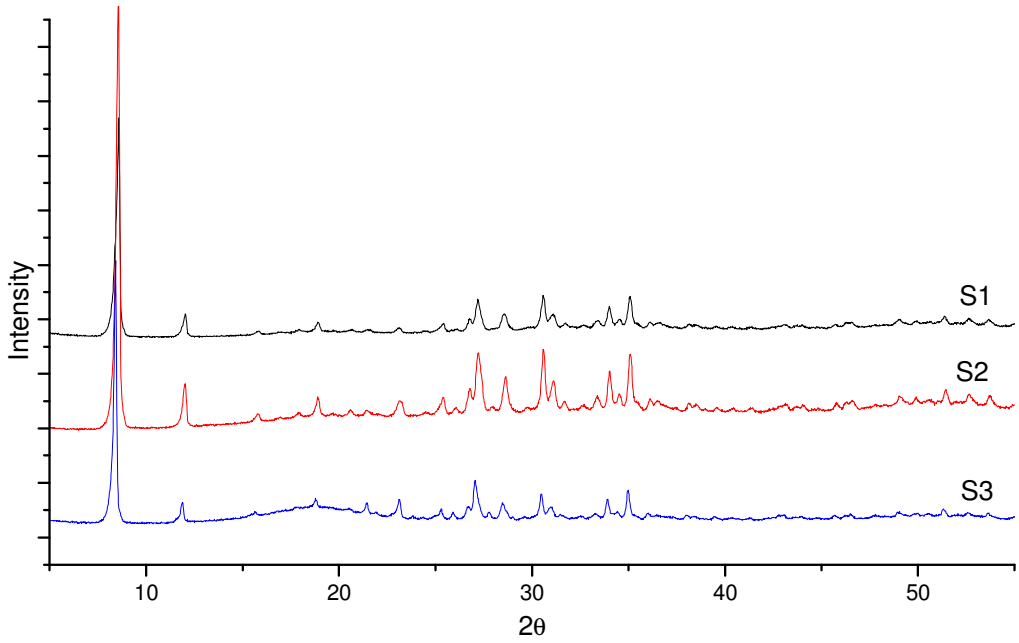

Figure 6-1: XRD Spectrum of "S/Cu≤3" Precipitate

The X-ray diffraction of the samples S1, S2 and S3 are shown in Figure 6-1 and Figure 6-2. The samples have very similar spectra suggesting they have the same structure. The sample S3 shows a small and wide peak around 2θ values between 15° and 25° due to the petroleum jelly (as confirmed by a blank).

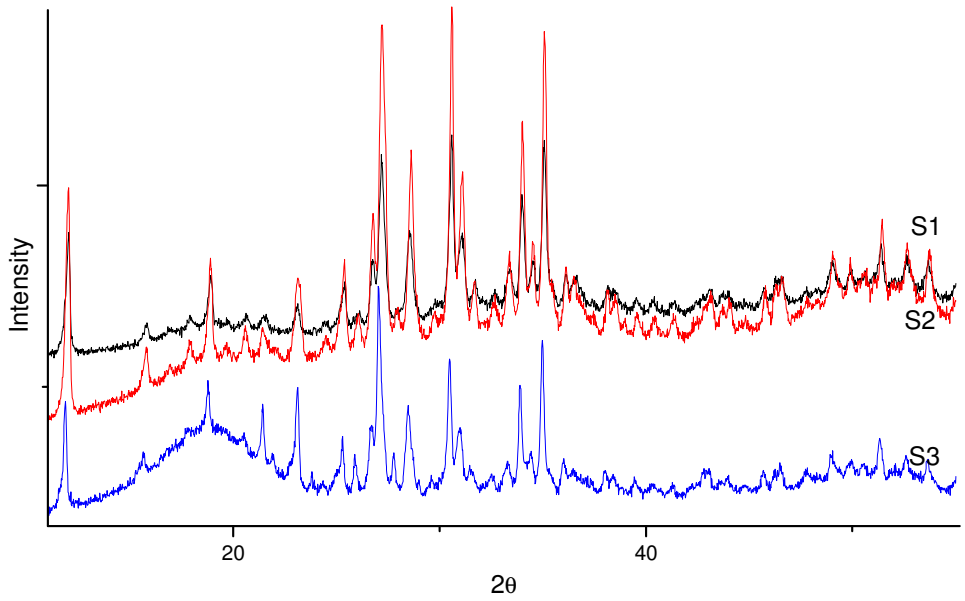

Figure 6-2: Detailed view of the Figure 6-1

The X-ray diffractions seen in Figure 6-1 show no match with any of the diffractograms in the JCPDS database. There is, however, agreement with the results published by Krunks et al (Krunks et al. 1997). The compound is thought to be mono-(thiourea)-copper(I)-chloridihydrate ($Cu(SCN_2H_4)Cl{\cdot}2H_2O$) (a complex formed by thiourea and the copper) because of the similarity between the X-Ray results obtained during this study and Krunks' data.

The X-ray diffraction results for sample S4 (Figure 6-3) is a match for the diffractogram of sulphur (S_8).

This white precipitate can be redissolved by agitation and addition of thiourea. A final yellow residue (S_8) is obtained. Figure 6-4 shows the XRD spectra for samples S1, S2 and S3 after the addition of thiourea. Each of the spectra can be attributed to sulphur.

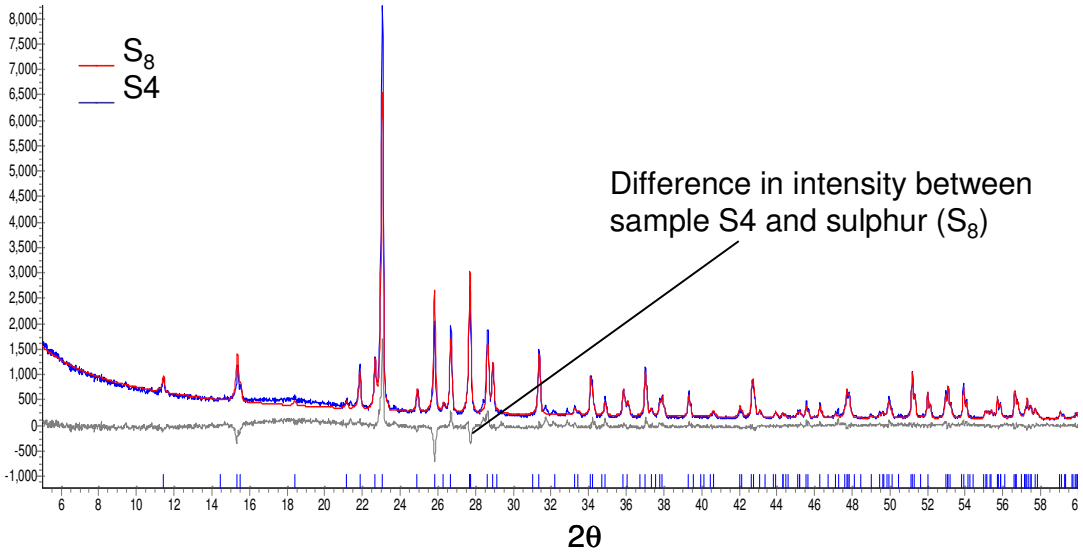

Figure 6-3: XRD Spectra of S4 sample and Sulphur (S8)

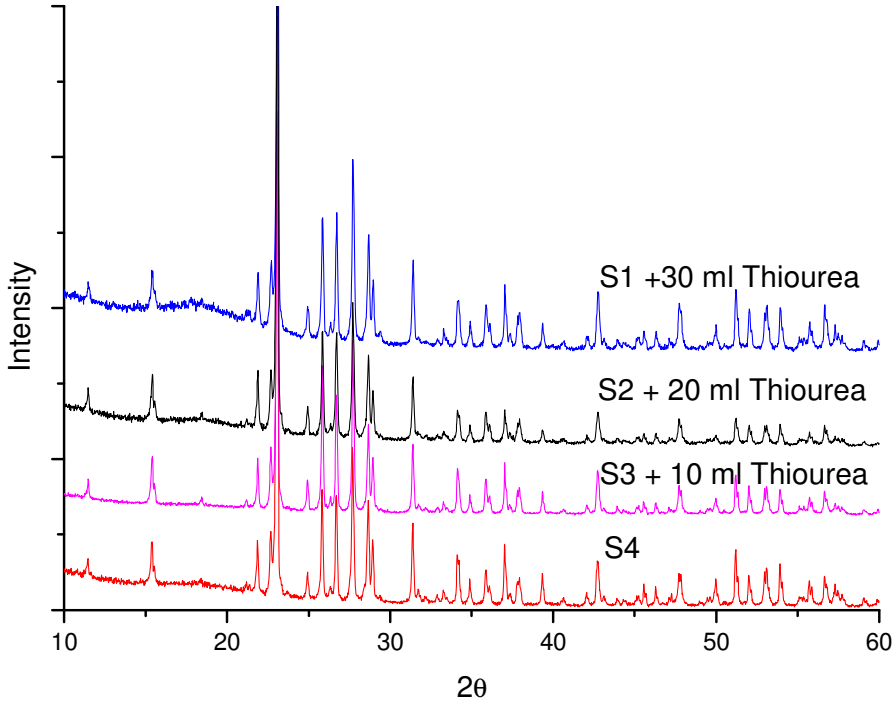

Figure 6-4: Results of adding thiourea to samples S1, S2 and S3

It is thought that when the amount of the thiourea is 3 or 4 times more than copper concentration, the weak C-S bond (C-S bond = 228.0kJ/mole) is loosened and the S-S bond (S-S bond = 266.9kJ/mole) starts to form until S_8 precipitates.

The possible reaction involves a redox stage in which the copper is reduced and thiourea is oxidised to formamidine disulphide (Szymaszek et al. 1977)

$$2Cu^{2+} + 2(NH_2)_2CS \leftrightarrows 2Cu^{+} + (NH_2)_2(NH)_2C_2S_2 + 2H^{+}$$

The formamidine can accept a proton (and remains in solution) while Cu^{+} can react with thiourea in solution and form the complex.

The reduction of Cu is confirmed by the change in the colour of the solution when thiourea is added (Ugai et al. 1981). A validation of this hypothesis could be obtained by studying the different magnetic behaviour of the copper in the two oxidation states. Compounds with no unpaired electrons are diamagnetic whilst compounds with unpaired electrons are paramagnetic. The Gouy method has been used to establish the difference between $CuCl_2$ (paramagnetic) and the precipitate (a complex of Cu^{+} and so diamagnetic). In the Gouy method the magnetic moment of the substance can be measured as an apparent change in weight due to the application of an external magnetic field. This phenomenon is caused by an inducted magnetic moment in the sample. A diamagnetic substance would show an increase in the recorded weight (because its magnetic moment is perpendicular to the magnetic field and thus is repulsed from the magnetic source) while a paramagnetic compound would show a decrease in the recorded weight (because its magnetic moment is orientated in parallel to the magnetic field and thus is attracted to the magnetic source). The picture of the experimental set up is shown in Figure 6-5. The powder was contained in a long glass cylinder which is supported on a digital balance. The top of the glass tube (which contains the sample) resides in a uniform magnetic field. The magnetic response was established by measurement of the overall force which was displayed by the balance. The magnetic flux was measured and calibrated using a Gauss meter.

The $CuCl_2$ produced a variation in weight as shown in as shown in Table 6-2 confirming the paramagnetic properties of the salt. On the contrary, the S3 precipitate did not produce any variation when the current was increased from 0A to 1A. When the current passed 1A, the magnetic field caused interference with the balance preventing further measurements from being taken.

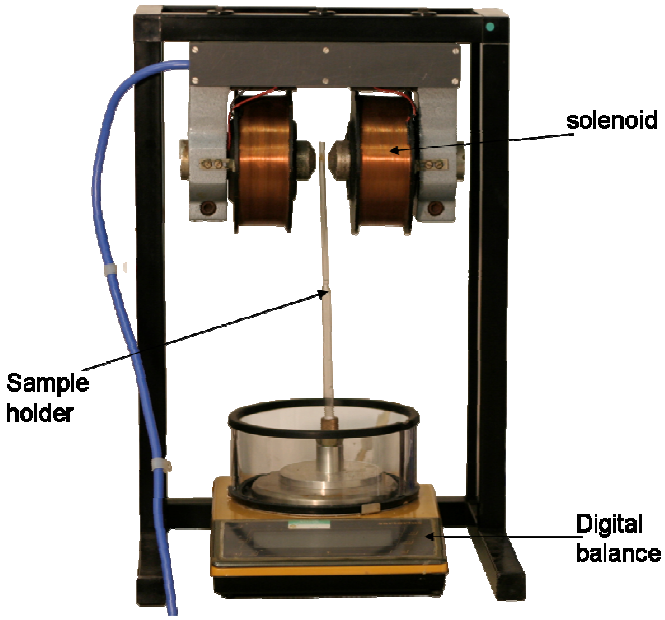

Figure 6-5: The Gouy method set up

Table 6-2: Variation of $CuCl_2$ weight with the magnetic field. In the first column is shown the current value while in second column the corresponding magnetic value is displayed. The last column shows the variation in weight of $CuCl_2$

I [A]	*B [T]*	*Variation of $CuCl_2$ weight [g]*
0	0.027	0
0.108	0.104	0
0.205	0.182	0
0.305	0.269	0
0.405	0.343	0
0.503	0.417	+0.002
0.601	0.489	+0.005
0.700	0.558	+0.009
0.801	0.621	+0.015
0.901	0.676	+0.018
1.001	0.719	+0.022

Another attempt to prove the variation of the oxidation number of the metal in the complex was done using the Oxford Maglab2000 instrument.

The following graphs (Figure 6-6) show magnetisation measurements on the two samples as a function of time at room temperature with an AC magnetic field strength of 1.6kA/m and a frequency of 883HZ

The precipitate shows a very low magnetization signal (between $-2*10^{-6}$ e $2*10^{-6}$ emu/g or between $-2*10^{-4}$ e $2*10^{-4}$ A/m). This means that the compound could be weakly diamagnetic.

$CuCl_2$ tested at the same field and the same frequency gives a signal 20-50 times higher than the precipitate. This shows that the salt is paramagnetic.

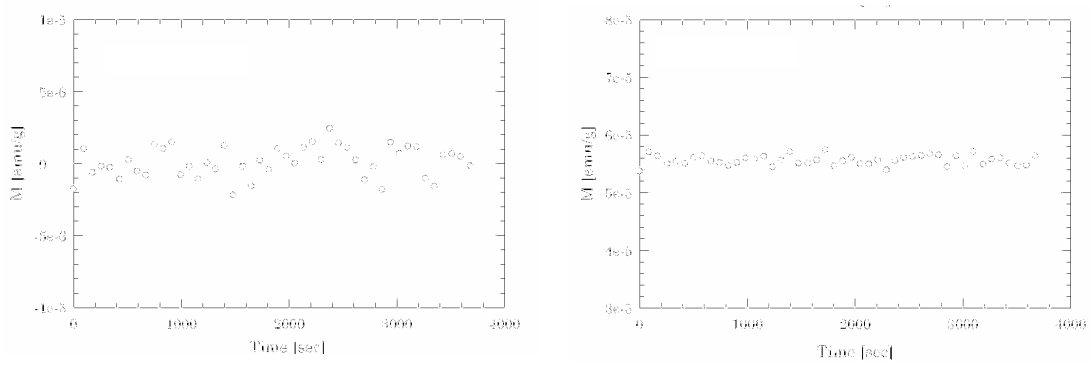

Figure 6-6: magnetization of the precipitate (left) and $CuCl_2$ (right)

6.1.1. Precipitate composition

The EDX results of the S3 precipitate (Figure 6-7B) confirms the presence of Cu, S, Cl and the SEM picture of the precipitate (Figure 6-7A) shows the needle shape structure in which the complex precipitates.

The precipitates were characterized using different techniques (such as ion chromatography, atomic absorption spectroscopy, elemental analysis, etc) to confirm the chemical formula of the precipitate. The precipitates (S1, S2 and S3) were prepared for the elemental analysis, atomic absorption spectroscopy and chromatography by dissolving them in hot HNO_3 (approx 70°C). Due to the oxidising nature of the acid, the precipitate was dissolved and the copper was oxidised to Cu^{2+} and the sulphur to SO_4^{2-} while the Cl^- ion was brought into solution.

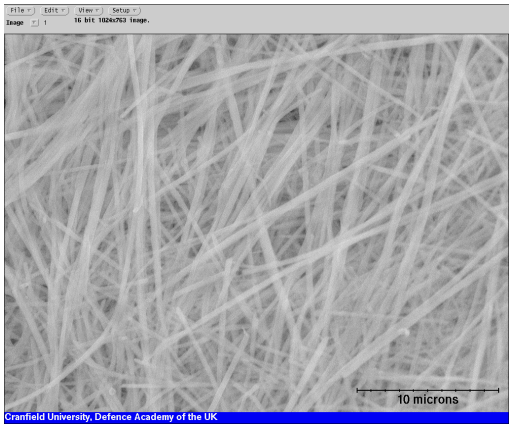

A

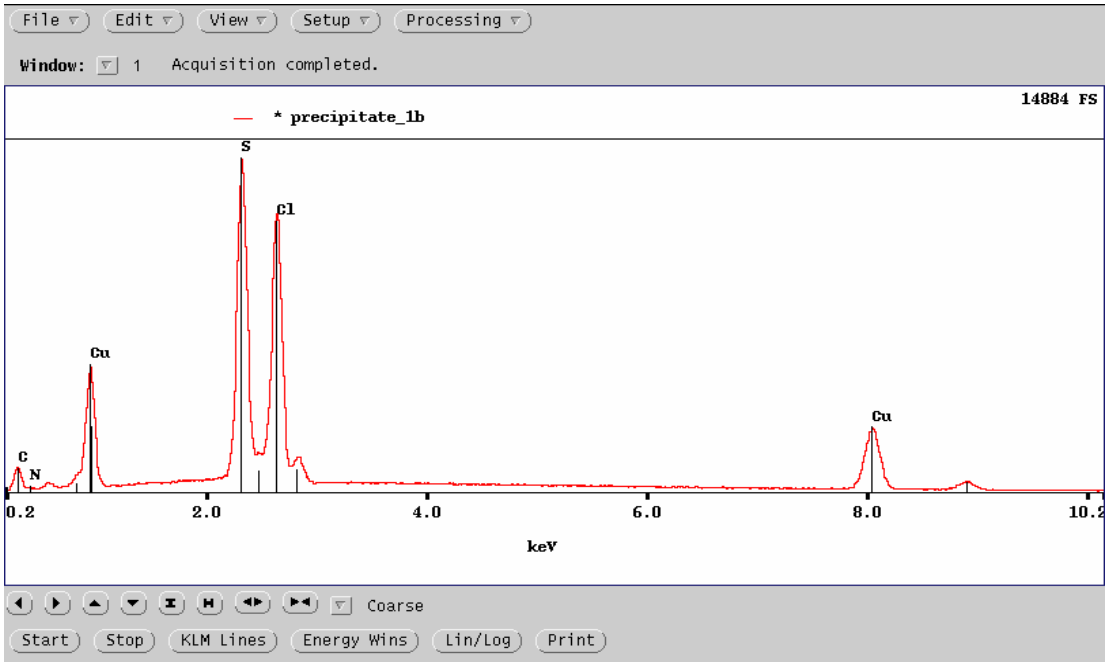

B

Figure 6-7: SEM (A) and EDX (B) pictures of the precipitate (sample S3)

Atomic absorption spectroscopy (AAS)

The AAS analysis was performed with a Varian – SpectrAA-10 Plus instrument.

Small amounts of samples S1, S2, S3 (0.256g±0.001) were dissolved by gently warming with diluted HNO_3 (1:2) until all the precipitates were dissolved. Deionised water was added to the solutions to avoid reduction in volume and the formation of HCl which could eventually evaporate.

The result of the AAS analysis is summarised in Table 6-3. The percentage of Cu was calculated using the assumption that the precipitates have different amounts of water of crystallisation (Figure 6-9 and Figure 6-10)

Table 6-3: Results of the copper analysis on the three precipitates using AAS

SAMPLE	*Theoretical %Cu*	*Sample %Cu*	*Error*
S1	$Cu(Th)Cl*0.75H_2O$ %Cu=33.69	33.86	± 0.26
S2	$Cu(Th)Cl*H_2O$ %Cu=32..90	32.37	± 0.16
S3	$Cu(Th)Cl*1.5H_2O$ %Cu=31.10	29.89	± 0.10

Ion Chromatography

The measurement of the Cl component is particularly difficult. Small amounts of precipitates (S1, S2 and S3) (0.256g±0.001) were collected in a vacuum flask and concentrated HNO_3 was added. A water pump was used to reduce the pressure to 14 mmHg. The flask was warmed up until the acid boiled and the precipitate was dissolved. The solution was then allowed to naturally cool down to room temperature before the flask was opened. This procedure was necessary because the HCl could be lost during the warm process (the procedure was checked using CuCl salts). The results are summarized in Table 6-4.

Table 6-4: Results of chloride analysis using ion chromatography

Sample	*Theoretical %Cl^-*	*Sample %Cl^-*	*error*
S1	Cu(Th)Cl*0.75H_2O %Cl=18.80	18.61	± 0.15
S2	Cu(Th)Cl*H_2O %Cl=18.36	18.01	± 0.11
S3	Cu(Th)Cl*1.5H_2O %Cl=17.54	17.34	± 0.13

The preparation of the sulphur samples for IC analysis was achieved by dissolving samples S1, S2 and S3 (0.256g±0.001) in concentrated HNO_3 and boiling the solution until the precipitate was dissolved. When HNO_3 was warmed up, a vigorous reaction started with the production of brown fumes (attributed to NO_2 gas).

The results of the IC analysis on sulphur are reported in Table 6-5.

Table 6-5: Results of sulphur (as SO_4^{2-}) analysis by ion chromatography

Sample	*Theoretical %S*	*Sample %S*	*error*
S1	Cu(Th)Cl*0.75 H_2O %S=6.80	6.99	± 0.15
S2	Cu(Th)Cl* H_2O %S=6.64	6.53	± 0.13
S3	Cu(Th)Cl*1.5 H_2O %S=6.35	6.39	± 0.13

Elemental analysis

The concentration of C, H and nitrogen were calculated using the elemental analysis method. The instrument used for the analysis was an Exeter Analytical model 440.

The sample preparation for elemental analysis was the same used for the IC of sulphur. Firstly solutions were weighed out into a tin capsule and sealed. They were then moved into a furnace at the operating temperature of 960°C where they were underwent combustion. As the samples were burnt (in oxygen atmosphere), heat was given off raising the temperature to 1600°C. The resultant combustion gases were passed over a catalyst to remove sulphur, halogens and any excess oxygen. The cleaned up gases passed over a detector and then through a tube of anhydrous magnesium perchlorate to remove water vapour. They then flew onto another detector to give a pair of values for the hydrogen content. A second detector was followed by a tube of ascarite which was used to remove carbon dioxide and it was followed by another detector which gave the pair of carbon values. Finally the nitrogen was determined by comparing the resultant gas against the pure helium carrier gas. The instrument was calibrated by running acetanilide as a standard every sixth run. Blanks were also run regularly.
The elemental analysis results are summarised in Table 6-6.

The experimental values agree with the theoretical value apart from the last one. This suggests that sample S3 contains more water than expected. The precipitate for this analysis was prepared separately. The difference between these results and the IC and AAS results (in which the sample S3 contains $1.5H_2O$ instead of $2H_2O$) could be dependent on the drying process.

Table 6-6: Summary of the elemental analysis results on the precipitate

Sample	*Theoretical %*	*Sample %*
	$Cu(Th)Cl*0.75H_2O$	
S1	%C=6.37 %N=14.85 %H=2.67	6.48±0.01 14.8±0.07 2.58±0.01
	$Cu(Th)Cl*H_2O$	
S2	%C=6.22 %H=2.61 %N=14.51	6.22 ± 0.07 2.49 ± 0.07 14.3 ± 0.07
	$Cu(Th)Cl*2H_2O$	
S3	%C=5.78 %H=2.23 %N=12.9	5.69 ± 0.01 2.39 ± 0.01 13.27 ± 0.01

Solubility

All the white precipitate samples were insoluble in polar and non-polar solvents. The solvents used for testing the solubility were acetonitrile, acetone, methanol, ethanol, water, dichloromethane, ethyl acetate, cyclohexane and chloroform.

Thermal analysis

Differential scanning calorimetry (DSC)

DSC analyses were performed with a Mettler DSC30 instrument. The temperature was varied from room temperature up to 500°C at 10°C/min.

The DSC graphs of the three samples are shown in Figure 6-8.

The first peak around 180ºC may be associated with the dehydration of the samples. This suggests that the samples may have contained water of crystallisation. The three samples show different peak shapes for the first peak. The precipitate S3 has a large/broad peak while samples S1 and S2 have narrow/sharp peaks. The peak at 180°C is followed by an endothermic peak which changes to an exothermic one, and corresponds to a dramatic weight loss detected with the TG analysis (Figure 6-9). These two peaks may coincide with the decomposition of the metal-organic compound and the formation of copper oxide (as proposed by Krunks ((Ugai et al. 1981; Krunks et al. 1997; Krunks et al. 1998)

The endothermic peak (T~280°C) is common to the three compounds while the position of the exothermic peak shifts and the increase in temperature is proportional to the amount of thiourea added to the solution. This may be caused by a different decomposition mechanism or an alternative reaction which masks the first peak. The sample S1 shows another peak at high temperature (T~450°C) where a possible oxidation reaction takes place as observed comparing Figure 6-9 and Figure 6-10 in the next section. The bases of this assumption is the fact that the behaviour of the three samples is different in air compared with the inert atmosphere during the thermogravimetric analysis.

The difference between the three samples and the shift of the peak may be the explained by the assumption that the three samples could be two structural isomers (as will be explained at the end of this section).

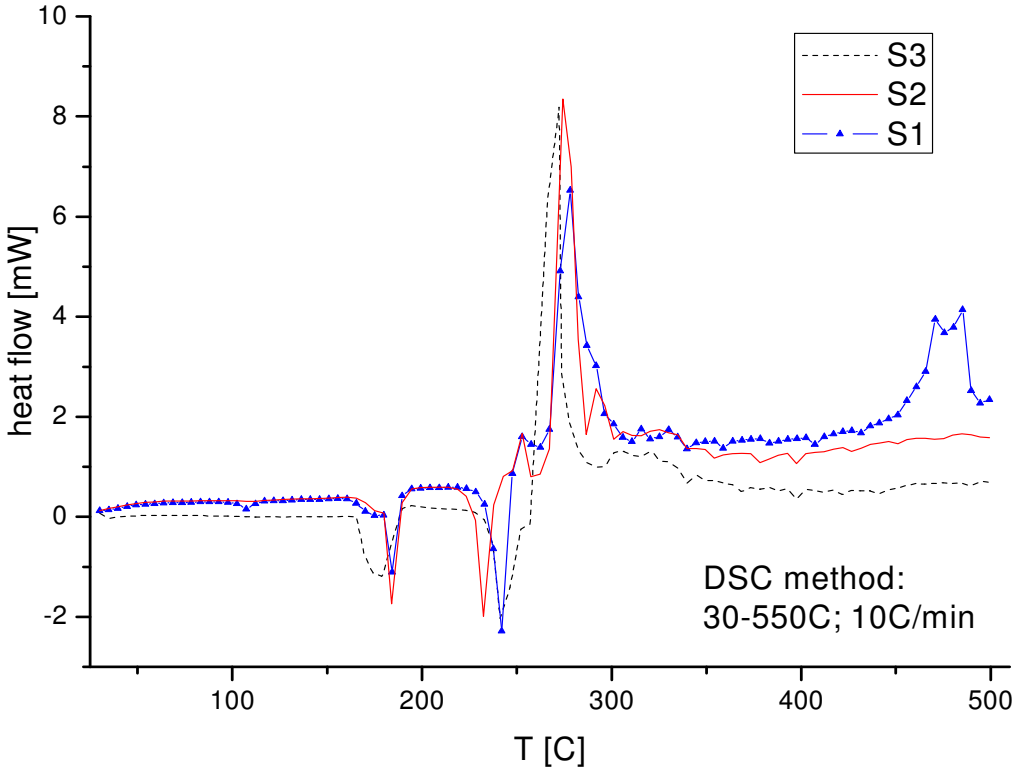

Figure 6-8: DSC analysis of the samples S1, S2 and S3

Thermogravimetry

The following graph shows the thermogravimetric analysis conducted on the three samples with a Mettler TG50 instrument (STARe software). The precipitates were heated up from room temperature to 500ºC at 10ºC/min.

As observed, all the samples have the same trend (Figure 6-9 and Figure 6-10). The TG curves show a mass loss around 12% in a range 20-150°C. It may correspond to a dehydration process. The amount of water of crystallisation is different for the three samples as shown in Figure 6-9. The amount of water lost during the heat treatment was connected with the variation of weight between the starting point (T=30°C) and the final point (T=146°C). The difference suggests that the amount of water should be around 5.45%

(S1), 6.39% (S2) and 7.23% (S3). These values are lower than the values obtained during the elemental analysis (sample S1, $\%H_2O$=7.1; sample S2, $\%H_2O$=9.32 and sample S3, $\%H_2O$=13.36).

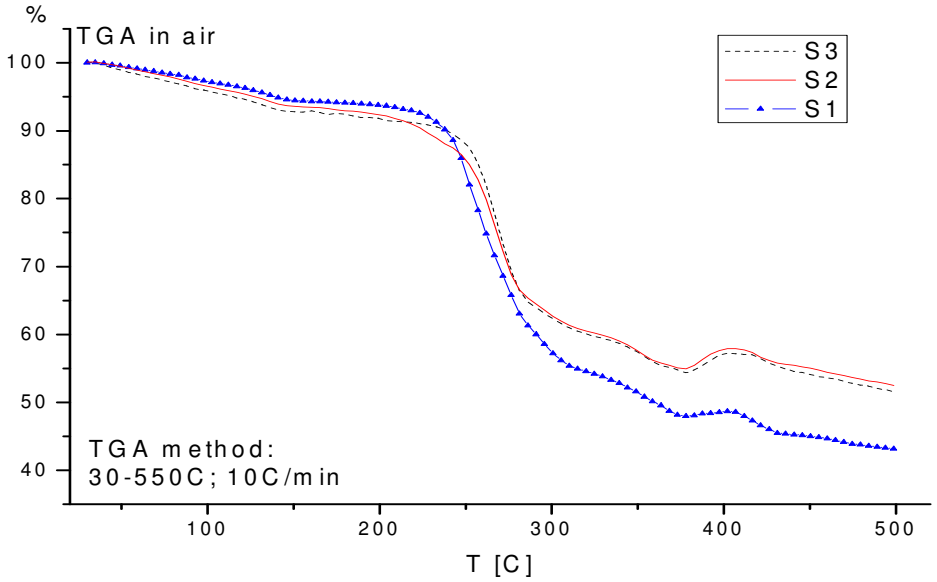

Figure 6-9: TGA analysis of the samples S1, S2 and S3

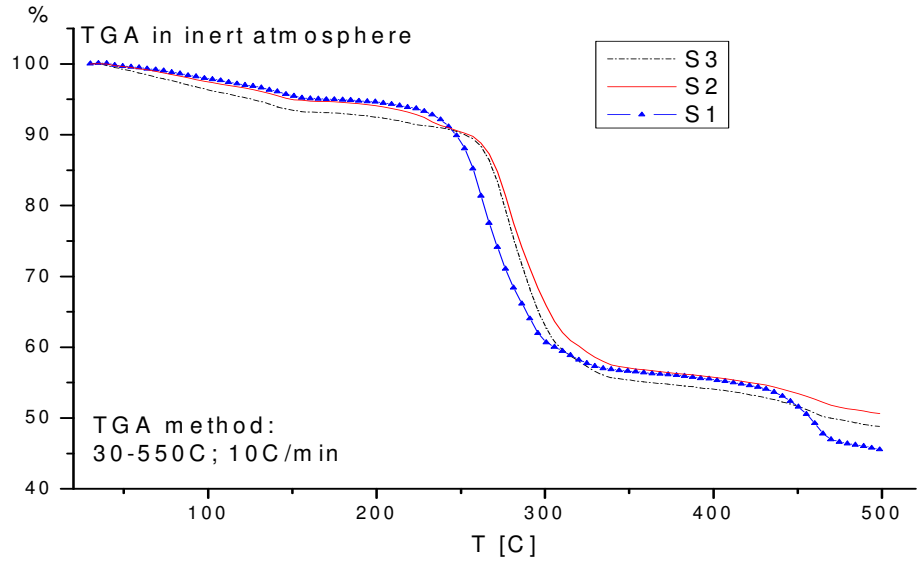

Figure 6-10: TGA in inert atmosphere of the samples S1, S2 and S3

The decomposition process observed on the DSC curve corresponds to the maximum loss of mass on the TG curve.

Samples S3 and S2 are similar while sample S1 has a different behaviour at high temperature (T~280°C) as observed in the DSC graph. The S1 curve shows a bigger loss of weight compared with the other two samples. The difference disappears when the TGA experiment is carried out in an inert atmosphere. This could suggest that the samples follow a different oxidation process. The fact that the three samples have the same trend simply suggest that the amount of gases lost is the same but it doesn't give any more information about the reaction mechanism.

Infrared spectroscopy

The IR graphs were recorded using a Bruker- Vector22 instrument.
The first spectrum collected was thiourea which will be the reference.
Region (Figure 6-11):
3370-3100 cm^{-1}: N-H stretching mode. The first two peaks at low frequency are assigned to the symmetric stretching while the third and the fourth (at 3100 cm^{-1}) assigned to the asymmetric stretching. The fourth peak is partially covered by background
1620 cm^{-1}: NH_2 bending
1470-1410 cm^{-1}: two peaks assigned to the C-N stretching
1080 cm^{-1}:NH_2 rocking
733 cm^{-1}: C=S stretching
494-417 cm^{-1}:N-C-N bending+ NH_2 torsion + N-C=S bending

The IR spectra may be used to determine the difference between the three samples but also to understand how the thiourea is connected to the metal (via S or via N)

The three samples are complexes formed by copper and thiourea. Comparing the IR spectra of these with thiourea (using the variation of the peak positions of the IR samples with

respect to the thiourea) it is possible to establish which atom is bonded to the copper. In fact both nitrogen and sulphur atoms can give their lone pairs for coordinating the metal.

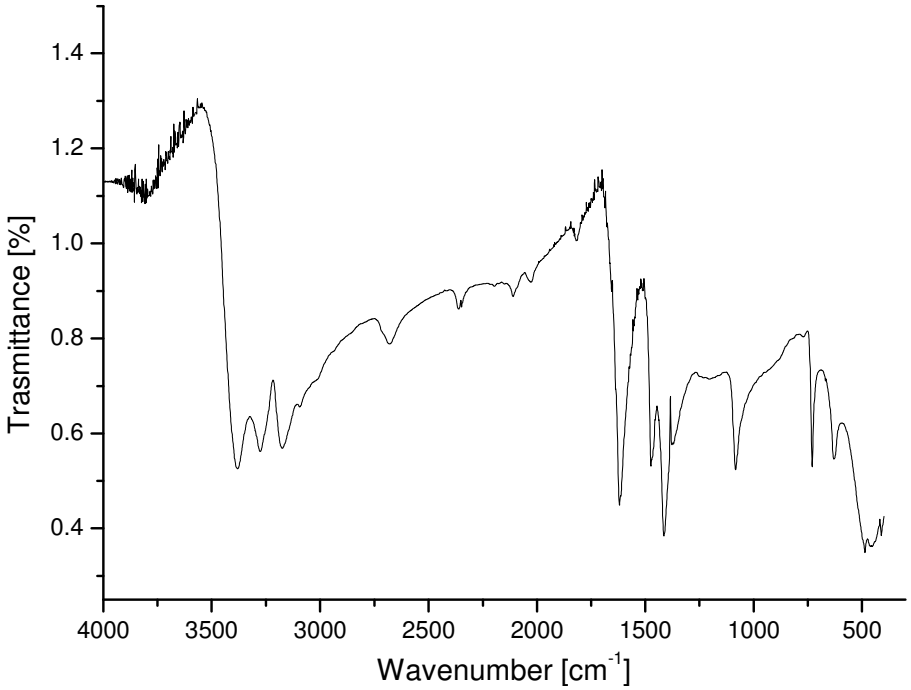

Figure 6-11: IR spectra of the thiourea

The following graphs show the spectra of the three precipitates (Figure 6-12, Figure 6-13 and Figure 6-14).

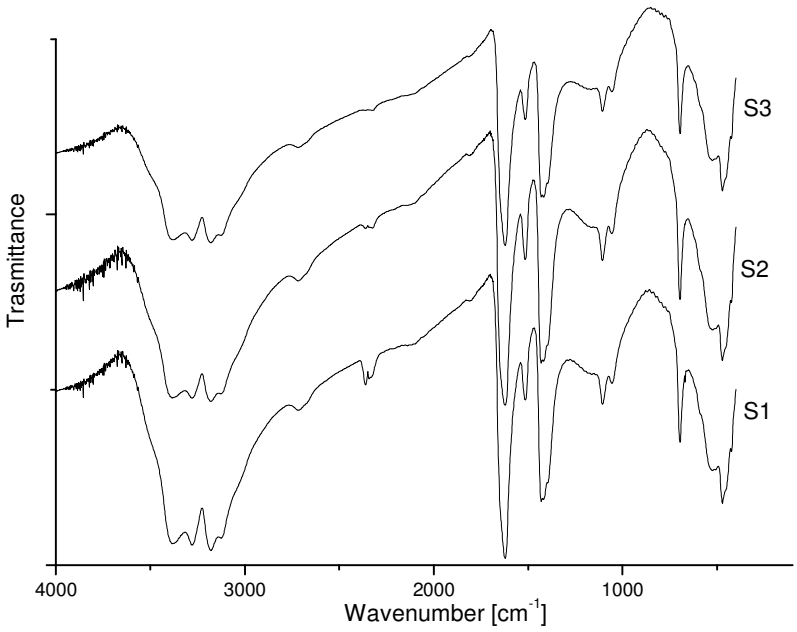

Figure 6-12: IR spectra of the samples S1, S2 and S3

No significant differences are detected between the samples but some information may be drawn by comparing these results with the thiourea.

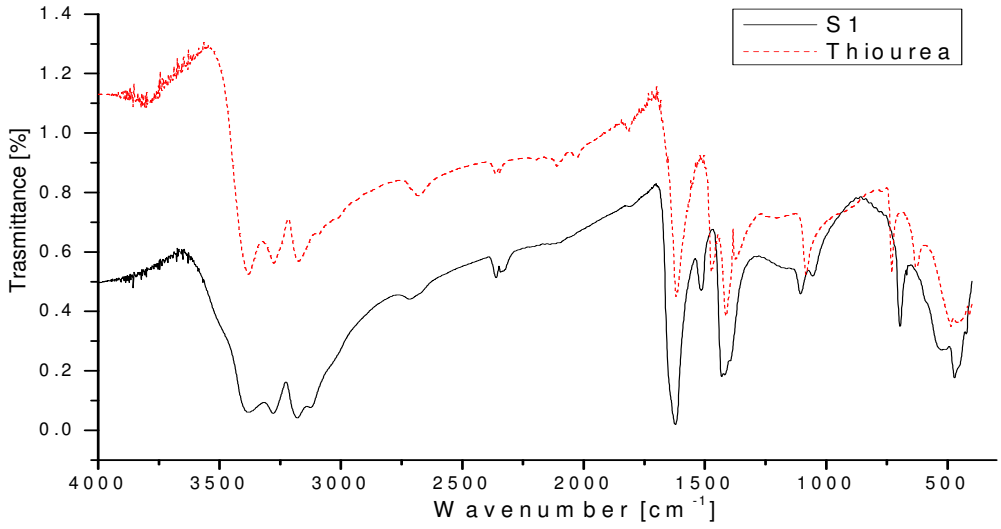

Figure 6-13: IR of the sample S1 and thiourea

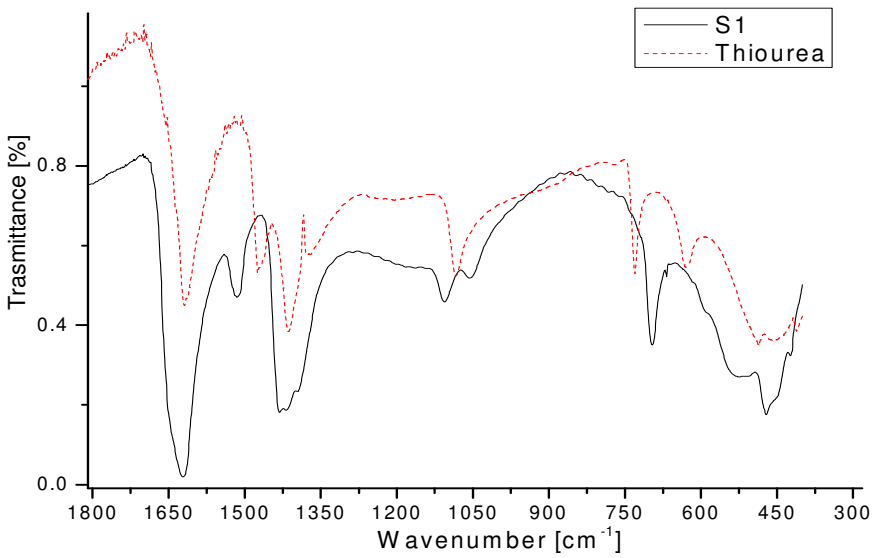

Figure 6-14: Detailed view of Figure 6-12

From Figure 6-14 considerable differences in the peaks positions and peaks shape are noticeable. For example for the C=S stretching (which shifts from 733cm^{-1} (thiourea) to 696 cm^{-1} (S1)), NH_2 rocking (thiourea = 1080cm^{-1} is spit into two (1106 cm^{-1} and 1055 cm^{-1}) and C-N stretching (which shifts from 1470 cm^{-1} (Thiourea) to 1512 cm^{-1} (S1))

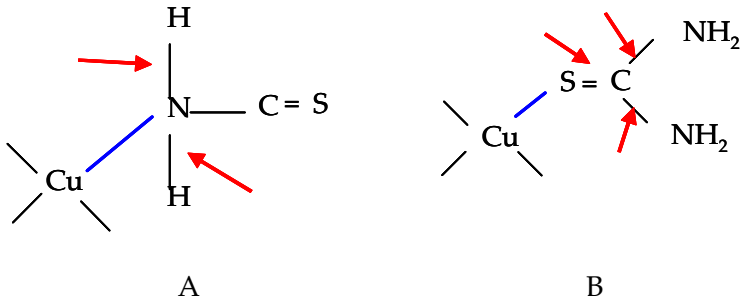

Figure 6-15: Effect of Effect of Cu-N coordination on the N-H bonds (A) and Cu-S coordination on (B)

If the Copper was coordinated to Nitrogen, this should provoke variations in the upper frequency region where the single N-H bonds are detected. This is not seen.

Alternatively if the Sulphur was coordinated to the copper this should cause a shift in the vibrational frequencies of C=S and C-N bonds. This second hypothesis is in good agreement with the experimental obseravtaions.

As anticipated early in this section, the samples could be formed by two different structural isomers. Cu(I) complexes can form different polymeric structures and clusters. Well known are the cases of $Cu_4I_4(PR_3)_4$ ad $Cu_4I_4(AsR_3)_4$ which can solidify in a cubane structure (Cotton et al. 1988) or in a step form (Lee 1991). In the first one, the four Cu atoms form a tetrahedron, the four PR_3 or AsR_3 groups are bonded to the four corners while the I atoms are typically bridges to the Cu. I atoms are located on the four faces of the tetrahedron. In the second structure, two Cu atoms are four-coordinated and two Cu atoms are three-coordinated.

Similar structures could be obtained during the precipitate formation. These possible structures are drawn in Figure 6-16.

It should be noticed that the three samples (S1,S2 and S3) could have identical diffractograms because one of two isomers could be amorphous and so undetected. This could also explain the TGA/DSG results. The two structures have different bondings which may slow down the decomposition process. This could generate dissimilar behaviour with increasing temperature. The two isomers could also be used to explain the IR results. The only IR sensitive bonds are copper-sulphur, copper-nitrogen and nitrogen-hydrogen which are the same for both structures and thus no change can be observed.

As stated early, the nitrate salts don't give any precipitate. An increment of the amount of thiourea leads to a change in the intensity of the colour of the solution (Figure 6-17). The absence of the precipitate is correlated with the strong oxidizing properties of the NO_3^- group. The nitrate group, in fact, stops the reduction of the copper which is the intermediate stage of the precipitate formation reaction.

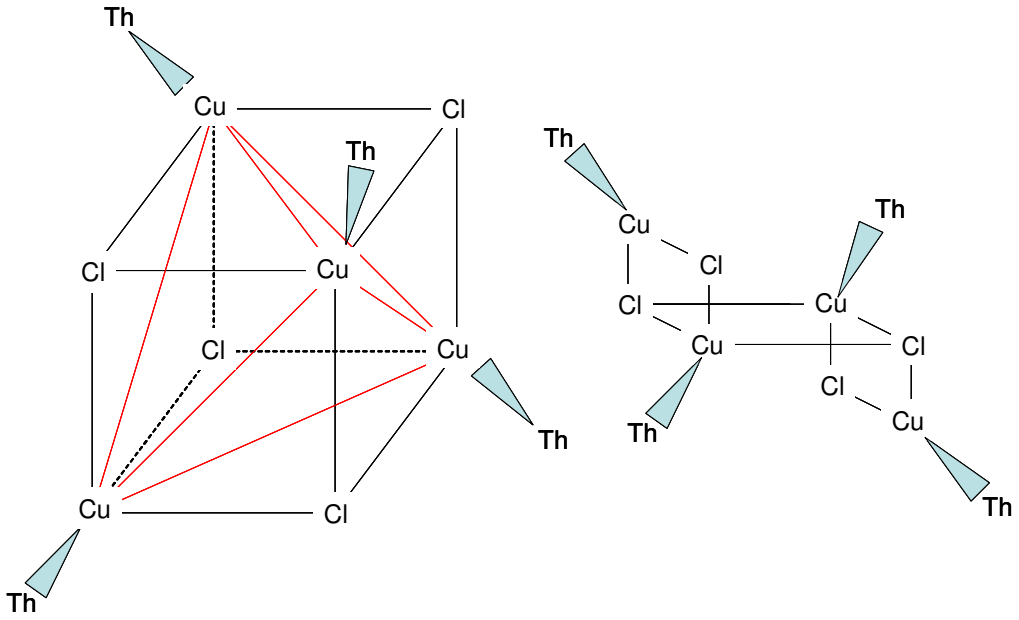

Figure 6-16: Cubane structure (left side) and step form (right side)

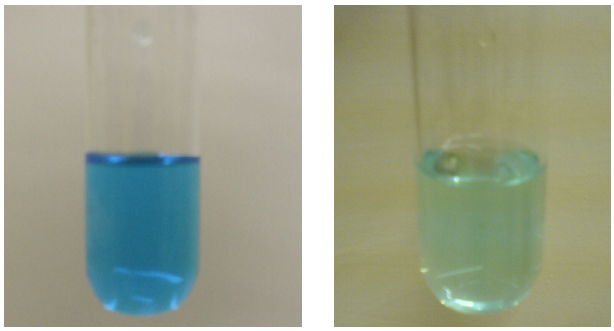

Figure 6-17: Change in Nitrate Solution Colour Intensity with Thiourea Concetration

6.2. The difference between chloride- and nitrate-based solutions

In this section various chloride and nitrate solutions were prepared and $CuInS_2$ films deposited by ESD. The effects of the different salts on the spray are first reported. Subsequently the deposited films are characterized structurally, compositionally and their electro-optical properties investigated.

Chloride based solution was prepared by dissolving $CuCl_2 \cdot 2H_2O$ (99.99%, Sigma Aldrich), $InCl_3$ (99,99%, Alfa Aesar) and thiourea (99%, Alfa Aesar) in deionized water (18 $M\Omega cm^{-1}$ at 25°C). Ethanol (99.99%, Fisher Scientific) was added to the solutions to reduce the surface tension of the starting solutions while $In(NO_3)_3$ (99.99%, Aldrich) , $Cu(NO_3)_2$ (98%, Aldrich) and thiourea (99%, Alfa Aesar) were used to prepare the "nitrate" solution. During this experiment, the solution concentration was maintained at 0.21M while the [S]/[Cu] and [Cu]/[In] molar ratios were fixed at 5 and 1 respectively (Malagoli et al. 2003).

SnO_2:F coated glass (1.8mm x 30mm x 10mm in thickness, length, depth respectively) and Silicon (10mm x 10mm x 1mm) were used as substrates. Silicon was chosen as the substrate for the RBS measurements as it doesn't cause any interference to the analysis.

The samples were deposited at 450°C, using an applied voltage of 18kVand at a needle-substrate distance of 5 cm. A summary of the deposition conditions is given in Table 6-7.

Table 6-7: deposition conditions of chloride and nitrate solutions

Chloride	*Flow rate [µl/min]*	*Time [h]*	*Nitrate*	*Flow rate [µl/min]*	*Time [h]*
Cl1	100	3	N1	100	3
Cl2	50	6	N2	50	6
Cl3	25	12	N3	25	12

The difference in spray cones between the two solutions (sprayed at 25µl/min) is shown in Figure 6-18 A and B obtained using the laser light source during the PIV tests.

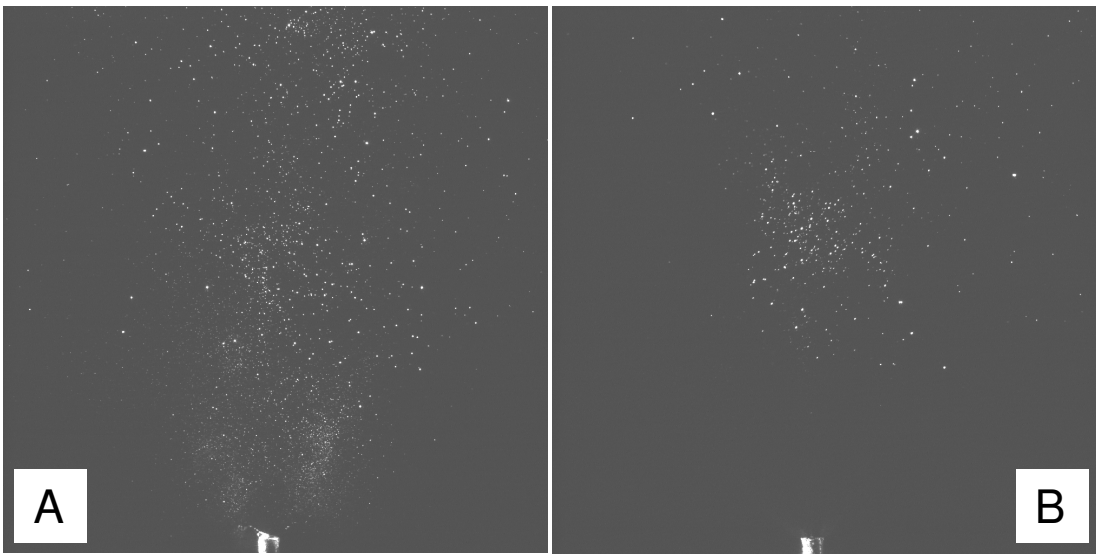

Figure 6-18: PIV Particle Images for Chloride and Nitrate Solutions (left and right respectively

The "chloride" image shows a more stable cone while the "nitrate" solution shows more unsteady cone behaviour during the deposition. This difference can be linked to the properties of the two starting solutions (which are compared in Table 6-8). As stated early in section 2.1, surface tension and conductivity affect the quality of the aerosol.

Table 6-8: Properties of Nitrate and Chloride Solutions

Variable	*Nitrate*	*Chloride*
Surface tension	27.1±0.3 dina/cm	6,6±0.6 dina/cm
Conductivity	2.93±0.1mS	4.38±0.1mS

The ability of a solution to form an aerosol is determined by the surface tension because it controls the maximum charge which can be distributed on the droplet's surface. The nitrate

solution has a higher surface tension value which could explain the difficulty in obtaining a uniform and steady cone during the deposition process.

The conductivity determines the size of the cone jet (Ganan-Calvo et al. 1996) and, in this case, the two solutions have similar properties which would suggest that the particle sizes of the two cones should be similar. This is confirmed from the particle images.

The velocity vector maps and velocity distributions (Figure 6-19 and Figure 6-20) show similar speed values (around 3.5 m/s), confirming the similar particle size distributions for the two solutions. However, the chloride solution has a more uniform flow field than the nitrate solution which as mentioned above is thought to be due to the different surface tension values.

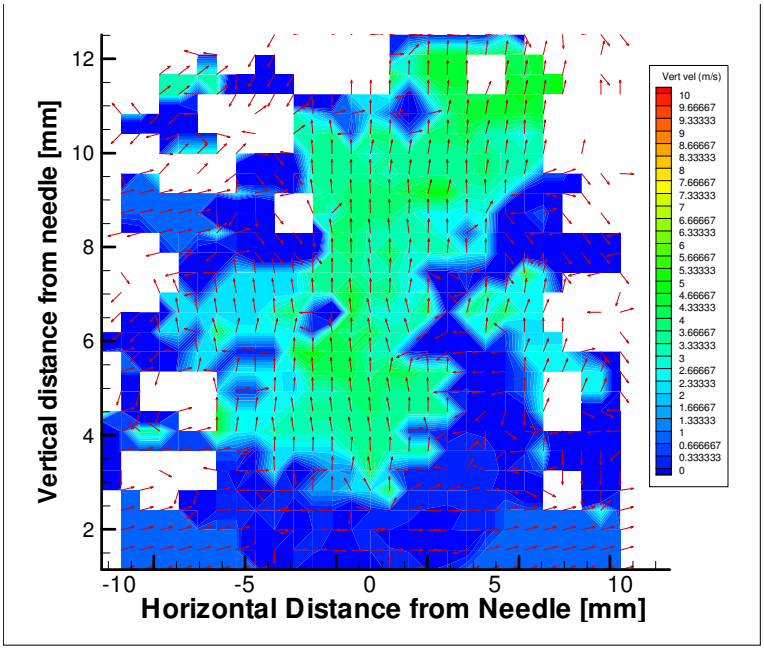

A

Figure 6-19: PIV Velocity Vector Maps of Nitrate Solutions (A)

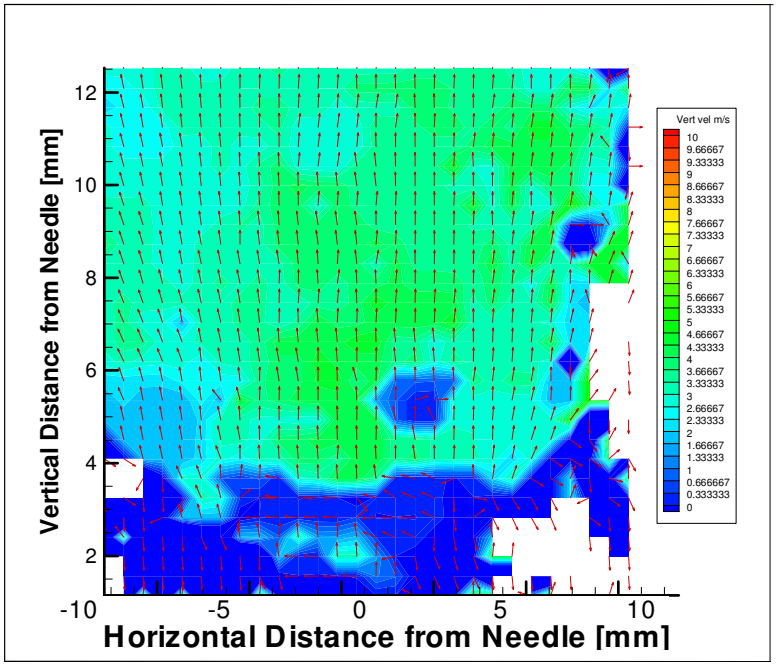

B

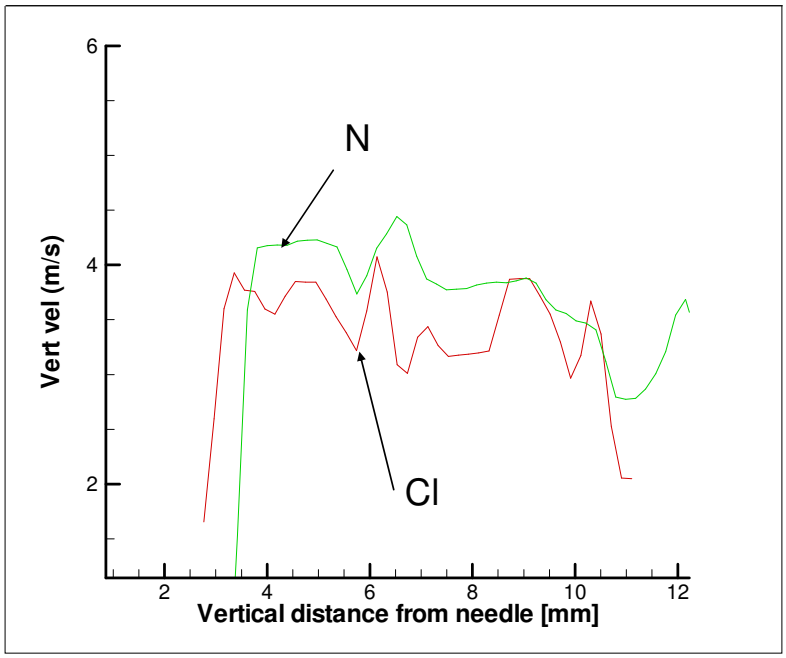

C

Figure 6-20: PIV Velocity Vector Maps of Chloride (B) Solutions and Vertical Velocity Profile from Needle Towards Substrate (C)

The effect of different solution flow rates on the velocity of the cone particles for the nitrate and chloride solutions is shown in Figure 6-21. The nitrate solutions have similar velocities for different flow rates. This is in contradiction with the theory (chapter 2) but it could be explained by the high surface tension of the starting solutions. This value determines the minimum size of the droplets and could overtake the effect of the variation of the flow rate. The chloride shows the ideal trend: the velocity of the particle within the aerosol is inversely proportional to the flow rate (section 5.1).

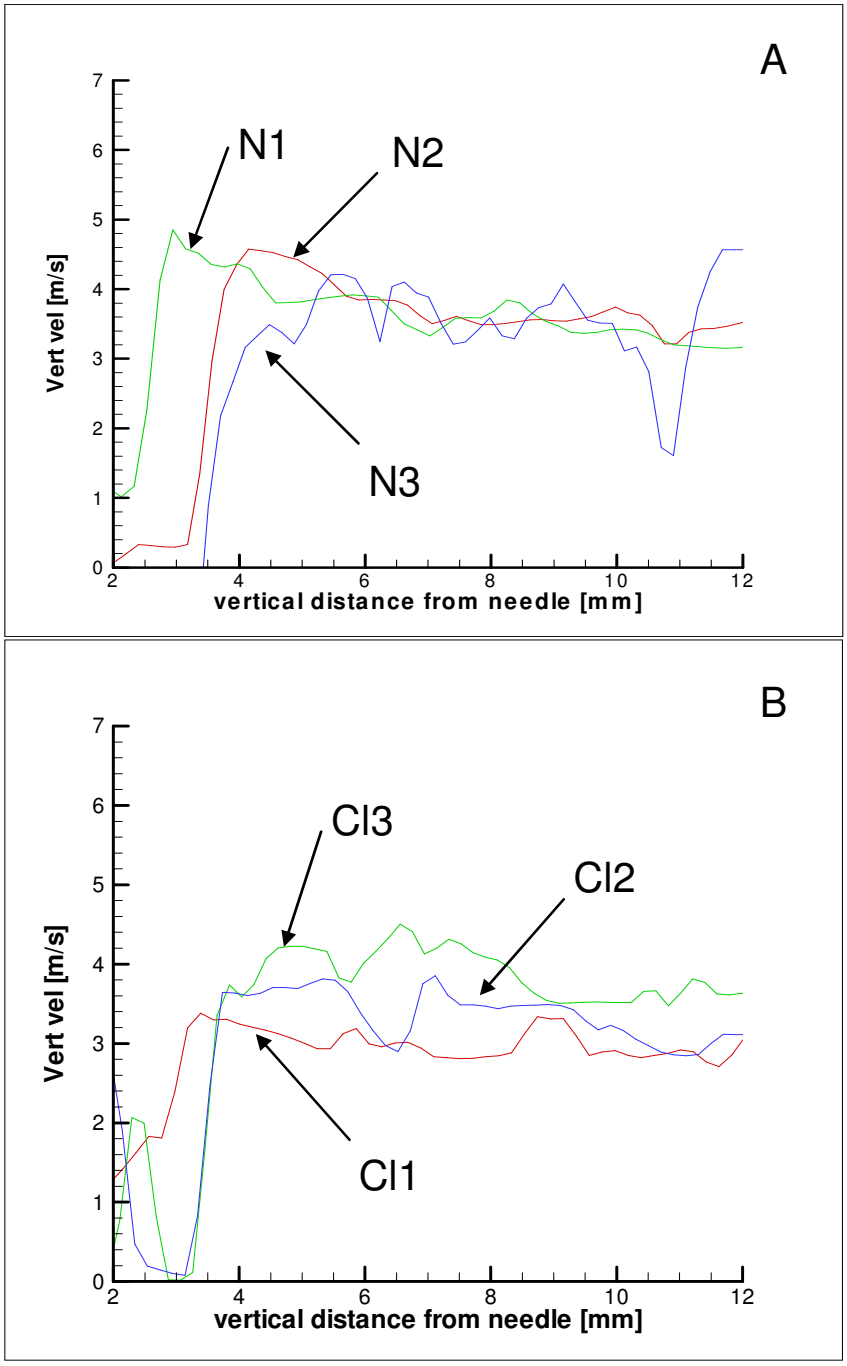

Figure 6-21: Vertical Velocity Profiles of nitrate solution (A) and chloride solution (B) for flow rates of 100µl/min (Cl1,N1), 50µl/min (Cl2,N2), 25µl/min (Cl3,N3)

The X-ray diffractograms of the chloride and nitrate films sprayed on SnO_2:F coated glass are shown in Figure 6-22 and Figure 6-23.

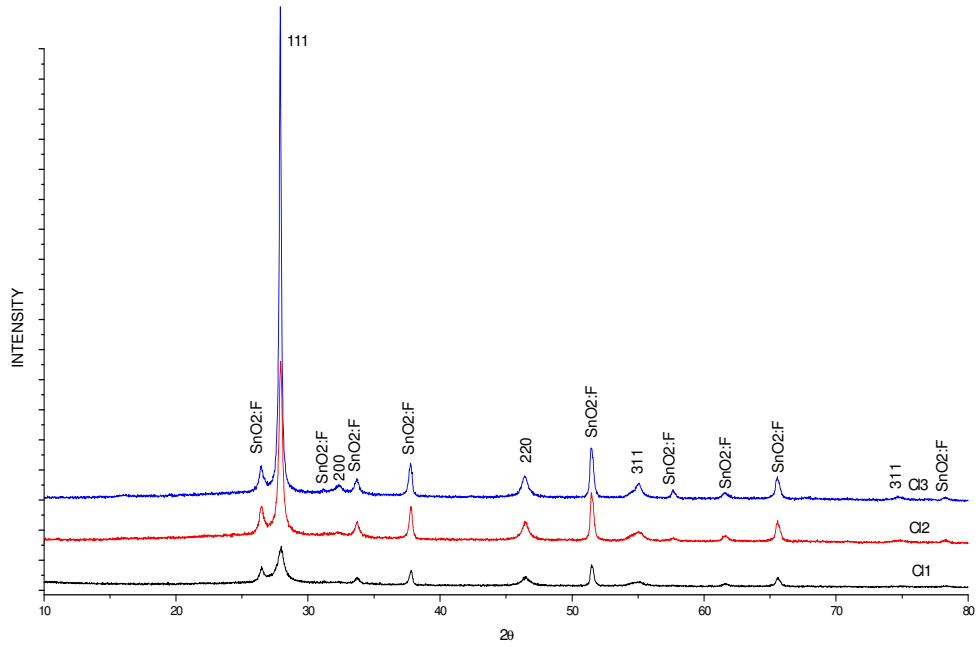

Figure 6-22: XRD of the chloride samples

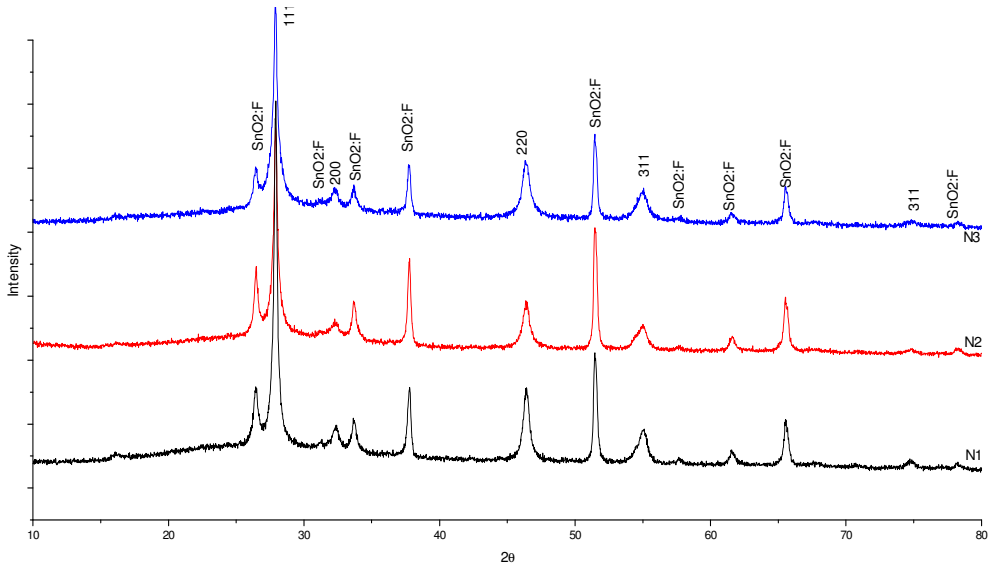

Figure 6-23: XRD of nitrate samples

Ignoring the FTO peaks, all the other peaks for the "chloride" samples are attributed to the $CuInS_2$ phase while the nitrate samples have an un-identified peak at 16.12°. The peak could be come from Cu_3InS_4 (PDF-38777). The nitrate peaks are broader and have lower intensity than chloride samples suggesting a reduced crystallinity.

As seen in section 5.3.2, the crystalline structure of the as-deposited films can change between the two polymorphic forms of the CIS system: sphalerite and chalcopyrite. A fit of the chloride and nitrate diffractograms shows that the structure for both is sphalerite.
In order to investigate the presence of the preferred orientation along one of the CIS planes, the intensity ratio of the peaks $2\theta = 46.8°$ and $2\theta = 27.9°$ (called I2/I1)and $2\theta = 55.1°$and $2\theta = 27.9°$ (called I3/I1) have been calculated and compared with the sphalerite theoretical values (as displayed in Table 6-9). The chloride and nitrate samples show that the intensity ratios are lower than the theoretical value. This means that the peak I1 ($2\theta = 27.9°$) is more intense suggesting a preferred orientation along the (111) plane. This difference between the sample value and the theoretical value (for the chloride samples) is inversly proportional to the flow rate. The preferred orientation of chloride samples increases when the flow rate is decreased suggesting a crystal texturing along the (111) plane.

The effects of different starting solutions compositions and flow rates on the as-deposited films have been investigated using the RBS technique. The RBS analysis was carried out using 1.6 MeV 4He ion beam, a detector solid angle 5msr at backscattering angle of 170°.

The RBS spectra have been fitted by assuming the presence of a single homogeneous layer of CIS on the substrate. Two RBS spectra of chloride and nitrate samples (sprayed at 25µl/min) are shown in Figure 6-24 and Figure 6-25. The shallow gradient of the data (between 120 and 240 channels) arises from the high surface roughness of the as-deposited films which is a characteristic of the ESD method.

Table 6-9: Peak intensity ratio of chloride and nitrate samples

	Flow rate [µl/min]	*Intensity*	
Samples		*I2/I1*	*I3/I1*
Cl1	100	0.31	0.2
Cl2	50	0.14	0.1
Cl3	25	0.06	0.05
N1	100	0.26	0.15
N2	50	0.28	0.18
N3	25	0.36	0.24

	Intensity	
Sphalerite	*I2/I1*	*I3/I1*
Theoretical	0.49	0.24

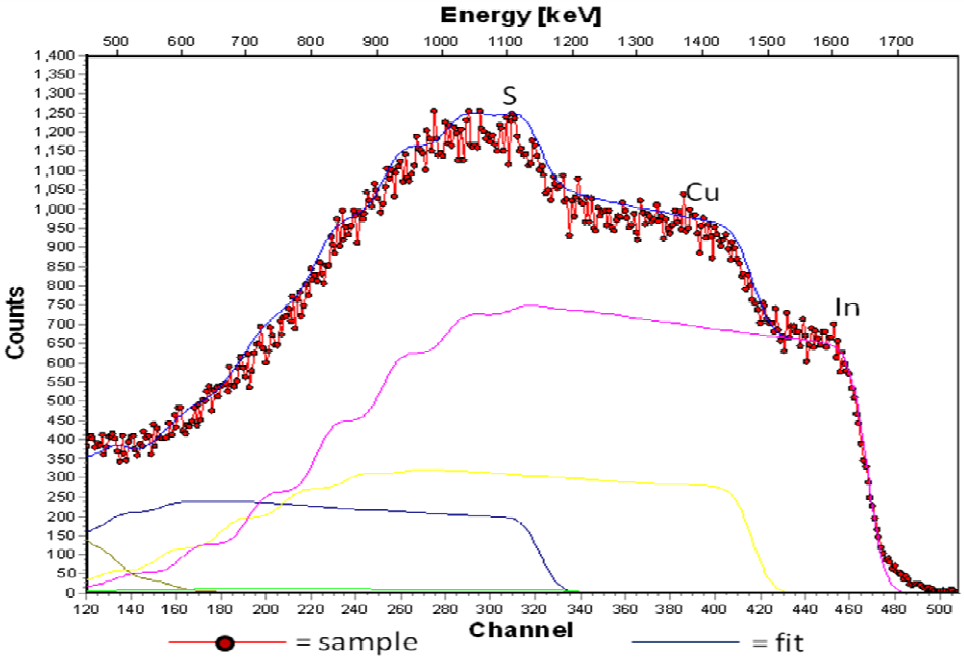

Figure 6-24: RBS spectra of chloride sample

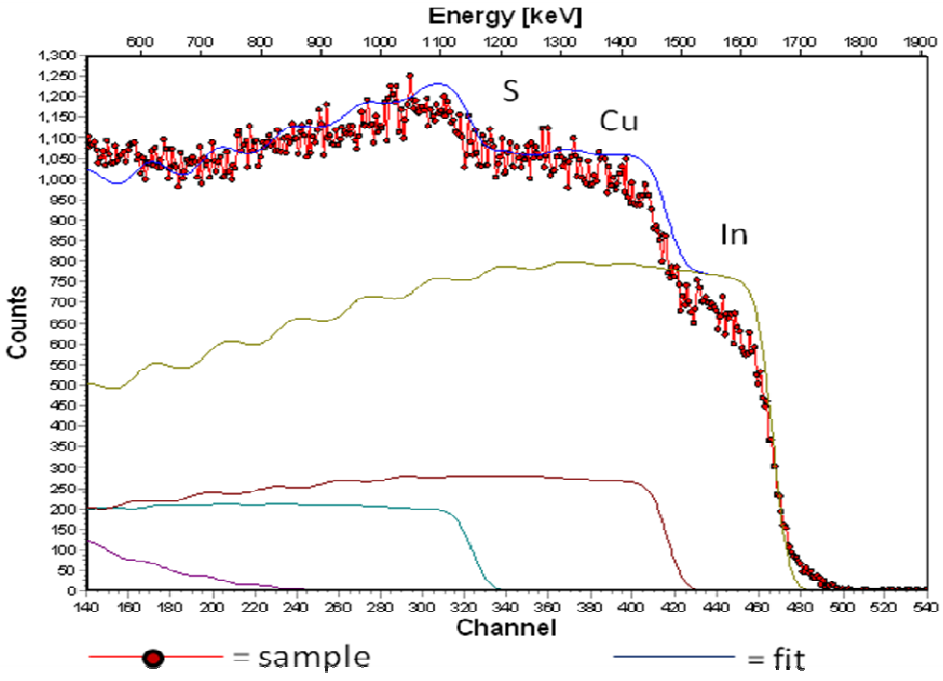

Figure 6-25: RBS spectra for the nitrate sample

The thicknesses of the as-deposited films are around 1.38µm for the chloride and 1.04µm for the nitrate (based on the density of $CuInS_2 = 4.748$ g/cm^3)

Table 6-10 shows the thicknesses of the chloride as-deposited films are quite similar indicating an independency of this variable from the solution flow rate. However, the nitrate films show a marked difference in thickness with the flow rate solution. The thicknesses should be constant because the total volume of sprayed solution is the same for all the samples. The reason for the large variation in thickness may be due to different properties of the starting solutions.

The nitrate samples have also higher surface roughness than the chloride films.

Table 6-10: thickness analysis of chloride and nitrate samples

Sample	*Thickness [µm]*	*Error [µm]*
Cl1	1.33	0.03
Cl 2	1.43	0.03
Cl 3	1.13	0.02
N1	0.66	0.01
N2	1.02	0.02
N3	1.43	0.03

The composition of the films follows a similar trend as that seen for the thickness. The chloride films have a composition close to the theoretical value (Table 6-11) while the nitrate films have an elemental concentration different from the expected values. Samples

N2 and N3 are S and Cu rich respectively. This non-ideal composition may explain the extra peak observed during the XRD analysis.

The characteristic of the film deposited from nitrate solution (thickness and composition) may be explained using the information obtained from the PIV images which show a non-uniform spray cone. The instability in the cone of the nitrate starting solutions results in a periodic aerosol which deposits less material onto the substrate for a given period of time when compare with the same flow rate conditions for the continuous chloride aerosol. This results in thinner nitrate as-deposited films. The difference in composition between the two starting solutions may be explained by the fact that nitrate samples are growing in distinct layers which are subjected to a heating process prior to the next layer being deposited.

Table 6-11: comparison of RBS Measured Stoichiometric Values of Cu, In and S in the as-deposited Films with the Theoretical Values

theoretical	*Cu*	*In*	*S*
	0.25	0.25	0.5
sample	*Cu*	*In*	*S*
Cl1	0.24±0.01	0.25±0.01	0.51±0.03
Cl2	0.22±0.01	0.23±0.01	0.54±0.03
Cl3	0.24±0.01	0.25±0.01	0.51±0.03
N1	0.23±0.01	0.23±0.01	0.54±0.03
N2	0.22±0.01	0.14±0.01	0.64±0.03
N3	0.36±0.01	0.23±0.01	0.41±0.03

Photovoltammetry measurements have been performed using the same set up described in section 5.11.

The nitrate samples don't show any photocurrent response. This behaviour could be attributed to the segregation of secondary phases (detected during the XRD analysis) at the grain boundaries or due to high nitrogen doping level or finally poor films due to non-uniform growth.

The photo-voltammetry results of chloride samples are shown in Figure 6-26. The three samples show a cathodic photocurrent (p-type) response which increases when the voltage is decreased. At a more negative voltage, recombination processes are unlikely because the electrons are more efficiently scavenged by the solution. The three films show a rise in the dark current when the potential is made more negative indicating an oxidation of the CIS layer.

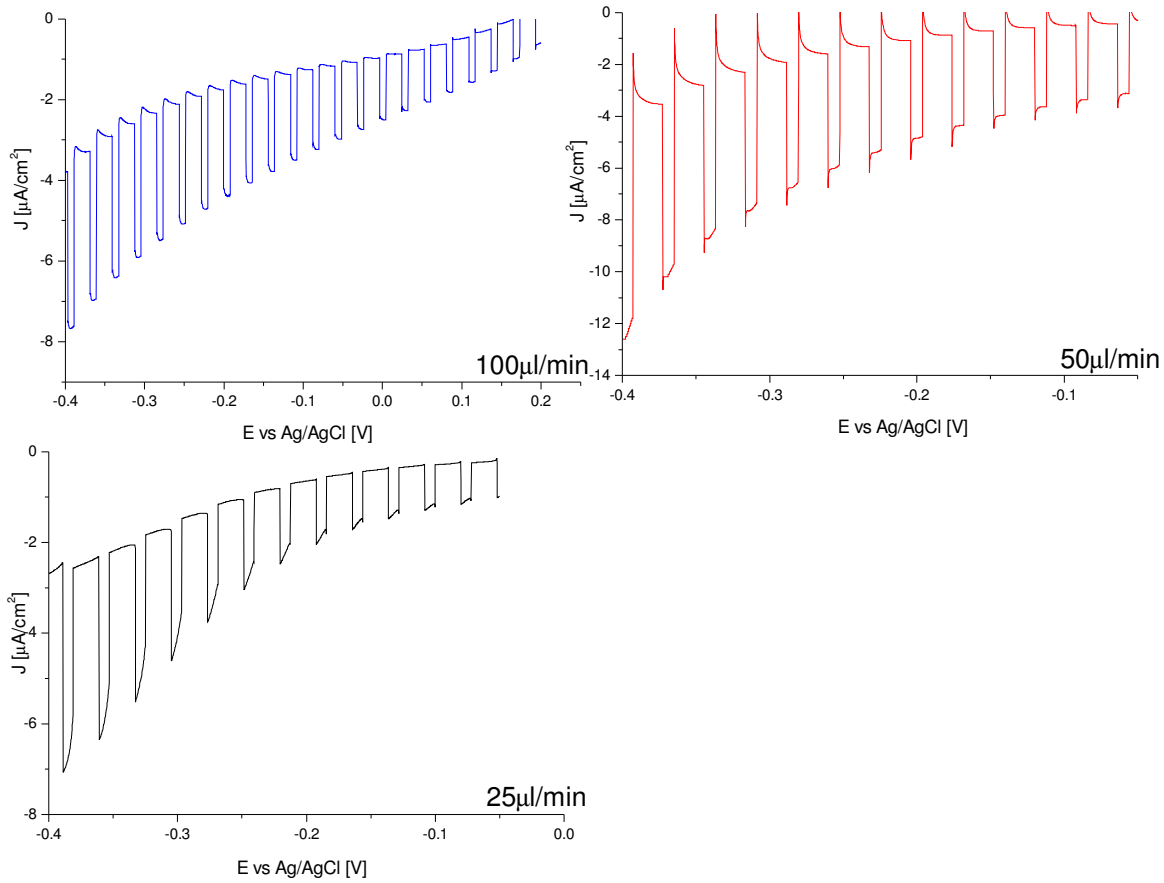

Figure 6-26: Photo-voltammograms of films deposited from the chloride solution

The EQE measurement set up has been described in section 5.3.2. The three chloride samples have similar trends (Figure 6- 27). The maximum quantum efficiency is around 16% (samples Cl2 and Cl3). The higher efficiency of the samples Cl2 and Cl3 could be connected with the slower thin film growth process.

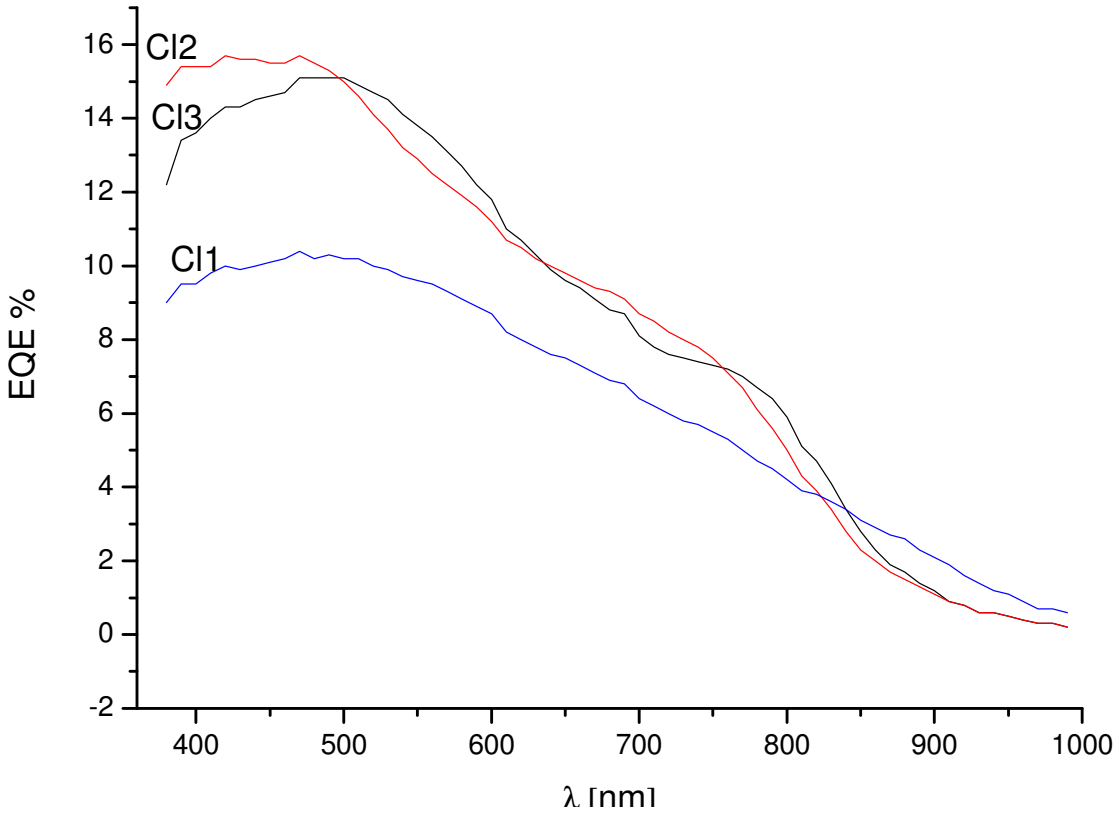

Figure 6- 27: EQE measurements of chloride samples.

6.3. S/Cu and Cu/In Molar Ratio Variation for chloride- and nitrate- based solutions

$CuCl_2 \cdot 2H_2O$ (99.99%, Sigma Aldrich), $InCl_3$ (99,99%, Alfa Aesar) and thiourea (99%, Alfa Aesar) were dissolved to prepare the "chloride" solution while $InNO_3$ (99.99%, Aldrich Chemical Company Ltd) , $CuNO_3$ (98%, Aldrich Chemical Company Ltd) and thiourea (99%, Alfa Aesar) were used to prepare the "nitrate" solution. The salts were dissolved in deionized water (18 $M\Omega cm^{-1}$ at 25°C) and ethanol (99.99%, Fisher Scientific). During this study, the solution concentration was maintained at 0.21M while the [S]/[Cu] and [Cu]/[In] molar ratios were varied between 5 and 5.7 (for S/Cu) and 0.6 and 3 (for Cu/In). The S/Cu

ratio has to be greater than 5 to avoid the precipitation of a Cu-thiourea intermetallic compound (Roncallo et al. 2007) as explained in section 6.2.

SnO_2:F coated glass (1.8mm x 30mm x 10mm in thickness, length and depth respectively) and Silicon (10mm x 10mm x 1mm) were used as the substrates. Silicon was chosen as the substrate for samples analysed by RBS as it causes less interference.

All samples in this study were deposited at 450°C, using an applied voltage of 18kV at a needle-substrate distance of 5 cm and a solution flow rate of 100µl/min. A summary of the starting solution conditions are given for all chloride and nitrate solutions in Table 6-12 and Table 6-13 respectively.

Table 6-12: Chloride starting solution conditions

Cl samples	*[Cu]/[In]*	*[S]/[Cu]*
Cl1	0.6	5
Cl2	0.75	5
Cl3	1	5
Cl4	1.5	5
Cl5	3	5
Cl6	1	5.3
Cl7	1	5.5

Table 6-13:Nitrate starting solution conditions

N samples	*[Cu]/[In]*	*[S]/[Cu]*
N1	0.6	5
N2	0.75	5
N3	1	5
N4	1.5	5
N5	3	5
N6	1	5.3
N7	1	5.5

6.3.1. Chloride sample

The results of the XRD analysis of the chloride samples in which the Cu/In molar ratio is varied can be seen in Figure 6-28. The three main $CuInS_2$ peaks (associated with the (111), (220) and (311) of the sphalerite structure) are observed in all the samples. The CIS formation is strongly dependent on the starting solution composition as seen in the XRD analysis. At higher indium concentrations (samples Cl1 and Cl2), the CIS peak intensities are low and the peaks are broad suggesting a poor crystallinity of these samples. Reducing the amount of indium (samples Cl3, Cl4 and Cl5) causes the peaks to become more defined and sharp indicating that as-deposited films are of better crystalline quality than for Cl1 and Cl2.

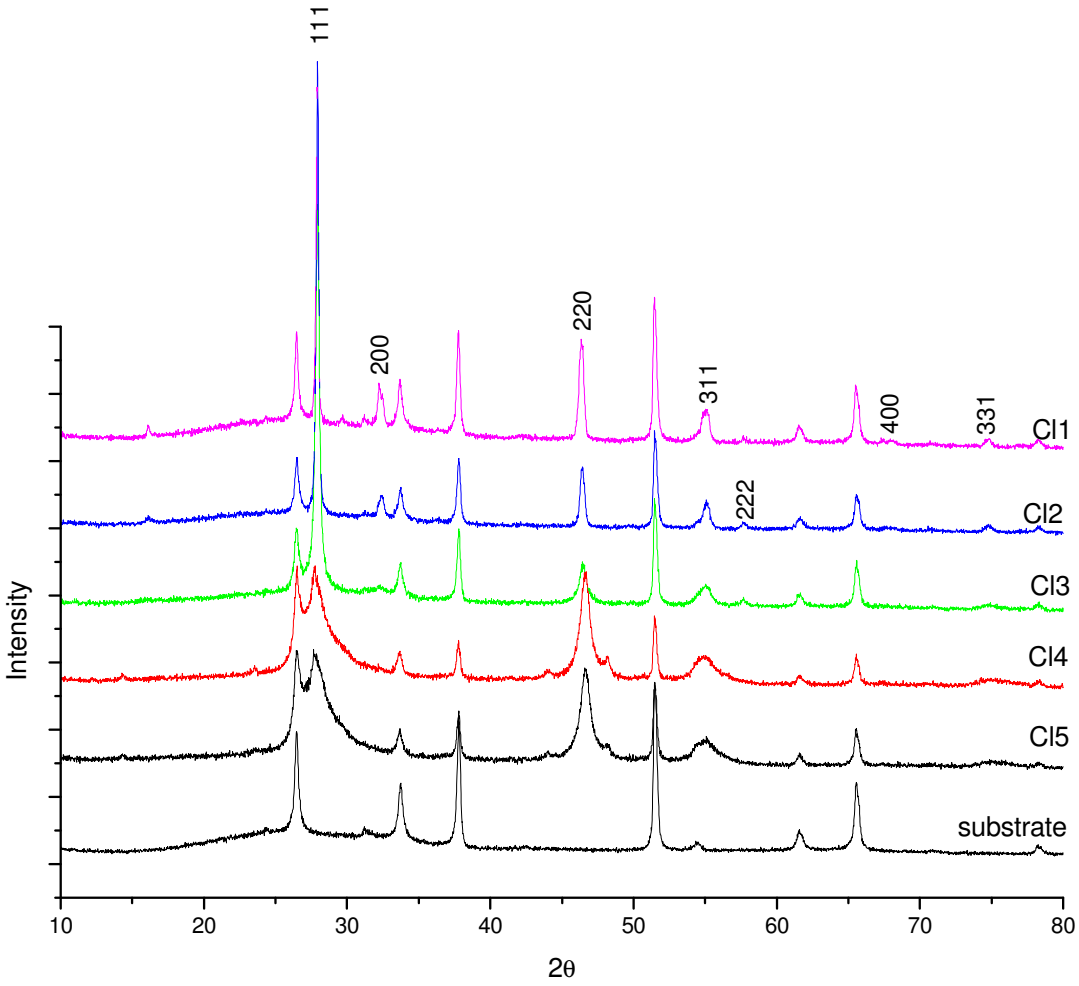

Figure 6-28: XRD analysis of the chloride samples deposited using different Cu/In molar ratios.

The films with indium rich starting solutions (Cl1 and Cl2) also show a strong preferred orientation along the (111) planes as shown in Table 6-14. The trend is reversed when the amount of indium is decreased. Samples Cl3 and Cl4 show a strong preferred orientation along the (112) plane. The order seems to change again for sample Cl5 where the I2/I1 value increases again.

Table 6-14: Chloride intensity ratios

	Intensity ratio		
Samples	*I2/I1*	*I3/I1*	*I3/I2*
Cl1	0.872	0.332	0.381
Cl2	0.963	0.344	0.357
Cl3	0.149	0.095	0.635
Cl4	0.161	0.088	0.549
Cl5	0.335	0.147	0.438
Theoretical	0.400	0.210	0.525

The sample prepared using [Cu]/[In]=1 starting solution (Cl3) doesn't show extra diffraction peaks since the solution elements are balanced. Some extra peaks are present in the diffractograms of the samples deposited using either a copper rich or indium rich starting solution. Samples Cl1 and Cl2 show extra reflections which have been attributed to the cubic $CuIn_5S_8$ compound (space group Fd-3m) as shown in Figure 6-29. $CuIn_5S_8$ exists in the pseudo-binary diagram between In_2S_3 and $CuInS_2$ (Binsma et al. 1980; Alvarez García 2002). The absence of In_xS_y phases suggests that the amount of indium is insufficient to form indium rich compounds. Samples Cl4 and Cl5 have a series of extra peaks which can be attributed to Cu_2S as shown in Figure 6-30. The number of these peaks increased between sample Cl4 and Cl5 demonstrating a clear connection with the starting solution composition. The Cu_2S phase appears and segregates on the surface of $CuInS_2$ prepared from low indium concentration solutions which is consistent with studies by other groups (Binsma et al. 1980; Dzionk et al. 1992).

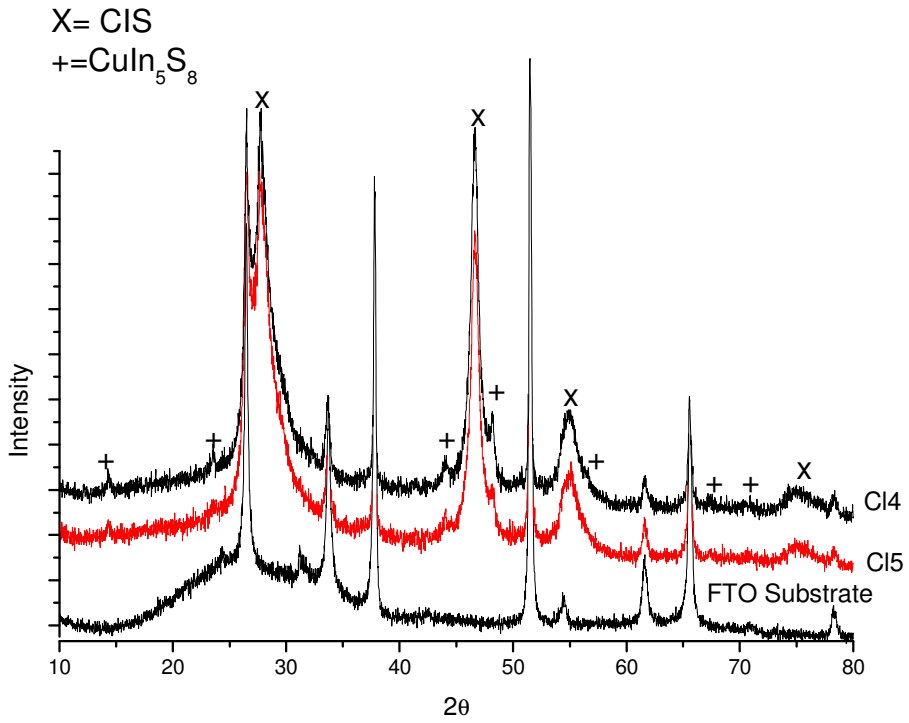

Figure 6-29: XRD of the samples Cl1 and Cl2

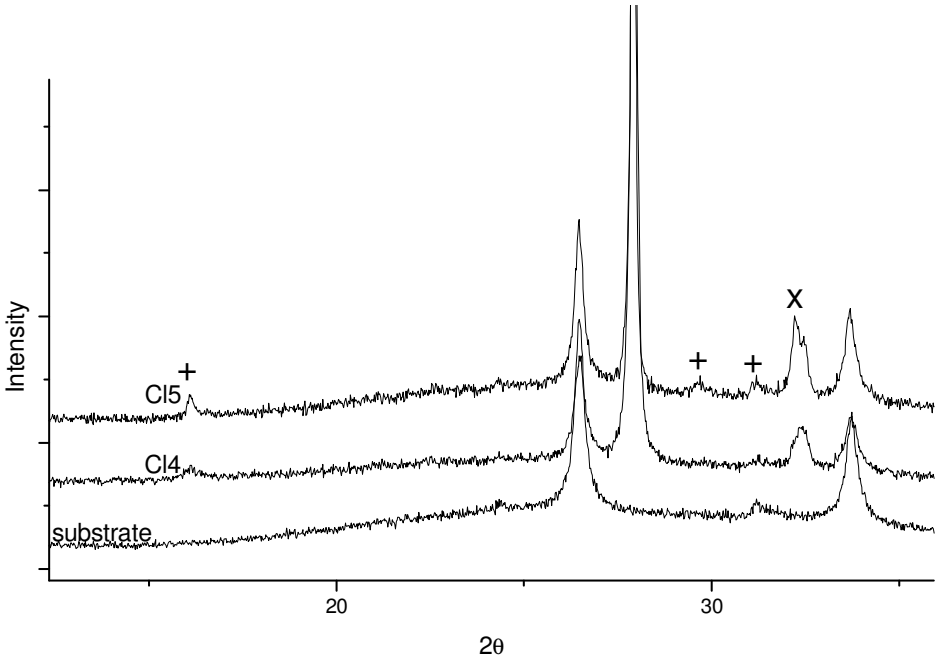

Figure 6-30:XRD of the samples Cl4 and Cl5

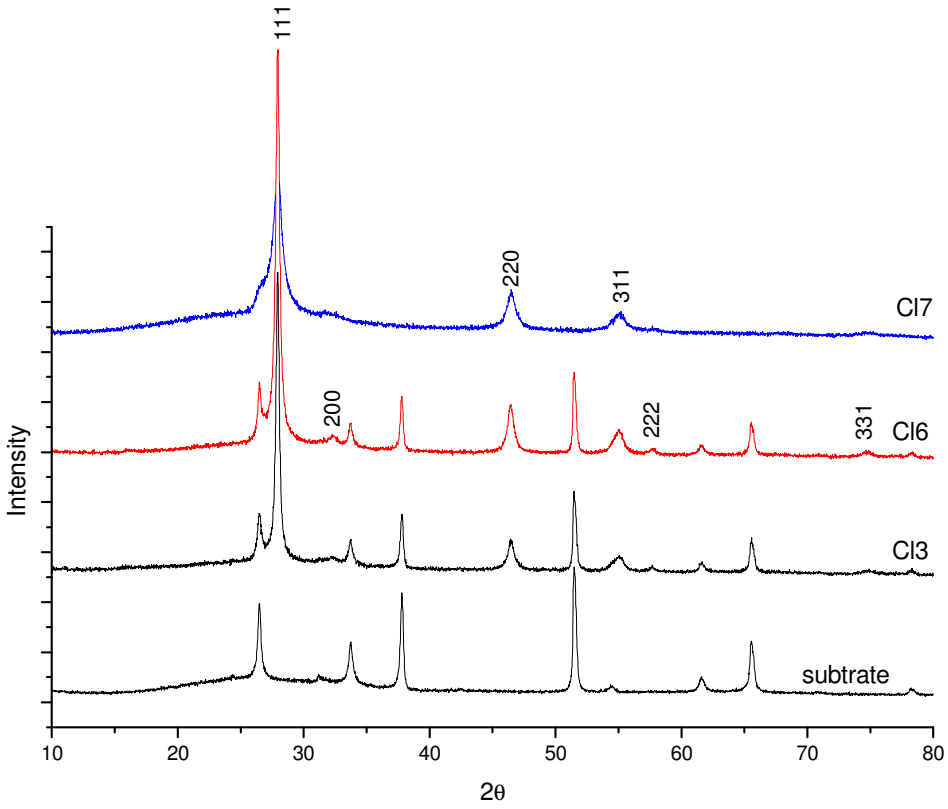

Figure 6-31: XRD of the chloride samples deposited using different S/Cu molar ratios.

XRD patterns of the samples prepared at different S/Cu molar ratios are presented in Figure 6-31. Sample Cl6 shows no peaks outside the $CuInS_2$ system. The peaks are sharp and well defined. The FTO peaks disappear in the XRD of the sample Cl7 which indicates a thicker as-deposited film which may be due to a variation in the starting solution properties leading to a change in the aerosol cone dimension or the spray properties. The results require further study.

The RBS measurements have been carried out using 1.6MeV 4He ion beam and a detector solid angle of 5 msr positioned at a back scattering angle of 170°. All samples for the RBS analysis are sprayed on silicon a substrate as stated previously.

The results of the RBS analysis of the chloride samples are summarized in Table 6-15 and Table 6-16. Samples Cl1 and Cl2 have poor adhesion to the substrate and the CIS films peel off during the analysis. Therefore the results for the Cl1 and Cl2 are unusable because they are non indicative of the real composition of the film.

Table 6-15: RBS results of Cu/In molar ratio variations on chloride as-deposited film composition

	Cu	*In*	*S*
Cl5	0.37 ± 0.02	0.10 ± 0.01	0.53 ± 0.03
Cl4	0.33 ± 0.02	0.16 ± 0.01	0.51 ± 0.03
Cl3	0.24 ± 0.02	0.23 ± 0.01	0.53 ± 0.03

Table 6-16: RBS results of Cu/In molar ratio variations on chloride as-deposited films thickness

	Thickness [µm]
Cl5	0.48 ± 0.02
Cl4	0.82 ± 0.04
Cl3	1.08 ± 0.05

The thickness of the CIS layer increases when the concentration of indium in the starting solution is increased. Since the total concentration of the starting solution is constant, the increase in thickness can be attributed to different cone spray mechanisms. The composition of the films also changes with the molar ratios. A perfect film should have an elemental percentage equal to Cu=0.25, In=0.25 and S=0.5 (because of the elemental composition of $CuInS_2$). Sample Cl5 has the highest copper rich CIS layer which agrees with the composition of the starting solution. The copper content of the film decreases when the Cu/In ratio of the solution is dropped.

The RBS measurements reveal that the samples are rough. The roughness value used to fit the RBS curve is constant for all the samples suggesting this variable is independent of the molar ratios but is connected with the deposition method.

The miniSIMS analyses of the chloride samples show similar results. The thickness of the CIS layer is based on the time required for the detection of the Sn ions from the substrate. The thickness of the layer increases with the indium concentration (Figure 6-32) as seen during the RBS analysis. The copper profile of three of the samples (Cl1, Cl3 and Cl5) is shown in Figure 6-33 where it can be seen that the sample Cl5 has a non-uniform profile. A similar trend can be observed for the variation of In (Figure 6-35) while the sulphur profile is more stable (Figure 6-34).

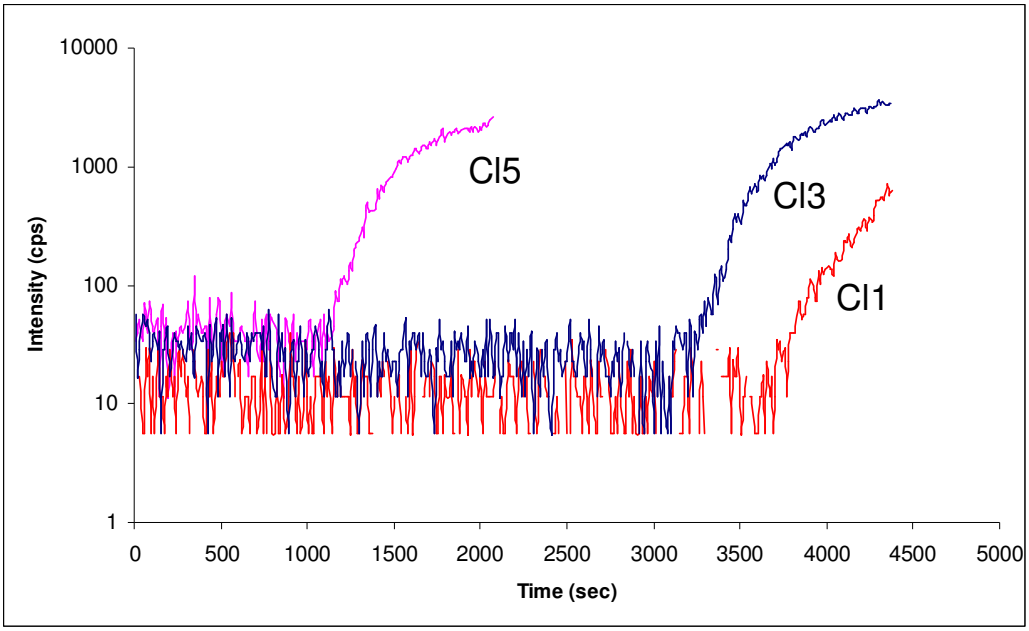

Figure 6-32: Results of miniSIMS analysis of CIS films showing the difference in film thickness for three of the samples

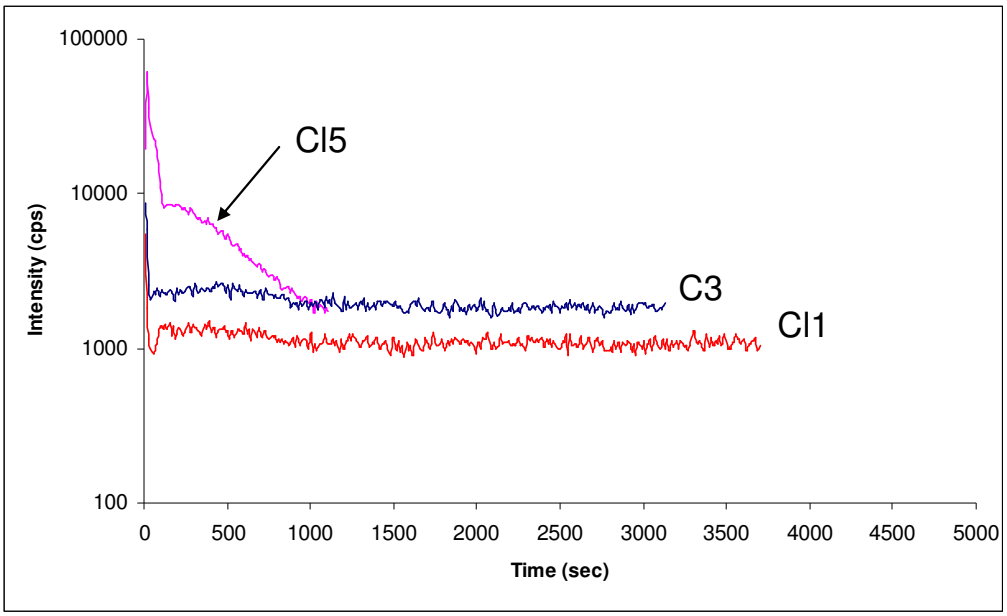

Figure 6-33: miniSIMS graph of the copper profile for the CIS-chloride samples.

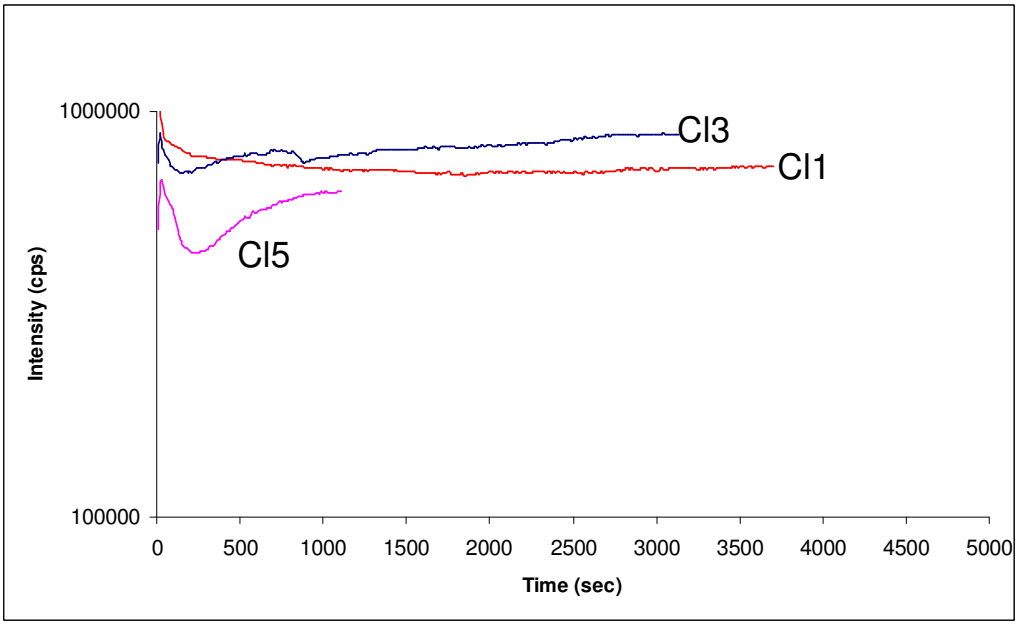

Figure 6-34: miniSIMS graph of the sulphur profile for the CIS-chloride samples

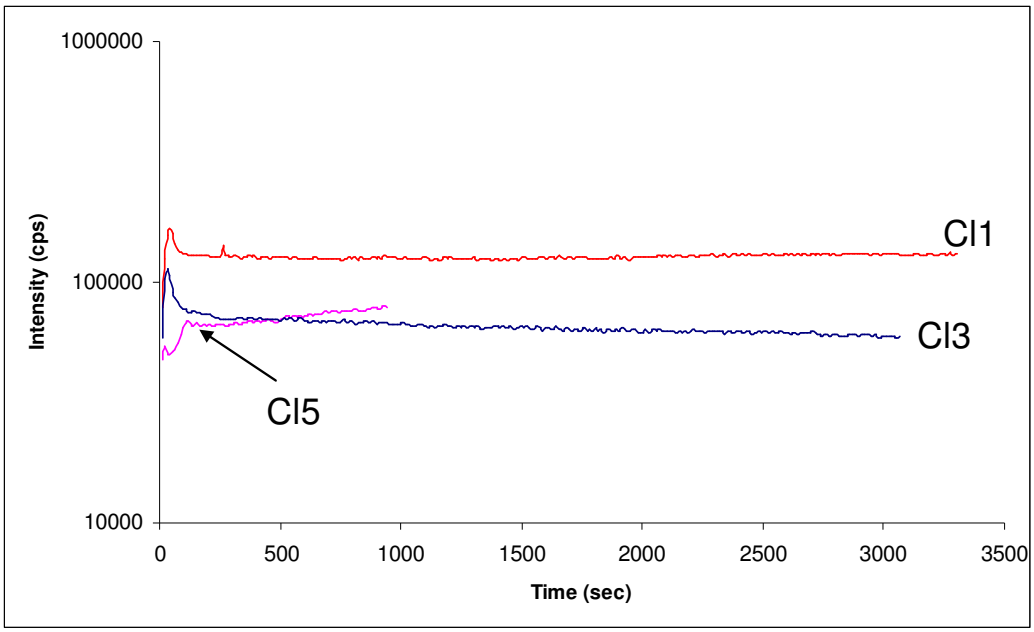

Figure 6-35: miniSIMS graph of the indium profile for the CIS-chloride samples

The compositions and the thickness of the samples prepared with different S/Cu molar ratios were analysed by RBS measurements. For the samples where the S/Cu molar ratio was altered (Cl6-Cl7), the composition is more stable than the previous samples (Cl1-Cl5). A reduction of the thickness is observed when the sulphur concentration is increased. This could be dependent on a variation of the properties of the starting solution. These results are summarised in Table 6-17 and Table 6-18.

Table 6-17: RBS results of S/Cu molar ratio variations on chloride as-deposited film composition

Sample	*Cu*	*In*	*S*
Cl3	0.24 ±0.01	0.23 ± 0.01	0.53 ± 0.03
Cl6	0.26 ± 0.01	0.23 ± 0.01	0.51± 0.03
Cl7	0.24 ± 0.01	0.25 ± 0.01	0.51± 0.03

Table 6-18: RBS results of S/Cu molar ratio variations on chloride as-deposited film thickness

Sample	*Thickness [µm]*
Cl3	1.089 ± 0.054
Cl6	1.072 ± 0.054
Cl7	0.732 ± 0.037

The miniSIMS spectra of the sample Cl7 is compared with Cl3. The profile of the copper and sulphur are similar for both the samples (Figure 6-36 and Figure 6-37) and same trend is observed for the indium.

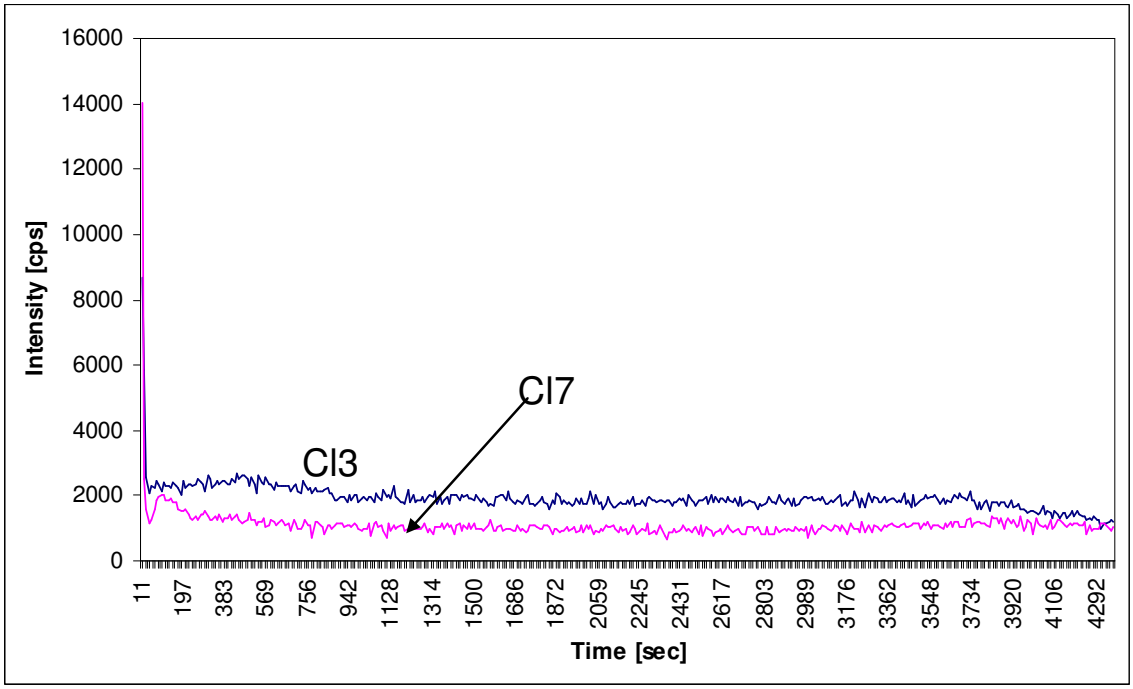

Figure 6-36: miniSIMS profile of the Cu for the samples Cl7 and Cl3

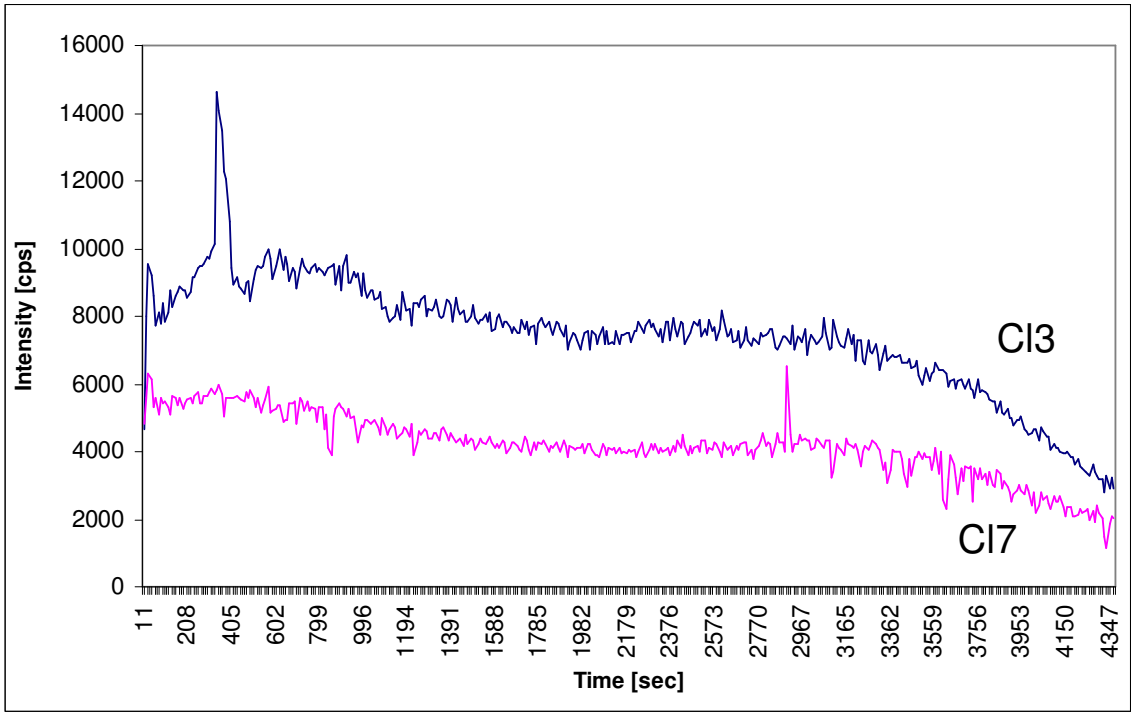

Figure 6-37: miniSIMS profile of the S for the samples Cl7 and Cl3

The photo-voltammetry analyses have been performed using the standard set-up as described in section 3.3.2.

The photovoltammetry of the chloride as-deposited films shows that only samples Cl2 and Cl3 have photo-responsive behaviour (as shown in Figure 6-38). The samples have a cathodic response suggesting that they are p-type materials. The Cl3 sample has a better response than the Cl2 sample. The level of response is correlated with the area under the peaks. The dark current (sample Cl2) appears around -0.55V suggesting a reduction of the elements (copper or indium) of the CIS layer around this voltage.

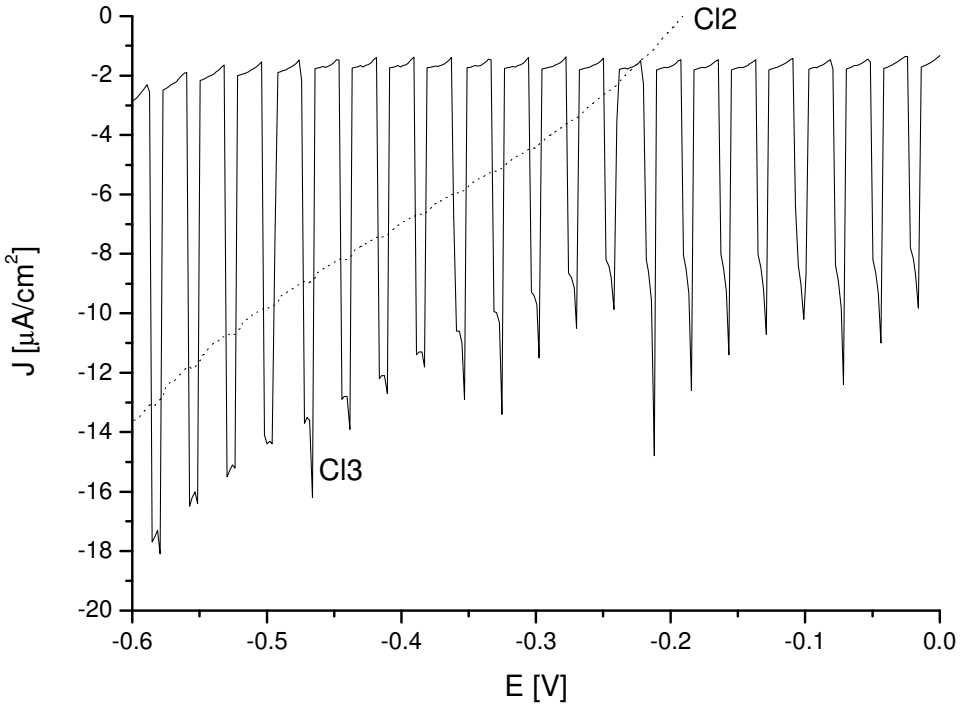

Figure 6-38 – Results of the photovoltammetry analysis of the Cl3 (—) and Cl2 (---) samples

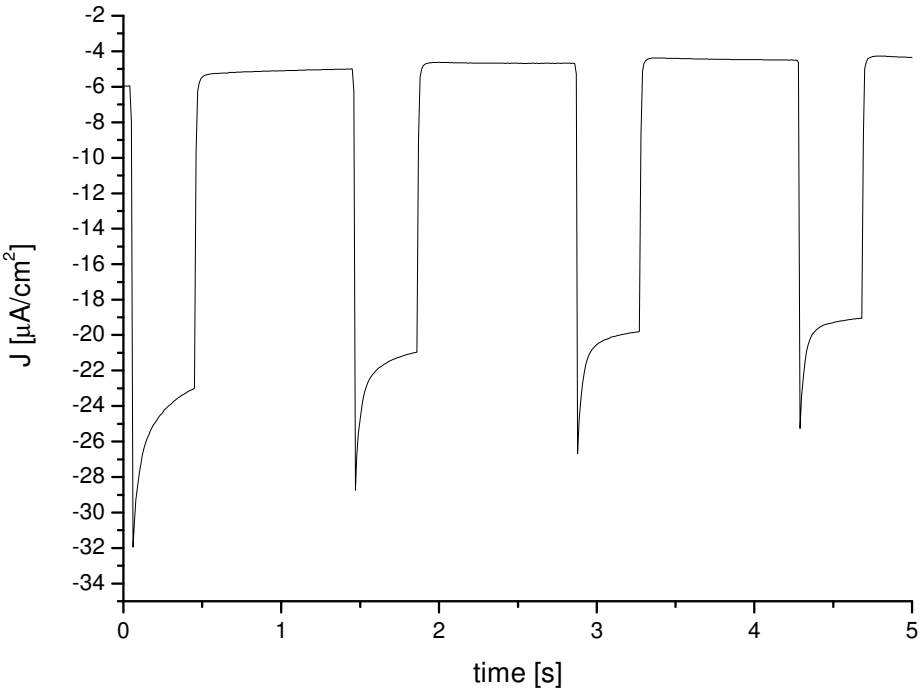

Figure 6-39 - Photocurrent transient response of sample Cl3 collected at E= -0.3V

The photocurrent response of sample Cl3 was also recorded by fixing the potential at E=-0.3V as shown in Figure 6-39. The sample has a negative current spike photo-response which it is thought is caused by the release of electrons trapped on the surface defects of the CIS layer. This causes a small current when the illumination is interrupted producing the characteristic spike-shape curve observed.

6.3.2. Nitrate samples

The nitrate sample deposited at low indium concentration (N5) exhibited poor adhesion with the FTO substrate and the film peeled off easily. The XRD pattern from sample N4 has low intensity and broad peaks but extra-phases are not detected in the diffractogram probably because the peaks of the impurities are covered by the broad CIS peaks as shown in Figure 6-40 where the Cl4 and N4 samples are compared. Samples N1, N2 and N3 are similar to the sister chloride samples (Cl1, Cl2 and Cl3). Samples N1 and N2 show the same extra peaks observed in the Cl1 and Cl2 diffractograms. The sample N3 shows no impurity reflections as seen for the sample Cl3.

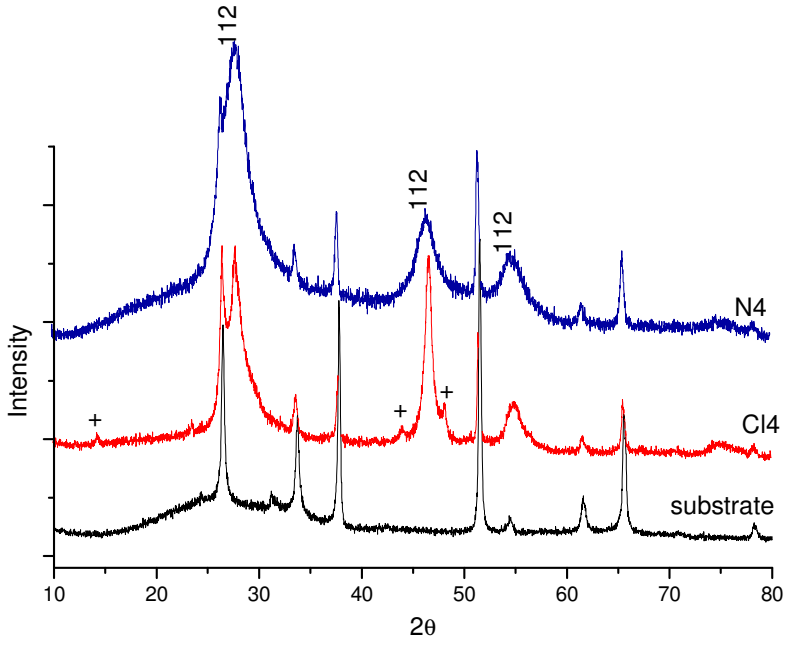

Figure 6-40: XRD of the samples N4 and Cl4

The RBS results of the nitrate samples analysis are summarized in Tables 6-19 to 6-22. The RBS of the nitrate samples shows that the as-deposited films are very rough.

Samples N1, N2 and N3 have similar compositions and thicknesses to each other suggesting that the as-deposited films are not sensitive to the [Cu]/[In] variations. Samples N4 and N5 have the same composition and thickness as the choride samples (Cl4 and Cl5) indicating that the molar ratio has a strong effect on the as-deposited films and it is more important than the type of starting solution used.

Table 6-19: RBS results of Cu/In molar ratio variations on nitrate as-deposited film composition

	Cu	In	S
N5	0.37 ± 0.02	0.10 ± 0.01	0.53 ± 0.03
N4	0.33 ± 0.02	0.16 ± 0.01	0.51 ± 0.03
N3	0.24 ± 0.01	0.23 ± 0.01	0.53 ± 0.03
N2	0.25 ± 0.01	0.23 ± 0.01	0.52 ± 0.03
N1	0.23 ± 0.01	0.23 ± 0.01	0.54 ± 0.03

Table 6-20: RBS results of Cu/In molar ratio variations on nitrate as-deposited film thickness

	Thickness [µm]
N5	0.482 ± 0.024
N4	0.822 ± 0.041
N3	1.089 ± 0.054
N2	0.893 ± 0.045
N1	1.250 ± 0.063

Table 6-21: RBS results of S/Cu molar ratio variations on nitrate as-deposited film composition

	Cu	In	S
N7	0.28 ± 0.01	0.25 ± 0.01	0.47 ± 0.02
N6	0.28 ± 0.01	0.24 ± 0.01	0.48 ± 0.02
N3	0.24 ± 0.01	0.23 ± 0.01	0.53 ± 0.03

Table 6-22: RBS results of S/Cu molar ratio variations on nitrate as-deposited film thickness

	Thickness [µm]
N7	0.536 ± 0.027
N6	0.554 ± 0.028
N3	1.089 ± 0.054

The nitrate samples show no photo-response and the cause could be attributed to the extra phases observed in the XRD analysis and the surface defects (i.e. pinholes) observed during the RBS tests.

6.3.3. Summary

The potential of the ESD was that by altering the starting solution composition, the properties of the as-deposited films could be refined and optimized. However it was found that the potential variation in the solution was limited.
PIV analysis of the aerosol cone reveals that chloride starting solution result in a more stable cone than the nitrate starting solution, the result of this is that chloride films are more uniform and crystalline than nitrate samples

The XRD analysis of the nitrate and chloride samples reveal that the starting solution molar ratio had a significant effect on the shape/intensity of the diffractogram peaks and the number of impurities present in the films.

The photo-chemical analyses of the samples reveal that the nitrate starting solution results in no-response films.

The precipitate (only observed in chloride solutions when the S/Cu molar ratio was less than five) is an intermetallic compound formed by copper, thiourea and chloride. It was found to be formed by the reduction of copper and oxidation of thiourea. The precipitate is thought to contain two isomers one of which is thought to be amorphous.

The photo-chemical analysis of the sample reveals that the nitrate starting solution results in non photoresponse films.

The best photoresponse from the as-deposited layer was achieved for a [S]/[Cu]=5 and [Cu]/[In]=1.

Chapter 7:

Window Layer

The deposition of metallic sulphide films has attracted the attentions of the scientific community due to their potential applications in fields such as photovoltaic components, sensors, photodiodes, etc. Within the "family" of metal sulphide compounds, ZnS and CdS have been subjected to more attention than the others because of the properties which were explained previously.

The aim of the study presented below is to deposit high quality ZnS films by ESD for use in solar cell devices.

The effect of different deposition conditions on the properties of the as-deposited films will be analysed along with the effect of different S/Zn starting solution molar ratios.

7.1. ZnS deposition

The starting solutions were prepared by mixing $ZnCl_2$ solution (1M) and thiourea solution (0.5M) ((Dedova et al. 2005). Ethanol (99.99%, Fisher Scientific) was added to reduce the surface tension and obtain a final solution concentration of 0.21M.

During the experiment, the solution concentration was held constant while the [S]/[Zn] molar ratio was varied between 0.5 and 3. The deposition temperature, applied voltage and flow rate were also varied.

All samples in this study were deposited onto SnO_2:F coated glass substrates of 1.8mm x 30mm x 10mm in thickness, length and depth respectively.

In the first part of the study the effects of different deposition conditions (temperature, applied voltage and flow rate) were investigated for a fixed starting solution composition of [S]/[Zn]=2.

In the second part of the study, the effect of different starting solution compositions ([S]/[Zn]=1;0.5;3) was investigated by fixing some of the deposition conditions (applied voltage and temperature) based on the results of the first study.

7.1.1. Deposition conditions

Deposition conditions used during the first study are summarised in Table 7-1.

.

The XRD of the as-deposited films reveals that all the samples deposited during this study show the three main peaks of ZnS ((111), (220) and (311) planes). The films grow with a cubic structure (sphalerite, space group = F-43 (N°216)) and the results also show that no extra phases were detected.

Table 7-1: Deposition conditions used during the first part of the metallic sulphide study.

[S]/[Zn]	*Deposition temperature [℃]*	*Voltage [kV]*	*Flow [µl/min]*	*Sample*
2	500	18	100	ZS1
			200	ZS 2
			50	ZS 3
2	500	22	100	ZS4
			200	ZS5
			50	ZS6
2	500	16	100	ZS7
			200	ZS8
			50	ZS9
2	450	18	100	ZS10
			200	ZS11
			50	ZS12
2	450	22	100	ZS13
			200	ZS14
			50	ZS15
2	450	16	100	ZS16
			200	ZS17
			50	ZS18
2	380	18	100	ZS19
			200	ZS20
			50	ZS21
2	380	22	100	ZS22
			200	ZS23
			50	ZS24
2	380	16	100	ZS25
			200	ZS26
			50	ZS27

The XRD analysis of the samples deposited at high temperature (500°C and 450°C) show a strong intense peak at 2θ=28.6 (111). The intensity reaches a maximum for the samples deposited at higher temperature (450°C and 500°C), high voltage (22kV) and low flow rate (50µl/min). This could suggest that the samples deposited in these conditions have a strong

preferred orientation along the (111) plane. To evaluate the preferred orientation of the as-deposited films, the intensity ratios (called I(1)/I(2)) of the (111) (2θ=28.6) and (220) (2θ=47.8) ZnS peaks and the intensity ratios (called I(1)/I(3)) of the (111) (2θ=28.6) and (311) (2θ=56.6) peaks were calculated for each of the samples and for the reference value (from PDF 7-566)). The intensity ratio (I(2)/I(3)) was also calculated for samples and for the reference diffractogram.

The [I(1)/I(2) experimental/I(1)/I(2)reference] for all the samples are plotted in Figure 7-1 whilst [(I(1)/I(3))experimental/(I(1)/I(3))reference] and [(I(2)/I(3))experimental/(I(2)/I(3))reference] are plotted in Figure 7-2 and Figure 7-3 .

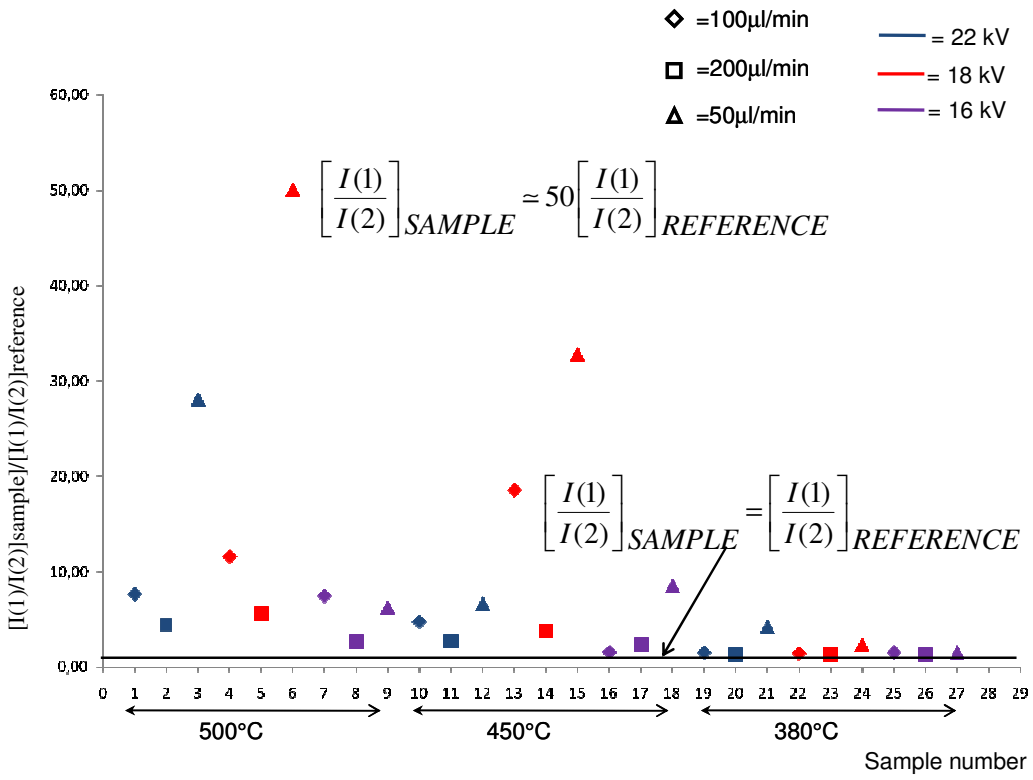

Figure 7-1: [I(1)/I(2)]sample]/[I(1)/I(2)reference] is plotted for each sample

All the samples deposited at 500°C and 450°C show a varying degree of preferred orientation. The maximum values are reached for the samples deposited at high voltage (22kV) and low flow rate (50µl/min).

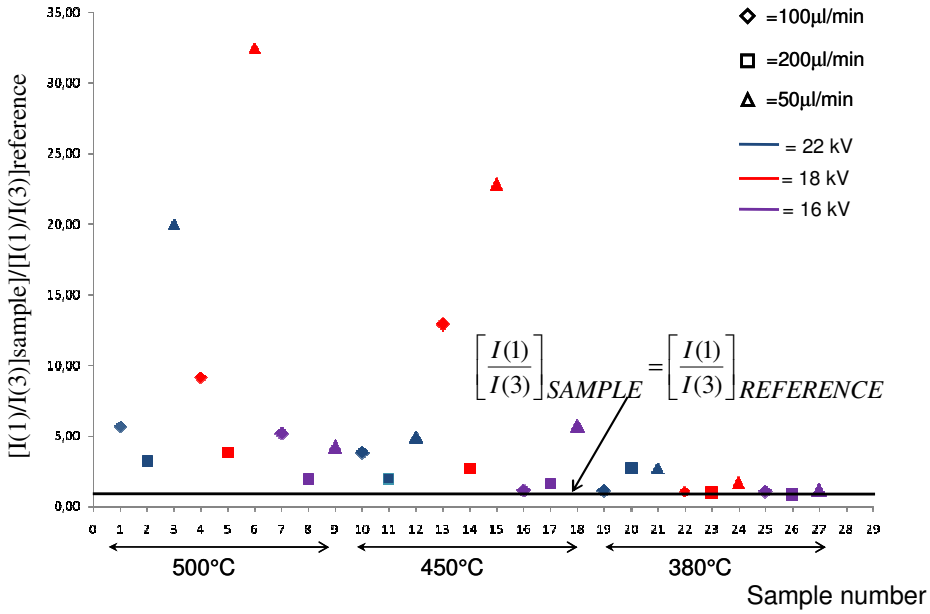

Figure 7-2: [I(1)/I(3)]sample]/[I(1)/I(3)reference] is plotted for each sample

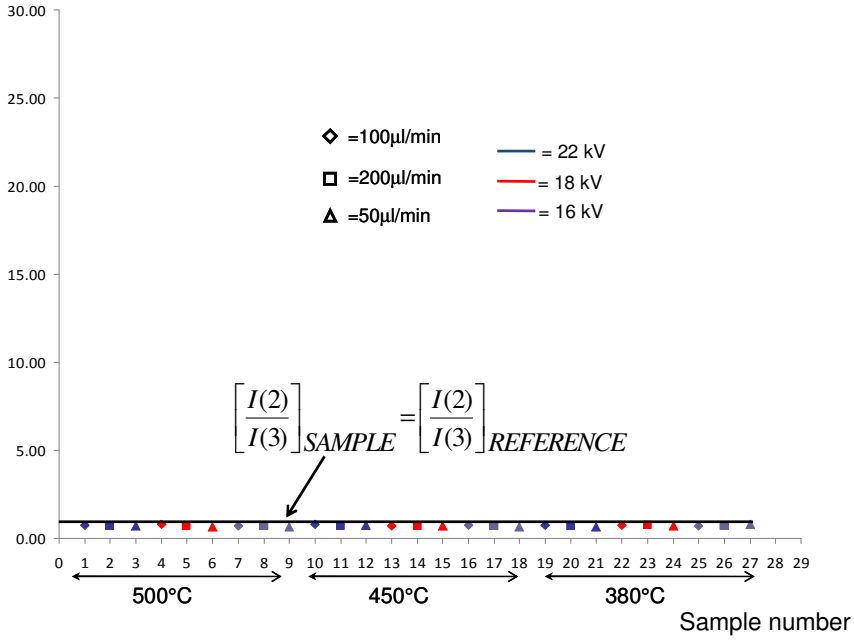

Figure 7-3: [I(2)/I(3)]sample]/[I(2)/I(3)reference] is plotted for each sample

As seen for the I(1)/I(2) ratio, the intensity ratio I(1)/I(3) of samples deposited at high temperature and high voltage is higher than that calculated for the theoretical diffractogram.

The intensity ratio (I2)/I(3) of the sample is almost equal to the intensity ratio calculated (solid horizontal line in Figure 7-1, Figure 7-2 and Figure 7-3).
From the analysis of the results presented in Figure 7-1, Figure 7-2 and Figure 7-3 it is possible to calculate that the samples deposited at high temperature, high voltage and low flow rate show a preferred orientation along the (111) plane. The (111) plane is the most dense of the cubic structure and thus we can assume that the samples deposited in these conditions tend to grow parallel to the substrate and along the highest atomic dense plane (Nakanishi et al. 1990; Blackmore et al. 1991)

Temperature

The XRD of samples deposited at different deposition temperatures are shown in Figure 7-4, Figure 7-5 and Figure 7-6. The samples deposited at low temperature (380^{o}C) have broad peaks indicating poor crystallinity. This trend is observed for all the samples (deposited at this temperature) independent of the other deposition conditions such as applied voltage.

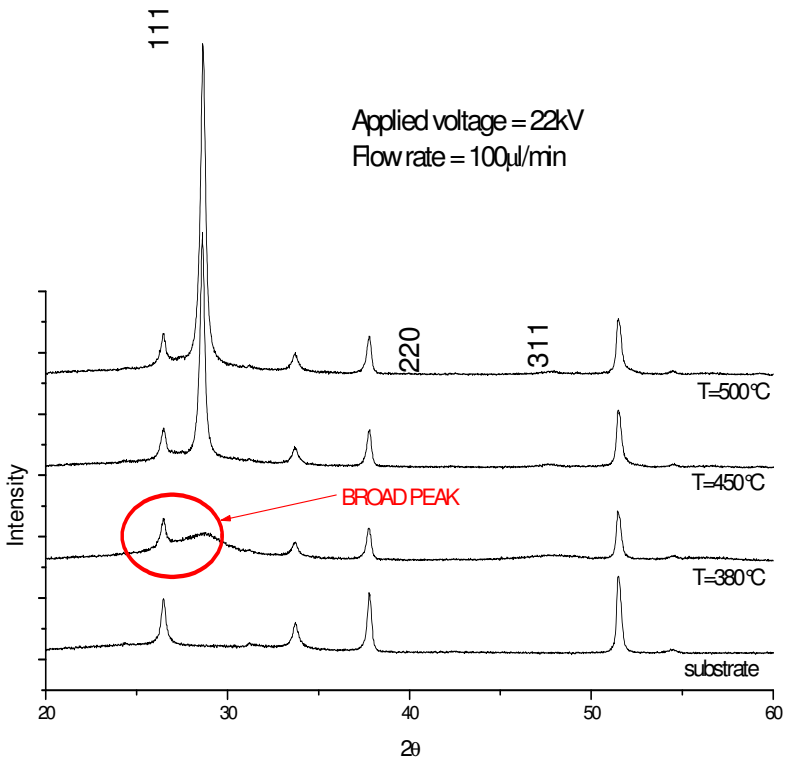

Figure 7-4: XRD of the samples deposited at 22kV, 100µl/min and different temperatures

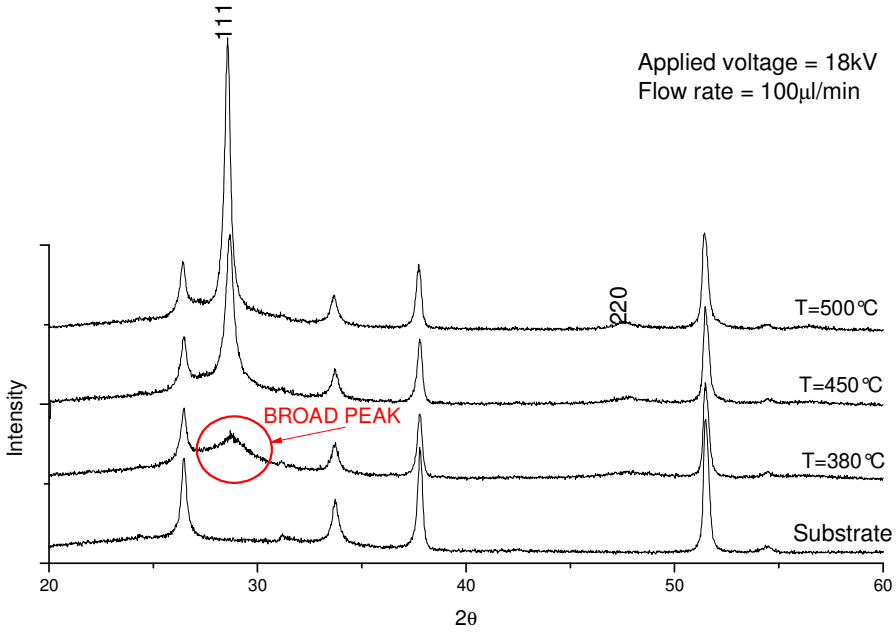

Figure 7-5: XRD of the samples deposited at 18kV, 100µl/min and different temperatures

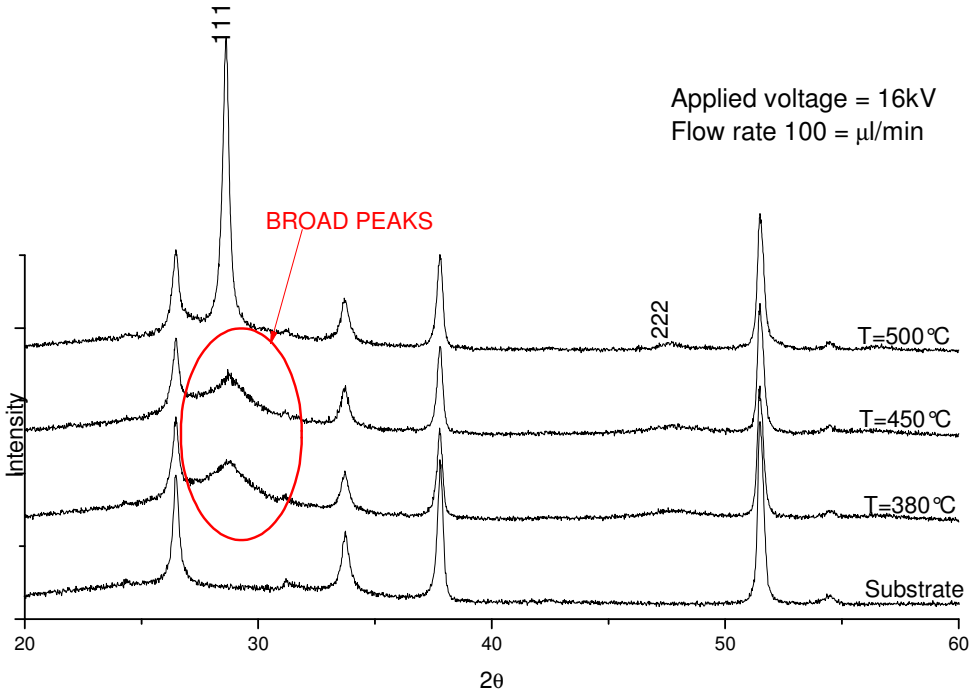

Figure 7-6: XRD of the samples deposited at 16kV, 100µl/min and different temperatures

Figure 7-7 shows the trend in the (111) peak intensity as a function of temperature and Figure 7-8 shows the corresponding FWHM trend. The curves show how the intensity of the peaks decreases while the FWHM increases as the deposition temperature is reduced (T = 380°C) suggesting a low quality material is deposited at 380°C (Afifi et al. 1995). These observations are more evident for the samples deposited at low voltage (16kV). In this case (Figure 7-6), the sample deposited at 450°C show this broad peak together with the sample deposited at 380°C. Temperature controls the dimension of the droplets and also the growth process as previously described (section 2.1.3). At low temperature the solvent doesn't evaporate before reaching the substrates and thus large droplets impinge on the substrate where they dry. Temperature also controls the growth of the film because it gives energy to the atoms or molecules to move and find the lower energy positions and thus to improve the crystallisation process. These results are in agreement with some results published in literature (Elidrissi et al. 2001).

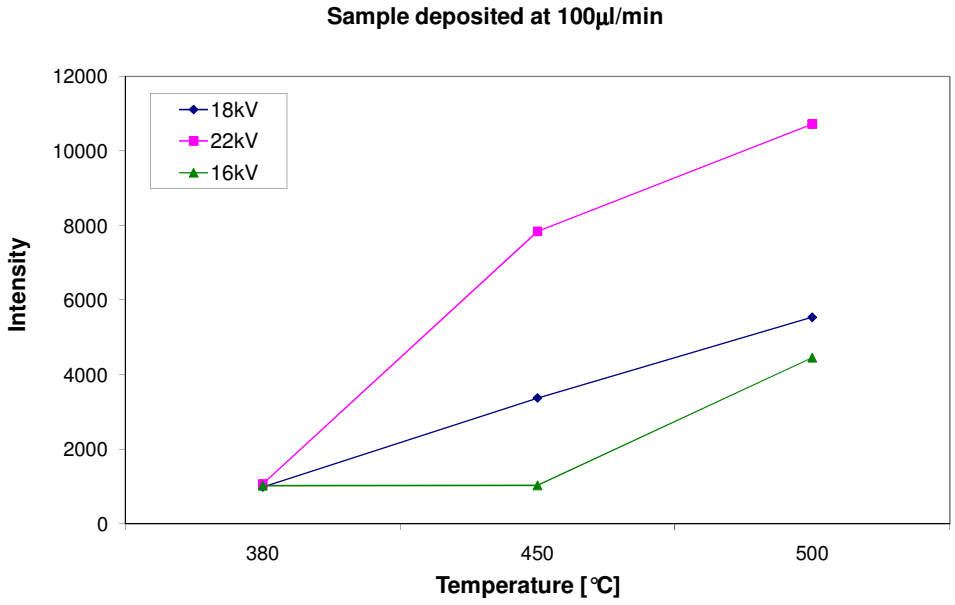

Figure 7-7: Variation of the (111) peak intensity of the samples deposited at 100µl/min versus the deposition temperature

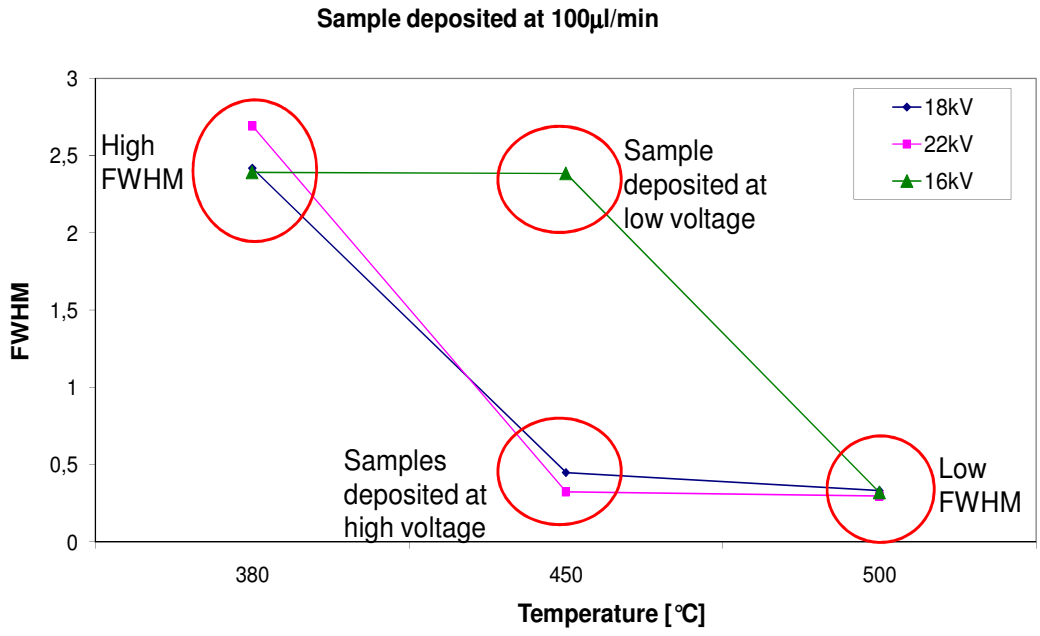

Figure 7-8: Variation of the (111) peak FWHM for the samples deposited at 100µl/min versus the deposition temperature

The quality of the films, as indicated by crystallinity, is reflected in the electrical properties as confirmed by EQE measurements. These measurements were carried out using the standard three electrode set up (section 3.3.2) and 0.5M solution of Na_2S. Only the samples deposited at high temperature (T=500°C) show a photocurrent response suggesting better quality films. All the samples deposited at lower temperature are not photoactive.

Voltage

The effect of the applied voltage is dependent upon the deposition temperature. At high temperature (T=500°C), a reduction of the applied voltage reduces the value of the peak (111) intensity of the ZnS (Figure 7-9) and the preferred orientation along the (111) plane as shown in Figure 7-10. These variations are independent of the thickness of the films because the intensity of the substrate peaks remains constant for all the samples.

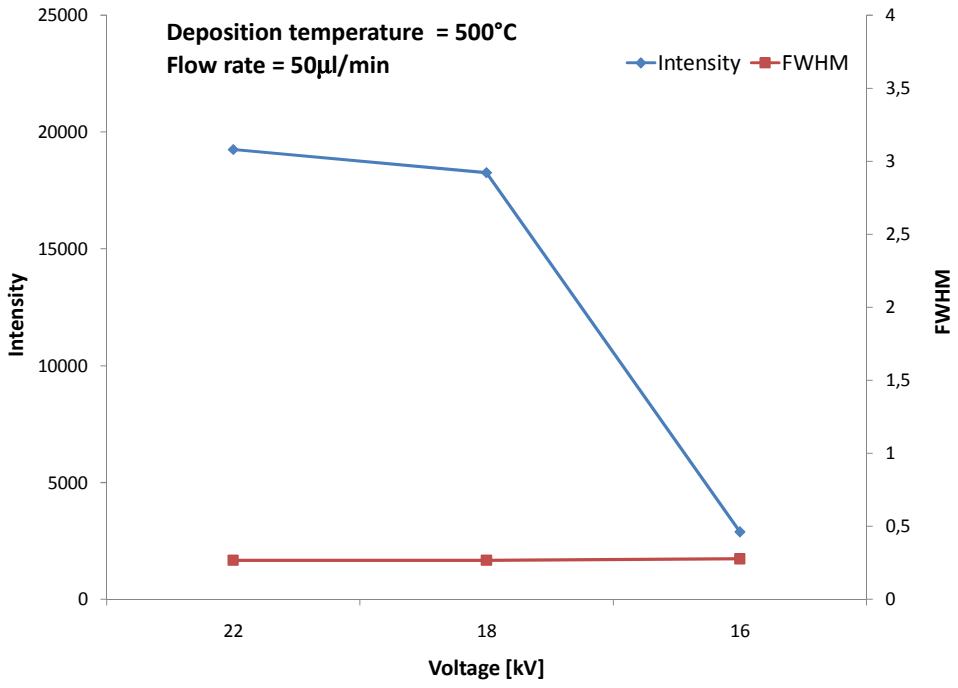

Figure 7-9: Effect of different deposition temperatures on the intensity and FWHM of the first ZnS peaks

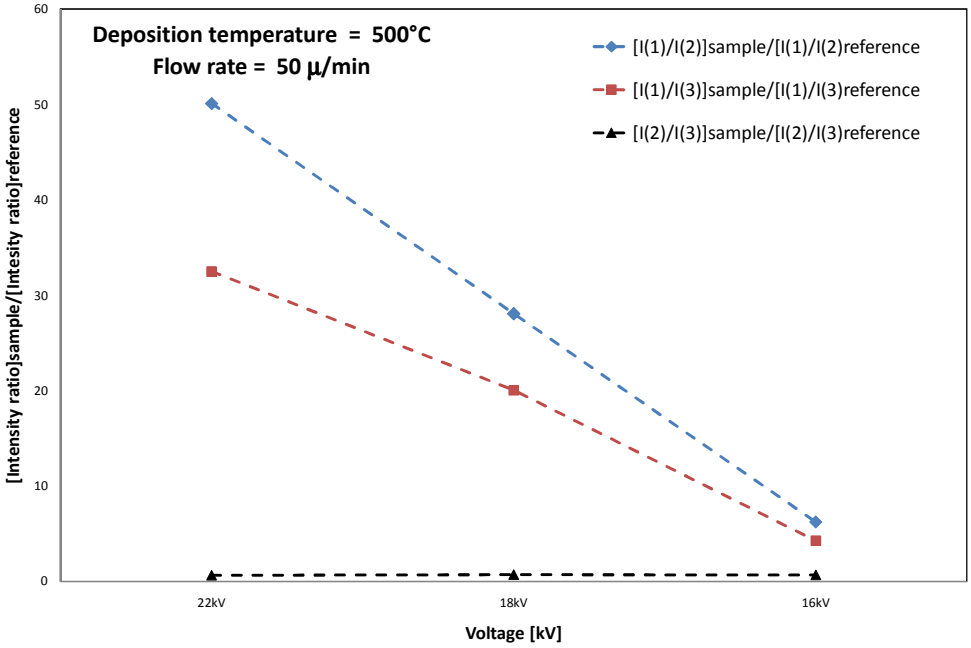

Figure 7-10: Variation of the [Intensity ratio]$_{sample}$/[Intensity ratio]$_{reference}$ ratio with the applied voltage

At the lower temperature (T=380°C) the peaks are broad and the intensity is low irrespective of the applied voltage (Figure 7-11). This is typical of poor quality films.

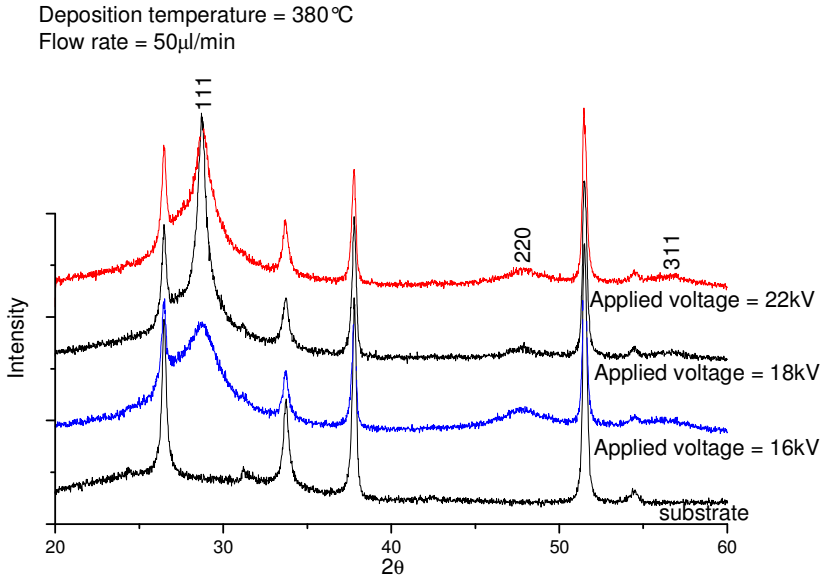

Figure 7-11: XRD of the samples deposited at 380°C and 50µl/min at different applied voltages.

All the samples deposited at high voltage (18 and 22kV) and high temperature (T=500°C) are photoactive while, among the samples deposited at 16kV, only ZS9 shows any photoactivity. In Figure 7-12 the effect of the applied voltage on the samples ZS3, ZS6 and ZS9 is shown. Samples ZS3 and ZS6 (deposited at 18kV and 22 kV respectively) show similar photocurrent responses (which is given by the area under the peaks) but sample ZS3 shows a strong dark current (causing the upward curve in the data) indicating either an alteration of the film or the film was pinholed (Morrison 1980). Similar trends are seen for samples deposited at different flow rates. These results confirm what was seen during the XRD analysis. The samples deposited at high voltage have better electrical-optical response than the samples deposited at low voltage.

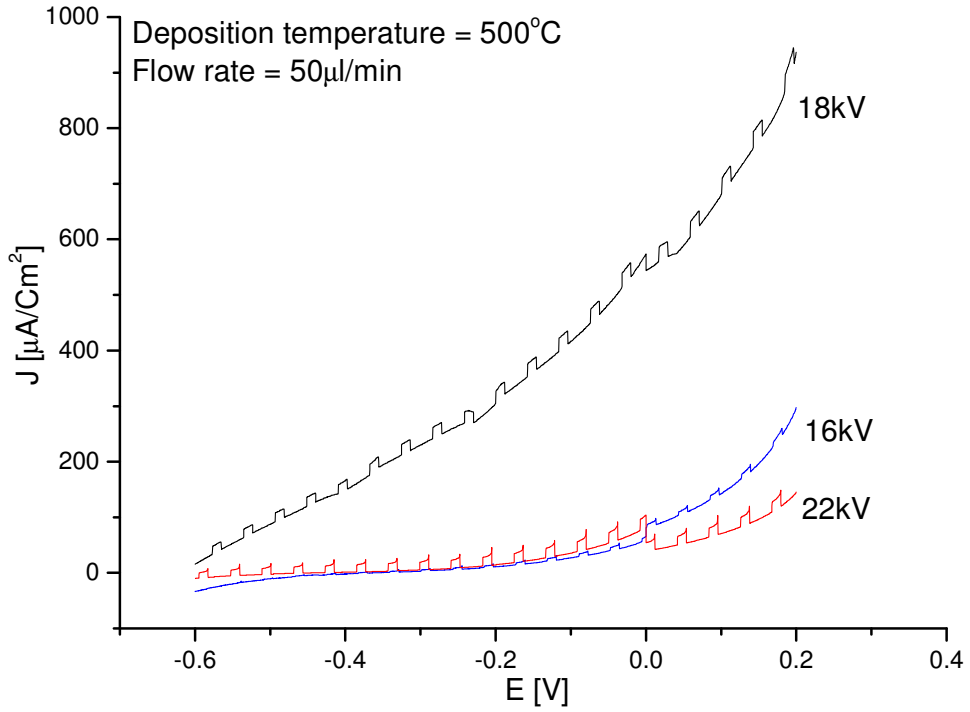

Figure 7-12: Photo-voltammetry of the samples deposited at different voltages (ZS3=18kV; ZS6=22kV; ZS9=16kV)

Flow rate

The effect of the flow rate depends on the deposition temperature and applied voltage. Diffractograms of the samples deposited at different flow rates show a decrease in the peak intensities and, in some circumstances, a variation of the shape of the ZnS peaks is observed. At high deposition temperature (500°C) and applied voltage (22kV), the intensity of the (111) peak decreases (while the FWHM increases) when the flow rate is increased (Figure 7-13). Similarity the preferred orientation decreases (Figure 7-14) as the flow rate increases. At low voltage (16kV), the sample deposited at 200µl/min seems to be less crystalline as seen during the variation of the applied voltage analysis (Figure 7-15). This agrees with the uniformity test results.

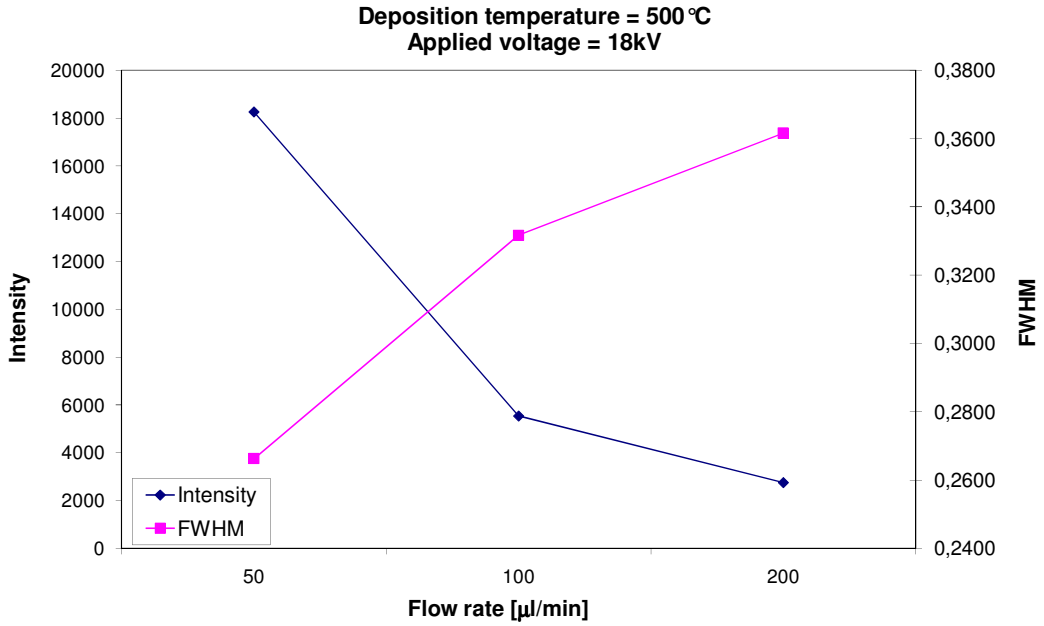

Figure 7-13: Variation of Intensity and FWHM of first ZnS peak with the flow rate

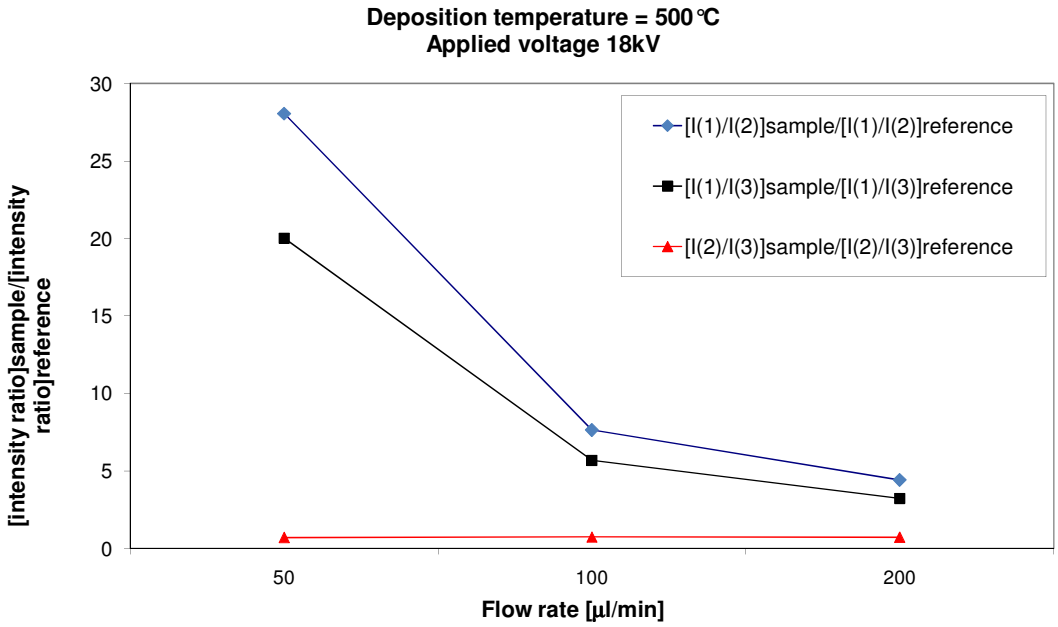

Figure 7-14: variation of [Intensity ratios]sample/[Intensity ratio]reference with the flow rate

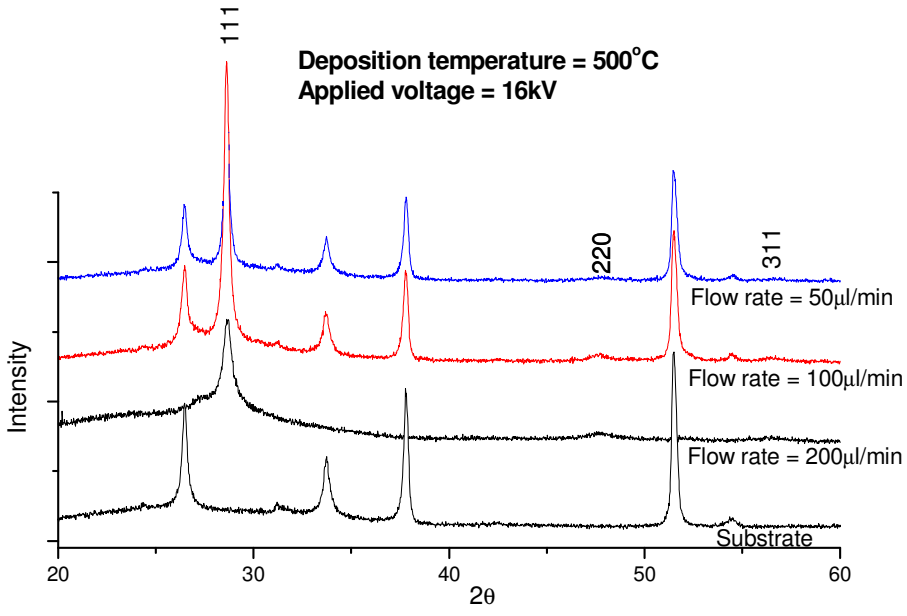

Figure 7-15: XRD of the ZnS samples deposited at different flow rates

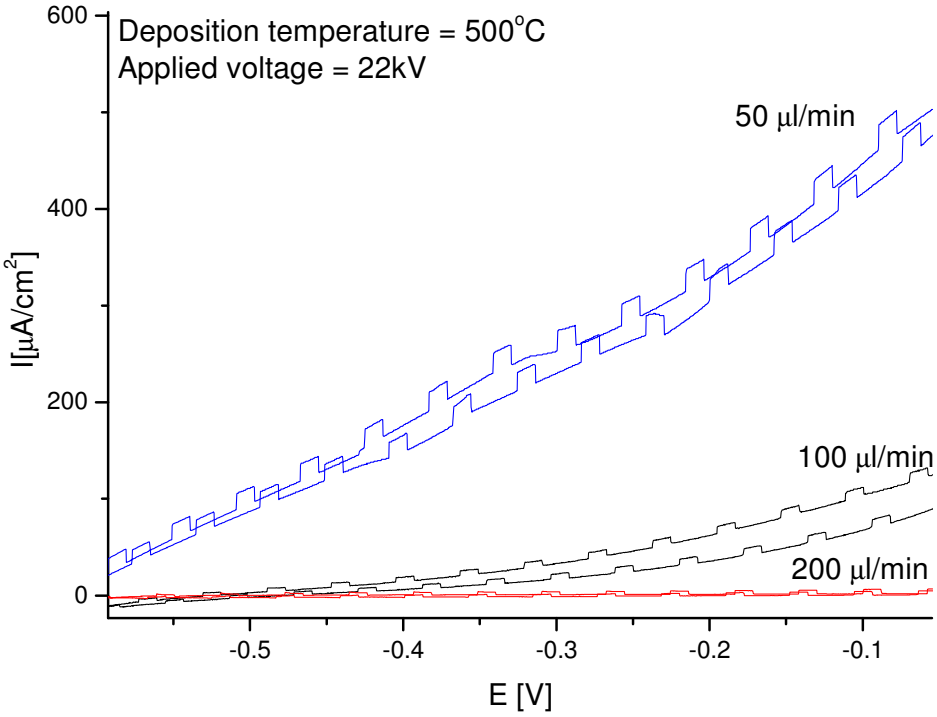

Figure 7-16: Photo-voltammograms of the samples deposited at different flow rate

An analysis of the variation of the photocurrent response with the flow rate can be done only for the samples deposited at high voltage (18 and 22kV). As seen previously the samples deposited at low voltage are not photoactive.

The samples deposited at low flow rate (50µl/min) show better photocurrent behaviour while this response decreases when the flow rate is increased (Figure 7-16). This is connected with the growth rate of the samples. At low flow, the film grows slowly and thus has fewer defects and so has a better response. This is in perfect agreement with the results obtained from the uniformity test.

Solution composition

The deposition conditions used during this study are summarised in Table 7-2.

Table 7-2: Deposition conditions used during the second part of the study.

[S]/[Zn]	*Deposition temperature[°C]*	*Voltage [kV]*	*Flow rate [µl/min]*	*Sample*
1	500	22	100	ZS 28
			200	ZS 29
			50	ZS 30
0.5	500	22	100	ZS31
			200	ZS 32
			50	ZS 33
3	500	22	100	ZS 34
			200	ZS 35
			50	ZS 36

All the samples deposited using different starting solution compositions and flow rates show the ZnS peaks with a strong preferred orientation along the (111) plane as was seen above.

Interestingly the results obtained during the photovoltammetry analysis show the effect of the flow rate to be more evident. Figure 7-17, Figure 7-18 and Figure 7-19 show the photovoltammetry analysis of the samples deposited from starting solutions with different S/Zn molar ratios.

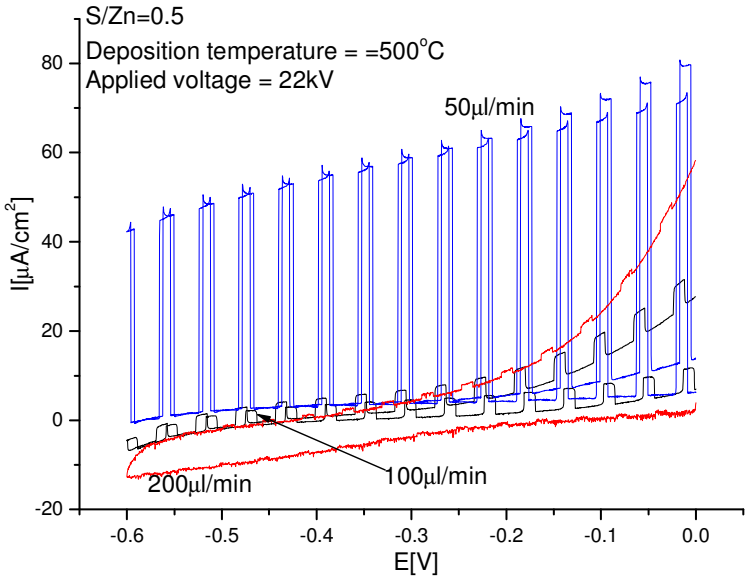

Figure 7-17: Photo-voltammetry of the samples deposited at 500°C, 22kV and using S/Zn=0.5 molar ratios.

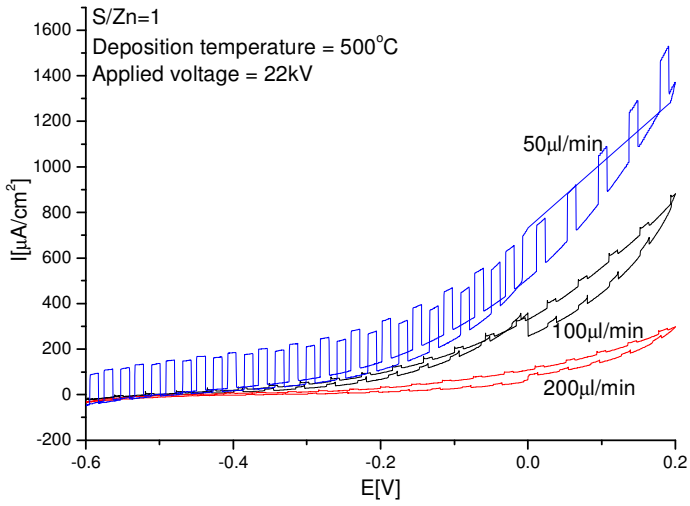

Figure 7-18: Photo-voltammetry of the samples deposited at 500°C, 22kV and using S/Zn=1 molar ratios.

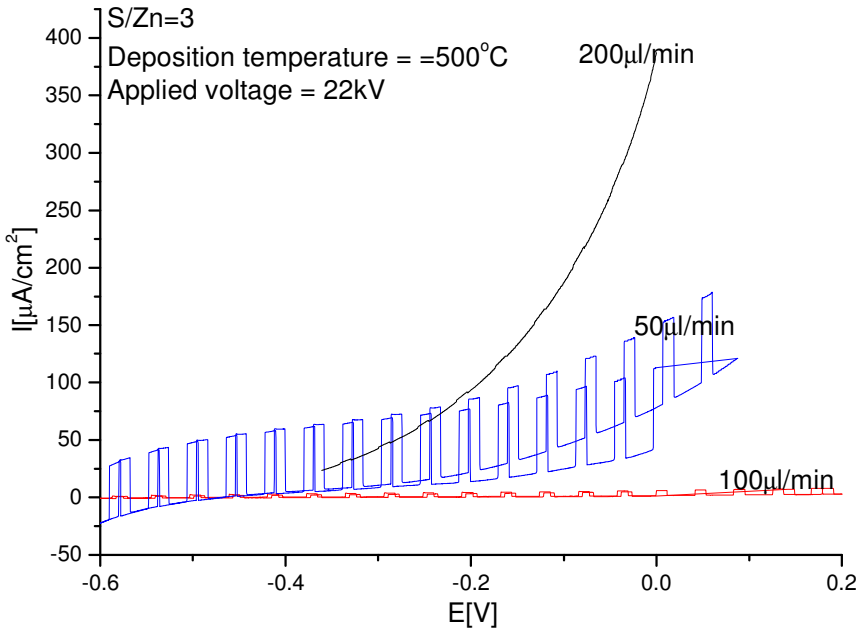

Figure 7-19: Photo-voltammetry of the samples deposited at 500°C, 22kV and using a S/Zn=3 molar ratio.

Another interesting result is obtained when comparing samples deposited in the same conditions but sprayed with different S/Zn starting solution molar ratios (Figure 7-20). In these cases the samples deposited with S/Zn=1 has the best response which was unexpected because since deposition of stoichiometric $CuInS_2$ films requires a sulphur-rich starting solution. Tiwari et al (Tiwari et al. 1985) states that sulphur is volatile and is lost during the deposition of the CIS. ZnS is thought to be more stable during the deposition process and thus doesn't need any excess of sulphur in the starting solution.

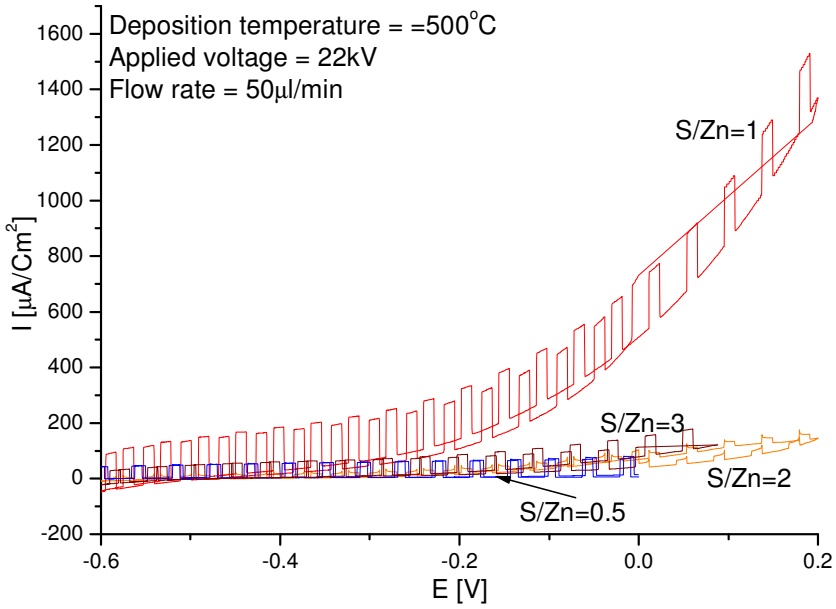

Figure 7-20: Photo-voltammetry of the samples deposited with different starting solution compositions

7.1.2. Summary

In this section the best conditions have been found for the deposition of high quality ZnS films. The as deposited films are photoactive only when they have been sprayed at high temperature (500°C). The applied voltage seems to have less effect (than for the CIS spray) on the photoresponse. Samples deposited at 18 and 22 kV have similar response (shown by the area under the peaks) but samples deposited at 16kV are less responsive to the incident light. The magnitude of effect of the flow rate on the response depends on the starting solution S/Zn molar ratio (where all the samples were deposited at 50µl/min). Finally, among the different S/Zn molar ratios, the samples sprayed at [S]/[Zn]=1 are more photoactive than those sprayed at other values.

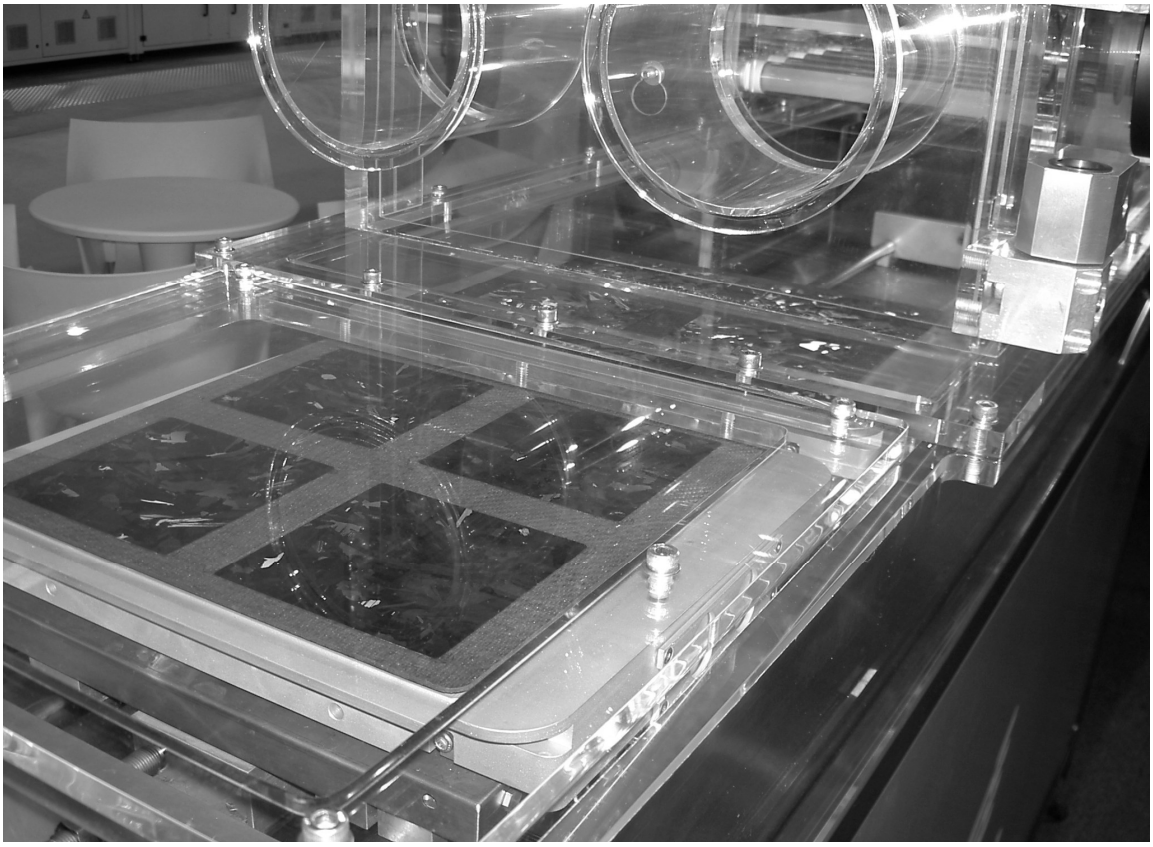

Chapter 8

Solar Cell Devices: Superstrate and Substrate configurations

The results obtained in previous chapters (5, 6 and 7) and the conclusions drawn from these results are used in the following chapter to deposit solar cell devices. Devices were made in both substrate and superstrate configurations. Substrate device comprise FTO/window layer/CIS/back contact. Superstrate device comprise Mo/CIS/buffer or window layer/TCO. The first attempt to build a device used CdS deposited by chemical bath as the window layer in a substrate configuration. CdS is a well known material and its properties have

been studied widely resulting in good efficiency CdS/$CuInS_2$ solar cells (Park et al. 1997; Klaer et al. 2001). The back contact for the substrate configured devices was sputter deposited Mo.

Subsequently, the CdS was replaced with a ZnS film deposited by ESD.

Superstrate configuration solar cells were prepared by depositing CIS onto Mo by ESD. A ZnS layer was then sprayed onto CIS also by ESD. The device was completed by a TCO layer (ZnO) deposited by sputtering.

8.1. Superstrate configuration

8.1.1. CdS Deposition

CdS was deposited using the chemical bath (CB) method (Chang et al. 2007; Devi et al. 2007; Pradhan et al. 2007; Vigil-Galan et al. 2007). Previous experiments at Cranfield (Ketipearachchi 2005) were used to define the CdS deposition process.

The CdS was deposited on glass/FTO substrates. The substrates were cleaned prior to use with deionised water ($18M\Omega cm^{-1}$), acetone (Fisher, 99.8+%) and Decon90. A solution containing $CdCl_2$ (2 mM), ammonium chloride (28 mM) and thiourea (57 mM) was diluted with deionized water to achieve a final concentration of 10.9 mM. The pH was adjusted to 10.5 using a 35% ammonia solution. The solution was continuously stirred at constant speed during the deposition process. The temperature was maintained constant at 70±2°C using a water bath. The CdS was deposited for 15 minutes. The thickness of the CdS layer was measured using the alpha-step method. The thickness was found to be in the range 150-200nm.

The CdS samples were characterised by electrochemical analysis using a three electrode set-up (as described in section 3.3.2). The electrolyte used for the analysis was Na_2S at 0.5M concentration.

The samples show high photocurrent response as seen in Figure 8-1 which confirms that the layer was of good quality.

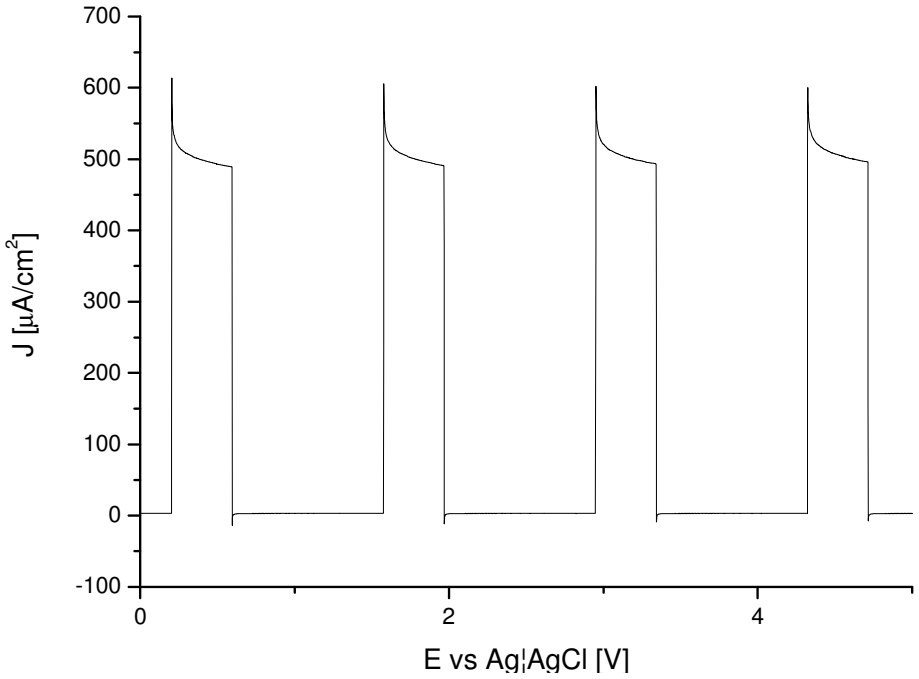

Figure 8-1: Photo-voltammetry analysis of the CdS layer showing the photocurrent response of the as-deposited film.

8.1.2. CIS deposition

The CIS films were deposited using the ESD on to FTO/CdS substrates at the solution flow rates summarised in Table 8-1 . Deposition temperature, needle-substrate distance, solution concentration and voltage were fixed at 450°C, 5cm and 21mM respectively.

Table 8-1: Solution flow rates used during the deposition of the CIS layers

Sample	*Flow rate [µl/min]*
CIS1	200
CIS2	100
CIS3	50
CIS4	25

The CIS films had a chalcopyrite structure as determined by XRD (JCPDS-65-2732) (Figure 8-2). This is contrary to earlier results (chapter 6) for the CIS deposited directly on FTO where the CIS had a sphalerite structure. This shows that CdS affects the growth of the CIS.

The diffractogram of the CIS sample contains peaks which are attributed to the FTO layer. Note there are no CdS peaks due to the CdS layer being very thin and poorly crystalline.

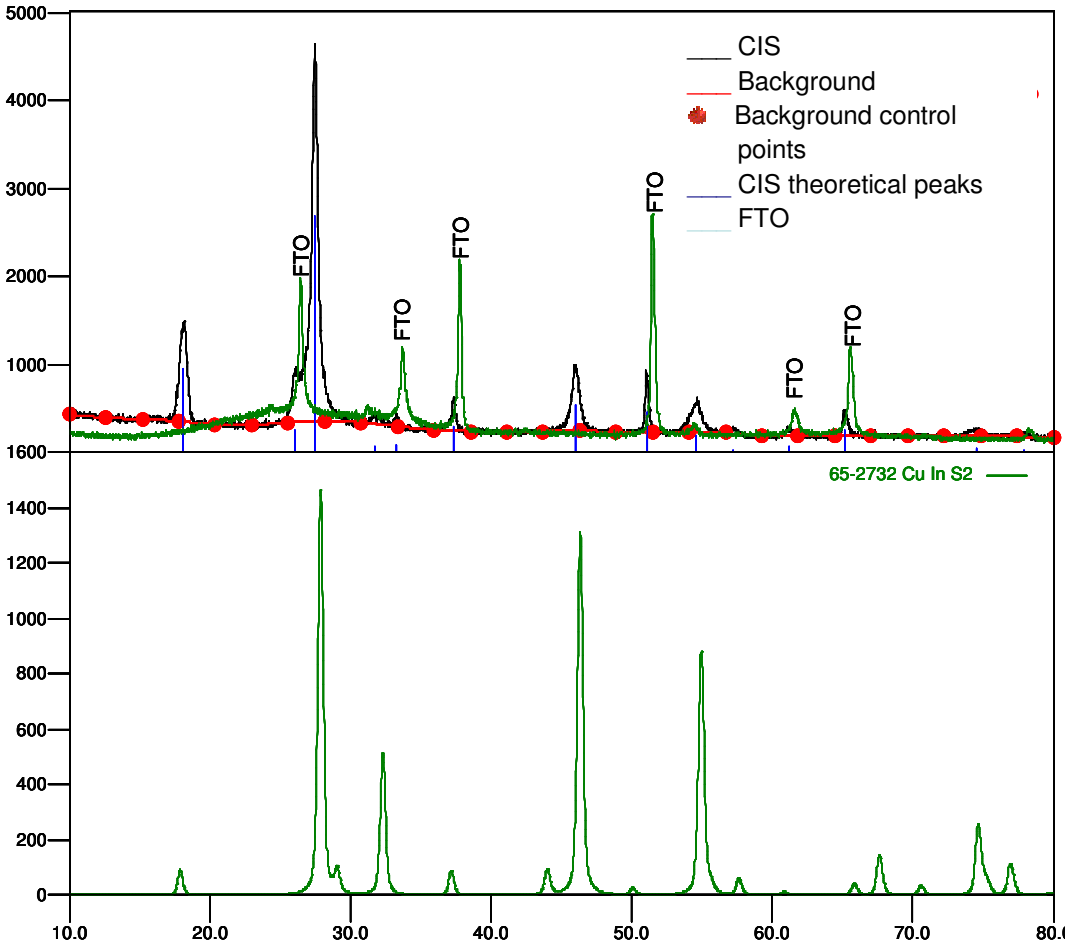

Figure 8-2: (TOP) XRD of the sample CSI2 and the substrate FTO; (BOTTOM) theoretical spectrum of $CuInS_2$ (tetrahedral)

The average grain size along the (111) plane (the most CIS intense peak in Figure 8-2), $S_{(hkl)}$, can be estimated for the (111) plane using the Scherrer equation

$$S_{(111)} = \frac{0.9 \cdot \lambda}{F_{(111)} \cos\theta} \tag{8.1}$$

where F is the FWHM of the (111) peak and λ is the wavelength used during the XRD analysis. The grain size decreases as the deposition flow rate increases as shown in Figure 8-3 which is consistent with the results from the uniformity test in chapter 5.

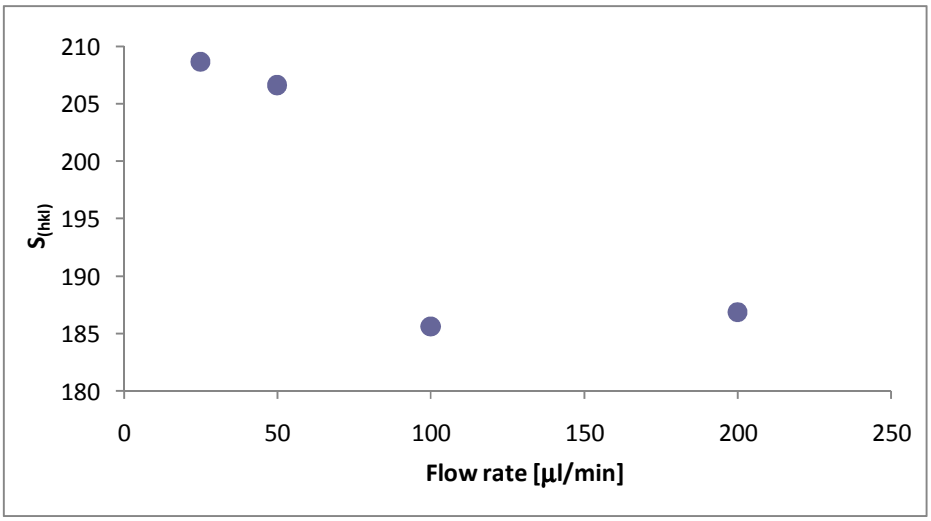

Figure 8-3: Variation of $S_{(hkl)}$ with solution flow rate

The cross-section SEM images of samples CIS2 and CIS3 are shown in Figure 8-4 and Figure 8-5 respectively. The samples have a thickness of 1.8-2.0µm. The samples appear dense, with a columnar structure, but have a high surface roughness. Some round perturbations are seen on the surface of the as-deposited films which are typical of the deposition technique.

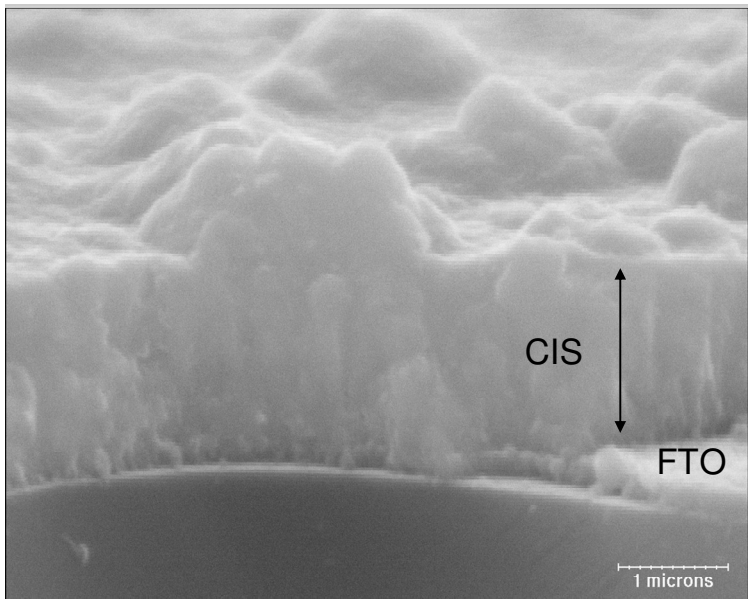

Figure 8-4: SEM cross-section image of sample CIS3

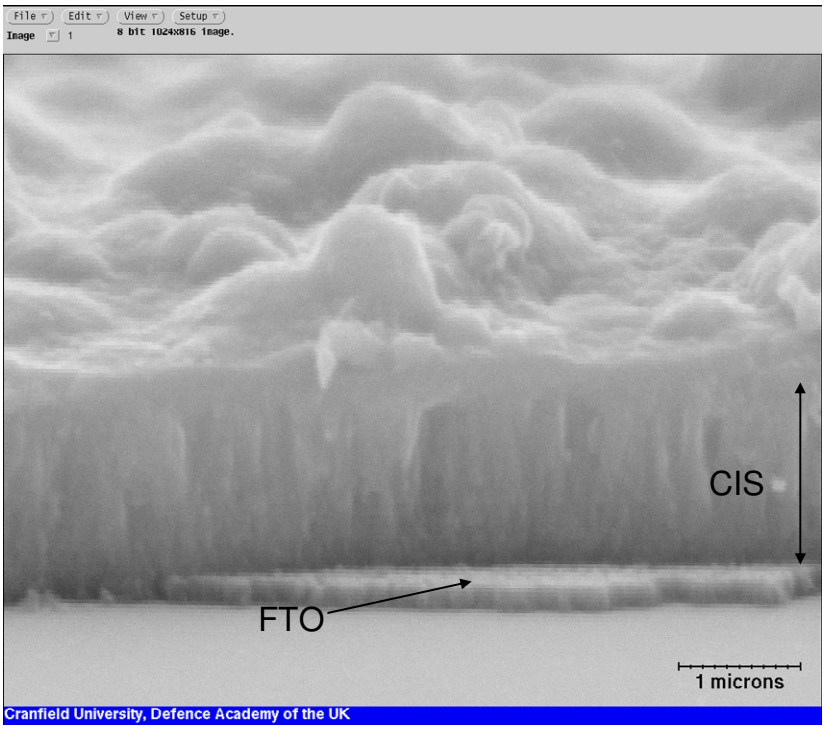

Figure 8-5: SEM cross-section image of sample CIS2.

Photoelectrochemical measurements of the n-p junction

The photoelectrochemical measurements of the n-p junctions were performed using a typical three-electrode configuration as described in section 3.3.2. Eu(IIII) nitrate solution was used as the electrolyte in the setup. The external quantum efficiency (EQE) of the samples CIS1, CIS2 and CIS3 are shown in Figure 8-6. The CdS/CuInS2 junctions show a good response with a the maximum value of 37.5%. The samples show a reduction in EQE with increasing flow rate which suggests that better quality samples are deposited at low flow rates.

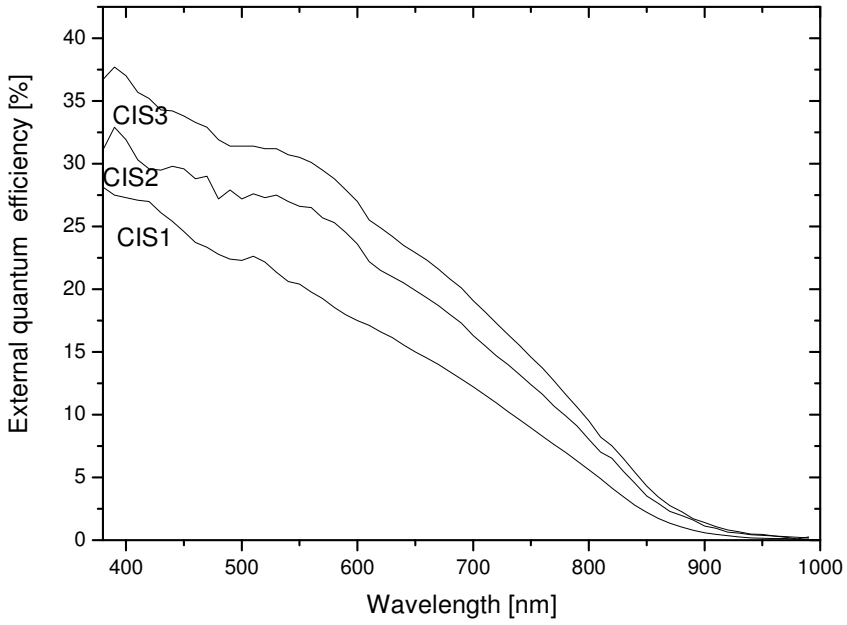

Figure 8-6: EQE measurements of the samples CIS1, CIS2 and CIS3.

The EQE of a semiconductor/electrolyte junction can be calculated using the Gärtner equation

$$\Phi = \frac{1-\exp(-\alpha W)}{1+\alpha L} \tag{8.2}$$

where α is the absorption coefficient of the material, *W* is the width of space-charge region and *L* is the minority-carrier diffusion length. As L→0, the equation can be re-written as

$$\Phi = 1 - \exp(-\alpha W) \tag{8.3}$$

For a direct semiconductor above the E_g, the absorption coefficient can be calculated from

$$\alpha h\nu = A(h\nu - E_g)^{1/2} \tag{8.4}$$

where A is a constant, h is the Planck's constant and ν is the frequency. Using (8.3) and (8.4), the band gap can be obtained by plotting $(ln(1-\Phi)h\nu)^2$ against $h\nu$. The curve should be linear for $h\nu > E_g$.

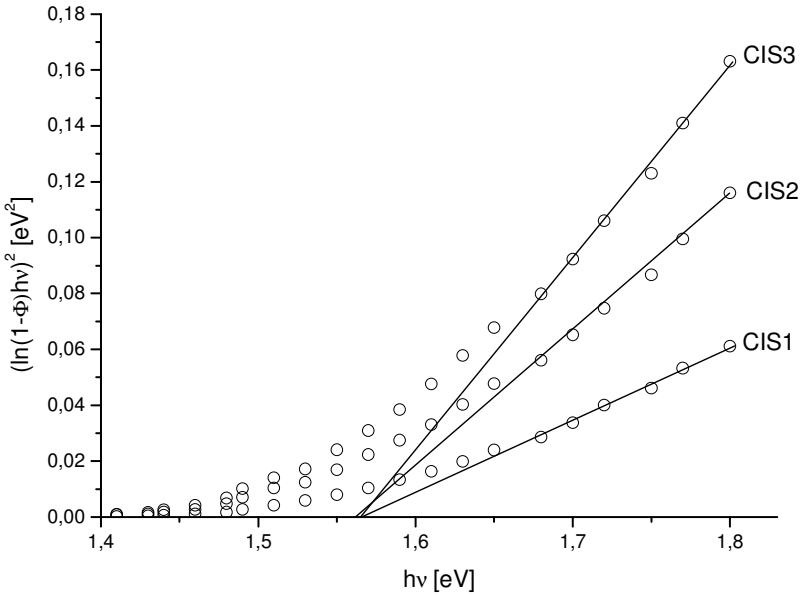

Figure 8-7: Band gap determination for the samples CIS1, CIS2 and CIS3.

The band gap calculated in this way from Figure 8-7 is around 1.56 ± 0.01 eV. This value is in agreement with results published in previous studies (Tell et al. 1971; Deshpande et al. 1983).

From the EQE results it is also possible to calculate the short circuit current of the device. This is done using the American Society of Testing and Materials AM1.5 reference spectrum (American Society for Testing and Materials). The current contribution of each wavelength in the spectrum to the device total current is calculated and is then multiplied by the EQE value at that wavelength. This value is then summed over all the wavelengths giving the maximum possible extractable current density (J_{sc}).

The power (P) is defined as the energy (E) transmitted in a given time (t) and the energy is given by the total number of photons (N_p) multiplied by the energy of the photon (E_p):

$$P = \frac{E}{t} = \frac{N_p E_p}{t} \tag{8.5}$$

The energy can be calculated using the well known Planck's constant (h), the speed of light (c) and wavelength (λ) so the power can be written as

$$P[W] = \frac{N_p h[Js] c[m/s]}{t[s] \lambda[m]} \tag{8.6}$$

The photon flux can be written as

$$\Theta[N_p / m^2 s] = \frac{P[J/s]}{Area[m^2]} \cdot \frac{\lambda[m]}{h[Js]c[m/s]} \tag{8.7}$$

Assuming that all the photons have been converted

$$\frac{I[A]}{Area[m^2]} = \frac{P[J/s]}{Area[m^2]} \cdot \frac{\lambda[m]}{h[Js]c[m/s]} e[C] \tag{8.8}$$

The integral of the AM1.5 curve centred between two extremes (20 wavelengths apart) gives *P/Area [J/sm^2]* e.g. the integral at 20nm is calculated between 10nm and 30nm. The EQE value (at the same λ used as the centre value of the integrals) is extracted from the measurements and then multiplied by the integral of AM1.5 at each wavelength to give the maximum extractable current for that wavelength. Each of these values is then summed to obtain the total current density, J_{sc}, available.

The values obtained for the three cells are summarised in Table 8-2 below.

Table 8-2: Summary of the Jsc value calculated using equation 8.8

Sample	*Jsc [mAcm^{-2}]*
CS1	2.3
CS2	3.0
CS3	3.5

8.1.3. Mo and Au Deposition

Two potential back contact materials were tested. These being Mo and Au. Each CdS/CIS sample was cut in half and one half taken to Bath University for the photoresponse measurements described in 8.1.2. The remaining halves were paired together under a single stainless steel mask for the back contact deposition as seen in Figure 8-8. The area of each spot was 0.126cm^2 ± 0.01cm^2. This setup allowed each half sample to yield 4 independent devices. The Mo back contacts were deposited by DC magnetron sputtering using an Argon pressure of $6 \cdot 10^{-3}$mbar, a power of 456W over a period of 30 minutes to obtain a thickness of approx. 1.5μm. During this process, 4 of the spots were blanked in order to

prevent Mo deposition in all 8 sites. The remaining 4 sites had Au back contacts deposited by using the physical evaporation method. 0.2914g (error) of gold wire (Goodfellow - 99.99%) was sublimated using a power of 65W for 10 minutes resulting in a film thickness of approximately 1 micron.

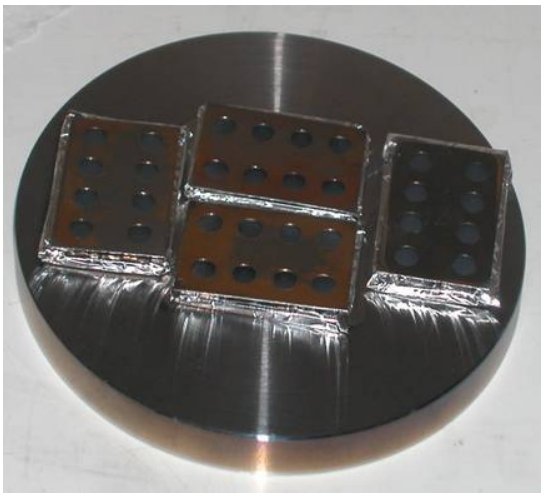

Figure 8-8: Stainless steel mask used to deposit Mo back contacts

The final sample back contact configuration for each half sample can be seen in Figure 8-9 below.

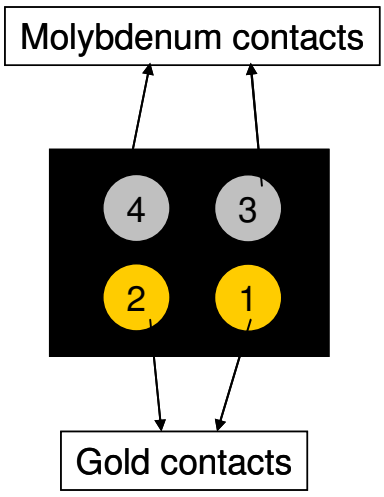

Figure 8-9: Detail of back contact arrangement on CIS cell

The device names used in the following analysis are summarised in Table 8-3 below.

Table 8-3: Summary of device notation for IV curve measurements taken from a set of 30 samples

Device	*CDS*	*CIS*	*Mo/Au*
D1	CDS	CIS1	Mo/Au
D2	CDS	CIS2	Mo/Au
D3	CDS	CIS3	Mo/Au
D4	CDS	CIS4	Mo/Au

The cells were characterised using the IV curve measurement method with a setup as described in section 3.3.1. The four cells show only a slight photo-conductive behaviour as summarised in Table 8-4.

Table 8-4: IV curve analysis results for complete cells

Sample D1					
Au Contact			*Mo Contact*		
Jsc	-4.28	mA/cm^2	Jsc	-4.28	mA/cm^2
Voc	0.221	V	Voc	0.234	V
Jmp	-2.46	mA/cm^2	Jmp	-2.46	mA/cm^2
Vmp	0.11	V	Vmp	0.12	V
FF	28.7	%	FF	29.5	%
eff	0.271	%	eff	0.296	%

Sample D2					
Au Contact			*Mo Contact*		
Jsc	-4.03	mA/cm^2	Jsc	-5.1	mA/cm^2
Voc	0.236	V	Voc	0.213	V
Jmp	-2.19	mA/cm^2	Jmp	-2.58	mA/cm^2
Vmp	0.11	V	Vmp	0.1	V
FF	25.3	%	FF	23.8	%
eff	0.243	%	eff	0.25	%

Sample D3					
	Au Contact			*Mo Contact*	
Jsc	-2.43	mA/cm^2	Jsc	-3	mA/cm^2
Voc	0.233	V	Voc	0.187	V
Jmp	-1.31	mA/cm^2	Jmp	-159	mA/cm^2
Vmp	0.11	V	Vmp	$9\ 10^{-2}$	V
FF	25.3	%	FF	25.5	%
eff	0.144	%	eff	0.143	%

Sample D4					
Au Contact			*Mo Contact*		
Jsc	$-3.00 \cdot 10^{-04}$	mA/cm^2	Jsc	$-3.00 \cdot 10^{-04}$	mA/cm^2
Voc	0.409	V	Voc	0.404	V
Jmp	$-1.49 \cdot 10^{-04}$	mA/cm^2	Jmp	$-1.59 \cdot 10^{-04}$	mA/cm^2
Vmp	0.21	V	Vmp	0.2	V

FF	25	%	FF	25	%
Eff	$3.12 \cdot 10^{-05}$	%	eff	$3.17 \cdot 10^{-05}$	%

The efficiency values obtained are extremely low compared with the values obtained during the electrochemical measurements. This suggests that a poor electrical contact exists between the metal and the CIS layer or that the quality of the Mo contact is poor. The resistivity of the metal is though to be high and this may be the case of the poor response of the devices.

8.1.4. Deposition of ZnS and preparation of FTO/ZnS/CIS/Mo devices.

The CdS layer used above was substituted with a ZnS layer even though it was established that the junction between Mo/$CuInS_2$ needed to be improved. The ZnS film was deposited based on the findings from chapter 7. The films were deposited at high temperature (500°C), high voltage (18kV) and low flow rate (50µl/min) for 4 different deposition times. The molar ratio and the solution concentration were fixed at S/Zn=2 and 0.21M respectively.

An estimation of the deposition time required for a given thickness of film was calculated from the RBS results obtained for the CIS. The value was extrapolated to result in a thickness of approx. 200nm. The thickness of the deposited layer could not be measured using the α-step technique because of high surface roughness of the films especially when the thickness of the layer is close to the limit of the α-step capabilities.

Samples were deposited using different deposition times as shown in Table 8-5. Unfortunately, because of an increase in resistivity as the thickness of the ZnS film increases, the samples deposited for 20, 30 and 60 minutes had to be discarded as the film quality was very poor in the centre of the sprayed face.

Table 8-5: Summary of ZnS film deposition times

Sample	*Time [min]*
ZS1	10
ZS2	20
ZS3	30
ZS4	60

The CIS films and the back contact were deposited onto the ZS1 films using the same 4 conditions described previously for the CdS window layer. None of the films showed photo-response during the IV curve analysis. This is thought to be due to the same problem with the Mo layer as noted in the CdS study.

8.2. Substrate configuration

The substrate devices were fabricated using the following configuration: Glass/Mo/CIS/ZnS/TCO.

CIS films were sprayed onto a Mo layer using the conditions described in section 8.1.2. The ZnS layer was then sprayed onto the CIS layer. The deposition process was complicated by the poor conductivity of the CIS layer compared with the FTO used in the substrate configuration. The ESD method does not deposit well when the conductivity of the substrate is poor (section 5.3.5). A visual analysis of the sample revealed the poor

quality of the as-deposited films. Large spots were visible on the ZnS surface due to the impact of big droplets against the substrate.

The TCO deposition onto the ZnS layer was performed in a number of steps. ZnO was deposited by magnetron sputtering to a thickness of ~ 50 nm then this layer was coated with ITO using a mask with a 5mm diameter hole. The Ni and Al contacts were sputtered in two consecutive depositions using a mask with 2mm diameter holes.

All the superstrate samples showed no photovoltaic behaviour during the IV curve analysis due to the large number of defects on the ZnS which it is thought to have compromised the response of the p-n junction.

8.3. Summary

CdS/CIS junction was deposited on FTO. The EQE was determined and the band gap calculated. The vale was found to be around 1.56eV which is in agreement with results published. The efficiency and the J_{sc} of the cells were about 35% and 3.0mA/cm^2 respectively.

Complete devices using the FTO/CdS/CIS/Mo and FTO/CdS/CIS/Au configurations were produced but a dramatic drop of the efficiency was observed and was attributed to a poor contact between the CIS and the metals.

The CdS layer was replaced with a ZnS layer and a device completed with the following configuration: FTO/ZnS/CIS/Mo. No photoresponse was observed for any of the devices. This is thought to be due to a reduction of the ZnS response and a bad contact between the CIS and Mo.

Finally, substrate configuration cells were prepared which showed no photo-current response. This was caused by a poor conductivity of the CIS layer which affected the ZnS deposition. This resulted in a poor quality ZnS layer and thus a poor p-n junction

Chapter 9:

Conclusions and Recommendations for further work

The final chapter is split in to two main sections. The first section contains the conclusions for the research based on the findings from the experimental programme. The second section outlines some recommendations for future work which would allow further development of the ESD technique for photovoltaic applications.

9.1. Conclusions

One of the key objectives of the research project was to investigate the feasibility of using the ESD technique to deposit $CuInS_2$ and ZnS thin films for photovoltaic applications. The overall aim was to produce $CuInS_2$ in a single step. An ESD rig was successfully designed to deposit thin films which allowed control of applied voltage, solution flow rate, deposition temperature, needle-substrate distance and solution composition (i.e. concentration and molar ratios). The large numbers of variables involved meant that a large number of films, deposited over a wide variety of different experimental conditions, had to be analysed in order to find the optimum deposition conditions. The development of the new image analysis test (uniformity test) for semi transparent films allowed the effect of different deposition conditions to be better understood and thus reduce the number of samples required for a sound understanding of the relationships between variables.

Analysis of the thin films sprayed using stainless steel and glass needles, in conjuction with analysis of the needles, revealed evidence of corrosion damage to the internal walls (of the steel needle) which led to the release of contaminating ions into the aerosol. This rendered stainless steel needles unusable for $CuInS_2$ deposition.

The ESD technique showed its potential and flexibility when it was used to deposit $CuInS_2$ on different substrates. FTO/Glass and aluminium substrates were used, however only the samples deposited onto FTO showed photo-current response. The lack of photocurrent response in the aluminium samples was caused by oxidation of the aluminium substrate during the deposition procedure.

The $CuInS_2$ formation reaction was studied and showed that during formation, the CIS underwent a redox reaction and produced an intermetallic compound. The formation of different precipitates was observed (when $CuCl_2$ and thiourea were used) and their composition analysed. At S/Cu molar ratios between 4 and 5, sulphur (S_8) is formed. At ratios less than 4, an intermetallic compound is formed which was found to be mono-(thiourea)-copper(I)-chloridihydrate. Two isomers were believed to exist in the precipitate, the effects of which were seen during the thermo-analysis.

Two sets of salts ($CuCl_2$ and $Cu(NO_3)_2$) were used to prepare the starting solutions and their behaviours assessed. A different aerosol cone shape was observed in the PIV results. The shape of the peaks in the diffraction patterns of the films deposited from the two salts also differed. This suggested the crystallinity of the films was affected by the different solution properties. The EQE in-solution analysis showed good light-current response for the films prepared from the chloride solution and an absence of response for the nitrate samples.

Different molar ratios were also tested for both nitrate and chloride solutions and the best photoresponse from the as-deposited film was achieved for [S]/[Cu]=5 and [Cu]/[In]=1. The other conditions resulted in additional non-optimum phases which were observed by XRD analysis.

A further objective of the project was to replace the CdS with ZnS primarily in order to remove cadmium from the device, but also to investigate the use of ESD for the deposition of ZnS.

ZnS films showed photo-current response only when they were deposited at high temperature (500°C). The films deposited at higher voltage (18 and 22 kV) showed similarly good photo response properties while the samples deposited at 16kV had poor response to the incident light. Samples deposited at low flow rate (50µl/min) were seen to give the best light-current response.

The molar ratio of the starting solutions (S/Zn) had a strong effect on the final properties of the films. Changing the molar ratio at the optimum deposition conditions was found to change the photocurrent response properties of the films. Of the S/Zn molar ratios studied the most photoactive film was obtained using a starting molar ratio equal to [S]/[Zn]=1.

Thus, our goal was to produce a $CuInS_2$/ZnS device with the potential for a sequential in-line production route. Finally, this production route would be compatible with the superstrate configuration, namely; glass/FTO/ZnS/$CuInS_2$/Mo. Currently we are using sputtered Mo as the back contact. An attempt was also made to prepare a device in the substrate configuration (TCO/ZnS/$CuInS_2$/Mo/glass). In both configurations the devices did not have any photocurrent response. We believe this is due to a poor junction between the $CuInS_2$ and the Mo. These conclusions were based on the results on the analysis of the $CuInS_2$/ZnS junction in solution where a good light-current response was observed. This poor performance was also made worse by the inferior quality of the ZnS layer compared to the CdS.

To conclude, during this project a powerful deposition method for photovoltaic materials was successfully developed. A new test for uniformity analysis was designed which is equally applicable to any semi-transparent thin film applications.
The deep study of the CIS layers deposited in different conditions represented the nucleus of this project. A further increment was achieved with the deposition of the ZnS layer. Issues with the back contact material tested unfortunately prevented the full potential of the

CIS-based devices from being realized. This was especially frustrating as the efficiencies of the junctions were so good prior to full device configuration.

9.2. Further work

$CuInS_2$ and ZnS photoactive films were both successfully produced using the ESD method. However, at the moment the performance of completed devices is significantly lower than expected. This is believed to be due to a poor junction between the $CuInS_2$ and the Mo. In order to improve this junction, deposition (ideally by ESD) of an additional thin buffer layer - $Cu_xIn_yS_z$, rich in copper– prior to the Mo deposition should be performed. A Cu rich layer is beneficial to device performance; however a wide range of compositions should be considered in order to measure the effect on the IV characteristics of completed devices. The same layer could be deposited by sputtering. A deep study of the metal deposition is necessary to control the thickness and the diffusion of the thin layer into the bulk. Intensive studies are also necessary to improve the quality of the Mo layer used as back contact. The resistivity of the layer has to be checked and possibly reduced.

Cone shape and particles velocity need to be further studied using the PIV technique for different molar ratios which could modify the properties of the starting solution.

Samples deposited by ESD show small grain size crystals which could affect the response of the material during the performances of the device. Annealing processes over a number of times/temperatures/ambient atmospheres could be investigated for $CuInS_2$ films and the effect on the IV characteristics studied.

A better understanding of the effect of the CIS growing process on the aerosol cone could be done using Laser Doppler Anemometry (LDA) because this can measure particle velocity and turbulence variation in time to very high resolution (up to 10kHz sampling rate) and would allow a more accurate characterisation of aerosol structure to be gained.

The ESD rig should be re-developed in a horizontal configuration instead of the vertical orientation used during this project. The growth of small crystals at the tip of the glass needle was observed during some depositions (especially at 25µl/min). The horizontal orientation of the needle could possibly eliminate this.

The possibility of engineering the bandgap of the CIS film could be investigated by the addition of doping elements such as aluminium. A suitable salt could be added to the solution in various concentrations and the effect on the films properties measured.

References

Afifi, H. H., S. A. Mahmoud, et al. (1995). "Structural study of ZnS thin films prepared by spray pyrolysis." Thin Solid Films 263(2): 248-251.

Alonso, M. I., K. Wakita, et al. (2001). "Optical functions and electronic structure of $CuInSe_2$, $CuGaSe_2$, $CuInS_2$, and $CuGaS_2$." Physical Review B 63(7): 075203.

Alvarez García, J. (2002). Characterisation of CuInS2 Films for Solar Cell Applications by Raman Spectroscopy. Department of electronic. Barcelona, Universitat de Barcelona.

American Society for Testing and Materials, A. ASTM G-173-03. .

Annica Andersson, N. J. P. B. N. Y. D. L. W. R. S. (1998). "Fluorine Tin Oxide as an Alternative to Indium Tin Oxide in Polymer LEDs." Advanced Materials 10(11): 859-863.

Asenjo, B., A. M. Chaparro, et al. (2008). "Study of $CuInS_2$/ZnS/ZnO solar cells, with chemically deposited ZnS buffer layers from acidic solutions." Solar Energy Materials and Solar Cells 92(3): 302-306.

Asenjo, B., Chaparro, A. M., Gutiérrez, M. T. and Herrero, J. (2006). "Electrochemical growth and properties of $CuInS_2$ thin films for solar energy conversion." Thin Solid Films 511-512: 117-120.

Assmann, L., J. C. Bernede, et al. (2005). "Study of the Mo thin films and Mo/CIGS interface properties." Applied Surface Science 246(1-3): 159-166.

Berkland, C., D. W. Pack, et al. (2004). "Controlling surface nano-structure using flow-limited field-injection electrostatic spraying (FFESS) of poly(,-lactide-co-glycolide)." Biomaterials 25(25): 5649-5658.

Bihri, H. and Abd-Lefdil, M. (1999). "Effect of an initially sulphur-rich sprayed solution on $CuInS_2$ thin films." Thin Solid Films 354(1-2): 5-8.

Binsma, J. J. M., Giling, L. J. and Bloem, J. (1980). "Phase relations in the system Cu_2S-In_2S_3." Journal of Crystal Growth 50(2): 429-436.

Blackmore, J. M. and A. G. Cullis (1991). "The structure of ZnS thin films deposited by r.f. sputtering." Thin Solid Films 199(2): 321-334.

Bouzouita, H., Bouguila, N. and Dhouib, A. (1999). "Spray pyrolysis of $CuInS_2$." Renewable Energy 17(1): 85-93.

Camus, C., Allsop, N. A., Gledhill, S. E., Bohne, W., Rohrich, J., Lauermann, I., Lux-Steiner, M. C. and Fischer, C. H. "Properties of Spray ILGAR $CuInS_2$ thin films." Thin Solid Films In Press, Corrected Proof.

Chang, C. H. and Y. L. Lee (2007). "Chemical bath deposition of CdS quantum dots onto mesoscopic TiO_2 films for application in quantum-dot-sensitized solar cells." Applied Physics Letters 91(5).

Chen, C. H., Emond, M. H. J., Kelder, E. M., Meester, B. and Schoonman, J. (1999). "Electrostatic Sol-Spray Deposition of nanostructured Cceramic Thin Films ELECTROSTATIC SOL-SPRAY DEPOSITION OF NANOSTRUCTURED CERAMIC THIN FILMS." Journal of Aerosol Science 30(7): 959--967.

Chen, C. H., Kelder, E. M., Jak, M. J. G. and Schoonman, J. (1996). "Electrostatic spray deposition of thin layers of cathode materials for lithium battery." Solid State Ionics 86-88(Part 2): 1301--1306.

Chen, C. H., Kelder, E. M., van der Put, P. and Schoonman, J. (1996). "Morphology control of thin $LiCoO_2$ films fabricated using the electrostatic spray deposition (ESD) technique." Journal of materials chemistry 6(5): 765-771.

Chen, X., L. Jia, et al. (2005). "Spraying modes in coaxial jet electrospray with outer driving liquid." PHYSICS OF FLUIDS 17(3): 032101.

Choy, K. L. (2001). "Processing-structure-property of nanocrystalline materials produced using novel and cost-effective ESAVD-based methods." Materials Science and Engineering: C 16(1-2): 139--145.

Choy, K. L. (2003). "Chemical vapour deposition of coatings." Progress in Materials Science 48(2): 57--170.

Choy, K. L. and B. Su (2001). "Growth behavior and microstructure of CdS thin films deposited by an electrostatic spray assisted vapor deposition (ESAVD) process." Thin Solid Films 388(1-2): 9--14.

Choy, K., Bai, W., Charojrochkul, S. and Steele, B. C. H. (1998). "The development of intermediate-temperature solid oxide fuel cells for the next millennium." Journal of Power Sources 71: 361-369.

Cloupeau, M. and B. Prunet-Foch (1989). "Electrostatic spraying of liquids in cone-jet mode." Journal of Electrostatics 22(2): 135-159.

Cloupeau, M. and B. Prunet-Foch (1990). "Electrostatic spraying of liquids: Main functioning modes." Journal of Electrostatics 25(2): 165-184.

Cloupeau, M. and B. Prunet-Foch (1994). "Electrohydrodynamic spraying functioning modes: a critical review." Journal of Aerosol Science 25(6): 1021-1036.

Coleman, H. and Steele, W. J. (1999). Experimentation and Uncertainty Analysis for Engineers. New York, John Wiley and Sons, Inc.

Cotton, F. A. and G. Wilkinson (1988). Adavanced inorganic chemistry, John Wiley & Sons.

De La Mora, J. F. (1992). "The effect of charge emission from electrified liquid cones." Journal of Fluid Mechanics 243.

De La Mora, J. F. and I. G. Loscertales (1994). "The current emitted by highly conducting Taylor cones." Journal of Fluid Mechanics 260: 155-184.

Dedova, T., M. Krunks, et al. (2005). "ZnS thin films deposited by spray pyrolysis technique." physica status solidi (c) 2(3): 1161-1166.

Deshpande, A. P., V. B. Sapre, et al. (1983). "X-ray spectroscopic study of ternary chalcopyrite semiconductors of the type $CuMS_2$ (M=Al,Ga,In,Tl)." Journal of Physics C: Solid State Physics 16(13): L433-L435.

Devi, R., P. Purkayastha, et al. (2007). "Photoelectric properties of CdS thin film prepared by chemical bath deposition." Indian Journal of Pure & Applied Physics 45(7): 624-627.

Dole, M., L. L. Mack, et al. (1968). "Molecular Beams of Macroions." The J ournal of Chemical Physics 49(5): 2240-2249.

Dzionk, C., Brussler, M. and Metzner, H. (1992). "Development of $CuInS_2$ solar cell material by PAC: bulk phases, thin films, and nuclear reaction doping." Nuclear

Instruments and Methods in Physics Research Section B: Beam Interactions with Materials and Atoms 63(1-2): 231-235.

Elidrissi, B., M. Addou, et al. (2001). "Structure, composition and optical properties of ZnS thin films prepared by spray pyrolysis." Materials Chemistry and Physics 68(1-3): 177-179.

Ganan-Calvo, A. M. and A. Barrero (1996). "A global model for the electrospraying of liquids in steady cone-jet mode." Journal of Aerosol Science 27(Supplement 1): S179-S180.

Ganan-Calvo, A. M., J. Davila, et al. (1997). "Current and droplet size in the electrospraying of liquids. Scaling laws." Journal of Aerosol Science 28(2): 249-275.

Garg, J. C., R. P. Sharma, et al. (1988). "Characterization of p-$CuInSe_2$ films for photovoltaics grown by a chemical deposition technique." Thin Solid Films 164: 269-273.

Gode, F., C. Gumus, et al. (2007). "Investigations on the physical properties of the polycrystalline ZnS thin films deposited by the chemical bath deposition method." Journal of Crystal Growth 299(1): 136-141.

Goldemberg, J. E. (2000). World Energy Assessment: Energy and the Challenge of UNDP / UN-DESA / World Energy Council, 500 pages

Gordillo, G., M. Grizalez, et al. (1998). "Structural and electrical properties of DC sputtered molybdenum films." Solar Energy Materials and Solar Cells 51(3-4): 327-337.

Grace J. M. and Marijnissen J. C. M. (1994). "A review of liquid atomization by electrical means." Journal of Aerosol Science 25(6): 1005-1019.

Greenwood, N. N. and A. Earnshaw (1984). Chemistry of the elements, Pergamon Press.

Grigoriev, D. and Choy, K. L. (2004). "Aerosol deposition of films in an electrical field: modelling and experiment." Scripta Materialia 51(9): 857--861.

Guillen, C. and J. Herrero (2003). "Low-resistivity Mo thin films prepared by evaporation onto 30 cmx30 cm glass substrates." Journal of Materials Processing Technology 143-144: 144-147.

Gurinovich, L. I., V. S. Gurin, et al. (1998). "Crystal structure and optical properties of $CuInS_2$ nanocrystals in a glass matrix." Physica Status Solidi B-Basic Research 208(2): 533-540.

Hahn, T., H. Metzner, et al. (2001). "Order and disorder in epitaxially grown $CuInS_2$." Thin Solid Films 387(1-2): 83-85.

Hahn, T., Metzner, H., Plikat, B. and Seibt, M. (2001). "Order and disorder in epitaxially grown $CuInS_2$." Thin Solid Films 387(1-2): 83-85.

Hou, X. and Choy, K.-L. (2005). "Synthesis and characteristics of $CuInS_2$ films for photovoltaic application." Thin Solid Films 480-481: 13--18.

Hou, X. and K.-L. Choy (2004). "Deposition mechanism and structural characterization of TiO2 films produced using ESAVD method." Surface and Coatings Technology 180-181: 15--19.

Huang, H., Yao, X., Wu, X. Q., Wang, M. Q. and Zhang, L. Y. (2004). "Morphology control of ferroelectric lead titanate thin films prepared by electrostatic spray deposition." Thin Solid Films 458(1-2): 71--76.

IEA, I. E. A. (2004). World Energy Outlook.

IPCC, I. P. o. C. C. (2007). Mitigation of Climate Change.

Iribarne, J. V. and B. A. Thomson (1976). "On the evaporation of small ions from charged droplets." The Journal of Chemical Physics 64(6): 2287-2294.

Jaffe, J. E. and A. Zunger (1983). "Anion displacements and the band-gap anomaly in ternary ABC_{2} chalcopyrite semiconductors." Physical Review B 27(8): 5176.

Jaffe, J. E. and A. Zunger (1983). "Electronic structure of the ternary chalcopyrite semiconductors $CuAlS_2$, $CuGaS_2$, $CuInS_2$, $CuAlSe_2$, $CuGaSe_2$, and $uInSe_2$." Physical Review B 28(10): 5822.

Jaworek and A. Krupa (1999). "Jet and drops formation in electrohydrodynamic spraying of liquids. A systematic approach " Experiments in Fluids Volume 27, Number 1 43-52.

Ketipearachchi, U. S. (2005). Fabrication and characterization of chemical bath deposited CdS thin films for CdTe based solar cells. Department of Materials and Medical Science. Shrivenham, Swiindon, Cranfield.

Klaer, J., K. Siemer, et al. (2001). "9.2% efficient $CuInS_2$ mini-module." Thin Solid Films 387(1-2): 169-171.

Krunks, A. M., A. E. Mellikov, et al. (1997). "Copper sulfides by chemical spray pyrolysis process." Physica Scripta T69: 189-192.

Krunks, M., Bijakina, O., Varema, T., Mikli, V. and Mellikov, E. (1999). "Structural and optical properties of sprayed $CuInS_2$films." Thin Solid Films 338(1-2): 125-130.

Krunks, M., Kijatkina, O., Mere, A., Varema, T., Oja, I. and Mikli, V. (2005). "Sprayed $CuInS_2$ films grown under Cu-rich conditions as absorbers for solar cells." Solar Energy Materials and Solar Cells 87(1-4): 207-214.

Krunks, M., Kijatkina, O., Rebane, H., Oja, I., Mikli, V. and Mere, A. (2002). "Composition of $CuInS_2$ thin films prepared by spray pyrolysis." Thin Solid Films 403-404: 71-75.

Krunks, M., Leskelä, T., Mannonen, R. and Niinistö, L. (1998). "Thermal Decomposition of Copper(I) Thiocarbamide Chloride Hemihydrate." Journal of Thermal Analysis and Calorimetry 53(2): 355-364.

Krunks, M., Mere, A., Katerski, A., Mikli, V. and Krustok, J. (2006). "Characterization of sprayed $CuInS_2$ films annealed in hydrogen sulfide atmosphere." Thin Solid Films 511-512: 434-438.

Krunks, M., Mikli, V., Bijakina, O. and Mellikov, E. (1999). "Growth and recrystallization of $CuInS_2$ films in spray pyrolytic process." Applied Surface Science 142(1-4): 356-361.

Krunks, M., O. Kijatkina, et al. (2002). "Composition of $CuInS_2$ thin films prepared by spray pyrolysis." Thin Solid Films 403-404: 71-75.

Krunks, M., T. Leskelä, et al. (1998). "Thermal Decomposition of Copper(I) Thiocarbamide Chloride Hemihydrate." Journal of Thermal Analysis and Calorimetry 53(2): 355-364.

Krunks, M., T. Leskelä, et al. (1998). "Thermal Decomposition of Copper(I) Thiocarbamide Chloride Hemihydrate." Journal of Thermal Analysis and Calorimetry 53(2): 357-364.

Krunks, M., V. Mikli, et al. (1999). "Growth and recrystallization of $CuInS_2$ films In spray pyrolytic process." Applied Surface Science 142(1-4): 356-361.

Lee, J. D. (1991). Concise Inorganic Chemistry Chapman &Hall.

G. C., Pratsinis, S. E., Schoonman, J. and Jansen, J. A. (2006). "Morphology of calcium phosphate coatings for biomedical applications deposited using Electrostatic Spray Deposition." Thin Solid Films 503(1-2): 69-78.

Leeuwenburgh, S. C. G., Wolke, J. G. C., Schoonman, J. and Jansen, J. A. (2004). "Influence of precursor solution parameters on chemical properties of calcium phosphate coatings prepared using Electrostatic Spray Deposition (ESD)." Biomaterials 25(4): 641-649.

Leeuwenburgh, S. C. G., Wolke, J. G. C., Schoonman, J. and Jansen, J. A. (2005). "Influence of deposition parameters on morphological properties of biomedical calcium phosphate coatings prepared using electrostatic spray deposition." Thin Solid Films 472(1-2): 105-113.

Leeuwenburgh, S. C. G., Wolke, J. G. C., Schoonman, J. and Jansen, J. A. (2006). "Deposition of calcium phosphate coatings with defined chemical properties using the electrostatic spray deposition technique." Journal of the European Ceramic Society 26(4-5): 487-493.

Leeuwenburgh, S., Wolke, J., Schoonman, J. and Jansen, J. (2003). "Electrostatic spray deposition (ESD) of calcium phosphate coatings." Journal of Biomedical Materials Research Part A 66A(2): 330-334.

Leicht, M., Stenkamp, D., Strunk, H. P., Wolf, D., Eisner, B. and Muller, G. (1999). "Nanoscopic crystallography of chalcopyrite $CuInS_2$ by techniques of convergent-beam electron diffraction." Philosophical Magazine A 79(5): 1033 - 1043.

Lopez, M. C., J. P. Espinos, et al. (2005). "Growth of ZnS thin films obtained by chemical spray pyrolysis: The influence of precursors." Journal of Crystal Growth 285(1-2): 66-75.

Luque, A. and S. Hegedus (2002). Hand book of photovoltaic science and engineering.

Marsillac, S., M. C. Zouaghi, et al. (2003). "Evolution of the properties of spray-deposited $CuInS_2$thin films with post-annealing treatment." Solar Energy Materials and Solar Cells 76(2): 125-134.

Matson, R. J., O. Jamjoum, et al. (1984). "Metal contacts to CuInSe2." Solar Cells 11(3): 301-305.

Mere, A., O. Kijatkina, et al. (2003). "Electrical properties of sprayed $CuInS_2$ films for solar cells." Journal of Physics and Chemistry of Solids 64(9-10): 2025-2029.

Miao, P., Balachandran, W. and Wang, J. L. (2001). "Electrostatic generation and theoretical modelling of ultra fine spray of ceramic suspensions for thin film preparation." Journal of Electrostatics 51-52: 43-49.

Moller, J., C. H. Fischer, et al. (1998). $CuInS_2$ as an extremely thin absorber in an eta solar cell. 2nd world conference and exhibition on photovoltaic solar energy conversion. Vienna, Austria.

Morrison, R. S. (1980). Electrochemistry at semiconductor and oxidized metal electrodes, Plenum Press.

Muller, K., R. Scheer, et al. (2004). "Preparation of stoichiometric $CuInS_2$ surfaces." Thin Solid Films 451-452: 120-123.

Nakanishi, Y., G. Shimaoka, et al. (1990). "Preparation of ZnS:Ag,Cl thin films emitting blue luminescence." Thin Solid Films 187(2): 323-329.

Neagu, R., Perednis, D., Princivalle, A. and Djurado, E. (2006). "Influence of the process parameters on the ESD synthesis of thin film YSZ electrolytes." Solid State Ionics In Press, Corrected Proof.

Neagu, R., Perednis, D., Princivalle, A. and Djurado, E. (2006). "Zirconia coatings deposited by electrostatic spray deposition A chemical approach." Solid State Ionics 177(17-18): 1451-1460.

Oja, I., Nanu, M., Katerski, A., Krunks, M., Mere, A., Raudoja, J. and Goossens, A. (2005). "Crystal quality studies of $CuInS_2$ films prepared by spray pyrolysis." Thin Solid Films 480-481: 82-86.

Olekseyuk, I. D., Davidyuk, H. Y., Parasyuk, O. V., Voronyuk, S. V., Halka, V. O. and Oksyuta, V. A. (2000). "Phase diagram and electric transport properties of samples

of the quasi-binary system $CuInS_2CdS$." Journal of Alloys and Compounds 309(1-2): 39-44.

Ortega-Lopez, M. and A. Morales-Acevedo (1996). Properties of $CuInS_2$ thin films for solar cells prepared by spray pyrolysis. Photovoltaic Specialists Conference, 1996., Conference Record of the Twenty Fifth IEEE.

Ortega-Lopez, M. and A. Morales-Acevedo (1998). "Characterization of $CuInS_2$ thin films for solar cells prepared by spray pyrolysis." Thin Solid Films 330(2): 96-101.

Park, G. C., H. D. Chung, et al. (1997). "Photovoltaic characteristics of $CuInS_2$/CdS solar cell by electron beam evaporation." Solar Energy Materials and Solar Cells 49(1-4): 365-374.

Pathan, H. M. and Lokhande, C. D. (2004). "Chemical deposition and characterization of copper indium disulphide thin films." Applied Surface Science 239(1): 11-18.

Peza-Tapia, J. M., V. M. Sanchez-Resendiz, et al. (2005). "Electrical and optical characterization of Na: $CuInS_2$ thin films grown by spray pyrolysis." Thin Solid Films 490(2): 142-145.

Pradhan, B., A. K. Sharma, et al. (2007). "Conduction studies on chemical bath-deposited nanocrystalline CdS thin films." Journal of Crystal Growth 304(2): 388-392.

PV TRAC, P. T. R. A. C. (2005). "A Vision for Photovoltaic Technology."

Ramanathan, K., M. A. Contreras, et al. (2003). "Properties of 19.2% efficiency ZnO/CdS/$CuInGaSe_2$ thin-film solar cells." Progress in Photovoltaics: Research and Applications 11(4): 225-230.

Rasband, W. (2007). ImageJ National Institutes of Health, USA.

Rayleigh, L. (1879). "On the Capillary Phenomena of Jets " Proceedings of the Royal Society of London 29.

Roncallo, S., J. D. Painter, et al. "A method to quantify the degree of uniformity of thickness of thin films." Thin Solid Films In Press, Corrected Proof.

Roncallo, S., Painter, J. D., Cousin, M. A., Rogers, K. D. and Lane, D. W. (2006). Effect of the deposition conditions on the uniformity of $CuInS_2$ thin films prepared by electrostatic spray deposition. 21th European photovoltaiv solar energy conference. Dresden, Germany: 1973.

Roncallo, S., Painter, J. D., Rogers, K. D., Lane, D. W., Cartwright, M., Healy, M. J. F., Ritchie, S. A. and Dale, P. J. (2007). THE EFFECT OF DIFFERENT STARTING SOLUTIONS ON $CuInS_2$ BASED SOLAR CELLS. 22nd European Photovoltaic Solar Energy Conference,. Milan, Italy, 2335.

Rosell-Llompart, J. and J. Fernandez de la Mora (1994). "Generation of monodisperse droplets 0.3 to 4 [mu]m in diameter from electrified cone-jets of highly conducting and viscous liquids." Journal of Aerosol Science 25(6): 1093-1119.

Sankapal, B. R., E. Goncalves, et al. (2004). "Wide band gap p-type windows by CBD and SILAR methods." Thin Solid Films 451-452: 128-132.

Schmelzeisen-Redeker, G., L. Butfering, et al. (1989). "Desolvation of ions and molecules in thermospray mass spectrometry." International Journal of Mass Spectrometry and Ion Processes 90(2): 139-150.

Schoonman, J. and Kelder, E. M. (1997). "Thin film solid electrolytes and electrodes for rechargeable lithium-ion batteries." Journal of Power Sources 68(1): 65--68.

Scofield, J. H., A. Duda, et al. (1995). "Sputtered molybdenum bilayer back contact for copper indium diselenide-based polycrystalline thin-film solar cells." Thin Solid Films 260(1): 26-31.

Szymaszek, A., Biernat, J. and Pajdowski, L. (1977). "Polarographic studies on the effect of thiourea on deposition of copper in the presence of 2M H2SO4." Electrochimica Acta 22(4): 359-364.

Taniguchi, I., van Landschoot, R. C. and Schoonman, J. (2003). "Electrostatic spray deposition of $Gd_{0.1}Ce_{0.9}O_{1.95}$ and $La_{0.9}Sr_{0.1}Ga_{0.8}Mg_{0.2}O_{2.87}$ thin films." Solid State Ionics 160(3-4): 271--279.

Taniguchi, I., van Landschoot, R. C. and Schoonman, J. (2003). "Fabrication of $La_{1-x}Sr_xCo_{1-y}Fe_yO_3$ thin films by electrostatic spray deposition." Solid State Ionics 156(1-2): 1--13.

Taylor, G. (1964). "Disintegration of water drops in an electric field " Proceeding of the royal society of London 280: 383-397.

Tell, B., J. L. Shay, et al. (1971). "Electrical Properties, Optical Properties, and Band Structure of $CuGaS_2$ and $CuInS_2$." Physical Review B 4(8): 2463.

Tembhurkar, Y. D. and Hirde, J. P. (1992). "Structural, optical and electrical properties of spray pyrolytically deposited films of copper indium diselenide." Thin Solid Films 215(1): 65-70.

Thomson, B. A. and J. V. Iribarne (1979). "Field induced ion evaporation from liquid surfaces at atmospheric pressure." The Journal of Chemical Physics 71(11): 4451-4463.

Tiwari, A. N., Pandya, D. K. and Chopra, K. L. (1985). "Electrical and optical properties of single-phase $CuInS_2$ films prepared using spray pyrolysis." Thin Solid Films 130(3-4): 217-230.

Ugai, Y. A., Semenov, V. N. and Averbakh, E. M. (1981). "Influence of complex formation on the production of Copper Sulphide films from aqueous solution of thiourea and copper(II) chloride by atomisation " Russian Journal of Inorganic Cemistry 26: 271-273.

Vigil-Galan, O., A. Morales-Acevedo, et al. (2007). "Characterization of CBD-CdS layers chemical bath and their relation with the with different S/Cd ratios in the efficiency of CdS/CdTe solar cells." Thin Solid Films 515(15): 6085-6088.

Wei, S.-H., S. B. Zhang, et al. (1999). "Band structure and stability of zinc-blende-based semiconductor polytypes." Physical Review B 59(4): R2478.

Wilhelm, T., Berenguier, B., Aggour, M., Kanis, M. and Lewerenz, H.-J. (2006). "Efficient $CuInS_2$ (CIS) solar cells by photoelectrochemical conditioning." Comptes Rendus Chimie 9(2): 294-300.

William, C. H. (1982). Aerosol Technology: Properties, Behavior, and Measurement of Airborne Particles. New York, John Wiley and Sons.

Working Group 3, S. T. a. A. G. o. t. E. P. t. P. (2007). A strategic research agenda for photovoltaic solar energy technology.

Wu, X., J. C. Keane, et al. (2001). 16.5%-efficient CdS/CdTe polycrystalline thin-film solar cell. 17th European Photovoltaic Solar Energy Conference, Munich, Germany.

Yamaga, S., A. Yoshikawa, et al. (1990). "Electrical and optical properties of donor doped ZnS films grown by low-pressure MOCVD." Journal of Crystal Growth 86(1-4): 252-256.

Yu, Y., Shui, J. L. and Chen, C. H. (2005). "Electrostatic spray deposition of spinel Li4Ti5O12 thin films for rechargeable lithium batteries." Solid State Communications 135(8): 485--489.

Yu, Y., Shui, J. L., Jin, Y. and Chen, C. H. (2006). "Electrochemical performance of nano-SiO2 modified $LiCoO_2$ thin films fabricated by electrostatic spray deposition (ESD)." Electrochimica Acta 51(16): 3292-3296.

Yukawa, T., K. Kuwabara, et al. (1996). "Electrodeposition of $CuInS_2$ from aqueous solution (II) electrodeposition of $CuInS_2$ film." Thin Solid Films 286(1-2): 151-153.

Zeleny, J. (1917). "Instability of Electrified Liquid Surfaces." Physical Review 10(1): 1.

Zhang, S. Q., Xie, S. and Chen, C. H. (2005). "Fabrication and electrical properties of Li3PO4-based composite electrolyte films." Materials Science and Engineering B 121(1-2): 160-165.

Zouaghi, M. C., T. B. Nasrallah, et al. (2001). "Physico-chemical characterization of spray-deposited $CuInS_2$ thin films." Thin Solid Films 382(1-2): 39-46.